Energy Reconstruction for Radio Neutrino Detectors

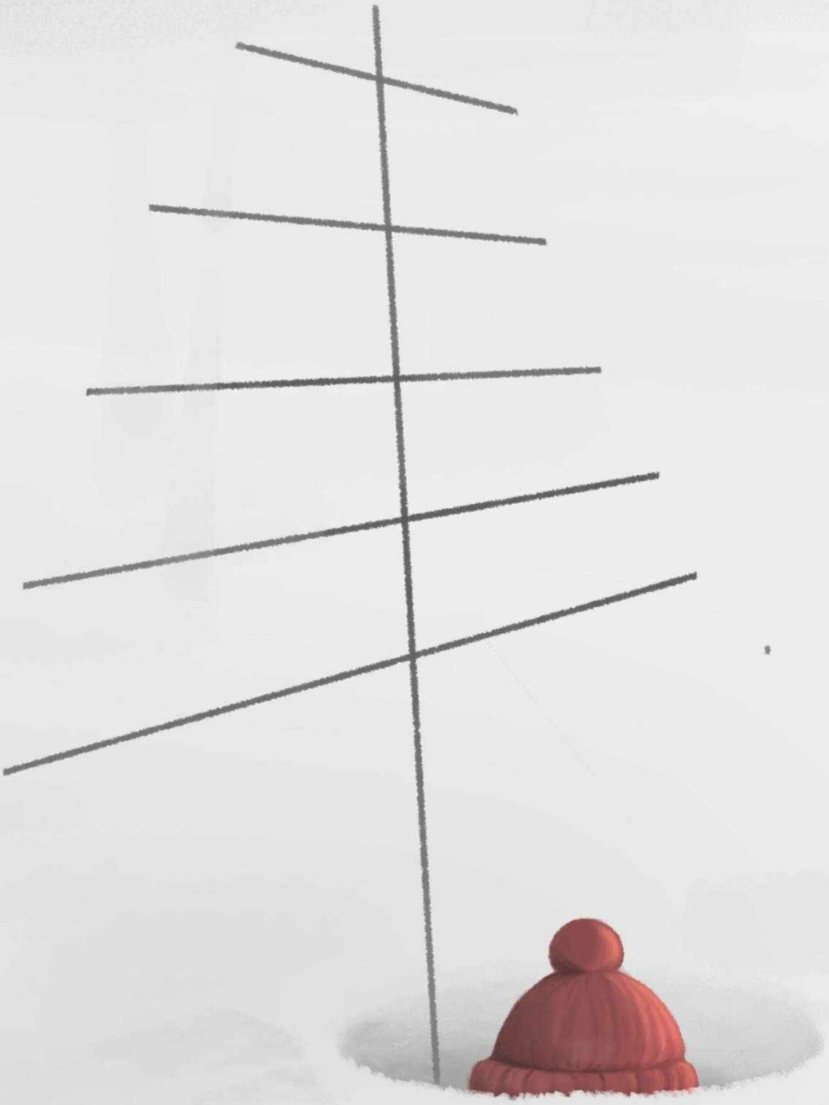

Christoph
Welling

front cover art by Eva Welling

Energy Reconstruction for Radio Neutrino Detectors

der Naturwissenschaftlichen Fakultät
der Friedrich-Alexander-Universität Erlangen-Nürnber
zur Erlangung des Doktorgrades Dr. rer. nat.
vorgelegt von
Christoph Welling

Als Dissertation genehmigt von der
Naturwissenschaftlichen Fakultät der Friedrich-Alexander-Universitat
Erlangen-Nürnberg

Tag der mündlichen Prüfung:	24.6.2022
Vorsizender des Promotionsorgans:	Prof. Dr. Wolfgang Achtziger
Gutachter:	Prof. Dr. Anna Nelles
	Prof. Dr. Kumiko Kotera
	Prof. Dr. Klaus Helbing

Abstract

Currently, the technique to detect neutrinos at the EeV energy scale by the radio signals emitted when they interact in glacial ice, is making the transition from small prototype experiments to full discovery-scale detectors. In the summer of 2021, construction started for the Radio Neutrino Observatory Greenland (RNO-G), the first detector large enough to be sensitive to the expected flux of cosmogenic neutrinos.

With the prospect of the first detection of a neutrino using the radio technique, the ability to reconstruct their properties from the radio signal becomes more and more important. The goal of this thesis is to develop methods that would allow for the reconstruction of the energy of a neutrino detected by RNO-G or a similar detector.

At the same time, radio detection is a well-established technique for cosmic ray observatories. The radio emission from air showers is due to very similar effects, and shares many properties with the radio signals expected from high-energy neutrinos. Thus, air showers can be a useful test case when trying to develop reconstruction techniques for radio neutrino detectors.

To reconstruct the energy of an air shower, radio cosmic ray observatories usually use the amplitude of the radio signal measured at a number of different locations. Such an approach is not feasible for a radio neutrino detector, because most events are expected to only be detected by a single radio station. Therefore, the first task was to develop a way to reconstruct the energy of an air shower using only a single detector station. This was accomplished by first using a technique called *forward folding*, which fits an analytic model to the measured waveforms, to determine the radio signal's frequency spectrum. By using the shape of this spectrum as a proxy for the angle under which the radio signal is recorded, called the *viewing angle*, the shower energy can be reconstructed with a resolution of around 15%.

The *forward folding* technique used to reconstruct the radio signal from an air shower relies on an accurate analytic model for the radio signal. This works well for the radio signals from air showers, whose spectrum can be described quite accurately by a simple exponential function, but applying it to signals from a neutrino poses some challenges. Their frequency spectrum is more complex and more difficult to predict on a per-event basis. Additionally, because the first radio detection of a neutrino has yet to occur, these models have to rely purely on simulations and are hard to verify experimentally. The solution to this was to use a method called *Information Field Theory*, and determine the most likely radio signal from the measured waveforms via Bayesian inference. Instead of an analytic model, the spectrum is described by its correlation structure, which makes very few a priori assumptions about the radio signal. The method is in fact shown to be flexible enough to be applied to radio signals from both air and neutrino-induced showers.

Finally, these techniques are combined to reconstruct the energy of neutrinos detected by a single RNO-G station. The location of the shower is determined using the differences in the signal arrival time between different antennas. The frequency spectrum of the radio signal is determined using the *Information Field Theory* method and used as a proxy for the viewing angle to estimate the shower energy. The energy of the neutrino that caused the shower is estimated using Bayes' theorem, taking into account the energy resolution of the detector and the unknown interaction inelasticity.

Zusammenfassung

Die Methode, hochenergetische Neutrinos anhand von Radiosignalen, die sie erzeugen, wenn sie in Eis interagieren, zu detektieren, befindet sich derzeit auf dem Weg von kleinen Prototyp-Experimenten zu den ersten Neutrino-Observatorien. Mit dem Bau des Radio Neutrino Observatory Greenland (RNO-G), der im Sommer 2021 begann, entsteht auf Grönland gerade der erste Detektor, der groß genug ist, um den Fluss kosmogener Neutrinos zu messen.

Mit der Aussicht auf die erste Messung eines Neutrinos mittels Radiodetektion wird es immer wichtiger, aus diesen Signalen die Eigenschaften des Neutrinos rekonstruieren zu können. Ziel dieser Arbeit ist es daher, Methoden zu entwickeln, mit denen die Energie der von RNO-G gemessenen Neutrinos bestimmt werden kann.

Radiosignale werden bereits benutzt, um Luftschauer zu detektieren. Kosmische Strahlung erzeugt Signale durch ähnliche Prozesse wie Neutrinos, sodass diese sich in vielen Eigenschaften ähneln. Es kann daher hilfreich sein, zunächst Luftschauer zu betrachten, um Methoden für Neutrinodetektoren zu entwickeln.

Radio-Detektoren messen das Radiosignal eines Luftschauers meistens an mehreren Positionen, um aus diesem "Fußabdruck" die Energie des Schauers zu bestimmen. Für einen Detektor wie RNO-G ist ein ähnlicher Ansatz nicht möglich, da ein Neutrino meistens nur von einer einzigen Detektorstation registriert wird. Folglich muss die Messung einer einzigen Station genügen. Zunächst wird das Frequenzspektrum des Signals mit einer Methode namens *forward folding* bestimmt, bei der ein analytisches Modell an die gemessenen Daten angepasst wird. Die Form des Spektrums dient dann dazu, den Betrachtungswinkel auf den Schauer abzuschätzen und dessen Einfluss auf das Radiosignal auszugleichen. Dadurch kann die Schauerenergie mit einer Auflösung von etwa 15% bestimmt werden.

Zwar funktioniert die *forward folding*-Methode gut, um das Radiosignal von Luftschauern zu rekonstruieren, sie setzt aber ein analytisches Modell der Signale voraus. Während bei Luftschauern das Spektrum durch eine einfache Exponentialfunktion gut beschrieben werden kann, ist es bei Radiosignalen von Neutrinos deutlich komplexer und nur schwer vorherzusagen. Ausserdem beruhen solche Vorhersagen auf Simulationen, die nur schwer experimentell zu überprüfen sind.

Eine Alternative bietet eine Methode namens *Information Field Theory*, bei der das wahrscheinlichste Radiosignal für die gemessenen Daten anhand Bayesscher Inferenz bestimmt wird. Das zu erwartende Radiosignal wird dabei anstatt durch ein analytisches Modell durch seine Autokorrelation beschrieben. Dadurch enthält diese Methode nur wenige a priori Annahmen bezüglich des zu erwartenden Signals und ist flexibel genug, um sowohl auf Luftschauer als auch auf Signale von Neutrinos angewandt zu werden.

Damit kann die Methode, die zur Messung der Energie von Luftschauern entwickelt wurde, auf Neutrinos übertragen werden, die durch eine RNO-G-Station detektiert werden: Zuerst wird der Ort des Schauers anhand der Ankunftszeiten des Radiosignals bei den Antennen der Station bestimmt. Anschließend wird das Spektrum des Radiosignals mittels *Information Field Theory* rekonstruiert und verwendet, um die Energie des Teilchenschauers zu ermitteln. Zuletzt wird die Energie des Neutrinos, unter Berücksichtigung der Detektorauflösung und der unbekannten Inelastizität der Neutrinointeraktion, bestimmt.

Contents

Chapter 1

Finding the Sources of Ultrahigh-Energy Cosmic Rays

Although cosmic rays have been known to exist for more than a hundred years [1], they are still among the more puzzling phenomena in astrophysics. Their energies can reach up to 1×10^{20} eV, far beyond anything achievable with particle accelerators on earth, which makes the question about their origins all the more fascinating. But to this day, despite the efforts of thousands of physicists and enormous experiments, the sources of cosmic rays remain a mystery.

1.1 Ultra-High Energy Cosmic Rays

The cosmic ray spectrum has its maximum at an energy of 0.3 GeV and extends up to 10^{11} GeV, where it shows a steep cutoff. Between those two energies, the cosmic ray flux is steadily decreasing following a power law $\Phi \propto E^{-\gamma}$, with a few breaks where the spectral index γ changes (see Fig. 1.1). The two most prominent of theses breaks have been labeled the *knee* and the *ankle*. At the lower energies, the spectral index has a value of $\gamma \approx 2.7$. At the *knee*, around $E \approx 2.0 \times 10^{15}$ eV, the spectral index starts to change to a value of $\gamma \approx 3.0$ and returns to $\gamma \approx 2.7$ at the ankle, around $E \approx 2 \times 10^{18}$ eV. Finally, there is a cutoff, where the cosmic ray flux begins to drop sharply. Measurements by the Telescope Array and the Pierre Auger Observatory, the two larges cosmic ray detectors, place this cutoff at different energies, 60 EeV and 40 EeV, respectively [8, 9], though both are compatible if systematic uncertainties are considered [6].

The arrival directions of cosmic rays at earth are close to isotropic. At lower energies, this is to be expected due to the deflection of cosmic rays by magnetic fields, which leads to a diffuse, random walk-like, propagation, and an isotropization, thus losing information about the direction of their sources. At energies on the EeV scale though, a proton from a nearby extragalactic source should only be deflected by a few degrees, and provide information about its origin. Despite this, as of today only large-scale deviations from isotropy have been found in the directions of UHECRs at 5σ significance.

At energies above 4 EeV, the Pierre Auger Observatory reports a dipole in the direction distribution [10] and an anisotropy in the right ascension of cosmic rays [11], while the Telescope Array (TA) discovered a clustering at energies above 57 EeV [12], dubbed the *hot spot*.

These findings are strong evidence for an extragalactic origin of cosmic rays at the highest energies, as the higher density of sources in the galactic plane should lead to a clustering of cosmic ray directions. The fact that the large-scale anisotropies

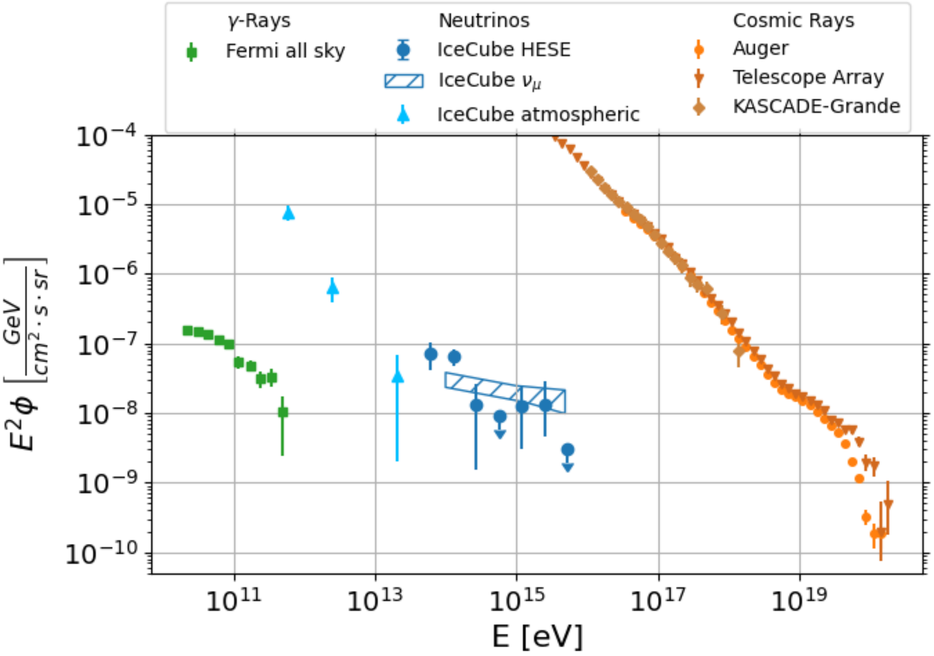

FIGURE 1.1: The three most important messenger particles for high-energy astrophysics: Diffuse γ-ray flux measured by Fermi [2], astrophysical neutrino flux from IceCube high-energy starting events [3] and ν_μ [4] as well as the atmospheric neutrino background [5]. For the cosmic ray flux, measurements by the Pierre Auger Observatory and Telescope Array [6] as well as KASCADE-Grande [7].

point away from the galactic center further supports this conclusion. It is also noteworthy that the TA hotspot is coincident with the location of the nearby starburst galaxy M82 [13]. Data from the Pierre Auger Observatory also suggests a significant contribution from M82, as well as from the nearby radio galaxy Centaurus A [14]. Though not at a 5σ level, these correlations further support an extragalactic origin of UHECRs.

Although these nearby objects may contribute to the UHECR flux, the small level of these anisotropies indicates that it is predominantly not originating from a few nearby, but instead a larger number of more distant sources. This has motivated the search for correlations between cosmic rays and catalogues of specific classes of astrophysical objects that are considered potential sources. But so far none of these have yielded statistically significant results at the 5σ level [15, 16, 17, 18].

To better understand the deflection of cosmic rays by magnetic fields, it is important to understand their chemical composition. The cosmic ray flux is in general dominated by light elements, especially hydrogen, but becomes heavier around the *knee* [19, 20], until it returns towards a light composition again. This is generally explained, along with the steepening spectrum, as the shift from galactic to extragalactic sources. Under this model, galactic cosmic ray spectrum is limited by the rigidity $R = \frac{E}{Z}$, where Z is the atomic number. This causes the lighter cosmic rays to reach their maximum energy first and the composition to become heavier. Eventually, even iron, the heaviest element expected to be abundant in cosmic rays, reaches its maximum energy and only the extragalactic flux remains. An increase in the cosmic ray mass is also observed between the *ankle* and the *cutoff* [21, 22, 23], but it is not yet clear if this is due to cosmic rays reaching their maximum rigidity or propagation effects. There is also some disagreement between measurements by the Pierre Auger Observatory and the Telescope Array, with the Telescope Array data suggesting a lighter composition. Despite this, both measurements are compatible with each other within systematic uncertainties.

The generally accepted acceleration mechanism for galactic cosmic rays is first order Fermi acceleration inside astrophysical shocks. In this scenario, material is ejected from some source and collides with another medium at rest, creating a shock front. Magnetic fields trap particles, which propagate diffusively and will occasionally cross the shock front from one medium into the other. In doing so, it will gain an amount of energy ΔE proportional to its prior energy. This cycle repeats until the particle diffuses out of the shock region and acceleration stops. It can be shown [24] that such a process produces a power law spectrum with a spectral index

$$\gamma = -\frac{\ln(1-P_e)}{\ln(1+\Delta E)} + 1 \approx \frac{P_e}{\Delta E} + 1 \tag{1.1}$$

where P_e is the probability of the cosmic ray to escape from the acceleration region in any given cycle. For an ideal shock (in which the speed of the shock front is much faster than the speed of sound in the medium) in interstellar gas $\frac{P_e}{\Delta E} \approx 1$, predicting a spectral index $\gamma \approx 2$. This is harder than the cosmic ray spectrum measured on earth, but the difference can be explained by propagation effects. Thus, the Fermi acceleration mechanism offers a general template for a cosmic ray source.

Shocks have been observed in a number of astrophysical objects. The open question is which of those, if any, are able to accelerate cosmic rays all the way up to the highest energies observed on earth. The *Hillas diagram* offers one criterion for an object to be able to reach the highest cosmic ray energies[25]. To conclude multiple acceleration cycles, the particle needs to be confined to the source region by magnetic fields. This is only possible if the gyroradius

$$r = \frac{E}{e \cdot Z \cdot B} \tag{1.2}$$

is smaller than the source region. In this equation E is the cosmic ray energy, B is the magnetic field strength, e the elementary charge and Z the atomic number of the nucleus. While this is a necessary, but not a sufficient condition, some conclusions can already be drawn from it. Heavier elements, with a larger Z, have a smaller gyroradius and therefore fulfill the Hillas condition up to higher energies. This would lead to a rigidity-dependent cutoff in the cosmic ray spectrum, that may explain the shift in the cosmic ray composition around the *ankle*.

One class of astrophysical objects that provides ideal conditions for first order Fermi acceleration to occur are supernova remnants (SNRs). During a supernova, matter is violently ejected from the star. As the ejecta propagate, they sweep up material from the interstellar medium, producing a shock front with strong magnetic fields. In some cases, a pulsar forms in the center of the supernova remnant (pulsar wind nebula), whose strong magnetic fields continue to eject plasma into its surroundings. Though SNRs provide ideal conditions for particle acceleration, and are the most abundant galactic gamma ray sources, the Hillas criterion restricts their maximum cosmic ray energy to around ~1 PeV. This is around the *knee* and fits neatly with the heavier composition observed there. Therefore, SNRs are generally accepted to be the primary sources of galactic cosmic rays up to PeV energies, while energies above that are dominated by a different, extragalactic, source population.

What exactly these extragalactic cosmic ray sources are, is still an open question.

To answer it, we do not have to solely rely on cosmic rays, but can also make use of other messenger particles, like high-energy neutrinos.

1.2 Neutrino Astronomy

One of the main challenges when trying to identify the sources of UHECRs is their deflection by magnetic fields. Fortunately, as the cosmic rays are accelerated, they will occasionally interact with matter or photon fields at or near the source. These interactions produce new particles, the most common of which are pions. The charged pions decay into muons and electrons, along with the corresponding neutrinos and antineutrinos

$$\begin{aligned} \pi^- &\rightarrow \mu^- + \overline{\nu}_\mu \rightarrow e^- + \overline{\nu}_e + \nu_\mu + \overline{\nu}_\mu \\ \pi^+ &\rightarrow \mu^+ + \nu_\mu \rightarrow e^+ + \nu_e + \overline{\nu}_\mu + \nu_\mu \end{aligned} \tag{1.3}$$

On the other hand, neutral prions predominantly decay into gamma photons

$$\pi^0 \rightarrow 2\gamma$$

This process implies a connection between high-energy neutrinos[1], cosmic rays and gamma rays.

Gamma rays have been observed from a large number of astrophysical objects, providing strong evidence for particle acceleration. However, the detection of gamma emission is not necessarily a proof of the acceleration of hadronic cosmic rays, as it may also stem from purely leptonic processes, such as inverse Compton scattering, where high-energy electrons scatter on target photons, increasing their energies up to several TeV. One possible origin for these target photons is through synchrotron emission by the same electrons in the source's magneteic field. In that case, the result is a characteristic energy spectrum, with a synchrotron peak at keV-MeV and a compton peak at TeV energies, which has been observed at a number of gamma ray sources [26, 27, 28].

Gamma rays as messenger particles for astronomy also have some limitations because of their propagation. At high energies, gamma rays interact efficiently with lower-energy photons from the extragalactic background light and the cosmic microwave background. These interactions produce pairs of electrons and positrons, thus dissipating the photon energy and effectively making the universe opaque to high-energy gamma rays [29, 30]. Therefore, gamma ray astronomy is either limited to sub-TeV energies or to sources within the pair production interaction length, which is around 300 GMpc at 1 TeV [31], so the high-energy gamma rays from the distant sources we expect for UHECRs are most likely invisible to us.

Neutrinos on the other hand, can propagate through the universe over practically infinite distances. They also cannot be produced efficiently by leptonic processes, making them a smoking gun for the acceleration of hadronic cosmic rays. Their small interaction cross section also allows them to escape from environments that would be opaque to photons. These properties make neutrinos, at least in theory, ideal messengers for the search for UHECR sources.

---

[1] Because in practice ν and $\overline{\nu}$ are extremely hard to tell apart using the experiments we are concerned with, we will drop this distinction from here on.

The existence of an astrophysical neutrino flux was first shown by the IceCube detector, a 1 km^3 neutrino detector at the South Pole, in 2013 [32, 33]. The latest results from the IceCube collaboration report a spectral index of $\gamma = 2.87^{+0.20}_{-0.19}$ [3], close to that of cosmic rays. Their arrival directions are distributed isotropically, with no association to the galactic plane, which is strong evidence for an extragalactic origin. Searches for correlations between neutrino directions and astrophysical source catalogs have so far not shown any clear connections, further evidence that cosmic rays are not produced by a small set of luminous sources, but a larger population of more common objects [34, 35].

The production process through pions suggests an ratio of 1:2:0 between the three neutrino flavors ν_e:ν_μ:ν_τ, but through neutrino oscillations this changes to a 1:1:1 ratio expected at earth. The flavor ratio measured by the IceCube experiment is consistent with this prediction, though uncertainties are still rather large [36, 37].

Neutrinos and gamma rays offer another approach to the search for the cosmic accelerators, that is not available using cosmic rays. Some source candidates, like gamma ray bursts, supernovae and tidal disruption events only last a relatively short time (by astronomical standards, at least). Over the large distances from these objects to us, even small deflections of cosmic rays prolong their travel times by hundreds of years compared to optical or radio signals. For gamma rays and neutrinos, their timing can give valuable hints at their origin. In fact, some of the best experimental evidence for neutrino emission from supernovae comes from the detection of neutrinos coinciding with the supernova 1987A. Since then, multi-messenger astronomy has be come more sophisticated, involving 'classical' observatories, as well as detectors for gamma rays, neutrinos and gravitational waves. Instruments with a large field of view send out alerts that can trigger follow-up observations by other observatories. Because they can see the entire sky at once, neutrino observatories are a potent instrument to send out those alerts.

In recent years, multimessenger observations of neutrinos and electromagnetic emissions have drawn attention to two source classes associated with supermassive black holes: active galactic nuclei (AGNs) and tidal disruption events (TDEs).

In an active galactic nucleus, the supermassive black hole at the center of a galaxy accretes matter from the environment around it, forming an accretion disk. In some cases, matter is ejected in powerful jets, which can reach well into the intergalactic medium. These jets can reach relativistic speeds and have long been theorized to be possible sources for UHECRs [38, 39]. Some AGNs, called blazars, have their jets pointed directly at earth, which makes them a prime source candidate for high-energy neutrinos.

On September 22nd 2017, IceCube detected a muon neutrino with an energy of 230 TeV and issued an alert that triggered follow-up observations in the radio, optical, X-ray and gamma band [40]. These observations showed the blazar TX0506+056, coincident with the neutrino's arrival direction, to be in a flaring state. This marks the first successful association between an individual neutrino event and its source at a significance of 3σ. Additionally, archival data showed a neutrino flare from the same blazar in 2014-15 at a significance on 3.5σ [41], though puzzlingly this was not accompanied by an increase in gamma ray emission.

A tidal disruption event (TDE) occurs when a star approaches a supermassive black hole and is torn apart by tidal forces. One such TDE was discovered in coincidence with a neutrino detected by IceCube [42]. Multi-wavelength observations supported a multi-zone emission model, with an outflow as well as a UV photosphere around the central engine, which would be an ideal source for neutrinos.

While these observations identify two promising source candidates, the lack of correlations between neutrinos and blazar catalogues or TDEs constrain the maximum contributions of these object classes to the total neutrino flux to 27% [43] and 39% [44], respectively. This means that a large part of the neutrino sources are still unaccounted for.

1.3 The Case for EeV Neutrinos

So far, astrophysical neutrinos have been detected with energies up to the tens of PeV range. This upper energy limit is due to the sharply falling spectrum and the limited size of detectors. However, certain source classes, like AGN [45] and gamma ray bursts [46, 47] have been theorized to also produce substantial EeV neutrino fluxes. EeV neutrino fluxes from other sources, like TDEs [48], are expected be too low to be detectable in the near future.

In fact, identifying an EeV neutrino source would provide clear evidence of cosmic ray acceleration to at least $\sim$10 EeV, since neutrinos produced via the pion channel typically carry about 5% or the primary cosmic ray energy. In the other hand, a PeV neutrino is a clear sign of hadronic cosmic ray acceleration, but not necessarily up to the EeV regime.

Additional ultra-high energy neutrinos, called *cosmogenic neutrinos*, are expected to be produced during the propagation of ultra-high energy cosmic rays [49]. Cosmic rays can interact with photon fields. If the center of mass energy of the interaction is larger than the mass of the delta resonance, it can efficiently produce charged pions, which decay into neutrinos, as shown in E.1.3.

The most abundant photons in the universe are from the cosmic microwave background (CMB), which have a peak photon energy of 0.2 meV. Because of this the minimum cosmic ray energy for efficient pion production is at $\sim 5 \times 10^{19}$ eV. For heavier elements, it is even higher as the Lorentz factor of a heavier cosmic ray is smaller for the same energy. At lower energies, other photon fields, like the extragalactic background light, can serve as scattering targets as well. This produces neutrinos predominantly in the PeV range and is a secondary effect at EeV energies [50].

The cosmic ray loses energy in through this effect, called the the GZK effect, leading to a suppression of the UHECR flux at the highest energies. This would be a possible explanation for the cutoff of the cosmic ray spectrum and the tendency towards a heavier composition. Alternatively, the cutoff may also be due to the cosmic ray sources reaching their maximum energies and the heavier composition due to rigidity-dependent acceleration [9]. Detecting the UHE neutrinos produced by the GZK effect, or constraining their flux, would give a clearer answer to this question.

Predictions about the scale of this cosmogenic neutrino flux can vary by several orders of magnitude depending on model assumptions [51, 52, 53, 9]. The assumption of a lighter composition, especially one with a large proton fraction, at the highest energies, generally leads to a higher cosmogenic neutrino flux, because of the smaller Lorentz factor for a heaver nucleus with the same energy. Because Telescope Array measurements suggest a higher cutoff energy and a lighter cosmic ray composition, models based on its data set tend to predict a more optimistic cosmogenic neutrino flux than ones based on Pierre Auger Observatory data. The choice of simulation codes for the cosmic ray propagation, and the assumptions made therein, can also influence the predicted neutrino flux [54]. Cosmogenic neutrinos could help to clarify these uncertainties.

Failing to detect cosmogenic neutrinos would put constraints on composition of cosmic rays above the minimum GZK energy. Because we know that cosmic rays with larger energy exists, a lack of cosmogenic neutrinos allows us to set limits on the proton fraction of cosmic rays at the highest energies [55]. This would have implications for correlations studies between cosmic ray directions and source catalogues, as a stronger deflection through magnetic fields needs to be assumed, and could confirm or exclude models that predict a substantial high energy proton fraction [56].

While UHECRs at an energy of, for example, 60 EeVare limited to the GZK horizon of about 50 Mpc and gamma rays are attenuated through photo-pair production with extragalactic background light photons, neutrinos at any energy have a practically infinite range and may be the only way to observe distant sources of high-energy particles. This leads to an interesting relationship between the evolution of UHECR sources over cosmic time and the abundance of UHE neutrinos [55]: Cosmic ray sources at high redshifts are beyond the GZK horizon, so any cosmic rays emitted by them can not reach us. However, any neutrinos they produced still can. So source classes that are more common at higher redshifts, such as gamma ray bursts [57] or AGNs [58] should lead to a higher cosmogenic neutrino flux than sources that tend to be closer, like TDEs [59, 48].

For these reasons, UHE neutrinos are a promising messenger particle to identify the sources of UHECRs. The direction of detected neutrinos can be used to point to their sources and issue real time alerts, like it is done at lower energies, but with the added benefit that they are directly related to the highest-energy cosmic rays. Measuring the UHE neutrino flux and spectrum could put significant constraints on models about composition, propagation and their sources.

The most promising technique to actually observe UHE neutrinos is the detection of radio signals from particle showers in glacial ice. This is a relatively new technique, which is just now making the transition from a few pathfinder experiments to the first discovery-scale detector. Accordingly, reconstruction techniques for this new type of observatory have to be developed, which is the focus of this thesis, in particular regarding the neutrino energy.

Meanwhile, the radio technique is well-established for the detection of cosmic rays. The radio emission from air showers is well understood and reconstruction techniques have already been developed. This presents an interesting opportunity: Because their radio emissions are very similar, we can use air showers as a test case to develop techniques we intend to use for showers in ice.

Chapter 2

Detecting Cosmic Rays with Radio Signals

At energies above the PeV range, the cosmic ray flux drops to levels on the order of a few particles per square meter per year, and direct detection becomes unfeasible. Because cosmic rays cannot penetrate through the atmosphere to ground level, experiments for direct cosmic ray detection have to be carried by high-altitude balloons or satellites, which limits their size as well as the duration of the experiment. At the highest cosmic ray energies around 10^{20} eV, the flux is on the order of a few particles per square kilometer per century, requiring cosmic ray observatories to cover thousands of square kilometers to be able to detect even a few of them.

The way to solve this problem is to detect secondary particles from cosmic ray interactions in the atmosphere. They produce a shower of secondary particles, called an *extensive air shower*, spread out over a large area, up to several square kilometers at the highest energies. By detecting these secondary particles, only a small fraction of the area of the detector has to be instrumented. The obvious downside is that any information about the primary cosmic ray, such as its direction, energy and particle type has to be inferred from the air shower. Doing so is a difficult process and requires a thorough understanding of the mechanics of air showers. In this chapter I will discuss the physics of air showers, how they can be used to reconstruct the primary cosmic ray properties, and how measuring their radio emissions can help in this.

2.1 Air Shower Physics

As a cosmic ray propagates through the atmosphere, it will eventually interact with a nucleus in the air, starting an air shower. The basics of the development of this air shower can be understood using the *Heitler model*, which provides a very simplified base on which to build [60]. In the Heitler model, a particle with an energy E_0 crosses a distance λ, called the *interaction length*, after which it produces two new particles of the same kind, each of which has the energy $E_1 = E_0/2$. This process repeats, with each particle of the n^{th} generation having an energy $E_n = \frac{E_0}{2^n}$, until E_n falls below a threshold energy and the process stops. Though the model is very simple, it is a good qualitative description and makes some accurate quantitative predictions: The number of particles N_{max} at the shower maximum scales linearly with the energy of the primary cosmic ray, while the distance the shower propagates before reaching the maximum is proportional to the logarithm of the primary cosmic ray energy. Still, the development of real air showers is more complicated and additional effects must be considered.

The Heitler model only considers one interaction between shower particles and the air. In reality, the particles in the shower constantly lose energy and some of them decay. Because of this, the number of particles in the shower does not follow the simple exponential growth up to the maximum suggested by the Heitler model, and decreases quickly afterwards.

A more accurate description of the shower development is given by the Gaisser-Hillas curve [61]:

$$N(X) = N_{max} \cdot {\frac{X - X_0}{X_{max} - X_0}}^{\frac{X_{max} - X_0}{\lambda}} \cdot \exp\left(\frac{X_{max} - X}{\lambda}\right) \tag{2.1}$$

where N_{max} is the maximum number of particles in the shower and λ the hadronic interaction length. The parameters X_0 describes the atmospheric depth at the point of the first cosmic ray interaction and X_{max} the depth of the shower maximum. They are given in terms of the *slant depth*, which is defined as

$$X(h) = \frac{1}{\cos(\theta)} \int_h^{\infty} dz\, \rho(z) \tag{2.2}$$

where θ is the zenith angle of the shower, h is the height above ground and ρ is the altitude-dependent density of the air. X_0 and X_{max} are strongly correlated to each other, as a shower that starts deeper in the atmosphere also tends to reach its maximum at a larger depth.

For a more detailed description of the processes in air showers, it is useful to differentiate between four different parts: The hadronic, electromagnetic and muonic components, and the invisible energy.

As the name suggests, a hadronic shower is driven by collisions of hadrons with the nuclei of air molecules, which produce more hadrons that continue the shower development. The most common hadrons produced in these cascades are the neutral and charged pions. Because the primary cosmic ray's first interaction will typically be via the strong force, an air shower starts with a hadronic shower that serves as the "backbone" for the other components.

The π^0 has a mean lifetime of only $\tau_{\pi^0} = 8.52 \cdot 10^{-17} s$, so a newly created π^0 almost always decays into two photons before it collides with another air molecule. These photons produce e^+/e^- pairs through pair production, which in turn produce high-energy photons through bremsstrahlung. This process repeats, causing an electromagnetic shower, as long as $E_\gamma > 2 \cdot m_e c^2$. Once the gamma energy falls below this threshold, pair production stops and the electromagnetic shower dies out as its constituent particles lose energy in non-radiative processes. Therefore, the hadronic component of an air shower is always accompanied by many smaller electromagnetic sub-showers, which together make up the electromagnetic shower component.

The interaction length of a hadronic shower is longer than the radiation length of electromagnetic showers. On the other hand, hadronic interactions typically produce more new secondary particles than electromagnetic ones, which leads to a faster dissipation of the particle energy. The consequence is that electromagnetic showers are characterized by a larger number of interactions, each of which has a relatively small impact on the overall shower development by itself. Therefore, electromagnetic showers tend to be more regular and less affected by shower-to-shower fluctuations.

The charged pions produced in the hadronic shower component primarily decay into muons (which make up the muonic component of the shower) and neutrinos.

Because the neutrinos do not interact further and muons only deposit a small fraction of their energy in the atmosphere, the energy they carry, called the *invisible energy*, makes up around 5-20% of the total shower energy and cannot be measured directly. Instead, it has to be inferred from Monte Carlo simulations [62, 63], or the number of muons detected at ground level [64].

Charged pions have a much longer lifetime $\tau_{\pi^\pm} = 2.60 \cdot 10^{-8} s$ than their neutral counterparts, so high-energy $\pi^\pm$ in an air shower can have decay lengths on the same order of magnitude as their interaction lengths. This leads to an interesting connection between the shower profile and the spectrum of the muonic shower component. High-energy muons have to be produced at an early stage of the shower development, when the individual particles still have a high energy. The high-energy pions needed to produce muons are more likely to interact before they can decay if they are produced in the denser, lower part of the atmosphere. Therefore a shower with a smaller X_0 tends to have a larger muonic component than one which developed deeper in the atmosphere. The same is true for more inclined showers, as they have to propagate a longer distance before reaching the denser parts of the atmosphere [65, 66]. The low-energy muons are produced at a later point in the shower by pions that have less energy and are therefore likely to decay before interacting regardless of air density. But the probability of the muon to decay before it reaches the ground becomes relevant, so inclined air showers produce a smaller number of low-energy muons at ground level.

In addition to pions, neutrinos can also be produced through the decay of charmed mesons produced in the air shower [67]. These *prompt neutrinos* follow a harder spectrum and are expected to become dominant over the conventional neutrino production around energies of 100 TeV, though at these energies the neutrino flux is dominated by neutrinos from astrophysical sources, making the detection of prompt neutrinos difficult [68].

Detection methods for extensive air showers can broadly be divided into two categories: Detection of particles at ground level and detection of light emitted by the shower. In many experiments, two or more of these methods are combined.

For particle detection at ground level, scintillation or water-cherenkov detectors are deployed on a grid. The spacing between individual detectors can vary from ~10 m (like the KASCADE detector [69]) or less to the ~1.5 km of the Pierre Auger Observatory [70] and the Telescope Array [71]. Which spacing to choose depends on the targeted cosmic ray energy range. Lower-energy air showers have a smaller footpring on the ground and therefore require a close spacing. To cover the large areas required at the highest energies, the spacing has to increased, which is possible due to the larger shower footprints.

As an air shower propagates through the atmosphere it emits Cherenkov light on a cone with an opening angle of ~1 °. The observatories using this effect can be divided into imaging and non-imaging Cherenkov detectors. The non-imaging technique, applied in experiments like TAIGA [72], uses an array of wide-angle light detectors to detect the ring of light on the ground created by the Cherenkov emission. An imaging air Cherenkov telescope (IACT) uses a mirror to focus the Cherenkov light into a camera. Though IACTs can also detect cosmic rays [73], their small field of view makes them best suited for gamma ray observatories [74, 75, 76, 77]. The spacing of non-imaging Cherenkov detectors is limited by the small opening angle of the Cherenkov cone, so these are used for energies up to the ~100 PeV range. For higher energies, the fluorescence light that is emitted from air molecules that were excited by the air shower are used. This emission is isotropic, which has the advantage that it can be detected from any angle, but at the cost of an overall dimmer light than from the Cherenkov effect. This makes the air fluorescence technique most useful at EeV energies, like the HiRes experiment [78] and the Pierre Auger Observatory [79].

The total number of particles in an air shower is proportional to its energy, but the particle number in the shower front at a given time changes as the shower evolves (see Eq. 2.1). Air cherenkov or fluorescence detectors detect light emitted throughout the shower development, provided it is fully developed before it reaches the ground, and can therefore use the atmosphere as a calorimeter to reconstruct the cosmic ray energy. Particle detectors on the ground can only measure a slice through the shower's profile and need to correct for the atmospheric depth of the detector's location. Most commonly, a function describing the lateral distribution of particles in the shower front is fitted to the measurements from multiple detector stations and the particle number at a specific reference distance from the shower axis is used as an energy estimator [8, 80].

The cosmic ray composition is more difficult to infer from air shower observations. The effect a different primary particle has on the shower development is most relevant at the very early stages, where the relatively small number of parameters also makes random fluctuations more relevant. Therefore it is easier to measure the overall composition of the cosmic ray flux, than measuring the particle type for a specific event.

The atmospheric depth X_0 at which a cosmic ray will undergo its first hadronic interaction and begin the shower development is randomly distributed following an exponential distribution

$$p(X_0) \propto \exp\left(-\frac{X_0 \cdot A^{2/3}}{\lambda}\right) \tag{2.3}$$

where A is the mass number of the particle and λ the hadronic interaction length. From this equation follows that X_0 tends to be smaller, and has smaller shower-to-shower fluctuations, for heavier primary cosmic rays. Additionally, heavier cosmic rays have a larger particle multiplicity in their first interaction, which makes the shower develop faster and further reduces fluctuations in the early shower development. Because the X_0 parameter is difficult to measure in practice, the mean value $\langle X_0 \rangle$ and standard deviations σ_{X_0} of the depth of the shower maximum are commonly used to estimate the composition of EeV cosmic rays. As a fluorescence telescope sees an air shower from the side, the longitudinal profile can be reconstructed from the light emission [81, 82].

Because high-energy muons are produced more efficiently higher in the atmosphere, air showers from heavy primaries have a larger muonic component. If a detector can distinguish between muons and the other shower particles, this can be used to measure the cosmic ray composition [19]. The fact that muons only rarely scatter during their propagation to earth can also be used to estimate the atmospheric depth at which they were produced, which is correlated with the shower maximum [83]. However, interactions in the early stages of shower development take place at center of mass energies beyond what is achievable with accelerators. Therefore, interaction models have to be extrapolated from measurements at lower energies, which introduces systematic uncertainties. Measurements by the Pierre Auger Observatory reported a measured muon content that is inconsistent with theoretical predictions [84].

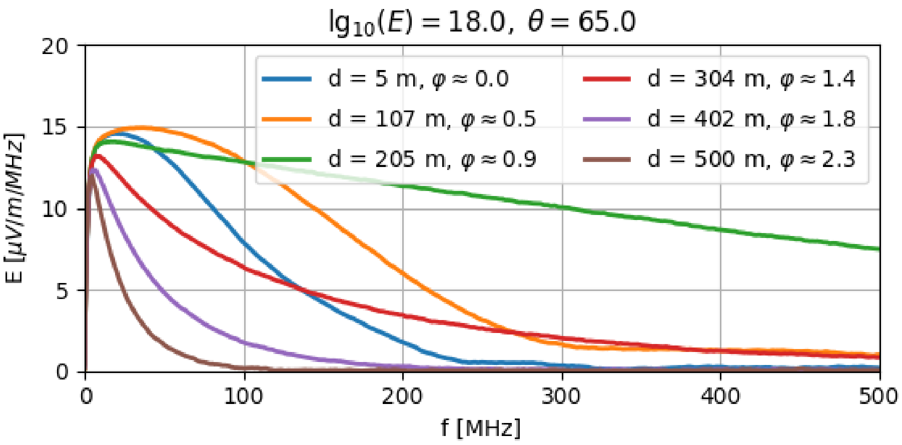

FIGURE 2.1: Example frequency spectra for the radio signal from an air shower with an energy of 10^{18} eV energy and 65° zenith angle observed at different distances d from the shower axis. For each distance, the approximate viewing angle φ is also given.

2.2 Radio Signals from Air Showers

As an air shower propagates through the atmosphere, it is affected by the Lorentz force due to the Earth's magnetic field, which accelerates positive and negative charge in opposite directions. However, particles in the shower undergo frequent collisions with molecules of the air, each of which effectively randomizes their lateral movement. Together, the result is a drift of positive and negative charges in opposite directions along $\vec{v} \times \vec{B}$, the direction of the Lorentz force, where $\vec{v}$ is the shower axis and $\vec{B}$ the geomagnetic field vector [85].

At the same time, electrons in the atomic shells of the surrounding material are scattered and join the shower front. Low-energy positrons in the shower also annihilate with electrons in the environment and are removed. The result is the build up of a net negative charge of the shower front, that grows with the shower development and decreases as the electromagnetic shower component dies out [86].

On a macroscopic level, these effects can be understood as inducing two time-varying currents, one perpendicular to the shower axis, one along it, that produce the radio signal [85]. The emission due to the Lorentz force, called *geomagnetic emission*, is usually the dominant radio signal from air showers. The signal from the the net negative charge of the shower front, called *Askaryan* or, in the context of air showers, *charge excess* emission, is subdominant, but will become important for showers in denser media. On a microscopic level, each electron and positron in the shower front emits a small radio signal. The overall emission from the shower can be simulated as the coherent sum of these smaller radio signals [87].

Thinking of the radio signal from an air shower as a sum of many smaller signals emitted as the shower evolves is also helpful to understand the structure of the radio signal on the ground, called the *radio footprint*. For an observer located on the Cherenkov cone, all of these pulses arrive at the same time[1] and interfere constructively, resulting in a single, short pulse. As the observer moves away from the Cherenkov cone, the arrival times of the individual pulses differ and the resulting

---

[1] Because the index of refraction changes with altitude, this is not exactly the case, but the discrepancy is small.

pulse becomes longer. Another way to view this process is in the frequency domain: Two radio signals arriving with a time difference Δt are shifted by a distance $\Delta l = c/n \cdot \Delta t$ relative to each other. As long as the wavelength λ is much smaller than Δl, the effect of the offset on the signal amplitude is minor. However, the loss in coherence is larger the shorter the wavelength, so the radio signal is shifted to lower frequencies, in addition to weakening overall, as an observer moves away from the Cherenkov cone [88] (see Fig. 2.1). As a result, the Cherenkov ring is more pronounced at higher frequencies [89]. At frequencies below ∼100 MHz, the depth of the shower front is smaller than the wavelength and signal coherence is maintained over whole footprint, and no Cherenkov ring is visible.

The shape of the radio footprint is further complicated by interference between the two emission mechanisms. The *geomagnetic* emission is polarized in the direction of the Lorentz force $\vec{e}_{v\times B}$, while the *charge excess* emission is polarized radially around the shower axis. Therefore, for an observer in a positive $\vec{e}_{v\times B}$ direction from the shower axis, both signals are co-polarized and interfere constructively, while they interfere destructively for an observer on the opposing side. The result is an asymmetry in the radio footprint [90]. The difference in polarization also allows to distinguish between the two emission mechanisms [91] and to measure their relative contributions to the total signal, showing that the *charge excess* emission makes up about 5 % to 20 % of the radio signal [92, 93].

The radio signal from an air shower is strongly beamed forward and the area illuminated by the radio signal, called the *radio footprint* is relatively small, on the order of hundreds of meters. The exception are very inclined showers, for two reasons: First, the shower maximum, where most of the radio emission is produced, is further away from the observer on the ground. Second, the ground plane is at an angle to the shower axis, so that the projection from the shower plane to the ground enlarges the footprint even further. As a consequence, the radio footprints of inclined showers can grow to a size of several kilometers [94].

2.3 Air Shower Detection with Radio Antennas

The possibility to detect cosmic rays using radio signals was first explored in the 1960s [95]. Though radio signals were detected in coincidence with air showers, the technology available at the time prevented it from being a useful tool for cosmic ray detection. This only changed relatively recently, when new digital technology made it possible to record the radio wave forms.

Radio detectors for cosmic rays are most commonly used along with "conventional" air shower detectors instead of as stand-alone experiments. This was initially helpful to understand the physics of radio emission from air showers, because data from other detectors could be used as a reference. For example, the LOPES experiment could use the KASCADE detector [96] it was co-located with. Now that the radio signals from air showers are well understood, this configuration allows both detectors to compliment each other. Examples for such configurations are Tunka-Rex [97] with the Tunka-133 and Tunka-Grande detectors or the *Auger Engineering Radio Array* (AERA) [98] with the other detectors of the Pierre Auger Observatory. As part of the Auger Prime upgrade, the the observatory will obtain a radio extension covering the whole array to extend radio detection to the highest energies [99, 100]. Though self-sufficient triggering on the radio signal itself has been shown to work in principle [101], most radio cosmic ray experiments use other detectors for triggering, either the cosmic ray observatory they are co-located with, or a set of dedicated particle detectors. Another way to "build" a radio cosmic ray detector is to use an existing radio telescope, as is done with LOFAR [102, 103] and proposed for the low-frequency component of the *Square Kilometer Array* (SKA-Low) [104]. Both were designed as interferometric radio telescopes, but can be used for air shower detection as well. Such a detector comes at a low cost, because existing hardware can be used, but the design is not optimized for air shower detection and uptime may be limited because other operations have priority.

The most common design for radio detectors is an array of individual stations. Each station uses 2 cross-polarized antennas, to measure the two horizontal components of the electric field. Adding a third antenna to measure all polarization components of the radio signal has been experimented with, for example at LOPES [105], but this design is rarely used. The spacing of the stations depends on the target energy, and the goals of the experiment. A small spacing, like LOFAR or SKA-low, allows for a more detailed measurement of the radio footprint, but the smaller detection area limits such an observatory to lower energies. Increasing the spacing allows to cover a larger area, but fewer stations will observe a signal and the maximum useful spacing is limited by the size of the radio footprint. The 1.5 km spacing of the Auger Prime radio detector is only feasible by focusing on very inclined showers, where the radio footprint has a size of several kilometers [94].

Air showers can also be detected using a smaller set of antennas clustered relatively close together. This approach is used for neutrino detectors, like ANITA [106] or BEACON [107, 108], which are also sensitive to cosmic rays, but will be discussed in more detail later.

Most radio detectors today operate in the 30 MHz to 80 MHz band. This is where the amplitude of the radio signal reaches its maximum (see Fig. 2.1) and is detectable inside the whole radio footprint instead of only on the Cherenkov ring. Even more important is the fact that this frequency band is little used for radio communications, making it relatively quiet for observatories near inhabited areas. Still, radio frequency (RF) noise, mostly from man-made sources is a major challenge, as they can mimic radio signals from air showers [109].

Because the amplitude of the radio signal is proportional to the number of particles, it can be used to measure the cosmic ray energy. The most precise way to do this is to fit a description of the lateral signal distribution of the radio signal on the ground, either from a parametrization or a simulated template, to the amplitudes of the radio signals detected in several stations and use it as an estimator for the cosmic ray energy [110, 111, 112]. The obtainable energy resolution with this technique is competitive with other methods and may be used as an alternative way to calibrate the absolute energy scale of a cosmic ray observatory [113] or to cross-calibrate different experiments [114, 115].

As discussed in Sec. 2.2, the radio signal is almost exclusively produced by the electrons and positrons in the shower front, so the radio method actually is only measuring the energy of the electromagnetic shower component. If the muonic component is measured by another detector, the ratio between electromagnetic and muonic shower component can be used to measure the cosmic ray composition (see Sec.2.1). This was for example done using AERA along with the AMIGA Muon Detector of the Pierre Auger Observatory and achieved resolutions comparable to other methods [116, 117]. While AMIGA only covers a relatively small part of the area of the Pierre Auger Observatory, the method can be extended to the whole array with the Auger Prime upgrade, which will install radio antennas on every detector station.

For very inclined air shower, the radio antennas measure the electromagnetic component, while the water Cherenkov detector is only sensitive to the muonic component, as the electromagnetic showers die out before reaching the ground [118, 99].

The other approach to determine the chemical composition of cosmic rays, measuring the shower maximum X_{max}, can also be done with the radio method. The smaller the atmospheric depth X_{max} of the shower maximum, the further it is away from the ground. This increases the size of the radio footprint, and can be used to reconstruct X_{max}[119]. The relative contributions of the geomagnetic and charge excess emission processes change with the shower maximum as well. The change in the shape of the radio footprint resulting from this can be used for an even more precise measurement of the shower maximum [120, 112] which is competitive with other methods.

Radio detectors can offer valuable capabilities for cosmic ray observatories, but so far they have mostly focused on the shape of the radio footprint for their measurements. This is mainly due to the small frequency band they operate in. Extending this band would allow to use the shape of the frequency spectrum in the event reconstruction and open up new possibilities for air shower observation.

2.4 Using the Frequency Spectrum for Air Shower Reconstruction

Fig. 2.1 shows how the shape of the frequency spectrum changes with the viewing angle from which the shower maximum is seen by an antenna: Higher frequencies are strongest on the Cherenkov cone and then die off as the observer moves away from it in either direction. Leveraging this relationship to reconstruct the cosmic ray energy is the basic idea behind the publication **Reconstructing the cosmic-ray energy from the radio signal measured in one single station** [121] (see chapter 4). By using the frequency spectrum of the radio signal as a proxy for the viewing angle, the cosmic ray energy can be reconstructed from the radio signal measured at a single location. Reconstructing the energy from a single radio station has already been done before (e.g. [122]) by extrapolating the measured amplitude to a reference distance, but for this the position of the shower core had to be known using the data from another detector, as opposed to this new method, which only needs the radio detector.

One application of this method is the cross-calibration of the energy scale of two cosmic ray observatories using the radio technique [113]. This has already been done with existing radio extensions of some observatories [114, 115], but the systematic uncertainties can be relatively large if the used radio antennas differ, and not all observatories have their own radio detector. A solution to this problem is a mobile array of radio stations [123], that is moved from one observatory to the other. Using the frequency spectrum of the radio signal reduces the number of necessary radio stations or allows to spread the available radio stations over a larger area to record more air shower events.

Another application is the detection of air showers by radio neutrino detectors, where they can be used as a calibration source and proof of concept for the detector performance. The ARIANNA experiment, which was used as an example in the publication, has demonstrated its sensitivity to cosmic rays, whose energy was reconstructed by an algorithm that also used the shape of the frequency spectrum [124], and achieved an energy resolution around 50%. This new method offers a more precise energy reconstruction and also works at lower signal-to-noise ratios. It has already been tested using cosmic ray events detected by ARIANNA and results were consistent with expectations [125].

The ANITA experiment reported the detection of air showers as well [126]. The method they developed to reconstruct their energy is also based on the shape of the frequency spectrum [127], but relied on a large set of Monte Carlo simulations specifically produced for each cosmic ray event and required a relatively high signal-to-noise ratio. Though the method presented in this thesis only considered down-going air showers, it can likely be adapted and offers the advantage of a smaller computational cost and a lower required signal-to-noise ratio, which will be especially useful for ANITA's successor experiment PUEO [128], which aims for a lower trigger threshold for air shower events.

Despite its usefulness to improve air shower detection, the main motivation to develop this method was as a test case for radio neutrino detection. Because in-ice radio detectors rely on the detection of radio signals by a single detector station, a similar reconstruction technique will be necessary to determine the energy of detected neutrinos. Because radio signals from air showers are much better understood than those produced by neutrino interactions, they are a valuable test case to demonstrate the validity of this method.

Chapter 3

Detecting Neutrinos with Radio Signals

The neutrino flux on Earth is dominated by solar neutrinos produced by nuclear fusion processes in the Sun, whose spectrum reaches up to MeV energies, above which neutrinos produced in air showers become dominant [129]. These foregrounds dominate over any flux that may stem from other astrophysical sources. It is only above energies of 100 TeV that the atmospheric neutrino flux drops low enough for an astrophysical flux to be detectable [32, 33, 68]. Thus, if we want to use neutrinos to identify the sources of cosmic rays, we are limited to the high-energy regime, where the flux of neutrinos is so small that gigantic detectors are required to observe them.

3.1 Signatures of High-Energy Neutrino Interactions

While the small cross section of neutrinos makes them attractive messengers for astronomy, it makes detecting them difficult in practice, because they will also be unlikely to interact with whatever detector material one may choose. The only known solution to this is to monitor large enough volumes of relatively dense material. The two most common materials used for this are water or ice, because they are somewhat transparent to light and occur naturally in large quantities.

At energies >10 GeV, the predominant interaction of neutrinos with matter is deep inelastic scattering with an atomic nucleus. Though the interaction cross section is initially small, allowing neutrinos to pass through Earth unhindered, it increases roughly linearly with neutrino energy [130]. At energies above 40 TeV, the cross section is large enough for the Earth to become opaque to neutrinos [131].

A neutrino can interact in one of two ways: Either via a neutral current (NC) interaction, mediated by the Z^0 boson, or a charged current (CC) interaction, mediated by the $W^\pm$ bosons. In an NC interaction with an atomic nucleus via deep inelastic scattering, momentum is transferred from the neutrino to a nucleon, without any changes in flavor. This momentum transfer then initiates a hadronic shower. The fraction of the neutrino energy that is transferred to the nucleon is described by the inelasticity y and heavily shifted towards small values of y [132], causing an irreducible uncertainty when trying to estimate the neutrino energy from the energy of the particle shower for these events.

If the neutrino interacts via a CC interaction, it produces a charged lepton corresponding to the neutrino flavor in addition to the momentum transfer to the nucleon. The three lepton types each produce a different signature, giving neutrino detectors some sensitivity to the neutrino flavor, provided they can distinguish between them.

At a center of mass energy close to the $W^\pm$ mass 80.38 GeV, corresponding to a neutrino energy of 6.3 PeV, the interaction between a $\overline{\nu}_e$ and an electron shows a resonance that greatly increases the cross section through the production of an on-shell W^+ boson [133]. An interaction consistent with this resonance was recently detected by the IceCube collaboration [134].

The electron produced by a ν_e causes an electromagnetic shower to develop together with the hadronic shower, making it difficult to distinguish this event type from an NC interaction. On the other hand, the entire neutrino energy ends up in these cascades, making it ideal for energy measurements.

The leptons produced by the other two neutrino flavors, the μ and τ, have larger masses which reduces their cross section and allows them to propagate through the detector material. At energies below $\sim$1 TeV, their energy loss $\frac{dE}{dX}$ is mostly through ionization of the surrounding material, but radiative losses become dominant at higher energies [135, 136]. These radiative losses are e^+/e^- pair production and bremsstrahlung, which cause an electromagnetic shower, and photonuclear interactions, which produce hadronic showers. As a result, high-energy μ and τ are accompanied by showers, which will have implications for radio detectors later.

Both μ and τ are unstable and decay into lighter particles. For the muon the dominant decay mode is

$$\mu^- \to \nu_\mu + \overline{\nu}_e + e^-$$

which results in the production of an electromagnetic shower by the electron. In practice however, its relatively long lifetime allows a muon at GeV or higher energies to propagate several kilometers before decaying. Therefore, the decay of a high-energy muon will in most cases happen outside of the detection volume.

The τ lifetime, on the other hand is short enough for it to decay close to its production point, except at ultrahigh energies. The τ is the only lepton heavy enough to decay into mesons, with decays into a τ neutrino and one or more pions making up a combined branching ratio of 64.79%. The two leptonic decay channels

$$\tau^- \to e^- + \overline{\nu}_e + \nu_\tau$$
$$\tau^- \to \mu^- + \overline{\nu}_\mu + \nu_\tau$$

have similar branching ratios of 17.89% and 17.39%. A hadronic decay will result in a hadronic shower and the decay into an electron in an electromagnetic shower, while a μ will just propagate without a shower. Except for the last decay channel, a CC interaction of a ν_τ will result in two showers, one from the initial neutrino interaction and one from the τ decay. These *double bang* event signatures are a clear sign for τ neutrinos, and two such events have been observed by the IceCube detector [37]. Though very distinctive in theory, the cascades for the two identified *double bang* candidates were only separated by 16 m and 17 m from each other, which made it difficult to identify them in practice. At EeV energies, the opposite problem becomes relevant: The τ mean decay length is on the order of tens of kilometers, which means it will most likely decay outside of the detection volume. Because of this, an EeV *double bang* event signature is not necessarily a sign of a τ decay but more likely to be caused by radiative losses from a μ or τ [137].

Showers in water or ice are governed by the same processes as air showers (Sec. 2.1), but affected by the higher density and therefore more frequent scattering of particles in the shower front. The most obvious consequence of this is a shorter shower, on the order of $\sim$10 m at EeV energies [138], as compared to the several kilometers of air showers. Similarly, the lateral width of showers in denser material is also smaller than in air. The shorter time scales between scatterings also suppress the production of high-energy muons because $\pi^\pm$ will in most cases interact again before they decay into muons.

At high energies, electromagnetic showers are affected by the Landau-Pomeranchuk-Migdal (LPM) effect [139, 140, 141]. The emission of bremsstrahlung by an electron in the shower front is not immediate but spread out over a small distance, called the formation length. The same is true for e^+/e^- pair production by a photon. For a highly relativistic electron, or a high-energy γ, the formation length can be larger than the mean free path of the electron and scatterings can no longer be treated as independent. If that is the case, interference between scatterings causes a suppression of the bremsstrahlung and pair production cross sections. As a result, the shower is elongated to 100 m length or more. Because the energy loss increases with decreasing energy, particles whose energy drops below the LPM threshold quickly lose their remaining energy, and the longitudinal shower profile becomes more irregular as well [137]. While a hadronic shower is not directly affected by the LPM effect because of the shorter length scales of the strong force, one may expect the electromagnetic sub-showers that accompany it to still be elongated. This is not the case for two reasons: First, the higher multiplicity of hadronic interactions causes the energy of individual particles to drop below the energy threshold for the LPM effect more quickly. Second, these sub-showers are predominantly initiated by the decay of π^0 into photons. At energies above ∼6.7 PeV, the π^0 decay length is larger than its interaction length in ice, so that electromagnetic showers are suppressed. The result is that the electromagnetic sub-showers typically start with energies below the LPM threshold [142].

3.2 Optical Neutrino Detectors

Detectors for astrophysical neutrinos in the TeV to PeV energy range work by detecting the Cherenkov light from neutrino interactions in water or ice. Most events detected by these types of experiments can be divided into two classes: *Tracks* from muons and *cascades* from showers. TeV muons can propagate through several kilometers of water or ice, so even a kilometer-scale detector is not large enough to fully contain most events. Therefore, part of the muon energy is deposited outside the detector volume and the energy resolution is somewhat limited. On the other hand, because a muon emits Cherenkov light over a long distance, its direction can be reconstructed at sub-degree accuracy [143, 144]. The effective volume for ν_μ is also increased because muons created by interactions outside the detection volume can enter the detector. On the other hand, muons produced in air showers can reach the detection volume as well, which makes them an additional background to muon neutrinos [145, 146]. They can be mitigated by only using muon tracks that start inside the detection volume or propagate upwards, or to use a detector at the surface to veto muons that are coincident with air showers [147]. Using a surface veto has the added benefit of reducing the background from atmospheric neutrinos as well as muons, but reduces the field of view to neutrinos coming from the direction of the surface detector.

Cascades from neutral current interactions or charged current interactions of ν_e and ν_τ on the other hand often deposit their full energy inside the detection volume and therefore offer a better resolution than tracks, around the ∼10 % level [144, 148]. The pointing resolution, on the other hand, is less precise because the cascade only propagates over a relatively short distance [32]. This is especially the case if ice is used as the detection medium, because Cherenkov photons are scattered multiple times before reaching the detector, so that the Cherenkov ring is not visible.

The field of high-energy neutrino astronomy using km^3-scale detectors in water or ice is currently very active, with several new experiments currently under construction and upgrades to existing ones on the horizon. One of the first large underwater neutrino detectors was the ANTARES experiment in the Mediterranean sea [149]. It consists of twelve cables which are anchored to the sea floor at 2475 m depth and held up by buoys, and hold a total of 885 digital optical modules (DOMs), which detect light, digitize the signal and send it to the surface. Though it could not detect a significant astrophysical flux above the atmospheric background [150], ANTARES was able to observe neutrino oscillations [151].

Building on experience from ANTARES, the KM3NeT telescope is currently under construction in the Mediterranean sea [152]. It will consist of the low-energy detector ORCA for energies above ∼1 GeV and the high-energy detector ARCA for the TeV to 100 PeV range, which are deployed at separate sites. The design is similar to ANTARES, with DOMs being suspended on strings. For ARCA, these are 230 strings at a spacing of 90 m between them to reach a detector volume of ∼1 km^3. Though the detector is still under construction, the first deployed ARCA strings were already able to observe atmospheric muons and use them to measure neutrino oscillation parameters [153, 154, 155].

Like KM3NeT, the Baikal-GVD experiment uses photomodules suspended on strings [156], but instead of the deep sea, it is located in lake Baikal at a depth of ∼1270 m below the surface. The strings are arranged in groups of 8 strings each, with a spacing of 60 m. The goal is to reach a detection volume of 1 km^3. The 8 clusters that have so far been installed, with an effective volume of 0.4 km^2, already demonstrated the detection of some neutrino candidates [157, 158].

Currently the largest neutrino detector is the IceCube Neutrino Observatory in the ice sheet at the South Pole [159]. It consists of 5160 DOMs suspended on strings inside 86 boreholes at a depth of 1450 m to 2450 m below the surface. The spacing of 125 m between boreholes and 17 m vertical spacing between DOMs allows IceCube to detect neutrinos with energies above 100 GeV inside a volume of 1 km^3. A set of 8 strings with a closer spacing of 41 m to 105 m and vertical spacing of 7 m between DOMs is used to detect neutrinos with a lower energy threshold of 10 GeV in order to measure neutrino oscillations using atmospheric neutrinos [160]. To date, IceCube is currently the only experiment that has detected a flux of high-energy astrophysical neutrinos [32] above the background of atmospheric neutrinos and has measured its spectrum up to PeV energies [161]. The *IceCube Gen2* proposal calls for the extension of IceCube with 120 new strings with an increased spacing of 240 m from each other [162], which would extend the sensitivity up to ∼10 PeV.

In water, the maximum spacing between photodetectors is limited by the absorption length of water, which is on the order of tens of meters [163, 164]. The absorption length of ice is longer, but light is scattered by small air bubbles and impurities in the ice, with scattering lengths of tens of meters [165]. Along with the difficulty of drilling kilometer-deep holes or deployment in the deep sea, this limits the volume that can be instrumented by optical modules at an affordable price. Fortunately, particle showers in ice also produce radio signals. These can be detectable over distances of kilometers, which makes them a promising signal for high-energy neutrino detectors.

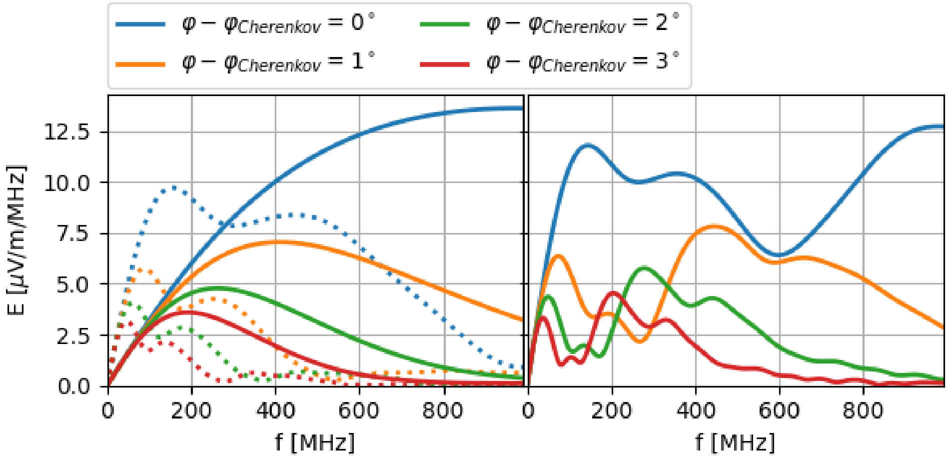

FIGURE 3.1: Example spectra of the radio emission from a ν_e with an energy of 10^{18} eV undergoing a charged current interaction observed at different viewing angles φ relative to the Cherenkov angle. Left: Signals from the hadronic shower (solid) and the electromagnetic shower (dotted). Right: Signals resulting from the combination of the hadronic and the electromagnetic showers.

3.3 Radio Signals from Neutrinos

Radio emission from particle showers in ice is governed by the same principles as from air showers (see Sec. 2.2), but with some key differences due to the different medium. The shorter scattering lengths of particles in the shower front suppress the geomagnetic emission process, so that only the Askaryan effect is relevant in practice. The higher index of refraction in ice ($\sim$ 1.78 in deep ice) means that the shower front propagates much faster than the radio signal. Instead of being beamed forward, the radio signal is emitted around the much wider Cherenkov cone ($\sim$56° opening angle). Because of this, the relevant scale for coherence of the radio signal around the Cherenkov angle is not the depth, but the lateral width of the shower front, which is around 10 cm [166]. As a result, the maximum in the frequency spectrum is at higher frequencies than for a signal from an air shower. Typical spectra for radio signals from showers in ice are shown in Fig. 3.1. While the spectrum of the radio signal from a hadronic shower has a rather simple and predictable spectrum, this is not always the case for electromagnetic showers. If the shower is affected by the LPM effect, its longitudinal profile is more irregular and may have several maxima. The individual shower maxima each effectively emit their own radio signal, which interfere. Depending on the distance between maxima, viewing angle, and frequency, those signals may interfere constructively or destructively. As a consequence, the radio signal from such a shower has a more irregular, and practically impossible to predict, spectrum. In addition, charged-current interactions of ν_e produce both a hadronic and an electromagnetic shower, whose radio signals also interfere. The result is an even more irregular frequency spectrum.

The Askaryan effect in dense media has been observed experimentally using accelerator beams and the resulting radio signal was consistent with theoretical predictions [167, 168, 169]. Simulation tools [138, 170] are not yet as advanced as those for air showers and use either parametrizations of the frequency spectrum [171, 172], or semi-analytic models which calculate the emission from a charge excess shower profile [173]. The situation is expected to improve with the new version of the CORSIKA simulation software [174], which will also be able to simulate showers in materials like ice, and which has already been used successfully for microscopic simulations of the radio emission of air showers [175].

Though there is no relevant background from atmospheric neutrinos at the energies at which radio detectors operate, muons from air showers may be a significant background. They can penetrate deep into the ice and start a particle shower there through radiative losses [137]. Because the muon itself is invisible to a radio detector, it may easily be mistaken for one produced by a neutrino. The severity of this background is difficult to estimate because of uncertainties on the number of high-energy muons produced in air showers, but they may occur with a rate similar to actual neutrino detections. A possible way to mitigate this is to use a surface radio array as a veto for the air shower [176].

While propagation effects on the signal, other than the $\frac{1}{r}$ weakening with distance, are negligible for air showers, this is not the case in ice, and the radio signal may be altered in several way as it propagates to the detector.

The uppermost layer of the ice sheet, called the firn, is made up of snow that is under pressure from the weight of the material above it. As the pressure increases with depth, the snow is compacted and slowly turns into bulk ice at a depth of $\sim$100 m to 200 m, depending on the location. The index of refraction changes as well, from around 1.3 near the surface to 1.78 in the deep ice. Measurements of the index of refraction profile $n(z)$ [177, 178] suggest it follows a function

$$n(z) = n_0 - \Delta_z \cdot \exp(z/z_0) \tag{3.1}$$

where n_0, Δ_z and z_0 have to be determined from measurements.

The changing index of refraction causes the radio signals to bend downwards as they propagate towards the surface, which has two major consequences for radio neutrino detectors. The first is that for an antenna at a given depth there exists a so-called "shadow zone" from where a radio signal cannot reach the antenna. This shadow zone starts near the surface, increasing in depth with distance from the station, and is smaller the deeper in the ice an antenna is. Horizontal propagation of radio signals from a pulser in the shadow zone has been observed [177], though they are not expected for a smooth $n(z)$ profile. They may be due to discontinuities in the index of refraction profile or reflective ice layers and could in principle give radio detectors some sensitivity to showers in the shadowed regions. In practice, the coupling of the radio signal to these propagation channels is around the percent level, so this is only a minor effect.

The other consequence is that, in addition to reaching the antenna directly, the radio signal may first propagate up to a point above the antenna and then refract downwards again, or it may be reflected off the surface of the ice. For most event geometries, this means that there are two raytracing solutions and therefore two radio pulses can be detected from the same shower. Because the two signals are emitted in directions corresponding to difference viewing angles, their amplitude can be very different, and often only one of them is actually strong enough to be detectable above the noise floor. If the shower is far away from the detector, or the antenna is placed close to the surface, the difference in viewing angle is smaller and events with two pulses (called *DnR* events, for "direct and reflected/refracted") are more likely to be observable.

During propagation, the radio signal is attenuated by the ice. Together with the $1/r$ decrease with distance, the weakening of the radio signal amplitude E after it travels a distance l is described by the relation

$$E = E_0 \cdot \exp\left(-\frac{l}{l_{att}}\right) \cdot \frac{l_{ref}}{l} \tag{3.2}$$

where E_0 is the electric field amplitude at a reference distance l_{ref} and l_{att} the attenuation length. The attenuation length of glacial ice has been measured to be on the order of 1 km [179, 180, 181, 182]. The attenuation length increases with lower ice temperature, which leads to a depth-dependent attenuation length profile for deep glacial ice. As the ice near the bottom tends to warm up, the attenuation lengths near the bottom are shorter as well.

Birefringence has been shown to exist at the South Pole [183], but is expected to be less pronounced at locations with a slower ice flow, such as near Summit Station, Greenland [184]. The consequence of birefringence is that the index of refraction profile, and therefore the signal propagation, is dependent on the signal polarization, causing a difference in the arrival times between different polarization states. This can have an impact on the trigger efficiency, as a signal may arrive as two weaker pulses instead of a single strong one and may complicate event reconstruction. On the other hand, if birefringence is well understood, the time differences between the polarization state is a possible alternative way to determine the propagation length of the radio signal. Unfortunately, birefringence at current and proposed radio detector sites has not yet been thoroughly characterized, though efforts to improve on this are ongoing.

Attenuation limits the distance at which a radio signal from a particle shower can be detected, as it needs to be above the thermal noise level when reaching the detector. Because the signal amplitude is proportional to the shower energy, this makes the energy range of an in-ice radio detector somewhat ill-defined. With lower neutrino energies, the effective volume of the detector also decreases until it is too small to be of any practical use. Where exactly this point is, is of course subjective, but typically values around 10^{17} eV are given as the minimum neutrino energies for in-ice radio detectors.

3.4 Radio Neutrino Detectors

The two main detection methods for UHE neutrinos are shown in Fig. 3.2. A neutrino can interact in ice and produce a shower, which is picked up by antennas in the ice [166, 185]. For ν_τ, an alternative channel is the production of a τ lepton through an interaction in the ground. The τ lives long enough to escape into the atmosphere, where it decays and produces an air shower, which can be detected. Because this channel is ultimately about the detection of an air shower, cosmic ray observatories can have some sensitivities to τ neutrinos as well. This is why some of the tightest current constraints on the EeV neutrino flux are from the Pierre Auger Observatory [186].

The idea behind the GRAND experiment [187] is to build a radio air shower detector that is optimized for this ν_τ channel. An array of antennas would be installed on one slope of a valley to detect radio signals from the mountains on the other side, which serve as a neutrino target. A total of 200,000 antennas are foreseen to cover an area of 200.000 km^2. These would not all be at the same site, but split into arrays of around 10,000 antennas each. The detector would work similar to those described in Sec. 2.3, but in a relatively wide frequency band of 50 MHz to 200 MHz, so that the Cherenkov ring of the radio footprint can be imaged.

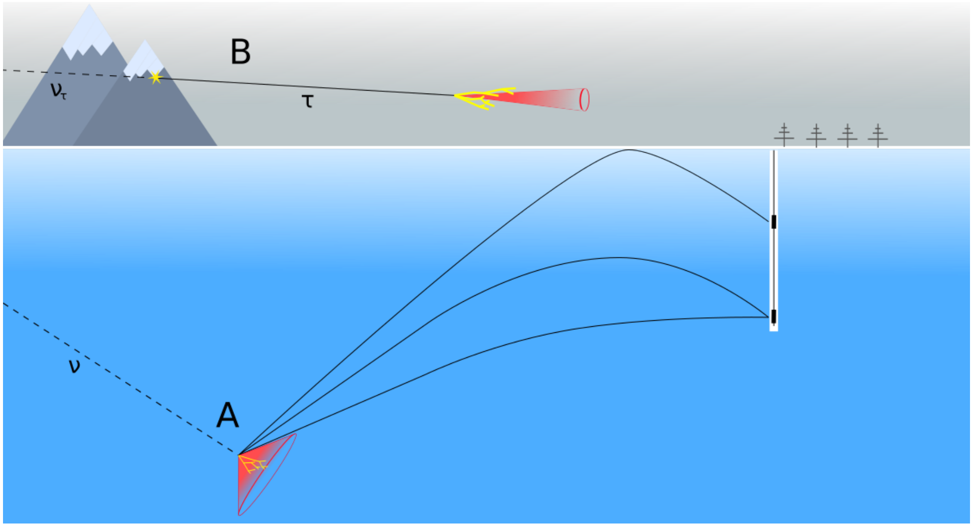

FIGURE 3.2: Illustration of the two most important detection channels for radio neutrino observatories: A neutrino interacts in ice and produces a shower (A), whose radio signal is recorded by antennas in the ice, or a ν_τ interacts in the ground and produces a τ, whose decay in the atmosphere produces an air shower (B).

To reduce the number of required antennas, the BEACON [107, 108] and TAROGE [188] experiments use small arrays of around 10 antennas on mountaintops with high prominence above the surrounding area. The necessary sensitivity is achieved thanks to the large area that is overlooked and an interferometric trigger allows BEACON to lower its energy threshold to 100 PeV. Like GRAND, such a detector would be distributed over several sites to achieve the desired sensitivity.

To increase the overlooked area, the ANITA experiment [106, 189, 190, 191], and its (planned) successor PUEO [128] use a high-altitude balloon, flying over Antarctica. Horn antennas on the balloon payload are sensitive to radio emission from the τ decay channel, or from neutrino-induced showers in the ice. Though the high altitude makes it possible to view $\sim 1.5 \times 10^6\,\mathrm{km}^2$ of ice at once, it comes at the cost of a limited experiment life time (under 1 month per flight) and a higher energy threshold of 1 EeV due to the large distance to the shower. The ANITA experiments did not report any neutrino detection, but the observation of a total of 6 of so-called "mystery events", that were consistent with an upwards-going air shower [192, 193, 194]. However, they were too far below the horizon to stem from a ν_τ, as it would have been absorbed while propagating through the earth. Though several possible explanations have been investigated [195, 196, 197, 198, 199], the origin of these events is still undetermined.

The other approach for neutrino detection with the radio technique is to install antennas directly in glacial ice. The RICE experiment [200, 201] deployed 20 dipole antennas in boreholes near the South Pole at depths from 100 m to 300 m. It demonstrated the feasibility of building an in-ice radio neutrino detector in Antarctica and operating it over several years and set new limits on the neutrino flux above 10 PeV.

Building on the experience with RICE, the *Askaryan Radio Array* (ARA) experiment was constructed [202]. It increased the volume of the monitored ice, compared to RICE, with a total of 5 radio stations, each representing an independent detector. Each station uses four 200 m deep boreholes arranged in a square with a width of 15 m. At the bottom of each hole are 2 bicone antennas for the vertical (Vpol), and 2 quadslot antennas for the horizontal (Hpol) polarization component of the radio

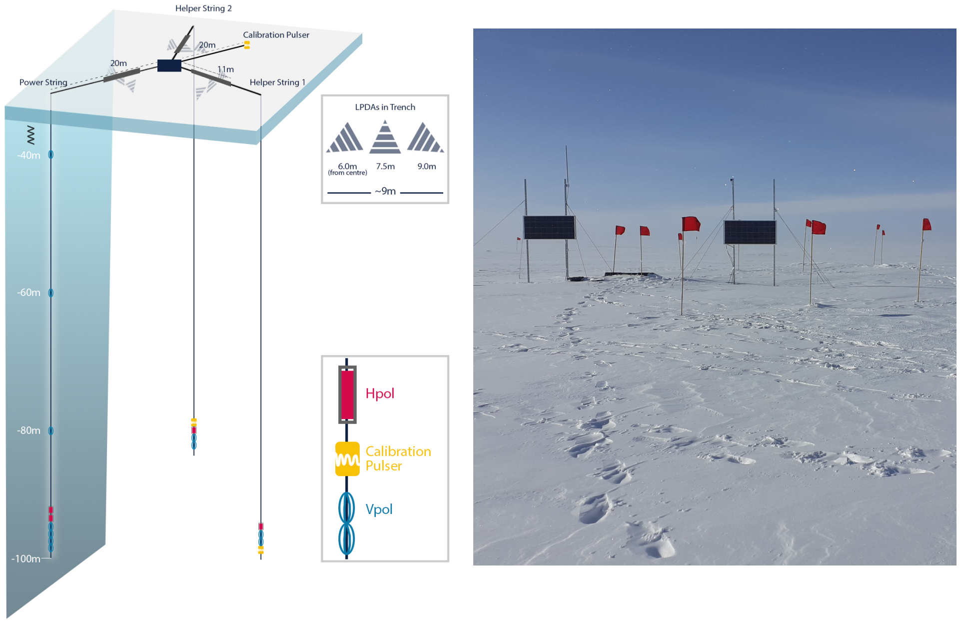

FIGURE 3.3: The Radio Neutrino Observatory Greenland (RNO-G). Left: Drawing of one of the detector stations. From [206] Right: Photograph of one of the RNO-G stations. The red flags mark the locations of antennas below the snow.

signal. For calibration, two additional holes with one Vpol and one Hpol antenna each are located about 40 m to each side of the station. One of the ARA stations was equipped with a phased antenna array, which allowed to trigger on radio signals with an SNR as low as 2 [203] by coherently summing the signal from 10 Vpol antennas.

A different approach was taken by the ARIANNA experiment on the Ross Ice Shelf in Antarctica [204]. Instead of in deep boreholes, antennas are buried in trenches only 1 m to 2 m below the snow surface. This comes at the cost of a smaller detection volume per station due to shadowing effects from the index of refraction profile (see Sec. 3.3), but has the advantage that the antenna design is also not restricted by the size of the boreholes, allowing the use of more sensitive logarithmic-periodic dipole antennas (LPDAs). Station designs have been iterated on for different stations, and some stations have been reconfigured, another advantage of the shallow deployment. In general, a station uses four or eight downward-pointing LPDAs [1], which can be supplemented by additional dipole antennas to improve the sensitivity to the vertical electric field component [205]. Each station is designed to operate autonomously, drawing power from a solar panel, potentially supplemented by a wind turbine. This way, the low per-station effective volume is offset by a lower per-station cost and easier deployment, allowing for a larger number of stations. Additionally, the ice-water interface at the bottom of the ice shelf acts as a mirror for the radio signals, increasing the detection volume and the field of view of the detector.

The in-ice radio detectors discussed so far are too small to be sensitive to all but the most optimistic expected neutrino fluxes. With the *Radio Neutrino Observatory Greenland* (RNO-G), the first discovery-scale radio detector is currently under construction [206]. The first three detector stations were deployed near Summit Station

---

[1] Antennas can also be pointed upwards, which makes the station sensitive to air showers.

at the top of the Greenland ice shelf in summer 2021, with a total of 35 planned to be built until 2024.

Each RNO-G station (see Fig.3.3) can be divided into a *deep* and *shallow* component. The shallow component is designed similar to ARIANNA, with LPDAs buried just below the snow surface. The LPDAs are grouped in three trenches of three LPDAs each. The middle LPDA is pointing upwards in order to detect air showers to use as a calibration source and to veto possible muon backgrounds. To each side of it is an LPDA pointing downward and to the side at an angle of 60 °, which are intended for neutrino detection. Thanks to their good broadband sensitivity, the LPDAs can improve the reconstruction of the radio signal, but their shallow deployment means most events will be in their shadow zone.

The deep component is more similar to the ARA experiment, with antennas deployed in three boreholes with a depth up to 100 m. Two of these holes contain a so-called *helper string*, with two vertically polarized dipole antennas (Vpols) and one quadslot antenna for the horizontal polarization component (Hpol). Additionally, one radio pulser on each *helper string* can be used to generate calibration signals.

The third string, called *power string*, is more densely instrumented. At the bottom is a set of four Vpol and two Hpol antennas with a spacing of 1 m. These four Vpol antennas are combined into a phased array trigger, like the one developed for the ARA experiment. Further up the string, with a spacing of 20 m are three more Vpol antennas. The signal from each antenna is fed into a low-noise amplifier directly above it, from where it is sent to the data acquisition (DAQ) system at the surface via a Radio Frequency over Fiber transmitter. There it is amplified once more, digitized and saved onto an SD card. A *Long Term Evolution* (LTE) telecommunications network transmits the data to a server at Summit Station, from where it is sent southwards via a satellite link. Additionally, a *Long Range Wide Area Network* (LoRaWAN) antenna at each station is available as a backup in case of problems with the LTE network. Power is provided from two solar panels and internal batteries, which limits operations to about 70% of the year. During the polar night, the stations switch into a low power mode, in which no data is taken. The possibility of extending winter operations by installing wind turbines, like those developed for ARIANNA [204], is currently being explored.

The experience gained from RNO-G will also influence the planned Gen2 upgrade to the IceCube detector [162]. Along with an extension of the optical array, it will include an array of radio stations to extend the sensitivity towards higher energies. Though the design is not finalized yet, the baseline design consists of several hundred deep stations, similar to RNO-G, supplemented by ARIANNA-like shallow stations. Therefore, reconstruction techniques developed for RNO-G will also be applicable to IceCube-Gen2.

3.5 Energy Reconstruction for Radio Neutrino Detectors

The main goal of this thesis is to develop a method to measure the energy of neutrinos detected by RNO-G. Because the inelasticity of the neutrino interaction cannot be measured, this in practice means to reconstruct the energy of the shower. Only for charged current interactions of electron neutrinos can this limit on the neutrino energy resolution be overcome, because the entire neutrino energy ends up in the two showers that are produced in the interaction. To be able to use this, a method to identify such events is necessary. While this is likely possible in principle, it is beyond the scope of this thesis.

In addition to measuring the neutrino spectrum at the highest energies, determining the energy of showers detected by RNO-G would also help to reduce the background of showers produced by muons from air showers. Their spectrum is steeply falling with energy [137], so the shower energy is one criterion that may be used to distinguish between muon background and signals from neutrinos.

The energy fluence ϕ^E of the radio signal arriving at an antenna of the detector station is connected to the energy of the shower E_s via the relation

$$\sqrt{\phi^E} \propto E_s \cdot f(\varphi) \cdot \exp\left(\frac{l}{l_{att}}\right) / l \tag{3.3}$$

The last term is the distance dependence from Eq. 3.2, and $f(\varphi)$ represents the dependence on the viewing angle φ.

To correct for the influence of the viewing angle on the radio signal, we adapt the method presented in Sec. 2.4 and use the shape of the frequency spectrum as a proxy for the viewing angle. Doing so first of all requires a way to reconstruct the radio signal that also works for the low signal-to-noise ratios expected for most detected neutrino events. In the case of air showers, this was solved by fitting an analytic model of the signal to the measured voltage waveforms [207]. Similar methods have also been developed for neutrino detection [208, 209, 210], using signal templates instead of an analytic model. These work well for the predictable spectra from hadronic showers, but not for the more irregular signals from the interference between the radio signals from the hadronic and electromagnetic showers produced by ν_e undergoing charged current interactions (see Fig. 3.1).

I developed a new method that can reconstruct these more complicated spectra, as well as the signals from hadronic showers, which is presented in the publication **Reconstructing non-repeating radio pulses with Information Field Theory** (Chapter 5). The reconstruction utilizes *Information Field Theory* [211, 212], a probabilistic method that allows signal inference from noisy data. The amplitude of the spectrum is described by its correlation structure, similar to a Gaussian process, so instead of using a specific parametrization or a physical model, only the "smoothness" of the spectrum is specified. Thus, only minimal prior assumptions about the spectrum are made, and the reconstruction can resolve "unexpected" features in the spectrum, like those arising from the interference between hadronic and electromagnetic shower signals. The method is in fact general enough to also work for air shower signals, which offers a practical test case using real data or (in this case) a well-verified simulation software.

Being able to resolve these features in the radio spectrum offers a way to identify charged-current interactions by electron neutrinos and thereby can give radio neutrino detectors some flavor sensitivity for ν_e. The accuracy of radio emission simulations can also be verified by comparing measured radio spectra to predictions. This is not as easy with the *forward folding* technique, for which the used template has to be assumed to be accurate.

Using the *Information Field Theory* technique to reconstruct the radio signal, I estimate the neutrino energy, with a method described in the publication **Reconstructing the neutrino energy for in-ice radio detectors** (Ch. 6). This is the first energy reconstruction method developed for a deep detector design such as RNO-G. The ARIANNA collaboration has developed energy reconstructions for a shallow detector design, based on *forward folding* [208] and machine learning [213]. These rely heavily on the presence of a DnR signal, which is much more likely for a shallow detector, so a different approach is needed for RNO-G.

The location of the neutrino interaction vertex is determined using a lookup table of signal travel times from given positions to each antenna to calculate the expected differences in signal arrival times between each pair of antennas. The position with the best agreement between expected and measured arrival times is found using the correlations of measured waveforms with a template, allowing the use of channels with a very low signal-to-noise ratio. With the interaction vertex known, the electric field spectrum is reconstructed with the *Information Field Theory* method. Finally, the shape of the spectrum is used as a proxy for the viewing angle, an approach which was adapted from the air shower reconstruction in Ch. 4.

The resolution on the shower energy under realistic conditions is estimated via a Monte Carlo simulation. Finally, the achievable neutrino energy resolution resulting from this and uncertainties in the neutrino interaction are estimated via Bayesian statistics.

Because there are still many uncertainties concerning RNO-G, the energy reconstruction method was deliberately designed to avoid making assumptions that were not strictly necessary or well-founded. Especially our knowledge about the ice properties around Summit Station and the propagation of radio signals through the ice is likely to improve in the near future. These changes can easily be incorporated by updating the lookup tables holding the signal travel times that were used for the vertex reconstruction. In a similar way, if our understanding of the relationship between the radio signal's frequency spectrum and the viewing angle improves, this can be incorporated by updating the used parametrization. Additionally, using a more "traditional" approach to reconstruct the energy is more transparent about what assumptions are made and how they affect the result, especially compared to machine learning methods. This is especially advantageous for a new detector concept that has yet to detect its first neutrino.

Chapter 4

Energy Reconstruction for Radio Cosmic Ray Detectors

4.1 Declaration of Authorship

The publication "Reconstructing the cosmic ray energy with the radio signal measured in one single station", published in the Journal of Cosmology and Astroparticle Physics, Volume 10, in 2019, describes a method to to reconstruct the energy of an air shower using measurements of the radio signal at a single location.

The basic idea to use the shape of the frequency spectrum for the energy reconstruction came from Anna Nelles and Christian Glaser. I developed the parametrizations to correct for the effect of the viewing angle and other factors like the distance to the shower maximum and to distinguish between observers inside and outside the Cherenkov ring. The forward folding method for the electric field reconstruction was mainly developed and implemented by Christian Glaser, though I contributed some improvements to its accuracy.

The study on the reconstruction performance and the effects of systematic uncertainties was also done by me, using the *NuRadioReco* software framework. Some reconstruction modules (for example filtering, resampling and the direction reconstruction) were already part of *NuRadioReco*. The code to perform the reconstruction steps that are the main focus of this paper was developed and implemented by me.

The text was first written by me, and then reviewed by the coauthors. All figures in the publication were produced by me.

4.2 Publication: Reconstructing the cosmic-ray energy from the radio signal measured in one single station

Journal of Cosmology and Astroparticle Physics
An IOP and SISSA journal

Reconstructing the cosmic-ray energy from the radio signal measured in one single station

C. Welling,[a,b,1] **C. Glaser**[c] **and A. Nelles**[a,b]

[a]DESY,
Platanenalle 6, 15738 Zeuthen, Germany
[b]Erlangen Center for Astroparticle Physics (ECAP),
Friedrich-Alexander-Universität Erlangen-Nürnberg,
Erwin-Rommel-Straße 1, 91058 Erlangen, Germany
[c]University of California Irvine,
Irvine, CA 92697, U.S.A.

E-mail: christoph.welling@desy.de, christian.glaser@uci.edu, anna.nelles@desy.de

Received May 28, 2019
Revised August 22, 2019
Accepted October 14, 2019
Published October 30, 2019

Abstract. Short radio pulses can be measured from showers of both high-energy cosmic rays and neutrinos. While commonly several antenna stations are needed to reconstruct the energy of an air shower, we describe a novel method that relies on the radio signal measured in one antenna station only. Exploiting a broad frequency bandwidth of $80 - 300$ MHz, we obtain a statistical energy resolution of better than 15% on a realistic Monte Carlo set. This method is both a step towards energy reconstruction from the radio signal of neutrino induced showers, as well as a promising tool for cosmic-ray radio arrays. Especially for hybrid arrays where the air shower geometry is provided by an independent detector, this method provides a precise handle on the energy of the shower even with a sparse array.

Keywords: cosmic rays detectors, ultra high energy cosmic rays, neutrino detectors

ArXiv ePrint: 1905.11185

JCAP10(2019)075

---

[1] Corresponding author.

https://doi.org/10.1088/1475-7516/2019/10/075

Contents

1 Introduction and scientific motivation

There is still no commonly accepted answer to the question of the origin of ultra-high energy cosmic rays. Detecting the radio emission of showers may bring us closer to an answer. Either through the detection of air showers, exploiting the excellent energy and composition resolution that comes with the radio method [1–5], or through the detection of the neutrino counterpart of ultra-high energy cosmic rays. Neutrinos can either be generated in interactions at the sources (*astrophysical neutrinos*), allowing for multi-messenger detection of for example gamma-rays and neutrinos [6–8] or as *cosmogenic neutrinos* [9–11]. These neutrinos are created through the interaction of ultra-high energy cosmic rays during propagation with the cosmic microwave or other photon backgrounds, making the neutrino flux sensitive to the composition of cosmic rays [12–14]. All models predict a low flux of these neutrinos beyond 10^{16} eV meaning that current detectors like IceCube are too small to detect a significant flux [15] at the highest energies. Due to the long attenuation length of radio waves of $\mathcal{O}(1\,\mathrm{km})$ in ice [16–18] allowing for sparse instrumentation, radio neutrino detectors are a promising alternative.

1.1 Method

When reconstructing particle showers, be it neutrino or cosmic-ray induced, typically two aspects are relevant: the energy and the shower development, i.e. the shower maximum for air showers and the vertex position for neutrinos. Radio detection of air showers has reached maturity already, where the energy is typically derived from reconstructing the footprint of the shower on ground [2, 19–21]. To this end, the footprint is sampled by many antennas. The radio footprint is typically smaller than the particle footprint, since it is primarily governed by the width of the Cherenkov cone, which depends on the distance to the shower maximum and not the energy of the shower. Especially for events with small zenith angles, this results in measurable signals on only a radius of the order of 100 m around the shower axis. In order to sample this footprint with at least three antennas, the radio arrays have to be relatively densely spaced. A much wider spacing would be needed to cost-effectively cover large areas, as it is the case for e.g. the radio component of the proposed AugerPrime upgrade to the Pierre Auger Observatory [22]. At a spacing on the order of 1 km the chances of being able to sample the full footprint of an air shower are small, unless targeting very horizontal showers ($> 60^\circ$) [23]. A similar challenge presents itself to proposed radio-based in-ice neutrino detectors (e.g. [24, 25]). With a detector spacing of more than 1 km it is unlikely for the radio signal from a neutrino interaction to be detected by more than one station. Since radio-neutrino detectors with surface antennas are also sensitive to air showers, detecting cosmic rays and reconstructing their energy will be a valuable tool for validating neutrino arrays, much like using muons in optical-Cherenkov neutrino experiments. Air showers show signal characteristics very similar to neutrino showers, making them both a background and a calibration tool.

In order to fully exploit this calibration signal, radio detection of air showers will need new reconstruction methods for neutrino arrays. In turn, sparse air-shower arrays may also benefit from these methods. We will present a method that derives the energy of an air shower from the signal in a single detector station, exploiting the shape of the frequency spectrum. This method, while carrying merit in itself, can also be seen as step towards energy reconstruction for neutrinos. For the neutrino reconstruction additional complexities such as a much wider Cherenkov angle, frequency-dependent attenuation [16–18], and a strongly changing index of refraction leading to curved paths will have to be treated. However, we anticipate that using the shape of the frequency spectrum will also be essential for the energy reconstruction of neutrinos.

1.2 Experimental context

Since all large radio neutrino arrays are still in the proposal stage [24–27], we have developed a method based on CoREAS Monte Carlo simulations [28]. However, in order to embed this method in realistic conditions, we have adopted a station design used in the pilot-stage array of ARIANNA [29], which has already been used for air shower detection [30]. A similar surface component employing log-periodic dipole antennas (LPDAs) is foreseen for all proposed in-ice neutrino arrays, which makes this a solid choice for air-shower reconstruction [24, 25]. We note that the detailed modelling of a detector is not critical for the success of the method, as long as a wide frequency range (> 100 MHz) is detected.

For the purpose of this article, we adopt a station layout of four upward-facing LPDAs buried in the snow at a depth of roughly 2 m below the surface. The antennas are distributed around a central tower, which in practice might be used for power and communications, but simply serves as symmetry center for this example. LPDAs on opposite sides of the central tower are 8 m apart from each other and form a pair, as they have the same orientation and therefore measure the same polarization. One pair measures the north-south, the other the east-west polarization of the radio signal.

We adopt typical ARIANNA hardware characteristics. They include a very broad-band LPDA, which is filtered with a 80 MHz high-pass and a 500 MHz low-pass filter. After amplification the signal is digitized by an analog-digital converter (ADC) with a sampling rate of 1 GHz. We also use the ARIANNA-style dual-threshold trigger scheme with a 4σ coincidence between at least two channels required for the station to trigger. As noise is an important factor for radio arrays, we use recorded noise from the set-up in Moore's Bay [30]. Adopting ARIANNA characteristics allows us to study the influence of *real* hardware characteristics as well as background effects to avoid an idealized study of the reconstruction capabilities. In appendix A we describe cross-checks for other locations on Earth, to exclude that the height and geomagnetic field at the ARIANNA site are a relevant factor.

In this analysis, we only use data from a single station and neglect possible additional information from other stations detecting the same air shower. While there will be some station coincidences in an array with a spacing in the order of 1 km, especially for horizontal showers, we use this conservative estimate to develop the reconstruction algorithm. The reconstruction of an individual shower will of course improve, if information from two or more stations is provided.

2 Radio signal reconstruction

The first step in the event reconstruction is the retrieval of the electric field from the voltage traces measured in the antennas, which in turn have to be retrieved from the recorded ADC counts. To do so, we use the NuRadioReco software framework. A detailed description of NuRadioReco and its event reconstruction methods is presented elsewhere [31], so only the reconstruction of the signal direction and the electric field will be covered here briefly, as they are essential for the energy reconstruction.

2.1 Arrival direction

The distance of 8 m between two antennas with the same orientation is small compared to the size of the air shower footprint at ground level. Therefore the radio signal measured in the two channels of an antenna pair can be expected to be very similar, only shifted by the difference in signal travel time between the antennas.

We define the correlation

$$\rho(\Delta n) = \frac{\sum_i (V_1)_i \cdot (V_2)_{i-\Delta n}}{\sqrt{\sum_i (V_1)_i^2} \cdot \sqrt{\sum_i (V_2)_i^2}} \tag{2.1}$$

between the voltage time traces V_1 and V_2 of the two channels in each pair, shifted by Δn samples relative to each other. The correlation $\rho(\Delta n)$ is normalized to $-1 < \rho(\Delta n) < 1$ to make it independent of the signal amplitudes.

Assuming a plane-wave front, we calculate the expected time difference and the corresponding Δn between antennas of each channel pair for a given signal direction and calculate $\rho(\Delta n)$. The direction of the recorded signal is determined by finding the direction for which the sum of $\rho(\Delta n)$ of both channel pairs is largest. Using this method, an angular resolution better than $1\,^\circ$ is achieved for signals that exceed a signal-to-noise ratio of 4.[1]

---

[1] We define the signal-to-noise ratio (SNR) as the ratio between half the peak-to-peak amplitude and the noise RMS.

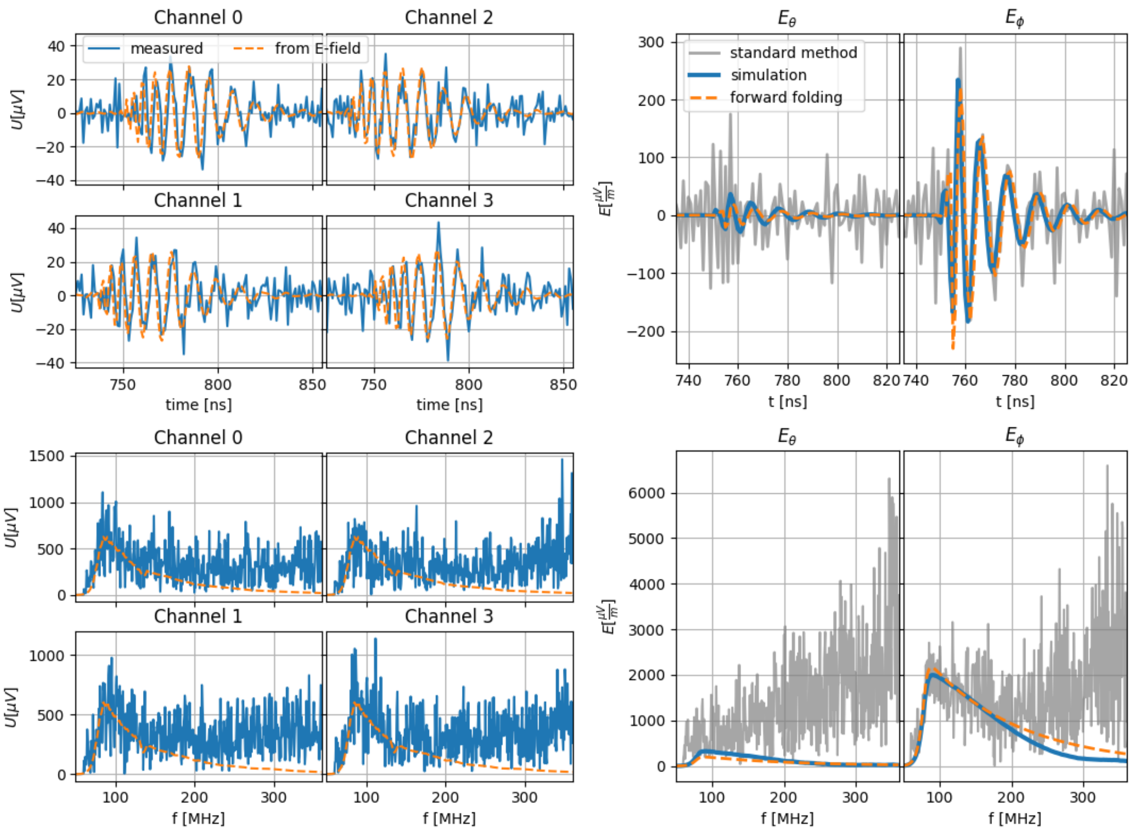

Figure 1. Example of the electric-field reconstruction using the standard and the forward folding technique. Left panels: voltage traces of four spatially displaced antennas. Shown are both the time- (top) and frequency domain (bottom). The solid blue curve represents the measured voltages whereas the dashed orange curve shows the analytic solution of the forward folding technique. Channels 0,2 and 1,3 are parallel, the measured signal only differs in noise contribution. Upper right panels: reconstructed electric field trace using both the standard (gray) and forward folding (dashed orange) technique in comparison to the simulated true (solid blue) values. Lower right panels: reconstructed amplitude spectrum using both techniques in comparison with the simulated truth (color scheme same as above).

2.2 Electric field

With the incoming direction of the radio signal known, it is possible to reconstruct the 3-dimensional electric field trace from the voltage traces measured by the antennas. Since the distances between a station's antennas are small, we can assume that all four channels measured the same electric field. Then, in Fourier space, the voltage traces in the antennas for a given electric field $\mathcal{E}^{\theta,\phi}$ are given by

$$\begin{pmatrix} \mathcal{V}_1(f) \\ \mathcal{V}_2(f) \\ \dots \\ \mathcal{V}_n(f) \end{pmatrix} = \begin{pmatrix} \mathcal{H}_1^\theta(f) & \mathcal{H}_1^\phi(f) \\ \mathcal{H}_2^\theta(f) & \mathcal{H}_2^\phi(f) \\ \dots & \\ \mathcal{H}_n^\theta(f) & \mathcal{H}_n^\phi(f) \end{pmatrix} \begin{pmatrix} \mathcal{E}^\theta(f) \\ \mathcal{E}^\phi(f) \end{pmatrix} + \text{noise}, \tag{2.2}$$

where $\mathcal{H}_i^\theta$ and $\mathcal{H}_i^\phi$ are the antenna responses of the i$^{\text{th}}$ antenna to the θ and ϕ components of the electric field. Eq. (2.2) is an overdetermined system of linear equations that can be solved for $\mathcal{E}^\theta(f)$ and $\mathcal{E}^\phi(f)$ via a χ^2 optimization to reconstruct the electric field. However, this method does not respond well to noise in the voltage traces [31]. We therefore use the so-called forward folding method instead, which provides a more accurate electric field reconstruction, especially with regards to the frequency spectrum by using an analytic model of the radio signal.

In the frequency domain, the electric field can be approximated by the equation

$$\begin{pmatrix} \mathcal{E}_\theta \\ \mathcal{E}_\phi \end{pmatrix} = \begin{pmatrix} A_\theta \\ A_\phi \end{pmatrix} 10^{f \cdot m_f} \, \exp(\Delta \, j) \tag{2.3}$$

that depends on only four parameters: the signal amplitudes A_θ, A_ϕ of the two orthogonal polarizations, the frequency slope m_f and a frequency-independent phase offset Δ. f is the frequency and j the imaginary unit.

The electric field is reconstructed by calculating $\mathcal{V}_i(f)$ for a given $\mathcal{E}_\theta(f)$, $\mathcal{E}_\phi(f)$ using eq. (2.2) and optimizing A_θ, A_ϕ, m_f and Δ through a χ^2 fit to the recorded voltage time traces. An example of such a forward folding reconstruction is displayed in figure 1. The voltage traces were generated by folding the electric field from an air shower simulated using CoREAS [28] with the detector response and adding a noise trace recorded by an ARIANNA station in the field. It shows that the forward folding method avoids the problem of over-estimating the electric field at higher frequencies that the standard method suffers from, resulting in a more accurate spectrum reconstruction. Especially the reconstruction of the frequency slope m_f is much more accurate than with the standard method. For a detailed comparison between the performance of the two methods, see [31].

From the electric field trace we calculate the energy in the radio signal per unit area, called the energy fluence [2]

$$\Phi_E = \epsilon_0 \cdot c \cdot \Delta t \cdot \sum_i |\vec{E}(t_i)|^2 \tag{2.4}$$

where ϵ_0 is the vacuum permittivity, c is the vacuum speed of light and Δt is the sampling rate. We note that we do not need to subtract noise from the energy fluence, because the forward-folding technique reconstructs an electric field free of noise.

3 Energy estimator

Our goal is to use the energy fluence Φ_E as an estimator in order to measure the energy in the electromagnetic shower. In our scenario, each air shower is only detected by a single radio station and no additional information about the shower geometry is available. Thus, an energy reconstruction from the energy fluence at a single point is challenging, as it is influenced by a number of factors other than the shower energy:

Angle to the magnetic field: the dominant emission process for air showers is the so-called geomagnetic emission, whose energy fluence is proportional to $\sin^2(\alpha)$ where α is the angle between the shower axis and the geomagnetic field.

Distance to the shower maximum: the radio signal gets weaker with increasing distance between the shower and the radio antenna. Since the largest part of the radio signal is emitted near the shower maximum, the signal energy fluence roughly scales with the geometric distance to the shower maximum $d_{X_{\max}}$ squared.

Viewing angle: we define the viewing angle φ as the angle between the shower axis and a line from the shower maximum to the antenna. Emission is strongest if φ is close to the Cherenkov angle (defined by $\cos(\varphi_{\text{Cherenkov}}) = \frac{1}{n}$, where n is the index of refraction at the shower maximum) and becomes weaker the larger the difference between the two gets.

For an estimator to achieve a good energy resolution, we need to take these factors into account and correct for them.

3.1 Procedure

Correcting for the angle to the magnetic field is rather straightforward, since the shower axis is very close to the signal direction and the magnetic field at any site can be measured directly. For the correction, it is useful to introduce a coordinate system that has one axis aligned with the shower axis $\vec{v}$, one in the direction of the Lorentz force $\vec{v} \times \vec{B}$ and the third one perpendicular to those two $\vec{v} \times (\vec{v} \times \vec{B})$. The energy fluence can then be split into the energy fluence of the two polarizations $\Phi_{\vec{v}\times\vec{B}}$ and $\Phi_{\vec{v}\times(\vec{v}\times\vec{B})}$. Since only the geomagnetic emission, which is polarized in the $\vec{v} \times \vec{B}$ direction, is affected by the angle to the magnetic field, only $\Phi_{\vec{v}\times\vec{B}}$ is corrected for this effect.

The distance d_{X_max} to the shower maximum is harder to account for, because the atmospheric depth X_max of the shower maximum is unknown. Fortunately, however, this effect is most relevant for inclined showers, where the shower maximum is far away from the observer. In this case, event-by-event fluctuations of X_max have little effect and d_{X_max} is mainly a function of the zenith angle [32]. It is therefore sufficient to assume a typical value for X_max and calculate the expected d_{X_max} based on the shower inclination. Based on [33] we use an average X_max of 750 $\frac{\text{g}}{\text{cm}^2}$.[2] To make sure that this assumptions was correct, we checked for correlations between the uncertainties on the reconstructed energy and X_max and found no such biases.

This lets us correct for those two effects by defining a corrected energy fluence

$$\Phi'_E = \left(\frac{1}{\sin^2(\alpha)} \Phi_{E,\vec{v}\times\vec{B}} + \Phi_{E,\vec{v}\times(\vec{v}\times\vec{B})} \right) \cdot \left(\frac{d_{X_\text{max}}}{1\,\text{km}} \right)^2 \tag{3.1}$$

which will be used as the basis for the energy estimator. We note that we ignore the influence of the second order charge-excess emission process on the $\Phi_{E,\vec{v}\times\vec{B}}$-component as it is small enough to not limit the resulting energy resolution. Since geomagnetic and charge excess emission can interfere both constructively and destructively depending on where the observer is on the $\vec{v} \times \vec{B}$ axis, the effect of the charge excess emission will largely average out and not lead to a systematic offset. In the future, the term $\sin^2(\alpha)$ may be replaced by $a^2 + (1 - a^2)\sin^2(\alpha)$ following the same approach as in [34] where a is the relative strength of the charge-excess component that depends on the distance to X_max and the shower axis, and can be parameterized as function of zenith angle using the work of [32].

The third correction for the effect of the viewing angle is more complex and has to be assessed in a Monte Carlo study. We use a first set of simulated air showers to derive the correction factor for the viewing angle and a second set to test the full energy reconstruction (see section 4).

---

[2] In fact, the value chosen for X_max has very little effect on the energy reconstruction. If a different X_max had been chosen, the zenith-dependent parameterization of the effect of the viewing angle (section 3.2) would compensate this.

The Monte Carlo data set was produced using 545 CoREAS [28] simulations of proton-induced air showers and their radio emission. The showers cover an energy range of 10^{16} – 5×10^{19} eV and random arrival directions with zenith angles between 0° and 80° and a uniform azimuth distribution. The energy range is set by the typical threshold of radio signals above the thermal and Galactic noise floor. This depends in detail on the experimental set-up but is typically at several PeV.

For each shower, the radio signal was simulated at 160 positions arranged in a star-like pattern around the shower core at an altitude of 30 m above sea level (the height of the ARIANNA detector on the Ross Ice shelf), and the detector response to the radio signal at each position was simulated. Radio simulations are in general time consuming, but every observer position can be used independently providing additional statistics. Also, since the radio signal stems from the electromagnetic component of the air shower, which is in general rather smooth, small air shower sets provide enough information. We find that we are not statistics limited (see also appendix A).

A simple-threshold trigger was simulated by requiring that at least two channels recorded a pulse larger than 60 mV ($\sim 3V_{rms}$) for the reconstruction to continue. A 10th order Butterworth bandpass filter with a passband of 80 −300 MHz was applied and a full event reconstruction was performed, using the forward folding technique described in section 2.2. The resulting data set was used to develop an energy estimator that can also account for the effect of the viewing angle.

3.2 Correction for the viewing angle

The shape and amplitude of a radio pulse emitted by an air shower differs depending on the viewing angle φ under which it is seen. Under small viewing angles, signals from different stages in the shower's development arrive simultaneously, leading to an amplified emission over a wide frequency band [35]. The resulting dependency of the frequency spectrum on φ has already been observed in the 30 − 80 MHz band [23, 36–38] and is used to reconstruct air shower energies by the ANITA experiment [39]. The method used by ANITA, however, requires dedicated Monte Carlo simulations for each reconstructed event and is therefore not suitable for large arrays with regular detections.

The radio signal is strongest if the viewing angle coincides with the Cherenkov angle at the location of the shower maximum. In this case, the radio signals emitted at the shower maximum add up coherently, leading to an amplification of the signal. If the event is seen from further off the Cherenkov cone, overlapping signals lose coherence and the amplitude decreases, as can be seen in the top row of figure 2. However, shorter wavelengths lose coherence faster than longer ones. The effect this has on the frequency spectrum can be observed with the frequency slope parameter m_f (see eq. 2.3), shown in the bottom row of figure 2. The small absolute value of m_f at the Cherenkov angle corresponds to a relatively flat frequency spectrum, while the larger m_f off the Cherenkov cone corresponds to a sharp dropoff towards higher frequencies in the spectrum. The event-by-event fluctuations in $\sqrt{\Phi'_E}/E_{\text{shower}}$ and m_f are large for $\theta < 10°$, but they decrease with increasing zenith angle. It is also worth noting that neither the change in $\sqrt{\Phi'_E}$ nor in m_f is symmetric around the Cherenkov angle.

Since m_f is a function of $\varphi - \varphi_{\text{Cherenkov}}$, it is possible to use it as a proxy for the viewing angle. This is done in figure 3, which shows $\sqrt{\Phi'_E}/E_{\text{shower}}$ as a function of m_f, with small $|m_f|$ corresponding to events seen by observers close to the Cherenkov ring and larger $|m_f|$ to those seen from further off the Cherenkov angle. Events are split into two groups: those where the station is located inside the Cherenkov ring and those seen from outside

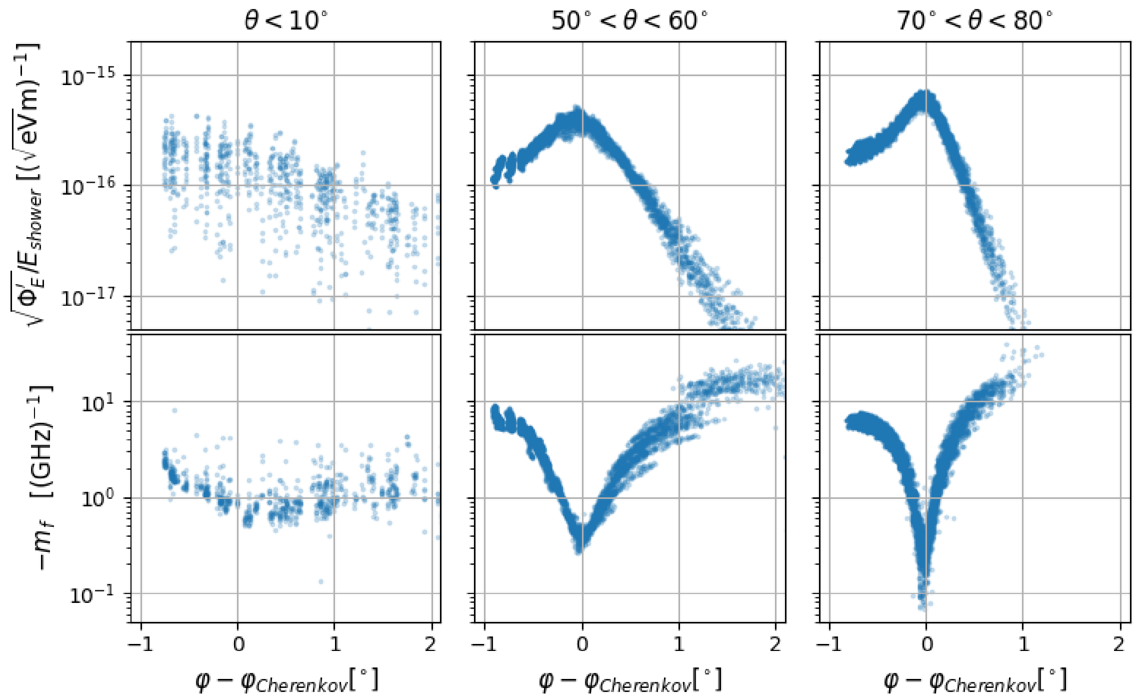

Figure 2. Top row: energy fluence of the radio signal over electromagnetic shower energy as a function of the viewing angle relative to the Cherenkov cone. Bottom row: frequency slope parameter m_f as a function of the viewing angle relative to the Cherenkov cone. Each column represents a different range of zenith angles θ. The Cherenkov angle is calculated using the index of refraction of the air at the shower maximum.

of it. While $\sqrt{\Phi'_E}/E_{\mathrm{shower}}$ and m_f show a clear correlation for larger zenith angles, the scatter for the $\theta < 10^\circ$ events is very large. This is likely due to the small angle between the shower axis and the geomagnetic field, which causes the charge-excess emission to become more prevalent compared to the geomagnetic emission. Since both signal components have a different polarization, they interfere constructively at positions in positive $\vec{v}\times\vec{B}$ direction and destructively in negative $\vec{v}\times\vec{B}$ directions. This causes the lateral distribution function (LDF) of the radio signal to no longer be rotationally symmetric in the shower plane. Together with the smaller dependence on the viewing angle (figure 2), this leads to the large scatter (see also discussion in appendix A).

We divide the events into 20 zenith angle bins with equal sky coverage and fit the function

$$\frac{\sqrt{\Phi'_E}}{E_{\mathrm{shower}}} = A \cdot \exp(-s \cdot (|m_f| \cdot \mathrm{GHz})^{0.8}) \tag{3.2}$$

to the distribution in each bin separately for events seen from within and from outside of the Cherenkov cone. The results are shown in figure 4. The zenith dependence of A can be parameterized by a second-order polynomial, the one of s by a straight line. The specific values for this parametrization are shown in table 1.

Using these parameterizations, eq. (3.2) can now be solved for E_{shower} to obtain an energy estimator using the zenith angle θ and the radio energy fluence Φ_E and frequency slope m_f. However, since events viewed from inside the Cherenkov cone have to be treated

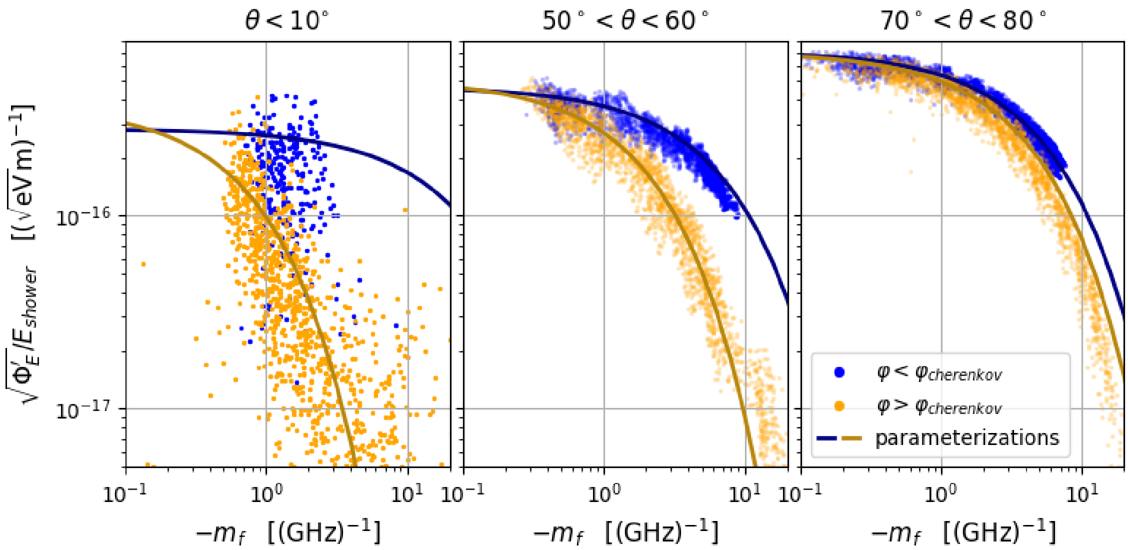

Figure 3. Energy fluence of the radio signal over electromagnetic shower energy as a function of the frequency slope parameter m_f for different zenith angles θ. Events are split into two categories: those viewed from inside the Cherenkov cone are displayed in blue, those from outside in orange. The lines show the parametrization eq. 3.2 for the center of the zenith angle bin.

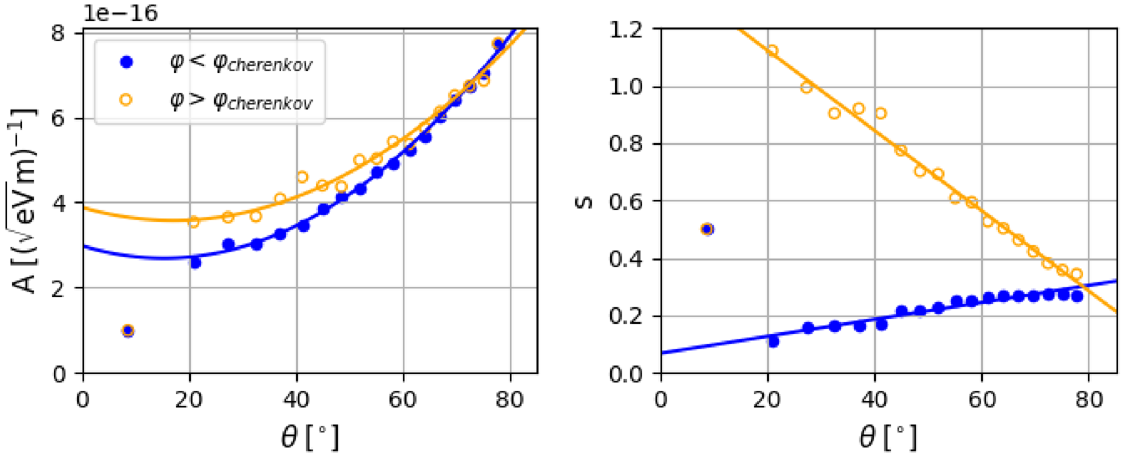

Figure 4. Results of the fits of eq. (3.2) for the different zenith bins. A quadratic and a linear function were fitted to the zenith dependence of the parameters A and s, respectively, and are shown as solid lines. Results for events seen from inside the Cherenkov ring are shown in blue, those seen from outside in red. Zenith angle bins $\theta < 30°$ were excluded from the fits.

separately from those seen from outside of it, a way to distinguish between the two is needed, which will be addressed in the next section.

3.3 Inside vs. outside of the Cherenkov cone

When reconstructing the electric field in section 2.2, we approximated the frequency dependence of $\log_{10}(|\vec{\mathcal{E}}(f)|)$ by a straight line. As is shown in figure 5, the actual radio signal

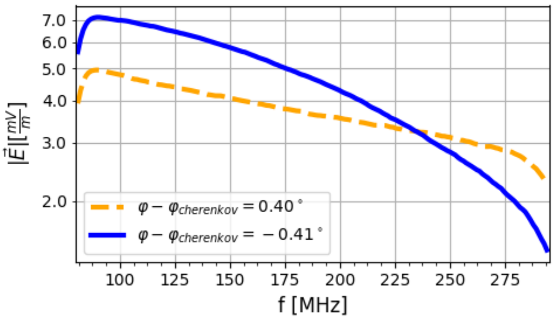

Figure 5. Spectra of the radio signals from the same air shower measured inside (blue) and outside (orange) of the Cherenkov ring. Both spectra deviate from the exponential parametrization used by the forward folding method, but while the spectrum curves upwards outside the Cherenkov ring, it curves downward inside of it. The sharp drop at 80 MHz and 300 MHz is caused by the bandpass filter.

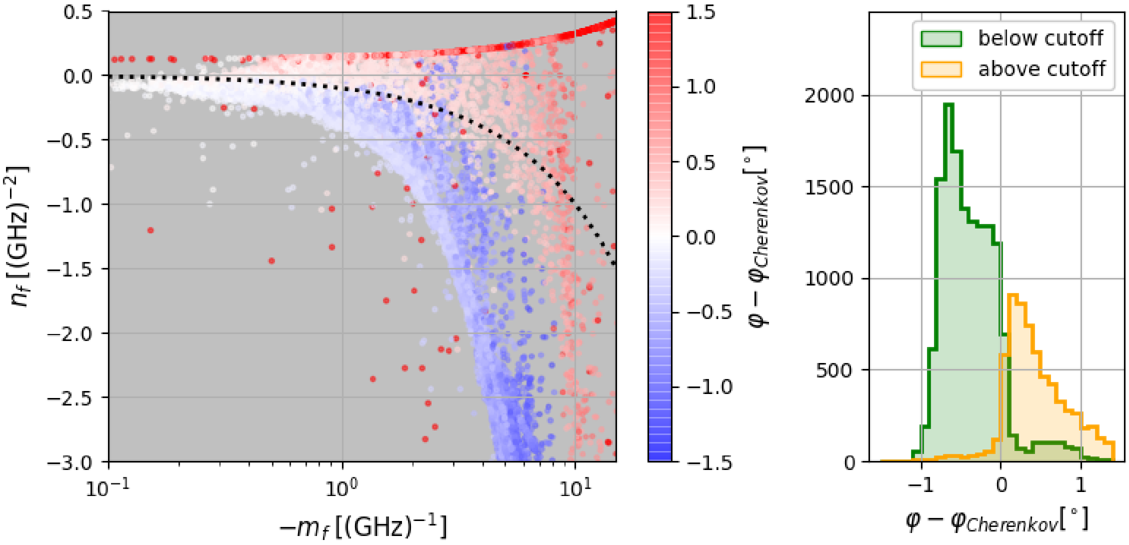

Figure 6. Left: relation between the spectrum slope parameter m_f and the quadratic correction parameter n_f for events with zenith angles $\theta \leq 30^\circ$. The color signifies the viewing angle φ relative to the Cherenkov cone, with events inside the Cherenkov cone in blue and outside in red. Right: distribution of the viewing angles φ relative to the Cherenkov cone for events above and below the black dotted cutoff line in the left plot.

deviates from this, with the frequency spectrum curving downward at higher frequencies for events seen from inside the Cherenkov ring and upward for those seen from outside of it. While the difference is small enough that it does not need to be taken into account when reconstructing Φ_E and m_f, it can be used to distinguish between the two event categories.

We extend the reconstruction of the electric field by an additional step, in which we modify eq. (2.3) by introducing an additional 2nd order term in the exponent:

$$\begin{pmatrix}\mathcal{E}_\theta \\ \mathcal{E}_\phi\end{pmatrix} = \begin{pmatrix}A_\theta \\ A_\phi\end{pmatrix} 10^{f\cdot m_f + (f-80\mathrm{MHz})^2\cdot n_f} \exp(\Delta j) \tag{3.3}$$

This pulse is fitted to the recorded voltage traces as described in section 2.2, using the results from fitting eq. (2.3) as starting values. The amplitudes A_θ and A_ϕ are allowed to change, while m_f is kept constant.

The relation between φ, m_f and n_f is shown in figure 6. Showers seen from within the Cherenkov ring tend to have a smaller n_f than those seen from outside of it. A simple linear function (black dotted line) can be used to separate the events into two groups: those above the line and those below it. Several cuts have been tested leading to similar efficiency and purity, so we have chosen to use the simplest. The histogram on the right shows the viewing angles relative to the Cherenkov cone of the two groups, demonstrating that these provide a good separation between events viewed from within and outside of the Cherenkov ring. A fraction of 90% of the events are either identified correctly or are less than 0.05° away from the Cherenkov angle. A mistake in the separation of events this close to the Cherenkov ring will result only in minor uncertainties on the reconstructed energy, as the energy parametrizations for both cases are very similar near the Cherenkov angle. One may notice that for large $|m_f|$, the discriminator seems to work very poorly, as events outside the Cherenkov ring tend to have small values of n_f. In principle, this could be improved by also defining a maximum value for $|m_f|$ above which all events are classified as being outside the Cherenkov ring. In practice however, the signals from these events are so weak that they are unlikely to be detected, making this additional step unnecessary.

As it was the case for the energy parametrization, this method works best for inclined showers. The difference in n_f for showers seen from within and outside of the Cherenkov ring tends to increase with the zenith angle. For small zenith angles, both event categories mostly overlap.

Knowing if the station is inside or outside of the Cherenkov ring, eq. (3.2) can now be used to determine the electromagnetic shower energy. The resulting energy reconstruction algorithm has been implemented as the *cosmicRayEnergyReconstructor* module in the *NuRadioReco* software framework [31], where one can see the full implementation in detail and use it to reconstruct the energy accordingly [40].

4 Obtainable energy resolution

Having developed an energy parametrization and a way to distinguish between air showers seen from inside and outside the Cherenkov ring, these can now be combined to reconstruct the shower energy. By performing this energy reconstruction on simulated air showers and comparing the result to the true energy, we can determine its performance under realistic conditions.

4.1 Monte Carlo data-set

To estimate the uncertainty of the reconstructed energies, a set of 200 CoREAS [28] simulations of air showers and their radio emissions was used. To mimic a realistic data set, the showers had an isotropic distribution of incoming directions up to a zenith angle of 80° and energies in the range of $10^{17}\,\mathrm{eV} < E < 10^{20}\,\mathrm{eV}$ with a spectral index of -2. For each air shower, the radio signal was simulated at 160 positions, arranged in a star-like pattern around the shower core. To achieve a realistic distribution of station positions, for each simulated air shower, 20 random positions within a radius of 2 km around the shower core were produced. For each of these random positions, the simulated electric field closest to it was determined

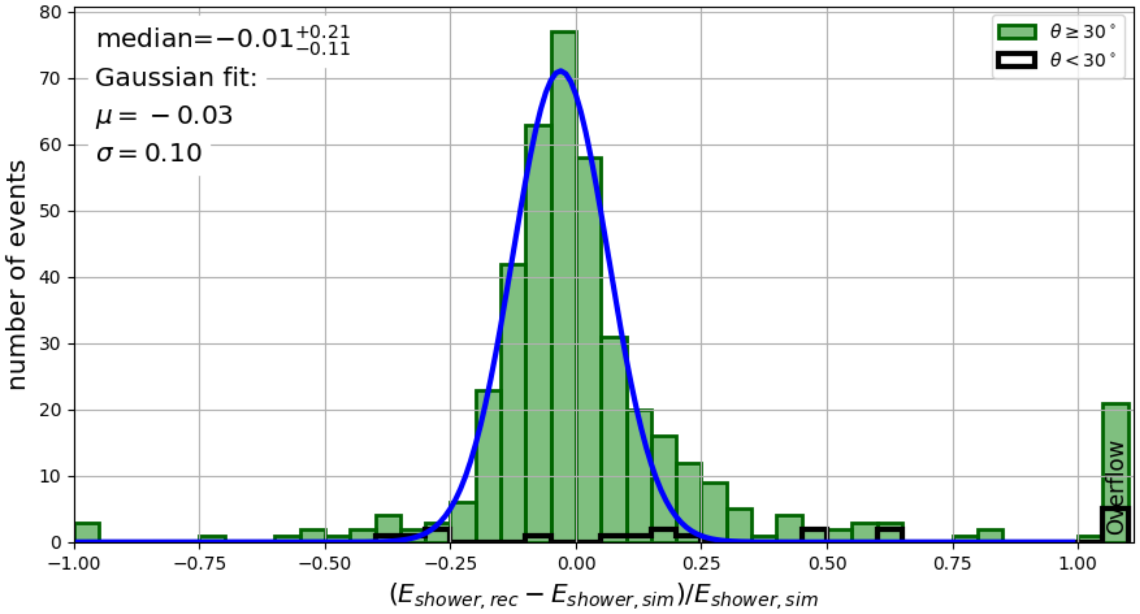

Figure 7. Uncertainties on the reconstructed energies for air showers with a zenith angle of $\theta \geq 30^\circ$ (green) and $\theta < 30^\circ$ (black). For $\theta \geq 30^\circ$ the distribution has a median of $-0.01^{+0.21}_{-0.11}$ with the uncertainties representing the 68% quantile. Fitting a Gaussian function to the histogram yields an average of $\mu = -0.03$ and a standard deviation of $\sigma = 0.10$. Note that the rightmost bin is an overflow bin.

and used in the analysis. More detailed information on the used Monte Carlo set is provided in appendix B.

Simulated electric field traces were folded with the antenna response and the effect of the signal chain was simulated to obtain the voltage traces. To account for the effect of noise, one of 100,000 forced-trigger events recorded by ARIANNA stations were randomly selected and its recorded voltage trace added. A dual-threshold trigger [29] was simulated by requiring the voltage pass both an upper and a lower threshold of ±80 mV (about 4 times the typical noise RMS) within 5 ns in at least 2 channels. Of the 4,000 radio pulses, 597 passed this selection. A 10th order Butterworth filter with a pass-band of 80 −300 MHz was applied to the voltages and a reconstruction of the incoming direction and the electric field was performed. The electromagnetic shower energy was estimated from eq. (3.2). Since the electric field reconstruction corrects for the detector response to the radio signal and the same detector description was used for simulation and reconstruction, the effect of uncertainties on the hardware components is neglected here. These concerns are addresses separately in section 4.3.

4.2 Energy resolution

The resulting energy resolution is shown in figure 7. While the energy reconstruction does not work well for vertical showers, for more inclined showers the distribution has a median of $-0.01^{+0.21}_{-0.11}$ with the uncertainties representing the 68% quantile. While the uncertainty is small for most events, there are several outliers where the energy was greatly overestimated. Most of these outliers happen with events that have a low signal-to-noise ratio. Because some periods have a higher noise level than normal [41], even a trigger with a threshold of 80 mV can produce events with a small signal-to-noise ration. Another problem can

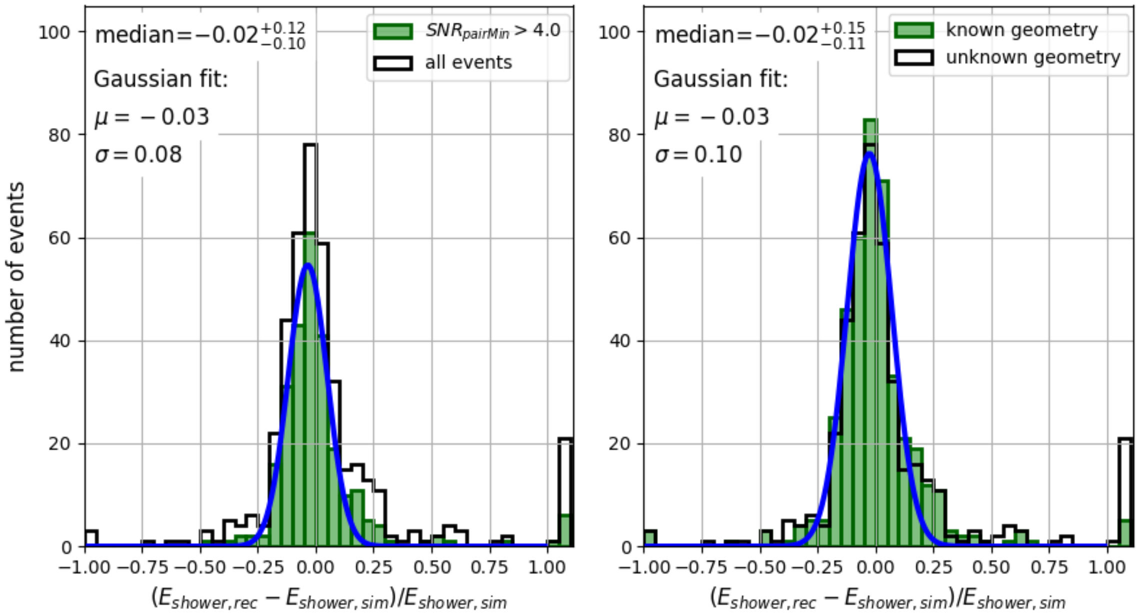

Figure 8. Left: energy resolution for air showers with a zenith angle of $\theta \geq 30°$ if a cut requiring the signal-to-noise ratio of at least one channel in each pair to be larger than 4 is applied, compared to the resolution without any cuts. In this case, the median is $-0.02^{+0.12}_{-0.10}$ with the uncertainties representing the 68% quantile. Fitting a Gaussian function to the histogram yields an average of $\mu = -0.03$ and a standard deviation of $\sigma = 0.08$. Right: achievable energy resolution if reliable information if the air shower was seen from inside or outside of the Cherenkov ring was available from another source. In this case, the distribution has a median of $-0.02^{+0.15}_{-0.11}$ with the uncertainties representing the 68% quantile. Fitting a Gaussian function to the histogram yields an average of $\mu = -0.03$ and a standard deviation of $\sigma = 0.10$.

occur with the direction reconstruction. Because each channel pair measures a different polarization, it is possible for the radio pulse to only be detected in one pair. In this case, the direction reconstruction is likely to produce a wrong result which in turn leads to a wrong reconstruction of the electric field and the energy. We therefore impose a stricter cut requiring that at least one channel in each pair has as SNR > 4. The resulting energy resolution is shown in figure 8 (left). With this cut, most of the outliers disappear and the resolution improves, with a median of $-0.02^{+0.12}_{-0.10}$.

It turns out that most of the outliers in figure 7 are caused by events viewed from within the Cherenkov ring being mistaken for events seen from outside of it. While an ARIANNA-like detector has no other way to identify if the station was inside or outside the Cherenkov ring, this task may be trivial for other radio detector designs, for example those that are part of a hybrid detector. Figure 8 shows the energy resolution if reliable information if the shower was seen from inside the Cherenkov ring or outside of it was available from some other source. In this case most outliers disappear and the resulting distribution has a median of $-0.01^{+0.15}_{-0.11}$ with the uncertainties representing the 68% quantile, having applied no SNR-cut. The remaining outliers are still mostly events with a relatively low signal-to-noise ratio, in which the electric field reconstruction did not converge properly.

It should be noted that this method, like all radio methods, reconstructs the energy in the electromagnetic cascade of the shower [34]. To get the cosmic ray energy, the invisible

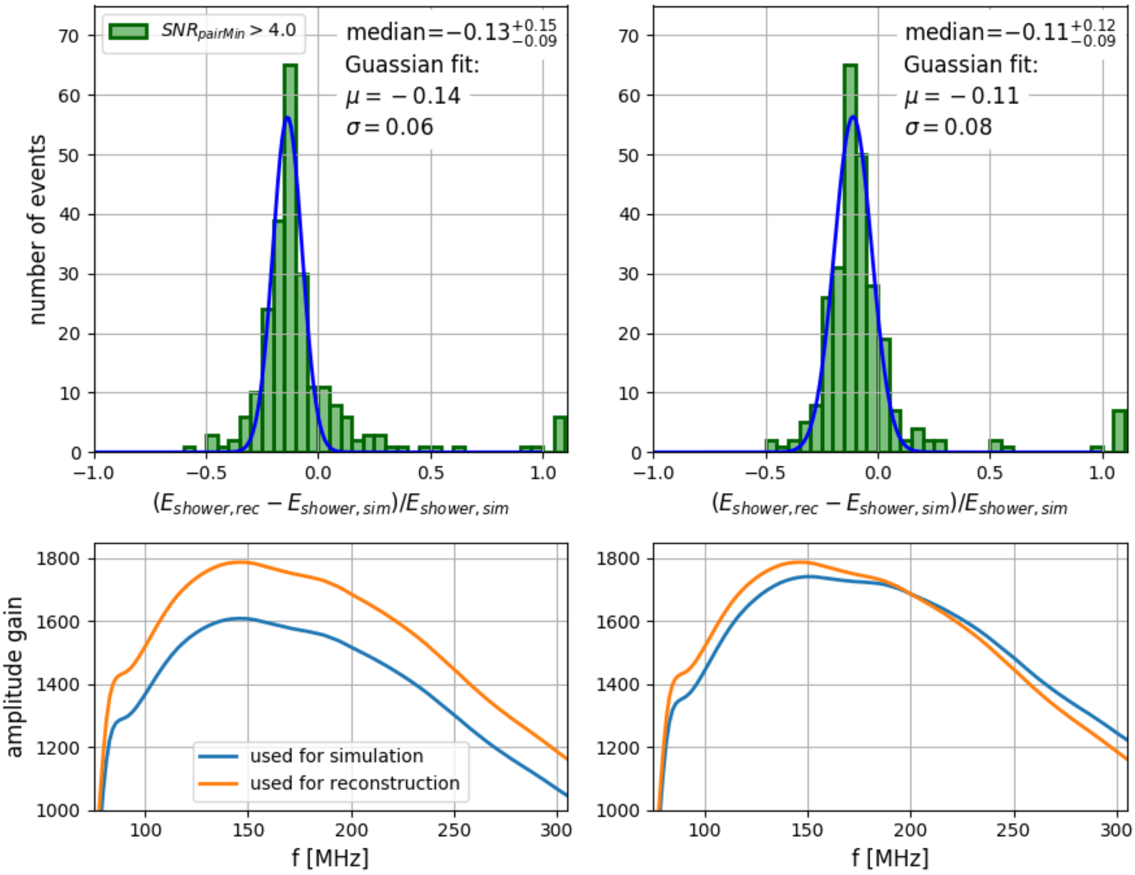

Figure 9. Effect of uncertainties in the amplifier response on the energy reconstruction. Top Left: resolution of the reconstructed electromagnetic shower energy if the amplifier gain is scaled by a factor of $p = 0.9$ (eq. 4.1). Top Right: resolution of the reconstructed electromagnetic shower energy if the amplifier gain is modified by eq. 4.2 with $q = 0.1$. Bottom: gain of the amplifiers used for the event simulation and reconstructions that resulted in the shower energy reconstructions shown above.

energy, which can be up to $\sim 20\%$ of the total shower energy, has to be taken into account as well [42].

4.3 Systematic effects of hardware uncertainties

Up to this point, the event simulation and reconstruction have used the same detector description, implying perfect knowledge of the detector response. This is, of course, not realistic, so in this section we will investigate the effect of hardware uncertainties on the energy resolution.

The procedure is as follows: we repeat the same simulation and reconstruction as in section 4, but when the detector response is simulated, certain aspects of the detector description are modified. Then, we reconstruct the event using the original detector description. This mimics the effect that uncertainties in the hardware would have on the event reconstruction.

The first investigated uncertainty is a deviation in the orientation of the antennas. We produce two sets of simulated events with one of the antennas rotated by 2° and 5° around the z-axis and perform a full event reconstruction using the default antenna orientation on both sets. The uncertainties on the reconstructed energies show no significant difference to those in figure 7. We therefore conclude that the influence of uncertainties on the antenna orientation on the reconstructed energy is negligible since 5° precision in the antenna orientation is easily achievable.

For the effect of uncertainties on the antenna or amplifier gain $g(f)$, we consider two different effects: the gain may be off by a constant factor for all frequencies. In that case, the energy fluence of the reconstructed radio signal would change, but the frequency slope m_f would remain unchanged. To test this, we scale the gain g by a constant factor p:

$$g' = p \cdot g \tag{4.1}$$

If the uncertainties in the amplifier gain are frequency-dependent, they may influence the reconstructed frequency slope m_f. To investigate this, the gain is modified by

$$g'(f) = g(f) \cdot \left(1 + q \cdot \frac{f - 200\text{MHz}}{200\text{MHz}}\right) \tag{4.2}$$

Because we operate in the 80 −300 MHz frequency band, this means the gain will be increased at one edge of the frequency band and decreased at the other by the same factor $q/2$. This modification will mainly affect the reconstruction of m_f, while the effect on Φ_E should be small.

The effect of these modifications to the amplifier gain are shown in figure 9. On the left, the gain was scaled by $p = 0.9$, on the right the slope was modified by $q = 0.1$. In both cases, the median shifted by $\approx 10\%$ compared to figure 7.

We tested changes in the amplifier gain for several values of p in the range $0.9 < p < 1.1$ and q in the range $-0.1 < q < 0.1$. In both cases, the shift of the median of the energy resolution is roughly linear with respect to p and q. The width of the Gaussian function fitted to the histogram showed little change, but the upper limit of the 68% quantiles increased for some modified amplifier gains. This was caused by errors in determining if the air shower was seen from inside or outside the Cherenkov ring, which caused additional outliers. Under the assumption of a known shower geometry, the 68% quantiles remained constant.

5 Discussion

We demonstrated that the signal detected by a single radio station is sufficient to accurately measure the energy in the electromagnetic part of an air shower. While the statistical uncertainty is better than 15%, additional systematic uncertainties from the hardware response, namely their influence on the energy fluence and the frequency spectrum, have to be considered, underlining the importance of a thorough calibration.

The estimator was developed in the context of a surface station of a neutrino array, but the concept can be applied to different detectors, both for cosmic rays and neutrinos, as long as the signal is measured in a broad-band going beyond 100 MHz.

5.1 Implications for cosmic-ray detectors

Our results may be applied to dedicated radio-based cosmic ray detectors in order to improve the accuracy of energy measurements. However, it requires a larger frequency band than the 30 −80 MHz band that most radio detectors today operate in, for two reasons: a larger frequency band makes the measurement of the frequency slope parameter m_f easier, as simply more data points are available for the reconstruction. Also, in the 30 −80 MHz band, the frequency spectrum can not be described by a simple exponential function [36, 37], so a more complex parameterization would have to be used, which makes the reconstruction more challenging. Together with an improved signal to noise ratio at higher frequencies [43], this makes the use of frequency bands outside the $30-80$ MHz band an attractive option.

The method developed in this paper is especially well suited for sparse arrays (antenna spacing $\sim \mathcal{O}(\mathrm{km})$), where many events are only detected by a small number of stations. Sparse arrays also often focus on the detection of inclined air showers, for which this method yields the best results.

In addition, combining the radio measurement of a shower with the measurement of muons provides an excellent estimator for the primary particle. It is shown in [44] that the ratio of the energy in the electromagnetic component of the shower, represented by the radio energy estimator, and the hadronic component, derived from the muonic component can be used as powerful discriminator. Thus, building a hybrid detector of radio antennas and muon detector, may successfully address the composition problem. If using the energy reconstruction method presented here, the array can even be sparse and therefore low-cost and competitive. It is also worth noting that one of the major sources for uncertainties is confusion between showers seen from inside and outside the Cherenkov ring. For hybrid experiments combining radio with other detection methods, this issue may be trivial (see e.g. [45]). We also developed and parameterized this method for a detector located at the South Pole and at the site of the Pierre Auger Observatory in Argentina (see appendix A).

5.2 Implications for neutrino detectors

The ability to measure the shower energy is a crucial requirement for any radio-based neutrino observatory. Experiments attempting to detect neutrino interactions in ice space their stations so far apart that a signal is expected to be only detected by a single station in most cases. This makes the ability to reconstruct the energy of a particle cascade from the measurement by one station alone essential.

By using air showers as a test case, we have explored a feasible way to achieve this. Because of the similarities between radio signals from air showers to those from neutrino-induced cascades in the ice, it is to be expected that our approach can be applied to neutrino detection as well. However, the radio signal from neutrinos shows additional complexities, such as an unknown vertex position, propagation effects through the ice and no dominant signal polarization due to a negligible geomagnetic emission. Therefore, further development is necessary in order to apply this method to neutrino detections. However, this method illustrates how a large band-width can be instrumental for the reconstruction and that methods like the forward folding of the pulse are robust to noise contributions.

6 Conclusions

We have presented a method to reconstruct the energy in the electromagnetic cascade of an air shower using radio signals recorded in the $80-300$ MHz band by a single detector station. By using a forward folding technique, we are able to measure the frequency spectrum of the signal more accurately and use it to estimate the viewing angle in relation to the Cherenkov angle. This information is combined with the energy fluence and the signal direction to provide an energy estimator.

The accuracy of this method under realistic noise conditions and using a realistic triggering scheme was investigated. For events with a sufficiently high signal-to-noise ratio, statistical uncertainties around 10% are achievable for the energy. Uncertainties in the orientation of the antennas were shown to be negligible while uncertainties in the amplifier gain have a significant effect and propagate linearly as systematic uncertainties on the reconstructed shower energy.

For cosmic-ray detectors, this method can be used to improve the accuracy of energy measurements, especially in sparse arrays, where often only measurements from a small number of stations are available. Regarding neutrino detectors, we have shown that it is possible to reconstruct the energy of a particle cascade from the signal of a single radio station, indicating a possible route towards the energy reconstruction for neutrinos at the highest energies.

Acknowledgments

We are thankful for the fruitful collaboration with our colleagues from the ARA and ARIANNA collaborations, especially for providing us with measured noise for this analysis. We acknowledge funding from the German research foundation DFG under grants NE 2031/2-1 and GL 914/1-1.

A Parameterization for other locations on Earth

Two additional tests were performed for other locations on Earth. The first location was the South Pole, which is the location of IceCube and its future extension IceCube-Gen2, which is planned to include a large radio array. Compared to Moore's Bay, the South Pole is at a higher elevation of 2800 m above sea level. While the geomagnetic field is nearly vertical at both the South Pole and Moore's Bay, it is weaker at the South Pole. Figure 10 shows the dependence of the corrected energy fluence of the radio signal Φ'_E and spectral slope m_f for different zenith angles for a radio detector at the South Pole. The distribution looks similar to the one shown in figure 2, indicating that the same method will work. Because of the higher elevation, the shower maximum is much closer to the detector than at Moore's Bay and in some cases, the shower can even be clipped by the ground before reaching its maximum. Shower clipping is a known issue for the radio detection of air showers [2] and reduces the achievable accuracy, as an unknown fraction of energy has not been deposited in the shower.

The second location we simulated was the site of the Pierre Auger Observatory, where the Auger Engineering Radio Array (AERA) is located [2]. Also, the Auger Observatory is in the process of being upgraded with radio antennas at all surface detectors [22]. The two main differences compared to Moore's Bay are the higher elevation of roughly 1500 m and the geomagnetic field, which has a zenith angle of 54 ° and is weaker compared to Moore's Bay. Figure 11 shows the dependence of the corrected energy fluence Φ'_E and spectral slope m_f on the viewing angle for a station at an elevation of 1564 m, where the Pierre Auger Observatory is, and at sea level (same longitude and latitude). As one can see, the differences in elevation only have a minor influence. The overall trend is again the same, one even observes less scatter at small zenith angles.

For a station in Antarctica, the energy of an air shower with a small zenith angle is difficult to reconstruct, because two effects coincide: the steep and featureless lateral distribution at small zenith angles and an almost vertical magnetic field. For small zenith angles, small angles α to the geomagnetic field cause the radio signal to no longer be rotationally symmetric around the shower axis. In addition, the lateral distribution of Φ'_E and m_f is flatter and provides less discrimination power for the position with respect to the shower axis.

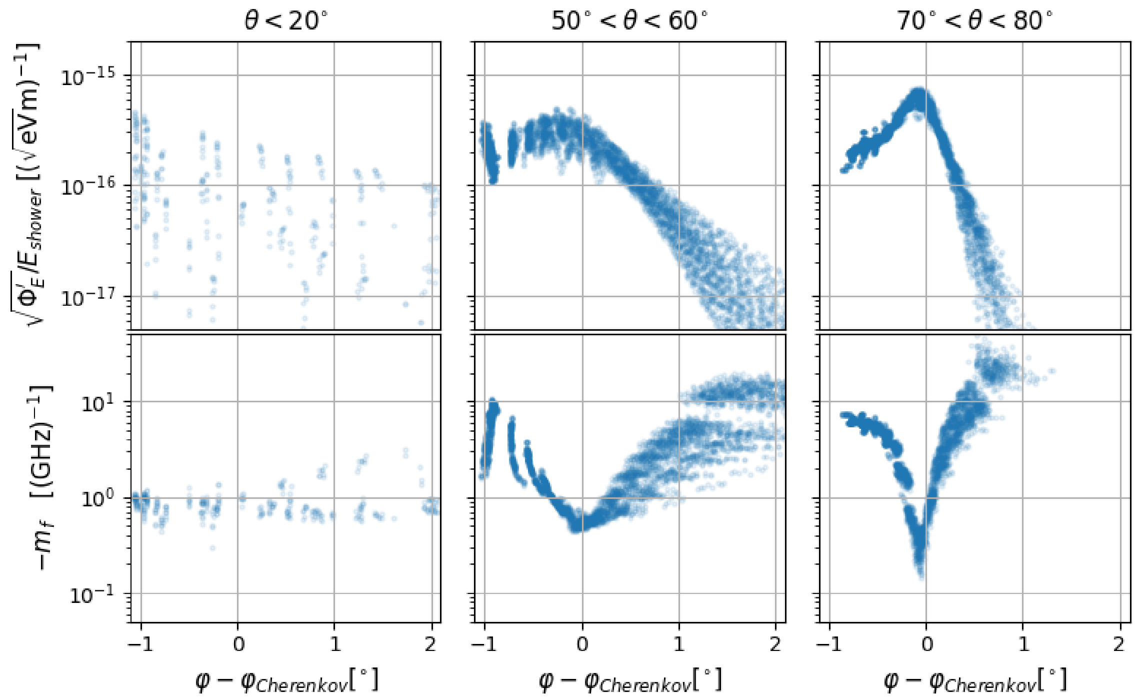

Figure 10. Lateral distributions of the energy fluence (top) and spectral slope (bottom) for simulated air showers at the South Pole at an altitude of 2800 m above sea level. This figure is equivalent to figure 2, so a more detailed description can be found there.

	$A = (a \cdot \theta^2 + b \cdot \theta + c) \cdot \frac{10^{18}}{m\sqrt{eV}}$			$s = m \cdot \theta + n$	
	a	b	c	m	n
Moore's Bay					
$\varphi < \varphi_{\text{Cherenkov}}$	442.46	-281.75	324.96	-0.1584	-0.07943
$\varphi > \varphi_{\text{Cherenkov}}$	394.08	-308.36	436.30	0.8070	-1.4098
South Pole					
$\varphi < \varphi_{\text{Cherenkov}}$	976.30	-1213.43	626.98	-0.2273	0.05627
$\varphi > \varphi_{\text{Cherenkov}}$	643.39	-667.08	478.06	1.3372	-2.1653
Auger					
$\varphi < \varphi_{\text{Cherenkov}}$	229.96	-123.75	110.51	-0.1445	-0.09820
$\varphi > \varphi_{\text{Cherenkov}}$	214.46	-111.01	119.18	0.5936	-1.1763

Table 1. Zenith dependence of the parameters A and s from eq. (3.2) for a station at Moore's Bay, the South Pole and the site of the Pierre Auger Observatory.

Because of the inclined magnetic field at the Auger site, the scatter at small zenith angles is smaller. Small values of α instead occur for more inclined showers, where they pose a smaller problem because of the more pronounced dependence of Φ'_E and m_f on the viewing angle.

The parametrizations shown in eq. (3.2) and figure 4 have been calculated for the South Pole and the Auger site as well and are shown in table 1 along with the ones for Moore's Bay.

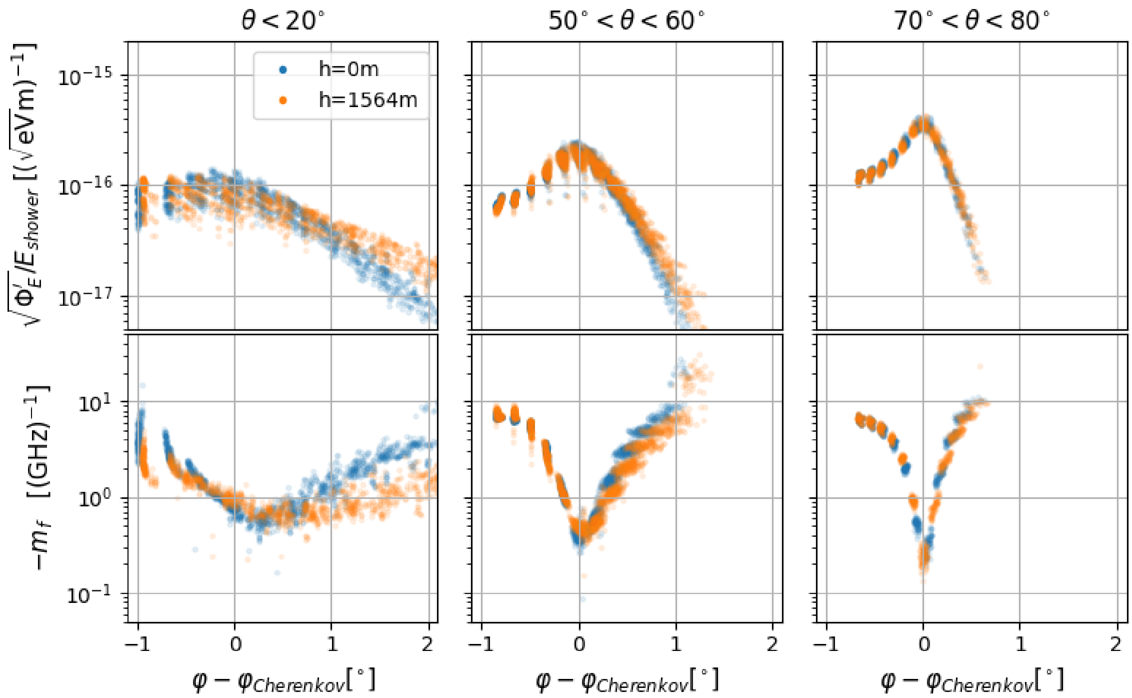

Figure 11. Lateral distributions of the energy fluence (top) and spectral slope (bottom) for simulated air showers at the site of the Pierre Auger Observatory. Simulations were done for detector stations at sea level (blue) and at an elevation of 1564 m above sea level, the elevation of the Pierre Auger Observatory (orange). This figure is equivalent to figure 2, so a more detailed description can be found there.

A detailed investigation of the achievable energy resolution at these locations would go beyond the scope of this paper, but it stands to reason that our method also works elsewhere and might even be able to provide better energy measurements for small zenith angles at locations with a less vertical magnetic field.

B Monte Carlo data set

The Monte Carlo data set to evaluate the performance of the energy estimator was generated by randomly generating an incoming direction for the cosmic ray from an isotropic distribution and an energy from a distribution with a spectral index of −2. Out of a set of CoREAS files, the one with properties most similar to those generated was selected for each generated event. The resulting distribution of zenith angles, azimuths and energies is shown in figure 12.

In each individual CoREAS file, observers are placed on a star-shape like pattern. Observers are placed symmetrically around the shower axis on the $\vec{v} \times \vec{B}-$ and the $\vec{v} \times (\vec{v} \times \vec{B})-$ axis, as well as on two lines bisecting the angle between the two axes.

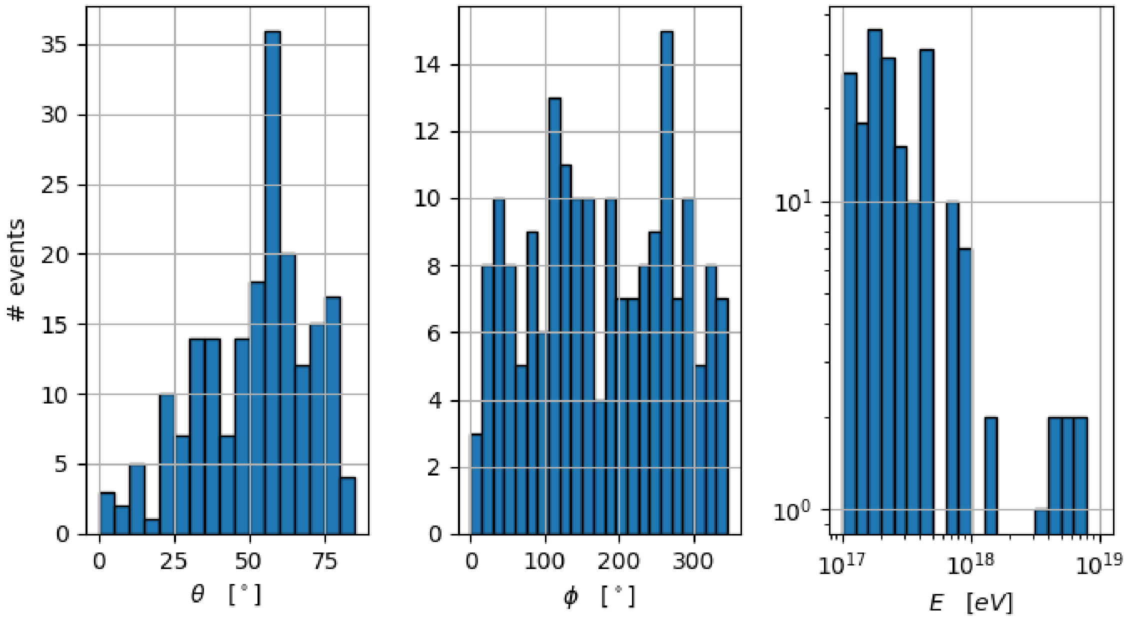

Figure 12. Zenith angles (left), azimuth angles (center), and energies (right) of the Monte Carlo data set used to evaluate the performance of the energy estimator.

References

[1] Pierre Auger collaboration, *Measurement of the radiation energy in the radio signal of extensive air showers as a universal estimator of cosmic-ray energy*, *Phys. Rev. Lett.* **116** (2016) 241101 [`arXiv:1605.02564`] [INSPIRE].

[2] Pierre Auger collaboration, *Energy estimation of cosmic rays with the engineering radio array of the Pierre Auger observatory*, *Phys. Rev.* **D 93** (2016) 122005 [`arXiv:1508.04267`] [INSPIRE].

[3] S. Buitink et al., *A large light-mass component of cosmic rays at* 10^{17}–$10^{17.5}$ *eV from radio observations*, *Nature* **531** (2016) 70 [`arXiv:1603.01594`] [INSPIRE].

[4] P.A. Bezyazeekov et al., *Reconstruction of cosmic ray air showers with Tunka-Rex data using template fitting of radio pulses*, *Phys. Rev.* **D 97** (2018) 122004 [`arXiv:1803.06862`] [INSPIRE].

[5] M. Gottowik, C. Glaser, T. Huege and J. Rautenberg, *Determination of the absolute energy scale of extensive air showers via radio emission: systematic uncertainty of underlying first-principle calculations*, *Astropart. Phys.* **103** (2018) 87 [`arXiv:1712.07442`] [INSPIRE].

[6] F. Halzen, *High-energy neutrino astrophysics*, *Nature Phys.* **13** (2016) 232 [INSPIRE].

[7] M. Ahlers and F. Halzen, *Opening a new window onto the universe with IceCube*, *Prog. Part. Nucl. Phys.* **102** (2018) 73 [`arXiv:1805.11112`] [INSPIRE].

[8] K. Murase and E. Waxman, *Constraining high-energy cosmic neutrino sources: implications and prospects*, *Phys. Rev.* **D 94** (2016) 103006 [`arXiv:1607.01601`] [INSPIRE].

[9] K. Greisen, *End to the cosmic ray spectrum?*, *Phys. Rev. Lett.* **16** (1966) 748 [INSPIRE].

[10] G.T. Zatsepin and V.A. Kuzmin, *Upper limit of the spectrum of cosmic rays*, *JETP Lett.* **4** (1966) 78 [*Pisma Zh. Eksp. Teor. Fiz.* **4** (1966) 114] [INSPIRE].

[11] V.S. Berezinsky and G.T. Zatsepin, *Cosmic rays at ultrahigh-energies (neutrino?)*, *Phys. Lett.* **B 28** (1969) 423 [INSPIRE].

[12] K. Kotera, D. Allard and A.V. Olinto, *Cosmogenic neutrinos: parameter space and detectabilty from PeV to ZeV*, *JCAP* **10** (2010) 013 [`arXiv:1009.1382`] [INSPIRE].

[13] M. Ahlers, L.A. Anchordoqui, M.C. Gonzalez-Garcia, F. Halzen and S. Sarkar, *GZK neutrinos after the Fermi-LAT diffuse photon flux measurement*, *Astropart. Phys.* **34** (2010) 106 [`arXiv:1005.2620`] [INSPIRE].

[14] A. van Vliet, R. Alves Batista and J.R. Hörandel, *Determining the fraction of cosmic-ray protons at ultrahigh energies with cosmogenic neutrinos*, *Phys. Rev.* **D 100** (2019) 021302 [`arXiv:1901.01899`] [INSPIRE].

[15] IceCube collaboration, *Differential limit on the extremely-high-energy cosmic neutrino flux in the presence of astrophysical background from nine years of IceCube data*, *Phys. Rev.* **D 98** (2018) 062003 [`arXiv:1807.01820`] [INSPIRE].

[16] S.W. Barwick et al., *Radar absorption, basal reflection, thickness and polarization measurements from the Ross Ice Shelf, Antarctica*, *J. Glaciol.* **61** (2015) 227 [`arXiv:1410.7134`] [INSPIRE].

[17] J. Avva, J.M. Kovac, C. Miki, D. Saltzberg and A.G. Vieregg, *An in situ measurement of the radio-frequency attenuation in ice at Summit Station, Greenland*, *J. Glaciol.* **61** (2015) 1005 [`arXiv:1409.5413`] [INSPIRE].

[18] S. Barwick, D. Besson, P. Gorham and D. Saltzberg, *South polar in situ radio-frequency ice attenuation*, *J. Glaciol.* **51** (2005) 231.

[19] A. Nelles et al., *The radio emission pattern of air showers as measured with LOFAR — a tool for the reconstruction of the energy and the shower maximum*, *JCAP* **05** (2015) 018 [`arXiv:1411.7868`] [INSPIRE].

[20] D. Ardouin et al., *Radio-detection signature of high energy cosmic rays by the CODALEMA experiment*, *Nucl. Instrum. Meth.* **A 555** (2005) 148 [`astro-ph/0504297`] [INSPIRE].

[21] LOPES collaboration, *Reconstruction of the energy and depth of maximum of cosmic-ray air-showers from LOPES radio measurements*, *Phys. Rev.* **D 90** (2014) 062001 [`arXiv:1408.2346`] [INSPIRE].

[22] Pierre Auger collaboration, *AugerPrime: the Pierre Auger observatory upgrade*, *EPJ Web Conf.* **210** (2019) 06002 [`arXiv:1905.04472`] [INSPIRE].

[23] Pierre Auger collaboration, *Observation of inclined EeV air showers with the radio detector of the Pierre Auger observatory*, *JCAP* **10** (2018) 026 [`arXiv:1806.05386`] [INSPIRE].

[24] J.A. Aguilar et al., *The next-generation radio neutrino observatory — multi-messenger neutrino astrophysics at extreme energies*, `arXiv:1907.12526` [INSPIRE].

[25] ARIANNA collaboration, *Targeting ultra-high energy neutrinos with the ARIANNA experiment*, *Adv. Space Res.* (2019) in press [`arXiv:1903.01609`] [INSPIRE].

[26] ARIANNA collaboration, *A first search for cosmogenic neutrinos with the ARIANNA hexagonal radio array*, *Astropart. Phys.* **70** (2015) 12 [`arXiv:1410.7352`] [INSPIRE].

[27] ARA collaboration, *Performance of two Askaryan radio array stations and first results in the search for ultrahigh energy neutrinos*, *Phys. Rev.* **D 93** (2016) 082003 [`arXiv:1507.08991`] [INSPIRE].

[28] T. Huege, M. Ludwig and C.W. James, *Simulating radio emission from air showers with CoREAS*, *AIP Conf. Proc.* **1535** (2013) 128 [`arXiv:1301.2132`] [INSPIRE].

[29] ARIANNA collaboration, *Design of the second-generation ARIANNA ultra-high-energy neutrino detector systems*, *IEEE Nucl. Sci. Symp. Med. Imag. Conf. Rec.* (2016) 7581856 [`arXiv:1511.07525`] [INSPIRE].

[30] S.W. Barwick et al., *Radio detection of air showers with the ARIANNA experiment on the Ross Ice Shelf*, *Astropart. Phys.* **90** (2017) 50 [`arXiv:1612.04473`] [INSPIRE].

[31] C. Glaser et al., *NuRadioReco: a reconstruction framework for radio neutrino detectors*, *Eur. Phys. J.* **C 79** (2019) 464 [`arXiv:1903.07023`] [INSPIRE].

[32] C. Glaser, S. de Jong, M. Erdmann and J.R. Hörandel, *An analytic description of the radio emission of air showers based on its emission mechanisms*, *Astropart. Phys.* **104** (2019) 64 [`arXiv:1806.03620`] [INSPIRE].

[33] D. Heck, M. Risse and J. Knapp, *Comparison of hadronic interaction models at Auger energies*, *Nucl. Phys. Proc. Suppl.* **122** (2003) 364 [`astro-ph/0210392`] [INSPIRE].

[34] C. Glaser, M. Erdmann, J.R. Hörandel, T. Huege and J. Schulz, *Simulation of radiation energy release in air showers*, *JCAP* **09** (2016) 024 [`arXiv:1606.01641`] [INSPIRE].

[35] K. Werner, K.D. de Vries and O. Scholten, *A realistic treatment of geomagnetic Cherenkov radiation from cosmic ray air showers*, *Astropart. Phys.* **37** (2012) 5 [`arXiv:1201.4471`] [INSPIRE].

[36] S. Jansen, *Radio for the masses*, Ph.D. thesis, Radboud University, Nijmegen, The Netherlands (2016) [INSPIRE].

[37] S. Grebe, *Finger on the pulse of cosmic rays*, Ph.D. thesis, Radboud University, Nijmegen, The Netherlands (2013) [INSPIRE].

[38] LOFAR CRKSP collaboration, *Characterisation of the radio frequency spectrum emitted by high energy air showers with LOFAR*, `PoS(ICRC2017)329` [`arXiv:1711.07749`] [INSPIRE].

[39] H. Schoorlemmer et al., *Energy and flux measurements of ultra-high energy cosmic rays observed during the first ANITA flight*, *Astropart. Phys.* **77** (2016) 32 [`arXiv:1506.05396`] [INSPIRE].

[40] *cosmicRayEnergyReconstructor.py*, https://github.com/nu-radio/NuRadioReco/blob/master/NuRadioReco/modules/cosmicRayEnergyReconstructor.py, (2019).

[41] S.W. Barwick et al., *Design and performance of the ARIANNA HRA-3 neutrino detector systems*, *IEEE Trans. Nucl. Sci.* **62** (2015) 2202 [`arXiv:1410.7369`] [INSPIRE].

[42] PIERRE AUGER collaboration, *Data-driven estimation of the invisible energy of cosmic ray showers with the Pierre Auger observatory*, submitted to *Phys. Rev.* **D** (2019) [`arXiv:1901.08040`] [INSPIRE].

[43] A. Balagopal V., A. Haungs, T. Huege and F.G. Schroeder, *Search for PeVatrons at the galactic center using a radio air-shower array at the South Pole*, *Eur. Phys. J.* **C 78** (2018) 111 [`arXiv:1712.09042`] [INSPIRE].

[44] E.M. Holt, F.G. Schröder and A. Haungs, *Enhancing the cosmic-ray mass sensitivity of air-shower arrays by combining radio and muon detectors*, *Eur. Phys. J.* **C 79** (2019) 371 [`arXiv:1905.01409`] [INSPIRE].

[45] TUNKA-REX collaboration, *Tunka-Rex: energy reconstruction with a single antenna station*, *EPJ Web Conf.* **135** (2017) 01004 [`arXiv:1611.09614`] [INSPIRE].

Chapter 5

Electric Field Reconstruction

5.1 Declaration of Authorship

The publication "Reconstructing non-repeating radio pulses with Information Field Theory", published in the Journal of Cosmology and Astroparticle Physics, Volume 4, in 2021, describes a method to use Information Field Theory to reconstruct radio signals from particle showers.

Information Field Theory was mainly developed by Torsten Enßlin and his group. I learned about this technique after attending the ECAP astroparticle School. It was my idea to apply this technique to the problem of signal reconstruction in neutrino detectors and was encouraged by my supervisor to independently pursue this analysis. IFT algorithms have been made available via the *nifty* software package, which was also used for this publication. I have developed and implemented the electric field reconstruction algorithm, with help from Philipp Frank, using the *nifty* and *NuRadioReco* software frameworks. The study on the reconstruction performance of the neutrino pulses was also done by me.

The majority of text of the publication was written by me, except for section 1.4 (an explanation of Information Field Theory), which was written by Philipp Frank. The text was reviewed and improved by all authors after that. All of the figures, except for the image of an RNO-G station in Fig. 3 (which was created by the RNO-G collaboration) were created by me.

5.2 Publication: Reconstructing non-repeating radio pulses with Information Field Theory

Journal of Cosmology and Astroparticle Physics
An IOP and SISSA journal

Reconstructing non-repeating radio pulses with Information Field Theory

C. Welling,[a,b] **P. Frank,**[c,d] **T. Enßlin**[c,d] **and A. Nelles**[a,b]

[a]DESY,
Platanenallee 6, 15738 Zeuthen, Germany
[b]Erlangen Center for Astroparticle Physics,
Friedrich-Alexander-Universität Erlangen-Nürnberg,
Erwin-Rommel-Str. 1, 91058 Erlangen, Germany
[c]Max Planck Institute for Astrophysics,
Karl-Schwarzschildstraße 1, 85748 Garching, Germany
[d]Ludwig-Maximilians-Universität München,
Geschwister-Scholl-Platz 1, 80539 München, Germany

E-mail: christoph.welling@desy.de, philipp@MPA-Garching.MPG.DE,
ensslin@MPA-Garching.MPG.DE, anna.nelles@desy.de

Received February 2, 2021
Accepted March 25, 2021
Published April 27, 2021

Abstract. Particle showers in dielectric media produce radio signals which are used for the detection of both ultra-high energy cosmic rays and neutrinos with energies above a few PeV. The amplitude, polarization, and spectrum of these short, broadband radio pulses allow us to draw conclusions about the primary particles that caused them, as well as the mechanics of shower development and radio emission. However, confidently reconstructing the radio signals can pose a challenge, as they are often obscured by background noise. Information Field Theory offers a robust approach to this challenge by using Bayesian inference to calculate the most likely radio signal, given the recorded data. In this paper, we describe the application of Information Field Theory to radio signals from particle showers in both air and ice and demonstrate how accurately pulse parameters can be obtained from noisy data.

Keywords: cosmic rays detectors, neutrino detectors, ultra high energy cosmic rays, ultra high energy photons and neutrinos

ArXiv ePrint: 2102.00258

https://doi.org/10.1088/1475-7516/2021/04/071

JCAP04(2021)071

Contents

JCAP04(2021)071

1 Introduction

The origin of the most energetic cosmic rays is still not conclusively identified. One approach to this problem could be *multi-messenger astrophysics*, where several types of cosmic particles are used to identify the sources of these ultra-high energy cosmic rays (UHECRs). Whatever sources produce UHECRs likely also emit high-energy neutrinos [1, 2], which are not deflected on their way to Earth. Additionally, the most energetic cosmic rays can interact with the cosmic microwave background to create high-energy neutrinos via the GZK effect [3–5]. Finding these *cosmogenic neutrinos* would also allow us to draw conclusions about the origins of UHECRs [6].

Considering this connection, it is not surprising that both cosmic ray and neutrino detectors face the same main problem at the highest energies: the steeply falling flux requires large effective areas, which lead to the construction of cosmic ray observatories that cover thousands of square kilometers [7, 8] and neutrino detectors with fiducial volumes on the cubic kilometer scale [9–11]. This is possible by not detecting UHECRs directly, but the showers they produce when interacting with the Earth's atmosphere, in the case of cosmic rays, or bodies of water or ice, in the case of neutrinos. One way of detecting these showers is to measure the radio signals they produce.

1.1 Detecting radio signals from particle showers

The emission of radio signals by particle showers in dielectric media has been proposed as early as the 1960s [12, 13]. At the time, technical limitations prevented its practical use for particle detectors, but advances in digital technology have turned this technique into a powerful method to detect high-energy particle showers. While it is used successfully for the detection of cosmic rays in several experiments (e.g. [14–16]), the use for neutrino detection in ice is just about to transition from prototype experiments [17, 18] to discovery-scale detectors [19, 20].

For a particle shower to emit strong radio signals, two conditions have to be met: first, there needs to be a separation of positive and negative charges in the shower front and the signals produced over the length of the shower profile need to overlap coherently, e.g. [21]. The separation of charges can be caused by two primary mechanisms: the *Askaryan effect* is the formation of a negative net charge in the shower front because positrons annihilate with electrons in the surrounding matter and Compton scattering accelerates electrons to become part of the shower. The other effect, called *geomagnetic emission* is the separation of charges by the Lorentz force from the geomagnetic field, which creates a positive and negative pole in the shower front. Because of its relatively high density, in ice the Askaryan effect is dominant. For air showers, geomagnetic emission is usually stronger, but the Askaryan effect has a significant contribution. It is possible to distinguish between both by the different polarization of their radio signals [22]. With Askaryan emission, the polarization is radial towards the shower axis while geomagnetic emission produces polarization in the direction of the Lorentz force.

The second required condition is similar to the Cherenkov effect. If an observer is positioned at the Cherenkov angle ($\sim 1^\circ$ in air, $\sim 54^\circ$ in ice) all radio emission produced during the shower development reaches it at the same time, leading to constructive interference. This means that the radio signal is strong on a cone around the shower axis. Compared to light in the visible spectrum, however, the much longer radio waves can maintain coherence more easily, so that even a few degrees off the Cherenkov angle, the radio signal is still strong enough to be detected, especially at lower frequencies.

After the radio signal has been emitted, it needs to propagate to the detector, during which it can be altered by propagation effects. For air showers, this is very straightforward: air is almost perfectly transparent for radio waves, so attenuation is negligible and the only modification to consider is a decrease in the electric field amplitude $|\vec{E}| \sim \frac{1}{R}$ with distance R of the observer from the shower maximum due to a widening of the illuminated area. In ice, the propagation of the radio signal from the emission region to the observer is much more complicated. The index of refraction of glacial ice changes with depth, which causes the ray path of the radio signal to be bent downward, instead of propagating in a straight line. Horizontal propagation of the radio signal has been observed as well [23–25], it seems, however, a secondary effect. The radio signal can also be reflected at the ice surface. Because of this, it is possible for multiple radio pulses from one shower to reach the same antenna. The attenuation length of radio signals in ice is on the order of 1 km [26–28], meaning that the absorption of the signal on the way to the detector has to be taken into account. The attenuation length is also frequency-dependent, meaning that it can change the shape of the frequency spectrum of the signal.

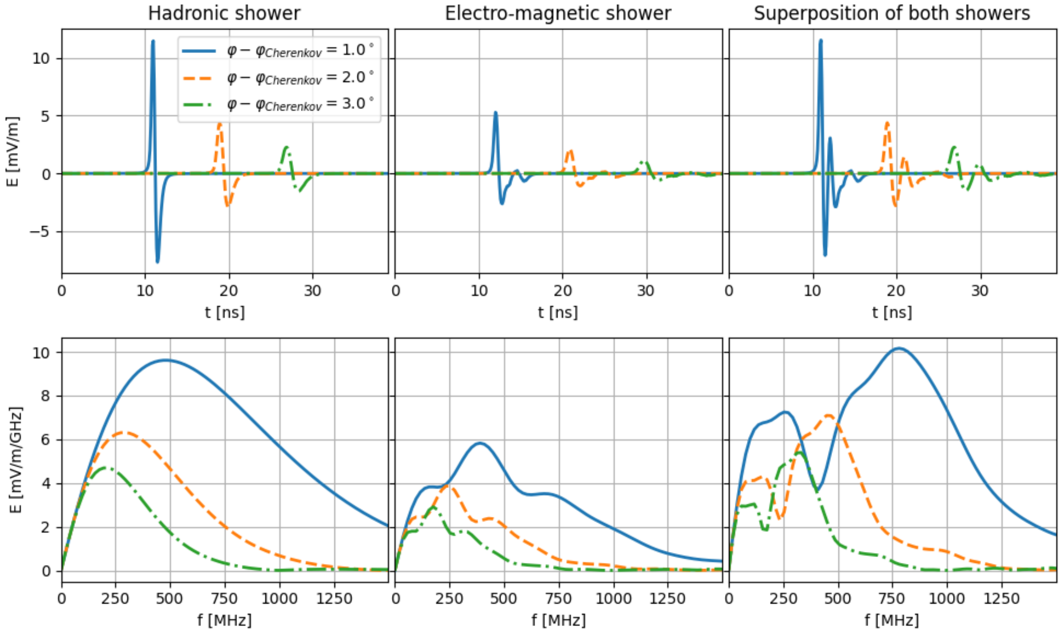

Figure 1. Examples of the radio signals from a particle shower in ice with a deposited energy of 1×10^{18} eV observed at a distance of 2 km in the time domain (top) and frequency domain (bottom). Left: radio signals from hadronic showers. Middle: radio signals from electro-magnetic showers. Right: superposition of the signals from a hadronic and an electro-magnetic shower. For better readability, the different pulses have been shifted in time. Simulations were performed with the *NuRadioMC* software framework [30] using the *ARZ* emission model [31].

1.2 Properties of radio signals from particle showers

The radio signal from a particle manifests as a short, linearly polarized pulse with a duration of the order of a few nanoseconds. In general, the amplitude of the radio signal is proportional to the shower energy E_{shower}, making it possible to reconstruct the energy of the primary particle from the radio signal. In practice, however, it is often easier to use the energy fluence of the radio signal

$$\phi_E = c \cdot \epsilon_0 \cdot \int \vec{E}^2(t)dt \tag{1.1}$$

for energy reconstruction, which scales with shower energy as $\phi_E \sim E^2_{\text{shower}}$ [29].

The amplitude also depends on the angle between the shower axis and the direction in which the signal is emitted, the so-called viewing angle. This is shown for in-ice showers in figure 1: as the difference between viewing angle and Cherenkov angle increases, the radio waves emitted during the development of the shower lose coherence and the overall signal becomes weaker. Looking at the frequency spectrum, this decrease in amplitude is not uniform over the whole bandwidth, but shorter wavelengths lose coherence more quickly and are suppressed. This means that, unless the viewing angle is very close to the Cherenkov angle, the radio signal is usually stronger at lower frequencies. This viewing angle dependence means that the shape of the frequency spectrum is an important property for the reconstruction of the shower energy, as it can be used as a proxy to correct for the loss of coherence if the radio signal is observed off of the Cherenkov angle. This technique has already been shown to work in the case of air showers [32] and is expected to be the preferred method for neutrino detection [19].

In the case of air showers, the frequency spectrum roughly follows an exponential function [33], for showers in ice, its shape is more complicated, as shown in figure 1. While a hadronic shower still produces a radio signal with a rather regular spectrum, a high-energy electro-magnetic shower is affected by the LPM effect [34, 35], making it longer and less smooth [36]. This means that there are effectively multiple smaller shower maxima, whose radio emissions interfere with each other, leading to a more irregular shape of the frequency spectrum. Even if the shower energy is too small for the LPM effect to occur, the charged-current interaction of an electron neutrino in ice will produce two particle showers: one hadronic shower from the nuclear recoil and one electro-magnetic shower from the electron produced in the interaction. The radio emissions from both showers interfere, which also leads to a rather complicated shape of the frequency spectrum. This makes it difficult to find a general analytic parameterization of the frequency spectrum, like it exists for air showers.

Because of these relationships between shower properties and the radio signal, calculating the electric field is an important step in the event reconstruction process of many radio detection experiments. In this paper, we present a new method to reconstruct the electric field from noisy antenna measurements, the software for which is freely available as part of the *NuRadioReco* software package [33]. How to best use the results from this method will depend on the specific detector setup and the goal of the analysis. One may also imagine using the presented method for event identification, however, we focus on reconstruction and provide a small outlook on possible applications in section 3.4.

1.3 Reconstructing the electric field from noisy data

For the reconstruction of the electric field $E(t)$ of the radio pulse from the recorded time-dependent voltage traces (waveforms) $U(t)$, it is useful to transform them into the frequency domain via Fast Fourier Transformation (FFT) to get the frequency spectrum $\mathcal{V}_i(f)$. The electric field is also expressed in the frequency domain by the two components $\mathcal{E}^\theta(f)$ and $\mathcal{E}^\phi(f)$, which describe the polarizations in the $\vec{e}_\theta$ and $\vec{e}_\phi$ directions, respectively.[1] If the incoming direction (θ, ϕ) of the radio signal is known, the antenna response of channel i to the $\vec{e}_\theta$ and $\vec{e}_\phi$ components of the electric field can be expressed by the vector effective length $\mathcal{H}_i^\theta(f, \theta, \phi)$ and $\mathcal{H}_i^\phi(f, \theta, \phi)$. The result is a system of linear equations, connecting the electric field to the waveform recorded by each channel:

$$\begin{pmatrix} \mathcal{V}_1(f) \\ \mathcal{V}_2(f) \\ \dots \\ \mathcal{V}_n(f) \end{pmatrix} = \begin{pmatrix} \mathcal{H}_1^\theta(f) & \mathcal{H}_1^\phi(f) \\ \mathcal{H}_2^\theta(f) & \mathcal{H}_2^\phi(f) \\ \dots \\ \mathcal{H}_n^\theta(f) & \mathcal{H}_n^\phi(f) \end{pmatrix} \begin{pmatrix} \mathcal{E}^\theta(f) \\ \mathcal{E}^\phi(f) \end{pmatrix} \tag{1.2}$$

If data from enough channels ($n = 2$) is available, in principle, solving this system of equations yields a reconstruction of the electric field (e.g. [37]). In practice, however, the recorded voltage waveforms are always contaminated by a certain amount of noise, so the resulting electric field will be contaminated, too. Especially, if the system of equations is over-determined ($n > 2$) an exact solution for (1.2) does not exist. In this case, the electric field is typically reconstructed by minimizing the sum of the squared errors on $\mathcal{V}_i(f)$ for each frequency bin (e.g. [33]).

This method works well in many situations, but it has some shortcomings, especially for low signal-to-noise ratios (SNR): figure 2 shows an example, in which the radio signal from an

---

[1] Since the detector is in the far field, the electric field in $\vec{e}_r$ direction can be assumed to be 0.

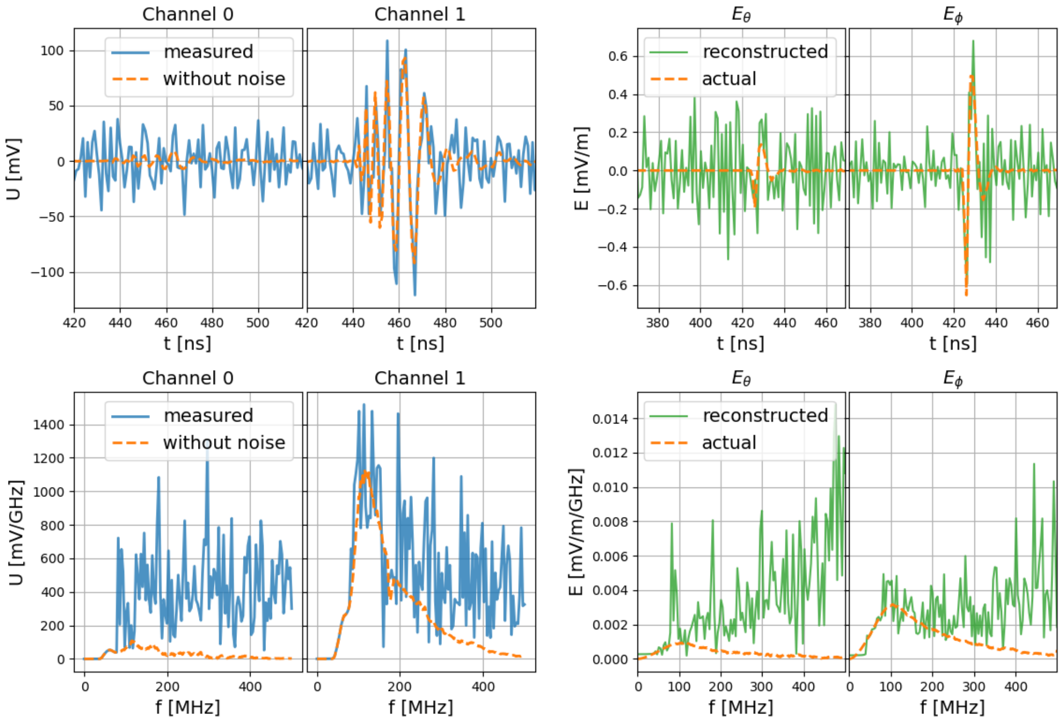

Figure 2. Example for the electric field reconstruction from noisy data by solving (1.2). Left: signals with (blue solid) and without noise (orange dotted) in the time-domian (top) and frequency domain (bottom). Right: reconstructed electric field (green solid) in the time domain (top) and frequency domain (bottom) compared to the true noiseless electric field (orange dotted).

air shower is reconstructed from the waveforms measured by two logarithmic-periodic dipole antennas (LPDAs). Both are pointing directly upwards and are angled 90 ° relative to each other, so that one is sensitive to the north-south and the other to the east-west component of the electric field. If one of the components of the electric field is small, as is the case for the $\vec{e}_\theta$ component in this example, it is overestimated, because noise is interpreted as coming from the radio signal. Especially if none of the antennas has a high sensitivity to one of the electric field components, errors in the reconstruction of the signal polarization can be large. For example, this would be the case for very inclined air showers, for which $\vec{e}_\theta$ is almost vertical, if it is detected by the antennas are only sensitive to the horizontal electric fields.

Another issue the shape of the frequency spectrum. It is usually not possible to construct a broadband antenna that has a uniform sensitivity over the entire frequency band. This can cause the reconstruction to overestimate the electric field at frequencies with low sensitivity, as any noise there is interpreted as being caused by the radio signal and not by noise. In figure 2, this is what causes the reconstructed electric field spectrum to rise with higher frequencies.

For these reasons, more advanced reconstruction methods are needed if one wants to use the electric field polarization and especially the shape of the spectrum for event reconstruction. In the case of air showers, a *forward folding* method has previously been developed, which fits a parameterization of the frequency spectrum to the data [32, 33]. Such parameterizations also exist for particle showers in ice, so the same approach is in principle possible for neutrino detectors. There are, however, caveats. While the shape of the frequency spectrum is relatively simple for hadronic showers and low-energy electromagnetic showers, the LPM effect causes the shower to become elongated and more irregular at high energies, which in turn makes the shape of the spectrum more irregular (see figure 1). On top of that, charged-current interactions of ν_e cause both a hadronic and an electro-magnetic shower, whose signals can interfere and cause a complicated spectral shape. This makes *forward folding* with a single signal parameterization a challenging approach for neutrino detectors.

Additionally, it seems prudent to avoid too much reliance on parameterizations derived from theoretical calculations. No neutrino interaction in ice has so far been identified by its radio signal, which would confirm that the spectrum of the electric field matches the predictions. Also, building bias-free confidence in these models when having detected a neutrino, will not be possible, if the reconstruction of the electric field is already using model-predictions. On top of that, propagation effects could alter the radio signal on its way from the source to the detector e.g. [24, 25, 38, 39]. These will be difficult to incorporate into an analytic parameterizartion, especially if the ice properties are not well known.

Therefore, we need a method that can reconstruct the electric field from the noisy waveforms recorded by the antennas, while also making only minimal, and well-founded, assumptions about what the result should look like. *Information Field Theory* can provide such a method.

1.4 Information Field Theory (IFT)

IFT [40, 41] is a statistical field theory developed to perform probabilistic reasoning about quantities (i.e. fields) that are defined over a continuous space. Specifically it extends information theory to square-integrable functions and allows for a probabilistic inference of such functions from noisy and incomplete observational data. IFT has successfully been applied in the past to various astrophysical data analysis tasks such as for example radio interferometry [42, 43], galactic tomography [44, 45], and galactic all sky imaging [46]. As fields are infinite dimensional quantities whereas the data is always finite dimensional, such inference problems are ill-posed and therefore a prior model is inevitable.

In this work a prior model for the electric field is defined by means of a generative process. Specifically

$$\mathcal{E} = s\left(\xi\right) , \tag{1.3}$$

where all elements of ξ follow the same probability distribution, called standard distribution, and therefore are independent and identically distributed random variables. Note that every continuous prior process can be expressed as a generative process by means of inverse transform sampling. In this work the standard distribution is set to be a zero mean Gaussian distribution with unit variance. This makes sampling from the prior distribution (see figure 4) very straightforward as a sample from the prior process is defined as the result of applying the generative mapping s to a sample from the standard distribution.

Combining the prior model with the likelihood of observing the measured voltage U given the electric field $\mathcal{E}$ gives rise to the joint distribution of U and ξ via the product rule for probabilities as

$$\mathcal{P}\left(\xi, U\right) = \mathcal{P}\left(U|\mathcal{E} = s\left(\xi\right)\right)\ \mathcal{P}\left(\xi\right) = \mathcal{P}\left(U|\mathcal{E} = s\left(\xi\right)\right)\ \mathcal{N}\left(\xi|0, \mathbb{1}\right) , \tag{1.4}$$

which is proportional to the posterior distribution $\mathcal{P}\left(\xi|U\right)$ up to a normalization factor independent of ξ.

For all but the simplest combinations of prior processes and likelihoods, integration w.r.t. the posterior is not possible analytically and therefore posterior expectation values cannot be computed directly and have to be approximated numerically. In this work we employ an approximation method based on variational inference, specifically we use Metric Gaussian Variational Inference (MGVI) [47]. MGVI approximates the posterior distribution as a Gaussian distribution with the additional constraint that the covariance is set to be the inverse of the Fisher-Metric, evaluated at the mean of the Gaussian distribution. Approximation is achieved by numerical minimization of the forward Kullback-Leibler divergence between the posterior distribution and the approximation w.r.t. the mean. This provides an accurate estimation of the first moment in terms of the mean, and provides a lower bound to the second moment of the posterior distribution. The posterior is accessed via sampling from the approximate distribution and posterior expectation values are approximated by means of sample averages. Further details of the numerical approximation can be found in [47].

2 Using IFT for the reconstruction of electric-field pulses

Using IFT to reconstruct the electric field of a radio pulse means, stated in IFT terms, constructing the probability $\mathcal{P}(\mathcal{E}|U)$, which states the probability of the electric field, given the voltages measured by the radio antennas and prior assumptions. For this, we need a model for the prior distribution of the electric field, a model of the detector response, which connects the electric field to the measured voltages, and of the noise.

We do this for two distinct, but similar use cases: the radio detection of neutrinos and of cosmic rays.

2.1 Use case: in-ice neutrino detection

For the case of in-ice detection of neutrinos, we show a simulation study of the Radio Neutrino Observatory in Greenland (RNO-G) [19]. RNO-G will consist of a total of 35 independent detector stations, placed on a grid with a spacing of 1.5 km at Summit Station, Greenland. Because of the large spacing, most neutrinos will be detected by only one station. Therefore, we consider only a single RNO-G station for this simulation study.

The layout of one RNO-G station is shown in figure 3. It can be separated into a *shallow* and a *deep* component. The *shallow* component consists of 3 arms with 3 logarithmic-periodic dipole antennas (LPDAs) on each of them. While they have excellent broadband sensitivity, their shallow depth makes it less likely that a radio signal from within the ice can reach them, so for most events, measurements from the LPDAs will not be available. The *deep* component consists of 3 holes going down to a depth of 100 m below the surface, in which cable strings with radio antennas on them are placed. One of the strings, called *power string*, holds a total of 9 antennas. Four of them are vertically polarized (Vpol) antennas spaced 1 m apart, which form a phased array trigger at the very bottom of the string. Three more Vpol antennas are positioned with a spacing of 20 m further up the string. Additionally, two horizontally polarized (Hpol) antennas are placed directly above the phased array. The other two so-called *helper strings* are more sparsely instrumented, with two Vpol and one Hpol antennas at a depth of about 100 m.

The design of the radio antennas is limited by the width of the boreholes they have to fit in. As shown in figure 3, for this reason the Vpol antennas have a higher gain than the Hpol antennas and a maximum gain at lower frequencies. Together with the fact that the radio signals detected with RNO-G tend to be more strongly polarized in the vertical direction, this means that the signal detected by the Hpol channels will often be hidden below the noise

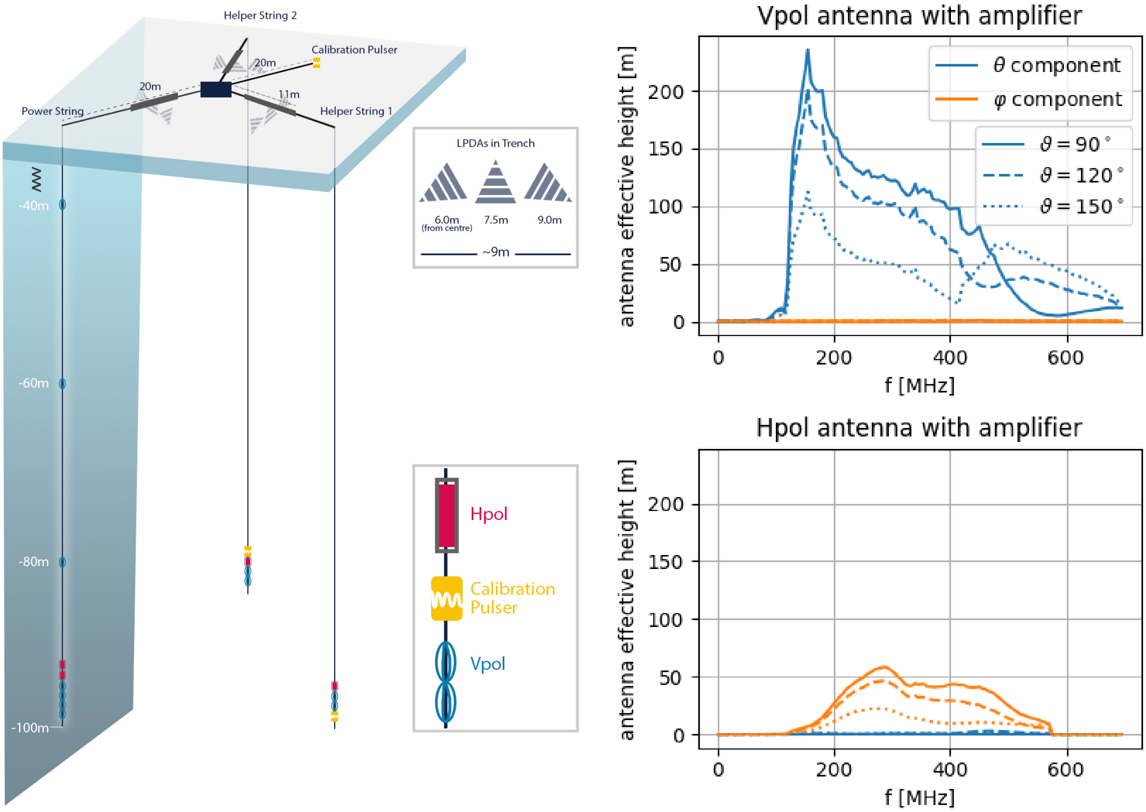

Figure 3. Left: one of the 35 stations that make up the RNO-G detector. The figure shows the station design as used for this analysis. RNO-G is still under construction and the station design may change. In particular the performance of the Hpol antennas will likely improve over what is shown in this article. For details, see [19], from where this figure is taken. Right: response of the amplifier and the antenna of the Vpol (top) and Hpol (bottom) channels as used in this analysis.

level, while it is only visible in the Vpols. It should be noted that at the time of writing the Hpol design of RNO-G was not finalized and this analysis uses the performance parameters of a first iteration, so experiment related performance will change in the future.

Depending on the arrival direction, the radio signal will reach each antenna at a different time. For a full reconstruction of the neutrino properties, this timing offset has to be obtained from data. How to do this best is beyond the scope of this paper. We therefore calculate the correct time offset from the location of the simulated interaction vertex. Radio-based neutrino detectors have shown sub-nanosecond timing accuracy and the ability to reconstruct the signal direction to better than 1 ° [18, 48], so correcting for time differences will likely not be the determining uncertainty.

For the purpose of demonstrating the IFT approach, we will only use the signals in the four Vpols making up the phased array and the two Hpols directly above them. These are located sufficiently close to each other that the radio signals reaching those antenna are very similar for most events. However, this is very dependent on the event geometry, so especially if the distance between the neutrino interaction vertex and the detector station is small, there can be differences in the signal, even between neighboring channels of the phased array. These manifest mostly as differences in the signal amplitude, while the shape of the spectrum tends to change less.

2.2 Model building

Using IFT for the purpose of reconstructing short, non-repeating pulses, first a model of the expected pulse has to be developed. The approach to modelling the signal and the detector response is as follows: first, the amplitude and the complex phase factor of the electric field spectrum are modeled independently from each other as real and complex numbers in the frequency domain, and then multiplied together. Next, the response of the antenna and the amplifier, which are also modeled in the frequency domain, are applied to this to get the spectrum of the voltages measured by each channel. Finally, the result is transformed into the time domain where it can be compared to the data.

To have the electric field amplitude on a predictable scale, we normalize the waveforms of all used channels, so that their overall maximum value is equal to 1. As this normalization factor is known, it can be reapplied afterwards to obtain the correct electric field strength. Because the detector is only sensitive in a certain range of frequencies, we apply a 10th order Butterworth filter with an according passband (in this case 132 MHz to 700 MHz) to the channel waveform.

The electric field spectrum is split into its amplitude $E(f)$ and phase $\varphi(f)$:

$$\mathcal{E}(f) = E(f) \cdot \exp(i \cdot \varphi(f)) \tag{2.1}$$

We model the amplitude $E(f)$ as a correlated, positive random process by means of a log-normal process, in which $s(f) = \log(E(f))$ obeys a Gaussian statistics. The correlation structure $S_{f,f'} := \langle s(f)\, s(f') \rangle_{(s)}$ of the logarithmic amplitude is assumed to be statistically homogeneous in f, but the exact form of S is unknown prior to observation. Following the prior model described in [43], we express S in terms of its eigen-spectrum $\tau(k) = |A(k)|^2$, with k being the Fourier partner of f and $A(k)$ an amplitude modulating function that turns standard white noise excitation variables $\xi'(k)$ into the Fourier space variables $s(k) = A(k)\, \xi'(k)$ that exhibit the correct statistics, $S_{k,k'} := \langle s(k)\, s(k') \rangle_{(s)} = 2\pi\delta(k - k')\, \tau(k)$. We place a prior on $\tau(k)$ such that it is preferably a power-law like spectrum $\propto k^{-\alpha}$, but allow for possible, differentiable deviations from this. We visualize this model by drawing random samples from the generative process and by plotting the results in figure 4. The top left plot shows the spectral power modulation function $A(k)$ for the function describing the electric field amplitude.[2] The slope $\alpha/2$ of this determines the smoothness of the electric field prior, with a steeper power spectrum (larger α) resulting in a smoother prior. The resulting electric field spectra are shown in the top right of figure 4. They are relatively smooth as a result of our choice of α, but other than that no prior assumptions are made, except for the 10th order Butterworth filter that is applied at the edges of the detector's passband. The small differences in the direction into which the radio signal reaching different channels was emitted can lead to small differences in the signal strength between channels. We want the model to be able to account for this. In case the signal-to-noise ratio is relatively small, we do not expect to be sensitive to such differences anyway, and would rather avoid adding additional free parameters. Anticipating the variation between channels is rather difficult as this is very dependent on the event geometry, so we opt for a simple measure here: if the signal-to-noise ratio (SNR)[3] of any of the measured waveforms is above 10, we multiply the spectrum

---

[2] Technically, this is a spectrum of a spectrum, and therefore k is defined in the time domain. We forego this subtlety here and use the notation that is usually used for the power spectrum.

[3] We define the signal-to-noise ratio as half the peak-to-peak amplitude, divided by the root-mean-square of the noise.

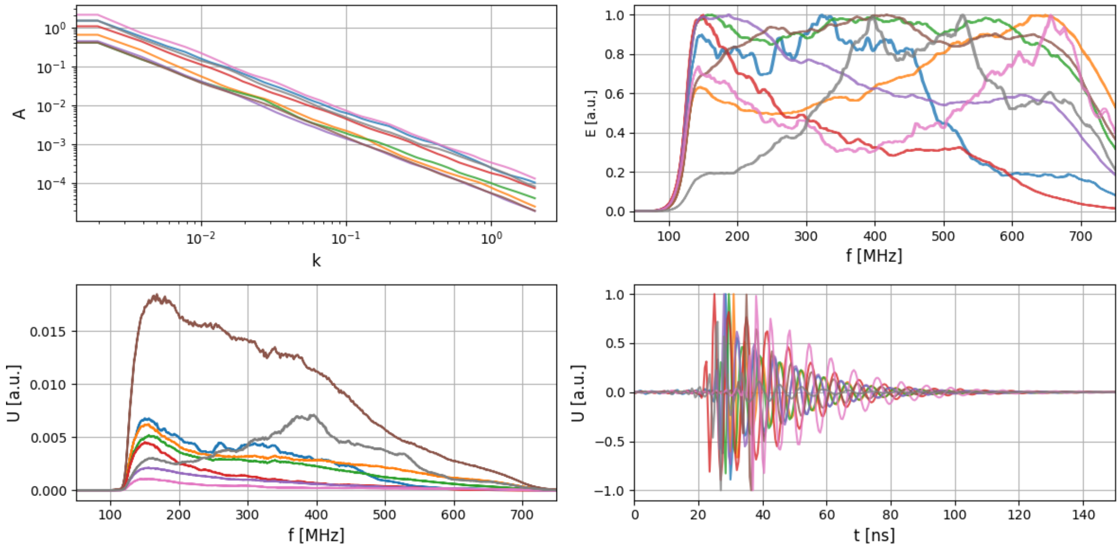

Figure 4. Samples drawn from the prior distribution of the IFT model. Top left: amplitude power of the Fourier modes k of the function describing the electric field spectrum. Top right: spectrum of the electric field. For better readability, all samples have been normalized to the same maximum value. Botton left: spectrum of the channel voltage. Bottom right: voltage trace in the time domain.

amplitude for each channel with an additional parameter a. This parameter's Gaussian prior distribution is centered around 1 with a standard deviation of $\sigma_a = 0.1$, which means that we assume the difference between channels to be relatively small, unless the data shows otherwise. If none of the channels reaches an SNR of 10, this parameter is left out, which forces the electric field at each channel to be the same. Whether or not to include this parameter is ultimately a judgement call. In general, it is better to avoid unnecessary free parameters in the model, on the other hand measuring these differences between channels provides additional information that could be used for the neutrino reconstruction and may be necessary for the IFT model to be able to fit the data. A simple SNR cut to decide this is rather crude and somewhat arbitrary, but it is good enough for our purposes here and may easily be substituted for a more advanced decision process, should it become necessary.

The electric field consists of a single, very short pulse. Modelling the phase as constant over the entire spectrum would result in a pulse at $t = 0$ that rolls over into the end of the waveform. Since a shift in the time domain corresponds to a slope of the phase in the frequency domain, we can shift the model pulse to the correct position in the waveform, by modelling the phase $\varphi(f)$ as a linear function

$$\varphi(f) = \varphi_0 + mf \tag{2.2}$$

where φ_0 and m are Gaussian variables. By choosing the mean $\bar{m}$ and standard deviation σ_m of the slope m, we can encode the position of the pulse in the recorded waveform as well as the uncertainty on it. This is useful, since the exact position of the pulse maximum can depend on the amplitude of the spectrum as well as the phase, making it tricky to determine the correct slope that should be used for the phase model ahead of time. Group delay in the antenna or amplifier response can also introduce small time offsets. With this fitting procedure, small timing errors of a few nanoseconds can be adjusted for.

Thus, the full prior distribution for $\mathcal{E}(f)$ is given as

$$\mathcal{P}\left(\mathcal{E}(f)\right) = \int \dots \int \delta\left(\mathcal{E}(f) - e^{s(f)+i(\varphi_0+mf)}\right) \mathcal{N}\left(s|0, S(\tau)\right)\ \mathcal{P}(\tau)$$
$$\mathcal{N}\left(\varphi_0|\bar{\varphi}_0, \sigma_0^2\right)\ \mathcal{N}\left(m|\bar{m}, \sigma_m^2\right) \mathrm{d}s\mathrm{d}\tau\mathrm{d}\varphi_0\mathrm{d}m. \tag{2.3}$$

The spectra of the θ and φ components of the electric field are identical to each other in shape, so the polarization can be described by a single parameter, called *polarization angle* defined as $\tan(\varphi_{pol}) = \frac{|\mathcal{E}_\phi|}{|\mathcal{E}_\theta|}$. This allows us to split the electric field spectrum into its $\vec{e}_\theta$ and $\vec{e}_\phi$ components:

$$\vec{\mathcal{E}}(f) = \mathcal{E}(f) \cdot \cos(\phi_{\mathrm{pol}}) \cdot \vec{e}_\theta + \mathcal{E}(f) \cdot \sin(\phi_{\mathrm{pol}}) \cdot \vec{e}_\phi \tag{2.4}$$

We want avoid to restrict the polarization a priori, so we model its prior probability with a Gaussian, but set the standard deviation σ_ϕ so large that it has negligible influence on the posterior distribution. This would in principle allow us to later on incorporate prior knowledge by decreasing σ_ϕ and setting the mean accordingly, if additional information is available, for example from the event geometry.

The antenna response to the radio signal is expressed through the vector effective length

$$\vec{\mathcal{H}}_i(f, \theta, \phi) = \mathcal{H}_i^\theta(f, \theta, \phi) \cdot \vec{e}_\theta + \mathcal{H}_i^\theta(f, \theta, \phi) \cdot \vec{e}_\phi, \tag{2.5}$$

with f being the frequency, θ and ϕ the zenith and azimuth angles of the incoming radio signal and $\vec{e}_\theta$ and $\vec{e}_\phi$ their respective base vectors. The voltage over the antenna output is then given by

$$\mathcal{V}_i^{\mathrm{ant}}(f) = \vec{\mathcal{E}}(f) \cdot \vec{\mathcal{H}}_i(f, \theta, \phi) = \mathcal{E}(f)\cos(\phi_{\mathrm{pol}})\mathcal{H}_i^\theta(f, \theta, \phi) + \mathcal{E}(f)\sin(\phi_{\mathrm{pol}})\mathcal{H}_i^\phi(f, \theta, \phi) \tag{2.6}$$

The complex amplifier response $A_i(f)$ can also be expressed by a multiplication in the frequency domain, yielding the voltage as it is recorded by the digitizer:

$$\mathcal{V}_i(f) = A_i(f) \cdot \mathcal{V}_i^{\mathrm{ant}}(f) = A_i(f) \cdot \mathcal{E}(f) \cdot \left[\cos(\phi_{\mathrm{pol}}) \cdot \mathcal{H}_i^\theta(f, \theta, \phi) + \sin(\phi_{\mathrm{pol}}) \cdot \mathcal{H}_i^\phi(f, \theta, \phi)\right] \tag{2.7}$$

The product of the amplifier and the antenna responses has been normalized, so that their overall maximum value (over all channels) is 1. As with the normalization of the voltage waveforms this can be reversed afterwards in order to get the correct values for the electric fields.

As these calculations are just a series of multiplications of each element of $\mathcal{E}(f)$ with a scalar, they can be expressed as a diagonal operator $\mathcal{D}$ that is applied to the electric field spectrum. The result is shown in the bottom left of figure 4. The prior samples for the voltage spectra look much more similar to each other than the electric field spectrum samples. This is because the antenna and amplifier characteristics have a large influence on the shape of the spectrum. Finally, the voltage $\mathcal{V}(f)$ is transformed into the time domain by applying the Fourier transformation operator $\mathcal{F}$ (figure 4, bottom right). The time shifts between the samples is due to the allowed uncertainty on the slope of the phase function.

This allows us to calculate the probability $\mathcal{P}(U|E)$ that a given electric field model yields the voltage measured by the detector. As any discrepancies between the voltage expected from the electric field model $\mathcal{FDE}(f)$ and the actual data must be due to the noise N, this means:

$$\mathcal{P}(U|E) = \mathcal{P}(N = U - \mathcal{FDE}) \tag{2.8}$$

If we have a probability for the noise distribution (which will be presented later) this allows us to calculate the posterior probability for a given electric field:

$$\mathcal{P}(E|U) \propto \mathcal{P}(E) \cdot \mathcal{P}(N = U - \mathcal{FDE}) \tag{2.9}$$

2.3 Use case: air shower detection

The radio signals from cosmic ray-induced particle showers in the atmosphere are produced by similar mechanisms to those from neutrino-induced showers in ice and share many features. Therefore, IFT can be used here as well to reconstruct the electric field. Additionally, since radio signals from air showers are better understood, they are offer a useful cross-check to test reconstruction methods for neutrino detectors.

While RNO-G has three upward-pointing LPDAs for air shower detection, we will use a different neutrino detector as a test case. The ARIANNA experiment [17] consists of 9 autonomous detector stations located on the Ross Ice Shelf in Antarctica and 2 more at the South Pole. Each station has 4 or 8 (depending on the station type) LPDAs, similar to those used for RNO-G, deployed at a depth of about 2 m below the ice surface. Two each of the antennas form a pair, which means that they are oriented parallel to each other, so that they measure the same component of the electric field. While most of the stations have their antennas pointed downwards, to detect radio signals coming from within the ice, they can be turned upwards as well, which turns the station into a cosmic ray detector. This was already used in the past to detect several cosmic ray events [48].

In addition to cosmic ray detection at the Ross Ice Shelf, we want to simulate another scenario as well: the reconstruction of inclined air showers at the site of the Pierre Auger Observatory in Argentina. The observatory is currently undergoing an upgrade, in which radio antennas will be installed on all water Cherenkov detector tanks [7]. Because of the large distance between the antennas, the radio array will be mainly focused on inclined showers, whose radio footprint on the ground is large enough to cover multiple stations. With antennas only sensitive to the horizontal components of the radio signal, reconstructing the electric field can be challenging for the reasons explained in section 1.3. In the arctic or antarctic, there is a trivial solution for this problem: the geomagnetic field is almost vertical, which means that the $\vec{e}_\varphi$ component is dominant, so the $\vec{e}_\theta$ component can just be ignored when estimating the energy fluence of the electric field. This is not necessarily the case at the Auger site, where the magnetic field is only inclined around $30\,^\circ$ and weaker. Thus, we want to show how this problem can be addressed via IFT.

Since all the assumptions made about the signal from in-ice showers also hold for air showers, only a few modifications to account for the different detector design are necessary: the antenna and amplifier response are simply replaced with the ones for the ARIANNA detector. They are sensitive at different frequencies, so the passband of the Butterworth filter that is applied is changed to 100 MHz to 500 MHz. Additionally, part of the radio signal will be reflected at the air-ice interface, but since the fraction of the signal that is reflected can be calculated separately for the $\vec{e}_\theta$ and $\vec{e}_\phi$ component, and only depends on the incident angle otherwise, this is done by simply modifying the antenna response. The radio footprint of an air shower at ground level is so large compared to the distance between the antennas that the scaling factor a between channels can be ignored.

2.4 Noise models

Modelling the noise for a detector at a given location is challenging, as there are typically many different sources: foremost human activity, but also emission from the Galactic center or other celestial objects as well as thermal emission from the surrounding ice or the detector itself can all contribute different forms of noise.

For the use case of air shower detection with ARIANNA, one can simply use real data: each detector station is regularly triggered on a timer. Since actual signal events are very rare, it can be assumed that these forced trigger events contain only noise, and their voltages can simply be added to the simulated waveforms in order to obtain simulated noisy data.

The noise distribution obtained from the ARIANNA forced trigger events is nearly Gaussian. This is likely due to the fact that most of the noise is thermal noise produced in the amplifiers, rather than impulsive signals picked up by the antennas from the surroundings.

This is not necessarily going to be the case for RNO-G, whose amplifiers are targeting a lower noise level. Its location in the arctic also means that the galactic center, which is a major source of radio emission in the sky, is not within the field of view. We therefore assume that most of the noise comes from thermal radio emission which is picked up by the antennas. We model this noise in the frequency domain, with a Rayleigh distribution on the amplitude of each frequency bin and a uniform distribution over $0 < \varphi \leq 2\pi$ of the phase and the polarization angle. In principle, antennas at different depths could detect different noise, as radio signals from the surface get attenuated and the temperature of the surrounding ice changes. For simplicity, we here assume the noise level to be the same for all channels.

In IFT, the easiest way to model noise is to assume a Gaussian distribution around 0, with a standard deviation σ_N, which is set for each channel individually by calculating the root mean square of the voltages outside the signal region. Thus we can substitute the noise term in eq. (2.9) with a Gaussian distribution $\mathcal{P}(N) = \mathcal{N}(N|0, \sigma_N)$.

This means we are technically using a slightly wrong noise model for a typical radio neutrino detector. However, it turns out that this does not hinder a precise electric field reconstruction and serves to demonstrate the resilience of our reconstruction to small errors in the noise model. In principle, our measurement model can easily accommodate more complex noise distributions, should the need arise.

3 Performance of the electric field reconstruction

With the posterior probability in eq. (2.9), we can reconstruct the electric field by finding its maximum. We do this using the software package `nifty` [49], which provides the necessary tools to formulate the described IFT models and perform the variational inference. In this section, we create realistic datasets from simulated neutrino and air shower signals and evaluate the ability of `nifty` to recover the original signal using our signal and data model.

3.1 Set-up of neutrino simulations

We use the NuRadioMC and NuRadioReco software packages [30, 33], to simulate the radio signals from neutrino-induced particle showers detected by an RNO-G station. In the first step, neutrino interactions are randomly generated in a cylinder of radius 5 km around the station up to a depth of 3 km, corresponding roughly to the thickness of the ice sheet at the RNO-G site. The neutrino energy is chosen randomly between 5.0×10^{16} eV and 1.0×10^{20} eV, following the combined spectrum of a GZK flux model [6] and the extension of the astrophysical neutrino spectrum measured by IceCube [50]. Neutrino flavors are assigned assuming a 1:1:1 mixing between the three flavors. In the second step, the radio emission is simulated using the ARZ model [31] and the signal is propagated through the ice. If the radio signal reaches the detector, the electric field is folded with the antenna and the amplifier response, which yields the voltage measured by each channel. We simulate a simple threshold trigger, that triggers if the maximum voltage in the lowest channel of the phased array is above 20 mV.

If the detector is triggered, we add noise with a root mean square of 10 mV, as described in section 2.4. Then the signal is upsampled to a sampling rate of 5 GHz and a 10th order butterworth filter with a passband of 132 MHz to 700 MHz, corresponding to the band where antenna and amplifier are sensitive, is applied.

Finally, we perform the electric field reconstruction on the resulting waveforms, using the four channels of the phased array and the two horizontal polarization antennas on the power string.

3.2 Test of the electric field reconstruction

The result of one of these reconstructions is shown in figure 5. We show only one of the Vpol and one of the Hpol channels, as the reconstruction results and the recorded waveforms are practically identical to the other channels, except for different noise. The reconstructed waveform matches the original signal very closely, even towards the end of the pulse, where it drops below the noise level. This is possible because much of the pulse shape is dictated by the group delay of the antenna and the amplifier, which is well known. We can estimate lower bounds on the uncertainties by drawing samples from the approximate posterior distribution provided by MGVI. The samples are shown in figure 5 as thin black lines, to visualize their variance. The uncertainty on any signal property, like for example the polarization, can be characterized thereby. For this, one calculates this quantity for each sample individually and investigates its resulting distribution, for example by providing its standard deviation as calculated from the samples.

We want to quantify the performance of the electric field reconstruction by looking at properties of the radio signal that are important for the reconstruction of the neutrino that produced the particle shower the radio signal came from. How well these are reconstructed will depend mainly on the signal-to-noise ratio, so we will show results divided into separate groups by the maximum SNR of any of the channels used in the reconstruction. The SNR is calculated by taking half the maximum peak-to-peak amplitude of the signal *before the noise was added* and dividing it by the root mean square of the noise that is added. The reason we use the waveform without noise to calculate the amplitude is that otherwise, it would be influenced by the noise as well as the underlying signal. If the signal is not much bigger than the noise level, its value is mostly influenced by random fluctuations in the noise. So, even though it is harder to calculate for real data, this definition makes it easier to compare low-SNR events when judging the performance of the electric field reconstruction. The trigger threshold and simulated noise level have been chosen so that the lowest SNR are around 2, which is also the expected trigger threshold for RNO-G.

The first quantity to check is the energy fluence Φ^E of the radio signal (see eq. (1.1)), which is needed to reconstruct the shower energy, from which the neutrino energy can be estimated. We look at the reconstruction quality of $\sqrt{\Phi^E}$, which is proportional to the shower energy, so the relative uncertainty on $\sqrt{\Phi^E}$ propagates directly to the uncertainty on the shower energy.

The result is shown in figure 6. On the left, it shows a scatter plot of the reconstructed vs. actual $\sqrt{\Phi^E}$. Except for a few outliers, the reconstruction is very close to the actual value, with a resolution on $\sqrt{\Phi^E}$ of around 20% even for events with SNR < 4 (see table 1). Because each antenna views the shower at a slightly different angle, the electric field at each antenna can have a different energy fluence, especially if the shower is relatively close. The horizontal errorbars extend from the minimum to the maximum energy fluence of all six channels used for the reconstruction, with the data point being at the mean. This also means

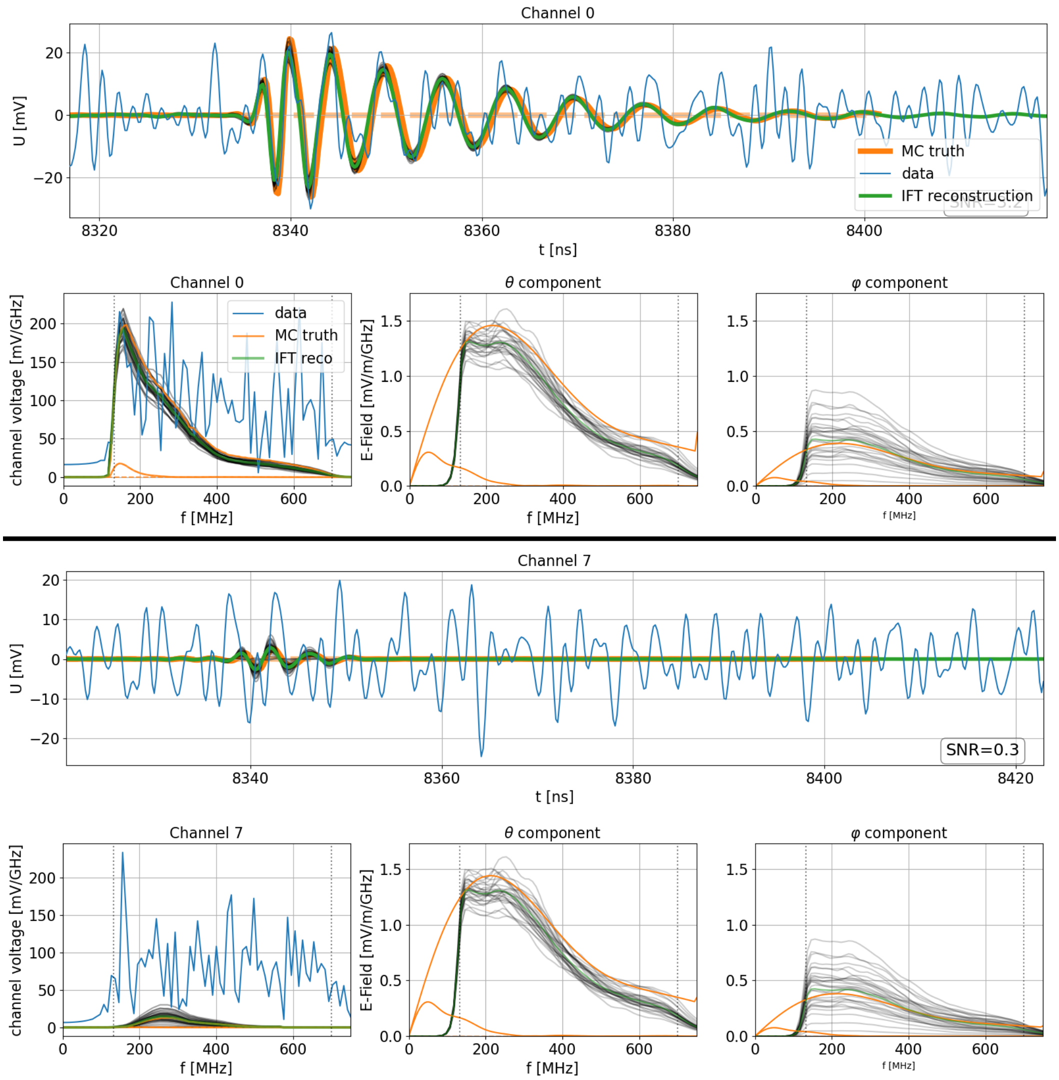

Figure 5. A result of an electric field reconstruction, shown for one of the Vpol (top) and one of the Hpol (bottom) antennas. 1st and 3rd row: waveforms of the noisy data (blue), the noiseless signal (orange) and the reconstructed voltages (green). 2nd and 4th row: spectrum of the channel voltage (left) and of the $\vec{e}_\theta$ (center) and $\vec{e}_\phi$ (right) component of the electric field. The thin black lines show posterior samples, drawn to visualize and quantify the uncertainties of the reconstruction. The 2nd orange line in the spectrum plots is a 2nd radio pulse from another raytracing solution, potentially visible in the waveform.

that the channels can have different signal-to-noise ratios, so the colors show the maximum SNR of all channels used in the reconstruction. For most events, the uncertainty on the energy fluence of the $\vec{e}_\phi$ component is larger than on the $\vec{e}_\theta$ component. This is because there are only two Hpol antennas, compared to the four Vpols, which also are less sensitive. Together with the fact that the signals tend to be polarized more vertically, this means that often there is only a very small signal in the waveforms recorded by the Hpol channels. In that case, only an upper limit on the $\vec{e}_\phi$ component of the electric field can be given. This is also the reason why the energy fluence tends to be more often under- than overestimated, as shown in table 1.

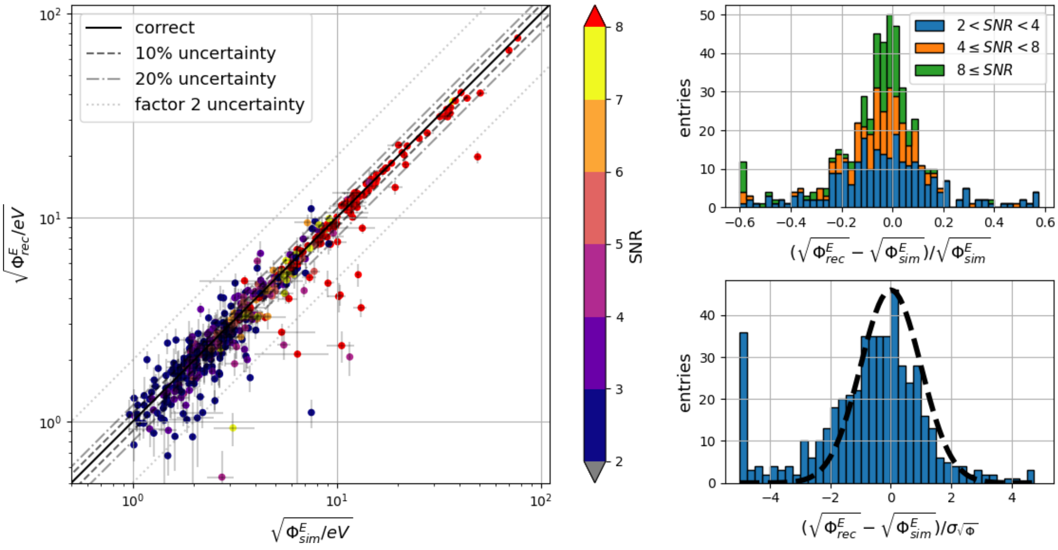

Figure 6. Reconstructed energy fluence of the radio signal from simulated neutrino-induced particle showers detected with RNO-G. Left: scatter plot of the reconstructed vs. the true square root of the energy fluence of the radio signal. Errorbars on the y-axis show the uncertainty estimated by the IFT algorithm, errorbars on the x-axis cover the range of values for the electric fields at all channels used in the reconstruction, with the data point being at the mean. The colors show the maximum signal-to-noise ratio of all channels used in the reconstruction. Top right: stacked histogram of the relative uncertainty on $\sqrt{\Phi^E}$ for different signal-to-noise ratios. Bottom right: uncertainties on the reconstructed $\sqrt{\Phi^W}$ as a multiple of the estimated uncertainty. For comparison, a Gaussian function with $\sigma = 1$ as drawn as well. The left- and rightmost bins in each histogram are overflow bins.

The IFT reconstruction algorithm also provides an estimate of the uncertainty $\sigma_{\sqrt{\Phi}}$ on $\sqrt{\Phi^E}$, shown as vertical errorbars. The bottom right of figure 6 shows the difference between reconstructed and actual $\sqrt{\Phi^E}$ divided by $\sigma_{\sqrt{\Phi}}$. It follows a Gaussian distribution with $\sigma = 1$, as would be expected if the estimated uncertainties are accurate.

There are some outliers, even at large signal-to-noise ratios, where the energy fluences are greatly underestimated. These can occur if either the data does not match the IFT model (which can happen for a few reasons) or if the reconstruction converges on a local minimum, usually because of a wrong phase. Fortunately, these errors are usually easy to spot on an individual event level and can be cut before an analysis. They are discussed in more detail in appendix A.

To reconstruct the shower energy and the neutrino direction, it is also important to know the shape of the electric field spectrum, as this contains information about the angle under which the detected radio signal was emitted. The frequency at which the electric field spectrum reaches its maximum varies a lot, depending mostly on the viewing angle and shower type (see figure 1) and may even be outside of the detector bandwidth, but for signals that are off-cone by more than 1 ° it tends to be somewhere around 250 MHz. Therefore we compare the energy fluence in the frequency bands at 130 MHz to 250 MHz and at 250 MHz to 500 MHz to give an estimate on how quickly the spectrum drops off after the maximum (if it drops at all). The reason for not using the whole bandwidth up to 700 MHz is that the antenna response depends on the incoming direction of the radio signal, and for some directions the sensitivity starts dropping at about 500 MHz (see figure 3). From these fluences

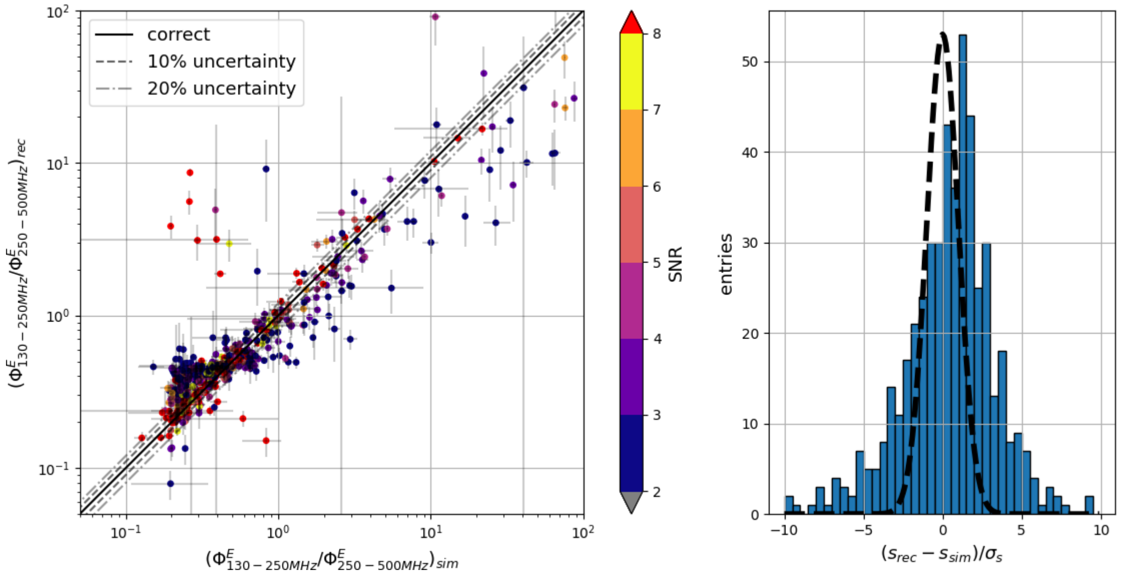

Figure 7. Reconstruction of the spectral shape parameter s for radio signals detected with RNO-G. Left: reconstructed vs. true simulated s. Horizontal errorbars show the range of values for all channels used for the reconstruction, vertical errorbars show uncertainty estimates by the reconstruction algorithm. Right: uncertainties on the reconstructed s divided by the uncertainties estimated by the reconstruction algorithm.

we calculate a shape parameter $s = \Phi^E_{130-200\mathrm{MHz}}/\Phi^E_{200-500\mathrm{MHz}}$, which we compare to the one from the simulated electric fields. This estimator for the viewing angle has the advantage that it is well-defined for any electric field spectrum. If we, for example, had used the position of the maximum of the spectrum, this would we be ill-defined for events where it is outside the RNO-G band or if there are multiple peaks.

As figure 7 shows, the IFT method is able to reconstruct the shape rather well for events with SNR > 3, with the exception of some outliers. Uncertainties tend to be larger than the lower bound estimated by the IFT algorithm. One may also notice that many of the events with a low signal-to-noise ratio are clustered in the lower left corner, with roughly the same reconstructed values for s. These are events that are viewed relatively close to the Cherenkov angle, for which the IFT reconstruction returns a flat frequency spectrum, as there is not enough information for a more detailed spectrum reconstruction. This result is useful though, since the falling spectrum of events further off the Cherenkov angle is still reconstructed well, so some information about the viewing angle is maintained.

The third parameter to look at is the polarization of the radio signal. The electric field vector points towards the shower axis, which helps to constrain the direction the neutrino came from, which makes the polarization an important quantity for the reconstruction of the arrival direction. We quantify the polarization by defining a polarization angle

$$\phi^{\mathrm{pol}} = \tan^{-1}\left(\sqrt{\Phi^E_\phi}/\sqrt{\Phi^E_\theta}\right) \tag{3.1}$$

where Φ^E_ϕ and Φ^E_θ are the energy fluence of the $\vec{e}_\phi$ and $\vec{e}_\theta$ components of the radio signal. This implies that the polarization angle lies in the range $0^\circ \leq \phi^{\mathrm{pol}} \leq 90^\circ$ by definition, where $\phi^{\mathrm{pol}} = 0^\circ$ means that the signal is polarized in $\vec{e}_\theta$ direction.

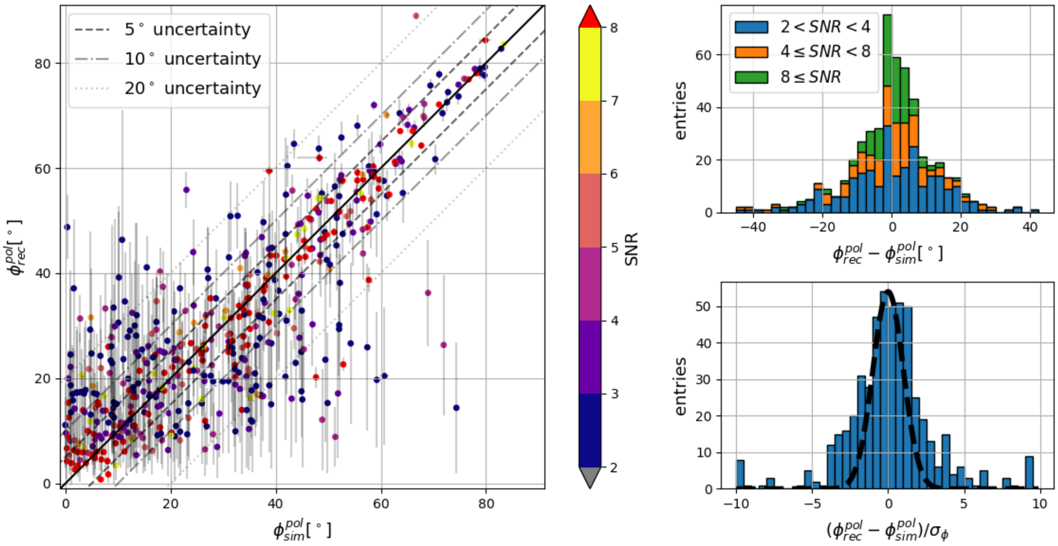

Figure 8. Reconstructed electric field polarization of the simulated radio signals detected with RNO-G. Left: reconstructed vs. true polarization angles. Errorbars represent the uncertainties estimated by the IFT reconstruction algorithm. Colors signify the maximum signal-to-noise ratio out of all channels used in the reconstruction. Top right: stacked histogram of the uncertainties on the reconstructed polarization angles for different signal-to-noise ratios. Bottom right: uncertainties on the reconstructed polarization angle divided by the estimated uncertainties. For comparison, a Gaussian function with $\sigma = 1$ has been drawn as well.

The results are shown in figure 8 and table 1. Even at signal-to-noise ratios below 4, the polarization can be reconstructed with an uncertainty of around 13°, which improves to better than 5° for SNR $>$ 8. The resolution of the polarization measurement is mostly limited by the lower sensitivity and smaller number of the Hpol antenna, as even a large SNR in the Vpol channels does not necessarily mean that there is also a large SNR in the Hpol channels. This is also the reason why the polarization reconstruction performs better for larger ϕ^{pol}: if the polarization angle is small, there is no detectable or only a very weak signal in the Hpol antenna waveform, so in practice, only an upper bound on Φ^E_ϕ can be estimated.

The errors on the reconstructed polarizations match the IFT estimates for the lower bound on the uncertainty rather well. It is worth mentioning that there is a potential systematic error on the polarization due to the detector layout: while the differences in signal polarization between channels are small enough to be insignificant, the overall signal strengths may vary. Because the $\vec{e}_\theta$ and $\vec{e}_\phi$ components of the electric field are measured by different antennas, this variation leads to wrong polarization reconstruction. This is a limitation of the detector, which is ignored in the IFT model, so it cannot be included in the uncertainty estimate.

3.3 Reconstruction of pulses from air showers

To test the IFT reconstruction of radio pulses from air showers, we use two sets, each containing 70 simulated air showers and their radio emission, generated with the CoREAS software [51]: one for a detector on the Ross-Ice-Shelf in Antarctica and one at the site of the Pierre Auger Observatory in Argentina. The main differences between these two locations are the different geomagnetic field and the different altitude, which is sea level at the Ross Ice Shelf and 1560 m a.s.l. at the Auger site. The cosmic ray energies are randomly dis-

	$2 \leq \mathrm{SNR} < 4$	$4 \leq \mathrm{SNR} < 8$	$8 < \mathrm{SNR}$
$\Delta\Phi^E$			
68% quantile	$[-0.37,\, 0.34]$	$[-0.30,\, 0.11]$	$[-0.28,\, 0.05]$
median	-0.06	-0.07	-0.06
$\Delta\sqrt{\Phi^E}$			
68% quantile	$[-0.20,\, 0.16]$	$[-0.16,\, 0.05]$	$[-0.15,\, 0.03]$
median	-0.03	-0.04	-0.02
$\Delta\phi_{\mathrm{pol}}$			
68% quantile	$[-12.4\,^\circ,\, 13.8\,^\circ]$	$[-9.5\,^\circ,\, 7.8\,^\circ]$	$[-4.9\,^\circ,\, 4.2\,^\circ]$
median	$0.3\,^\circ$	$0.7\,^\circ$	$0.0\,^\circ$

Table 1. Uncertainties on the reconstructed signal energy fluence Φ^E, its square root and the polarization for radio signals by an RNO-G station. For each property, the 68% quantile and the median of the distribution of reconstruction errors are given.

tributed between 5.0×10^{17} eV and 1.0×10^{20} eV with a spectral index of -2. The cosmic ray directions are distributed isotropically, with the air showers at the Auger site restricted to zenith angles $\theta > 50^\circ$, as we want to test the suitability of the method for inclined showers specifically. For each shower, the electric field is simulated at a set of positions arranged around the shower core in a star-like pattern (see e.g. [52]). For each simulated shower, a set of 20 positions around the shower core is chosen at random and the station positions closest to each position are selected, which results in a realistic distribution of shower axis positions relative to the station. The electric field is folded with the response of each antenna and amplifier to get the waveform recorded by each channel. As we do not have the detector response of the Auger radio component, we use the ARIANNA detector for both locations. A time shift is applied to the waveforms to account for the difference in travel time between antennas. We simulate a trigger by requiring that the signal in at least two channels passes both a minimum and a maximum threshold of -20 mV and 20 mV, respectively, within 5 ns of each other. This is similar to the trigger used in the ARIANNA experiment [48], except that the threshold corresponds to roughly 2σ, compared to the 4σ trigger that is actually used. We chose a lower threshold, because we are triggering on the noiseless waveforms, so pure noise triggers are not an issue, and we are especially interested in the performance of the IFT method at low signal-to-noise ratios.

The waveforms for each channel are cut to a length of 256 samples, to match the length of the noise samples measured by the ARIANNA detector and a randomly selected noise recording is added to each channel. We do not have any recorded noise from the Auger site, so we use recordings from Moore's Bay for both detector locations. The waveforms are upsampled to a sampling rate of 5 GHz and a 10th order butterworth filter with a passband of 100 MHz–500 MHz as applied. Then the electric field reconstruction is performed. We use the settings as for the neutrino case, except for the slope of the phase. This is because the ARIANNA antennas and amplifiers introduce a different delay to the radio signal, which has to be corrected for.

To assess the quality of the electric field reconstruction, we use the same three properties as for the neutrino case: the signal energy fluence, the shape parameter and the polarization. The results for the square root of the signal energy fluence are shown in figure 9 and 10 for a

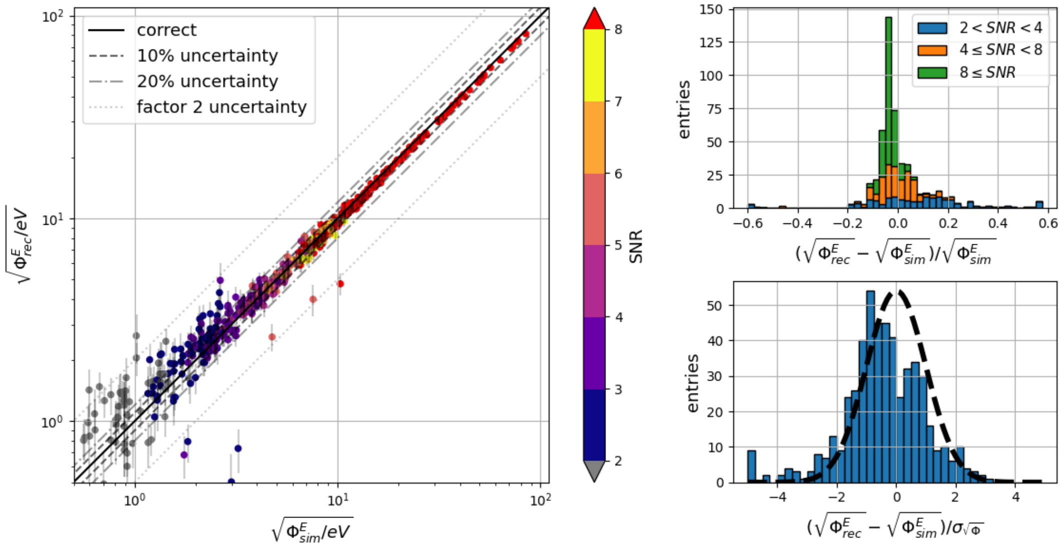

Figure 9. Reconstruction of the energy fluence of radio signals from air showers detected with an ARIANNA-like detector at Moore's Bay. Left: reconstructed vs. actual $\sqrt{\Phi^E}$ of the radio signal. The vertical error bars show the uncertainties estimated by the IFT reconstruction algorith. Top right: error on the reconstructed $\sqrt{\Phi^E}$ of the radio signal for different signal-to-noise ratios. Bottom right: errors on the reconstructed $\sqrt{\Phi^E}$ divided by their estimated uncertainties.

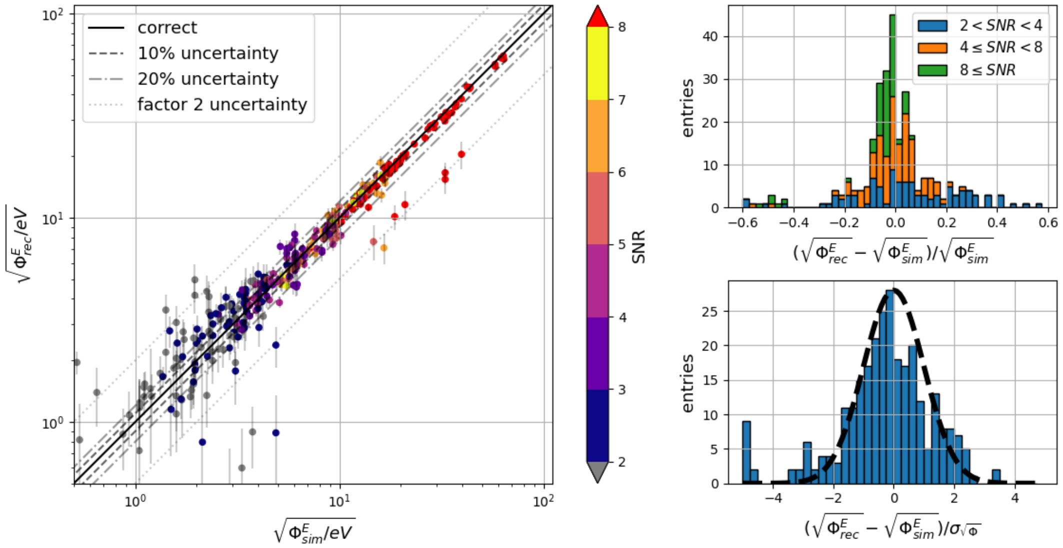

Figure 10. Reconstructed energy fluence of the radio signals from inclined air showers detected with an ARIANNA-like radio detector at the site of the Pierre Auger Observatory. Left: scatter plot of the reconstructed square root of the energy fluence $\sqrt{\Phi^E}$ vs. the actual energy fluence of the radio signal. The errorbars show the uncertainty estimated by the IFT reconstruction algorithm. Top right: stacked histogram of the errors of the reconstructed $\sqrt{\Phi^E}$ for different signal-to-noise ratios. Bottom right: errors of the reconstructed $\sqrt{\Phi^E}$ as a multiple of the estimated uncertainty. For comparison, a Gaussian function with $\sigma = 1$ is drawn as well. The left- and rightmost bins in each histogram are overflow bins.

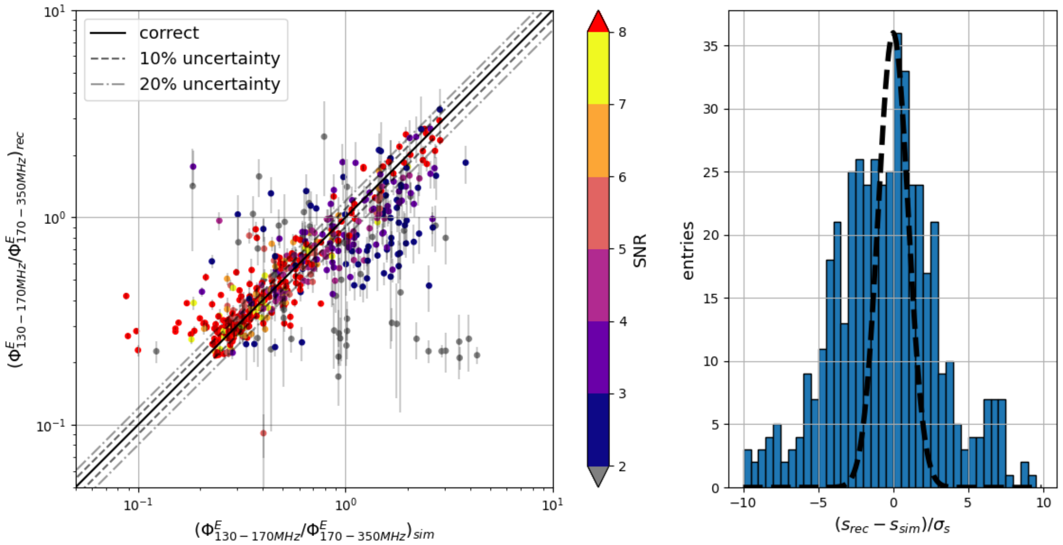

Figure 11. Reconstruction of the spectral shape parameter s for radio signals from air showers detected with an ARIANNA station at Moore's Bay. Left: reconstructed vs. actual shape parameter. Error bars show the uncertainties estimated by the IFT algorithm. Right: errors on the reconstructed shape parameter divided by its estimated uncertainties.

detector at Moore's Bay and the site of the Pierre Auger Observatory, respectively. Because the LPDAs are more sensitive than the Hpol antennas used for RNO-G, especially for the $\vec{e}_\phi$ component, the energy fluence reconstruction performs better than in the neutrino case. Because we used real noise, some events had maximum SNRs lower than 2, which are shown in gray in the scatter plot, but left out of the histograms.

For the shape of the frequency spectrum, we use the ratio between the energy fluence in two different frequency ranges again, but we chose different passbands this time. The reason is, that the spectra of radio signals from air showers reach their maximum typically around 80 MHz, which is outside of the recorded band, and is much weaker at higher frequencies than the signals from a shower in ice. Therefore, for many events, the energy fluence in the 250 MHz–500 MHz is practically 0, making that parameter useless. Instead, we use the 130 MHz–170 MHz and the 170 MHz–250 MHz passbands. The results are shown in figure 11 and figure 12. For events with SNR > 3, the reconstruction works well, though uncertainties are again underestimated.

The results of the polarization reconstruction are shown in figure 13 and figure 14. Even at SNR just over 2, the uncertainty on the reconstructed polarization angle is around 10° and drops to a few degrees at higher SNR (see table 2). Interestingly, the uncertainties are roughly the same between the simulations for Moore's Bay and the inclined showers at the Auger site, despite the low sensitivity to $\vec{e}_\theta$ for inclined showers.

3.4 Implications for radio detectors

We have shown that *Information Field Theory* can be used to reconstruct radio signals detected with the Radio Neutrino Observatory in Greenland (RNO-G), even at low signal-to-noise ratios just above the trigger threshold.

The energy fluence of the radio signal is proportional to the square of the shower energy, so the relative uncertainty on $\sqrt{\Phi^E}$ translates directly to the uncertainty on the shower energy.

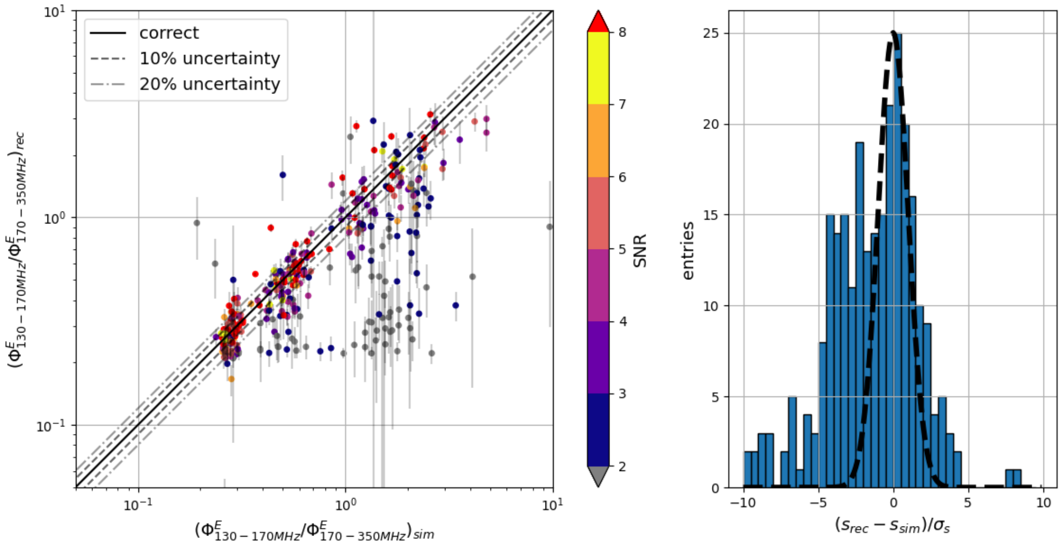

Figure 12. Reconstruction of the spectral shape parameter s for radio signals from inclined air showers detected with an ARIANNA-like detector at the site of the Pierre Auger Observatory. Left: reconstructed vs. true shape parameter. Error bars show the uncertainties estimated by the IFT algorithm. Right: errors on the reconstructed shape parameter divided by its estimated uncertainties.

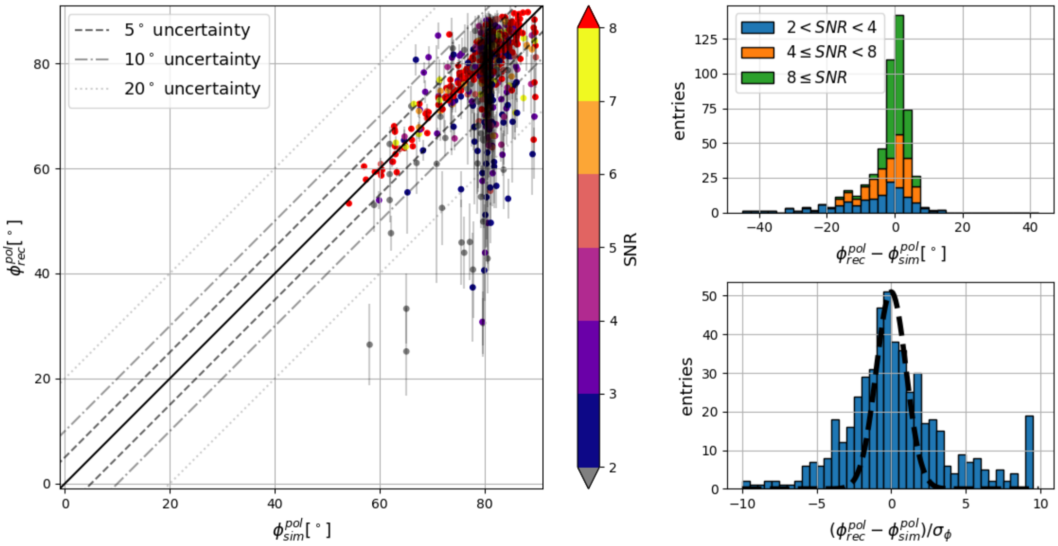

Figure 13. Reconstruction of the polarization for radio signals from air showers detected with an ARIANNA-like detector at Moore's Bay. Left: reconstructed vs. actual polarization angle. Error bars show the uncertainties estimated by the IFT algorithm. Top right: stacked histogram of the error on the reconstructed polarization angle for different signal-to-noise ratios. Bottom right: errors on the reconstructed polarization angles divided by the estimated uncertainties.

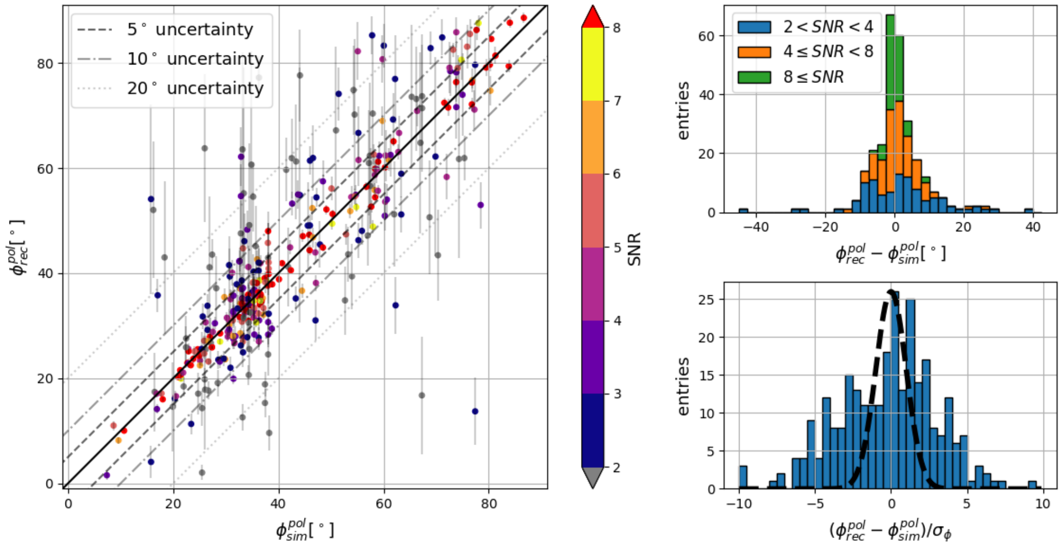

Figure 14. Reconstruction of the polarization for radio signals from inclined air showers detected with an ARIANNA-like station at the site of the Pierre Auger Observatory. Left: reconstructed vs. actual polarization angle. Error bars show the uncertainties estimated by the IFT algorithm. Top right: stacked histogram of the error on the reconstructed polarization angle for different signal-to-noise ratios. Bottom right: errors on the reconstructed polarization angles divided by the estimated uncertainties.

However, the uncertainty on the fraction of the neutrino energy that is deposited into the shower is around a factor of 2 [53], thus dominating over the uncertainty on the energy fluence. Therefore, further improving the energy fluence reconstruction will have very little effect on the reconstructed neutrino energies.

The shape of the electric field spectrum affects both the energy and the neutrino direction reconstruction, as it depends on the angle to the shower axis at which the signal is emitted. As shown in figure 1, this relationship is difficult to quantify in general and to attempt this beyond the scope of this paper. As we are not aware of another robust method to obtain the frequency spectrum at low SNR events, other than fitting a specific electric field model to the data [33], IFT currently seems like the best option to do this for neutrino detection.

The resolution on the signal polarization is mainly limited by the low gain of the horizontally-polarized antennas resulting from their constrained geometry. The polarization is needed to constrain the neutrino direction: if one only knows the direction of the radio signal, the neutrino direction can only be constrained to a cone with an opening angle equal to the emission angle, which is close to the Cherenkov angle. Using the fact that the radio signal is polarized radially around the shower axis, a measurement of the polarization can be used to resolve where on the cone the neutrino direction is. Thus, if the polarization angle is misreconstructed by a small angle $\Delta\phi_{\mathrm{pol}}$ it causes the neutrino direction to be off by

$$\delta \approx \sin(\theta_C) \cdot \Delta\phi_{\mathrm{pol}} \approx 0.8 \cdot \Delta\phi_{\mathrm{pol}} \tag{3.2}$$

with a Cherenkov angle $\theta_C = 56°$.

While these IFT results already look promising, it should be noted that only six out of the 24 channels available for RNO-G were used in this study. This was done because the IFT model used required the radio signal at all used channels to have a very similar shape and

	Moore's Bay		
	$2 \leq \mathrm{SNR} < 4$	$4 \leq \mathrm{SNR} < 8$	$\mathrm{SNR} < 8$
$\Delta\Phi^E$			
68% qtl.	$[-0.17, 0.62]$	$[-0.13, 0.12]$	$[-0.11, -0.02]$
median	0.20	-0.01	-0.07
$\Delta\sqrt{\Phi^E}$			
68% qtl.	$[-0.08, 0.28]$	$[-0.07, 0.06]$	$[-0.05, -0.01]$
median	0.10	-0.01	-0.04
$\Delta\phi_{\mathrm{pol}}$			
68% qtl.	$[-17.3^\circ, 3.2^\circ]$	$[-8.6^\circ, 3.61^\circ]$	$[-1.5^\circ, 2.7^\circ]$
median	-2.8°	0.0°	0.4°

	Auger		
	$2 \leq \mathrm{SNR} < 4$	$4 \leq \mathrm{SNR} < 8$	$\mathrm{SNR} < 8$
$\Delta\Phi^E$			
68% qtl.	$[-0.29, 0.62]$	$[-0.17, 0.12]$	$[-0.13, -0.01]$
median	0.07	-0.03	-0.07
$\Delta\sqrt{\Phi^E}$			
68% qtl.	$[-0.15, 0.27]$	$[-0.09, 0.06]$	$[-0.07, 0.00]$
median	0.04	-0.01	-0.03
$\Delta\phi_{\mathrm{pol}}$			
68% qtl.	$[-8.0^\circ, 11.0^\circ]$	$[-3.8^\circ, 5.7^\circ]$	$[-1.5^\circ, 2.0^\circ]$
median	1.1°	0.2°	-0.3°

Table 2. Uncertainties on the reconstruction of the signal energy fluence Φ^E, its square root and the polarization angle ϕ_{pol} for radio signals from air showers detected by an ARIANNA station at Moore's Bay and from inclined air showers detected by an ARIANNA station at the site of the Pierre Auger Observatory. For each quantity, the 68% quantiles and the median of the distribution of errors in the reconstructions are given. For Φ^E and $\sqrt{\Phi^E}$ they are relative errors, fpr ϕ_{pol} they are absolute errors, in degrees.

roughly the same amplitude, which can be assumed to be always the case for the channels in the phased array and the Vpol antennas directly above them, but not necessarily for the others. How much the radio signal varies between channels depends on the event geometry, most importantly the distance to the shower. So if the event geometry is known, one can determine if it makes sense to include additional channels. This decision can also depend on the signal-to-noise ratio and the goal of the reconstruction: if some channels have a very high SNR, it may make sense to reconstruct each of them individually to compare the radio signal at different positions, while at low SNR, all available channels may be necessary to get a estimate of the signal properties. While these considerations are beyond the scope of this paper, they can lead to further improvements in the signal reconstruction. Finally, additional channels could be included by dropping the requirement that the spectral shape has to be identical from the IFT model. IFT offers options to build models in which the shape of the spectrum is correlated between channels, but does not have to be the same.

As in the neutrino case, the energy of cosmic-ray induced air showers is proportional to the square root of the energy fluence of the radio signal. While the uncertainty on the signal energy fluence for a detector at Moore's Bay is comparable to the one obtained with the standard reconstruction [33], IFT performs much better regarding the polarization, with a similar accuracy to the *forward folding* method.

To our knowledge, the only radio detector currently using the shape of the frequency spectrum for cosmic ray detection is ANITA [54], where a parametrization was fitted to the electric field spectrum of the radio signal in order to estimate the energy. As the electric field was reconstructed by unfolding the measured voltages and the antenna responses, this approach requires a large signal-to-noise ratio, so IFT could be used in order to lower the reconstruction threshold. A similar approach has been developed for ground-based cosmic ray detectors [32], in which the *forward folding* technique was used to reconstruct the radio signal. While IFT would likely not improve the precision of the energy reconstruction, not having to rely on a specific parametrization can be an advantage in itself, if one wants to use a lower passband where the parametrization with an exponential function no longer holds or if the origin of the radio signal may not be entirely clear. Unfortunately, most radio detectors have to limit their band to the 30 MHz to 80 MHz band, because of the noise from radio communications at other frequencies. This small band limits the use of the spectrum for event reconstruction.

When reconstructing the simulated data set for the Pierre Auger Observatory, the IFT method showed a similar performance, demonstrating that it also works for inclined showers. Currently, the Pierre Auger Observatory only uses the horizontal components of the electric field if the incoming zenith angle is larger than 60 ° [14], meaning that information about the full radio signal is lost and the signal polarization is practically unknown. With IFT, the full electric field could be made available, which should improve the performance of the event reconstruction.

3.5 Cross-check: electric field reconstructions on pure noise

If a detector is self-triggering, there is a chance that a random noise fluctuation is mistaken for a genuine trigger. In this case, it is desirable that the electric field reconstruction is not forced to return a realistic-looking result, but either provides evidence that something is wrong or returns a result that looks non-physical to make it clear that no signal was present.

To test how IFT behaves, we run the same reconstruction we used for RNO-G events, but this time the channels recorded pure noise. A typical example of the result of such a reconstruction is shown in figure 15. The reconstructed electric field is very small, so that the reconstructed voltage is very small as well, compared to the noise level. This alone is evidence that there is likely no actual radio pulse in the data, but looking at the thin gray lines visualizing the uncertainties, we see that the electric field being 0 is within the margin of error. Thus, this result can be considered a "correct" electric field reconstruction, as it returns that the radio signal is, at most, very small.

3.6 Cross-check: systematic uncertainties

So far we used the same detector response for the simulations and the reconstruction, which implies perfect knowledge of the detector properties. In reality, this is of course hardly possible. While the response of most parts of the signal chain can be measured with great precision in the lab prior to deployment, modelling of the antennas carries larger uncertainties. The surrounding ice, for example, influences the antenna response, which is difficult to recreate

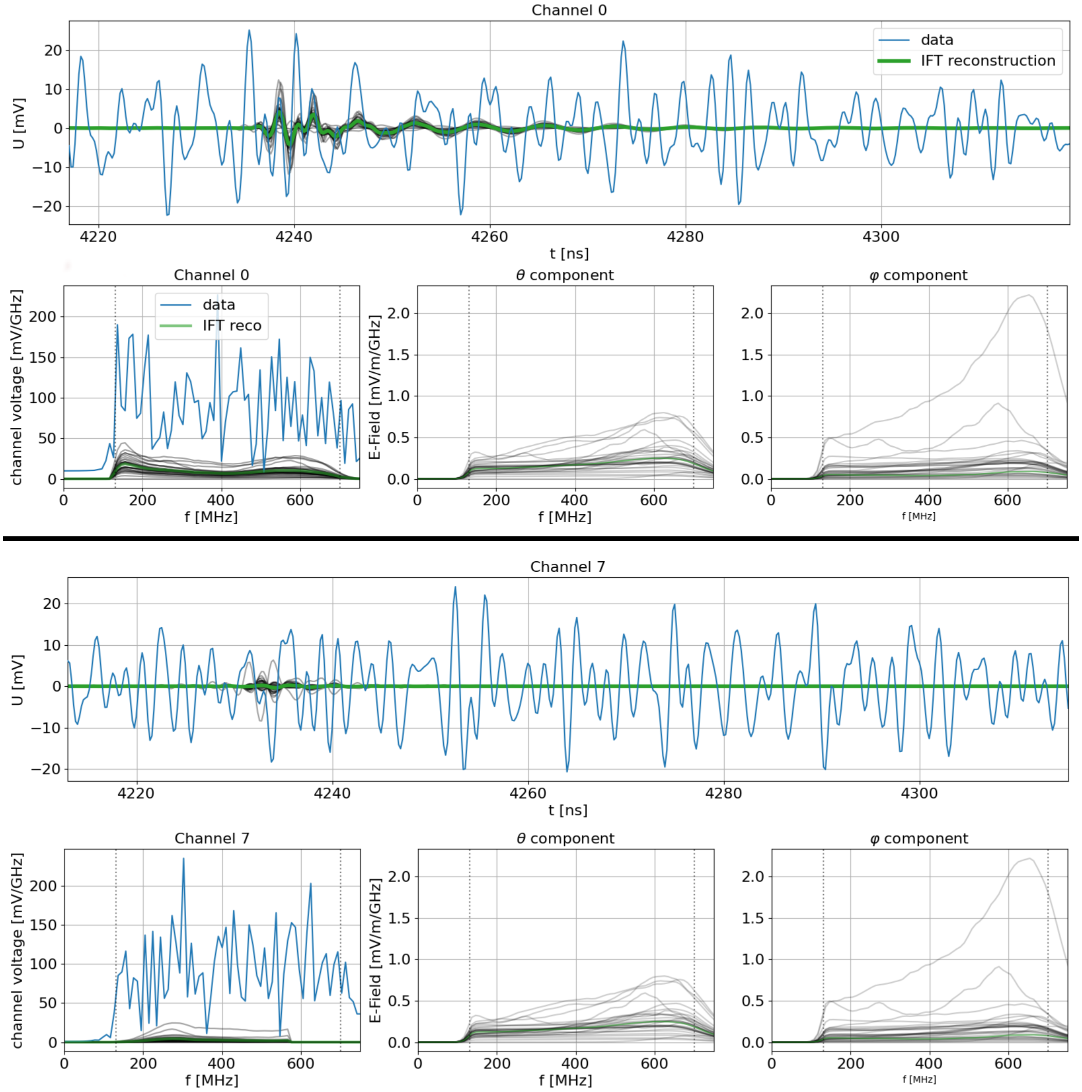

Figure 15. Results of the reconstructed electric field of an RNO-G event containing only noise, for one of the Vpol (top) and Hpol (bottom) channels. 1st and 3rd row: waveforms of the data (blue) and reconstructed voltage (green). 2nd and 4th row: spectrum of the voltage (left) and the $\vec{e}_\theta$ (center) and $\vec{e}_\phi$ component of the electric field. The thin black lines are the samples used to estimate uncertainties, which are drawn to visualize the uncertainties on the reconstruction.

in the lab. Therefore the most common way to solve this problem is to use simulations and cross check them with pulser measurements after deployment.

In addition, the antenna gain and phase response also depends on the signal arrival direction at the antenna, so a incorrect reconstruction of the signal direction will also result in using an incorrect antenna response.

For RNO-G several revision of Vpol antennas and bore-hole diameters were considered and fully simulated. We can make use of this to mimic the effect of an incorrect antenna model by running the IFT reconstruction on the same event as shown in figure 5, except this time the antenna model for an earlier revision is used. This represents a very pessimistic assumption about the uncertainty on the antenna model, as the for the revision included

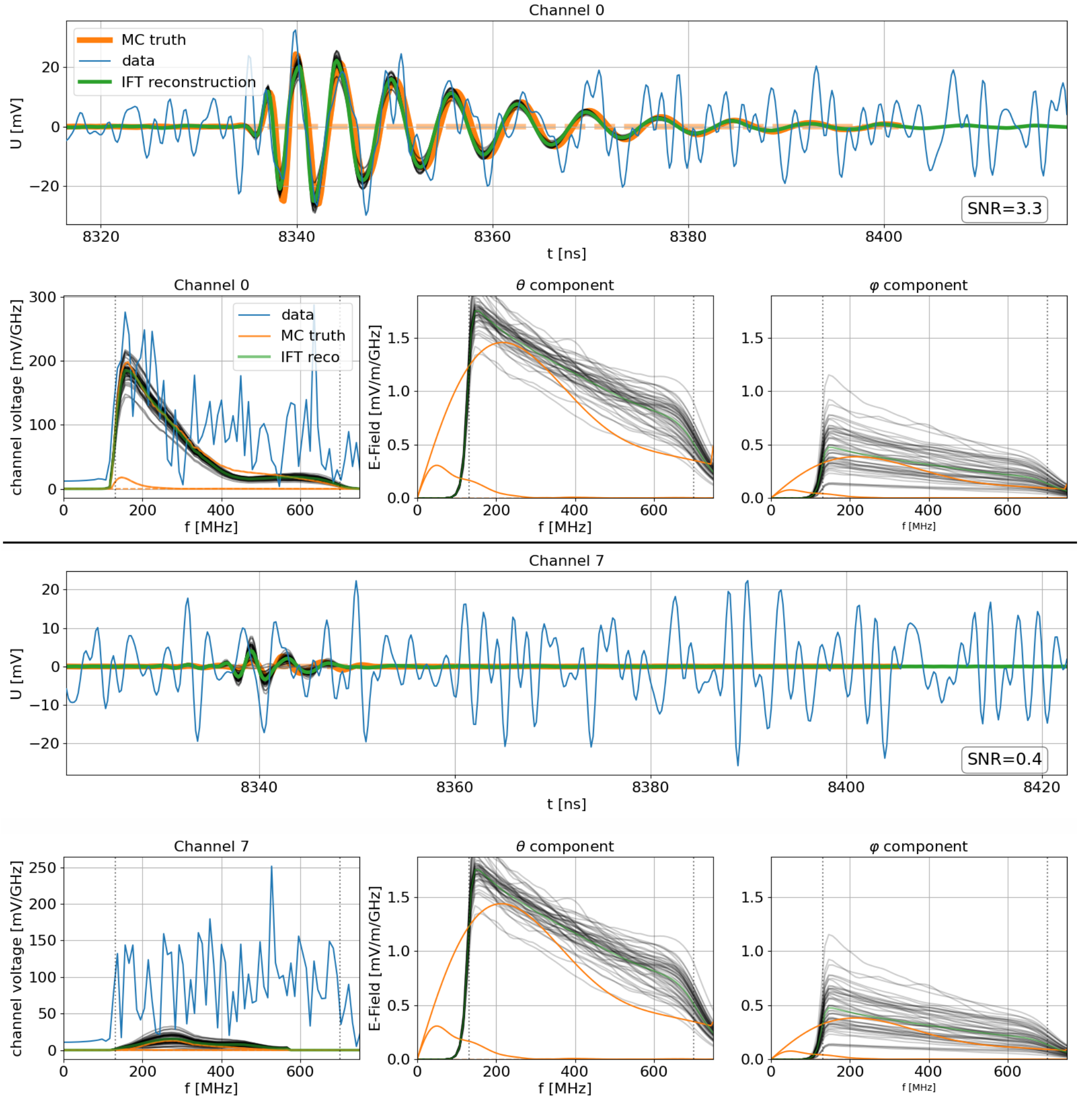

Figure 16. Result of the electric field reconstruction for the same event as shown in figure 5, but for this an incorrect Vpol model is used for the reconstruction.

simulations were run with a borehole almost twice as wide, resulting in both a different overall shape and resonances in the model.

The result is shown in figure 16. At first sight, it looks like the reconstruction of the electric field performed rather poorly. However, voltages measured in the channels are still reconstructed well. Comparing the two antenna models in detail, it explains that the electric field amplitudes at frequencies below 200 MHz and above 400 MHz are overestimated, since the used Vpol model is much less sensitive there.

From this illustrative exercise, we can conclude that a systematic uncertainty on the antenna response it not an issue for the IFT method itself, but will influence how the voltages measured by the channels are translated into an electric field.

JCAP04(2021)071

4 Conclusion

One of the key steps in the event reconstruction for radio-based particle detectors is determining the electric field of the radio signal from the voltage waveforms measured with its antennas, which is difficult to do accurately because they are always contaminated by noise from the surrounding environment. The *Information Field Theory* method presented in this paper offers a solution to this issue.

When applied to a simulated neutrino event, IFT moderately improves the reconstruction of the overall electric field amplitude, but its main strength lies in the ability to reconstruct the shape of the frequency spectrum and the polarization, even at low signal-to-noise ratios. This is especially important for neutrino detectors, where most events are expected to be close to the trigger threshold, and the low event rate prohibits strict quality cuts. Experiments like the Radio Neutrino Observatory Greenland (RNO-G) or the radio component of IceCube-Gen2 will certainly profit from applying IFT to the detected pulses. By using a non-parametric model for the frequency spectrum, we make minimal prior assumptions about the expected signal, which is an advantage for an experiment attempting the first detection of a neutrino-induced particle shower via its radio signal.

Making minimal assumptions about the radio signal also has the advantage that the same method can be applied to other kinds of radio pulses, like those emitted by an air shower. The improved electric field measurement allows new reconstruction methods using the shape of the frequency spectrum and the polarization of the radio signal. With IFT, it is also possible to reconstruct the full electric field for inclined air showers.

For these reasons, Information Field Theory can be a valuable asset to improve the precision of radio-based particle detectors and move their analysis threshold to lower energies.

Acknowledgments

We are grateful to the ARIANNA collaboration for allowing us to use a fraction of their noise data to show the suitability of the method for measured data. This work was carried out with support from the German research foundation (DFG), under grant NE 2031/2-1.

The source code to perform the reconstructions shown in this paper is publicly available as part of the *NuRadioReco* open source software package [33].

A Failed reconstructions

As shown in, for example, figure 6, sometimes the IFT reconstruction produces outliers, where the result does not come close to the actual radio signal. These outliers occur mainly for two reasons.

In the case of the neutrino detector, there can be events that do not match the IFT model. The most common cause is when two different radio pulses arrive shortly after another and overlap. This can happen with certain event geometries, in which the propagation time differences between the ray that reaches the antenna directly and the one that is refracted downwards are very small.

The other way a double pulse can occur is if a high-energy electron neutrino interacts via charged current interaction. This produces two showers: one hadronic shower from the nucleon recoil and one electromagnetic shower from the electron produced in the process. Usually, both showers overlap and their radio signals can be treated as coming from a single shower. However, at high energies the LPM effect [34, 35] elongates the electromagnetic shower [36]. As the particle showers propagate through the ice faster than the radio signals, there can be a noticeable time difference between the signal from the hadronic and the electromagnetic showers. In that case, there are practically two different radio pulses.

As we assume that only one radio signal is present in the data, the model is thus not suitable those two situations.

The second reason for the IFT reconstruction to fail is that the variational inference can converge on a local minimum, if the slope of the phase is estimated incorrectly. This can cause the IFT reconstruction to estimate a wrong signal timing, and only fit to part of the radio pulse. This is especially a problem for detectors where a large group delay in the signal chain elongates the signal recorded by the channels. This is the case for the current ARIANNA detector and argues for a signal chain with less group delay for future detectors.

For in-ice showers, a second effect plays a role: because the shower front propagates significantly faster than radio signal, signals from the early stage of the shower development arrive after the ones from the later stages, if the observer is located inside the Cherenkov ring. To such an observer, it looks like the shower propagation is happening in reverse, and the radio signal is mirrored on the time axis. In Fourier space, this corresponds to a sign change in the slope of the linear function describing the phase, compared to an observer outside the Cherenkov ring. The prior probability distribution of the slope is centered around one value, so only one of these cases (the observer outside the Cherenkov ring in this paper) is taken into account. Fortunately, most of the phase of the measured voltage is dictated by the antenna and amplifier response, so the reconstructions usually work for observers inside the Cherenkov ring as well. Nevertheless, the reconstruction quality could be improved by testing both configurations of the phase slope and determining which one yields a better result. An additional benefit would be the ability to determine which side of the Cherenkov ring the antenna is on, which provides additional insight on the event geometry.

Fortunately, both of these mis-reconstructions are easily identified. A typical example is shown in figure 17: the reconstruction converged on a pulse timing that misses the start of the radio signal and tries to find a solution that matches the tail of the pulse. However, much of pulse shape is dictated by the group delay of the antenna and amplifier, so it is difficult to find a reconstruction for the amplitude of the frequency spectrum that matches the data. The result is a spectrum that has multiple peaks and drops to zero in between. This feature in the spectrum can be used to identify events where the electric field reconstruction likely failed.

Of course, assuming that the signal timing is known, it is also possible to check if the signal time of the reconstructed radio pulse matches.

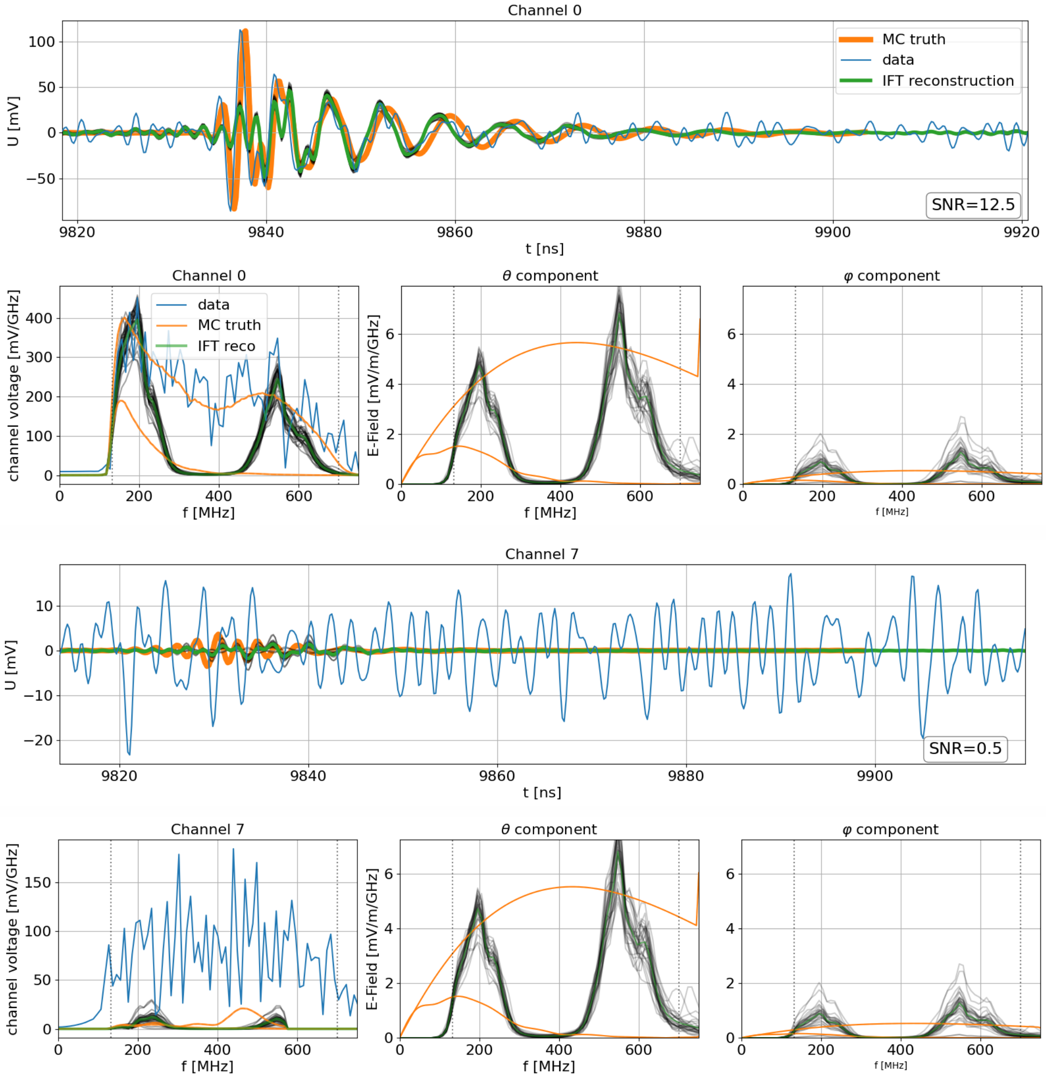

Figure 17. Results of a failed electric field reconstruction of an event detected by an RNO-G station. Shown are one of the Vpol (top) and one of the Hpol (bottom) channels. 1st and 3rd row: waveform of the data (blue), the actual signal (orange) and the reconstruction (green). 2nd and 4th row: spectrum of the channel voltage (left) and the $\vec{e}_\theta$ (center) and $\vec{e}_\phi$ (right) component of the electric field. The thin gray lines are the samples used for uncertainty estimation.

References

[1] F. Halzen, *High-energy neutrino astrophysics*, *Nature Phys.* **13** (2016) 232.

[2] K. Murase and E. Waxman, *Constraining High-Energy Cosmic Neutrino Sources: Implications and Prospects*, *Phys. Rev. D* **94** (2016) 103006 [`arXiv:1607.01601`] [INSPIRE].

[3] K. Greisen, *End to the cosmic ray spectrum?*, *Phys. Rev. Lett.* **16** (1966) 748 [INSPIRE].

[4] V.S. Berezinsky and G.T. Zatsepin, *Cosmic rays at ultrahigh-energies (neutrino?)*, *Phys. Lett. B* **28** (1969) 423 [INSPIRE].

[5] G.T. Zatsepin and V.A. Kuzmin, *Upper limit of the spectrum of cosmic rays*, *JETP Lett.* **4** (1966) 78 [INSPIRE].

[6] A. van Vliet, R. Alves Batista and J.R. Hörandel, *Determining the fraction of cosmic-ray protons at ultrahigh energies with cosmogenic neutrinos*, *Phys. Rev. D* **100** (2019) 021302 [`arXiv:1901.01899`] [INSPIRE].

[7] Pierre Auger collaboration, *The Pierre Auger Observatory and its Upgrade*, *Science Reviews — from the end of the world (Argentina)* **1** (2020) 8.

[8] Telescope Array collaboration, *The surface detector array of the Telescope Array experiment*, *Nucl. Instrum. Meth. A* **689** (2013) 87 [`arXiv:1201.4964`] [INSPIRE].

[9] M. Ahlers and F. Halzen, *Opening a New Window onto the Universe with IceCube*, *Prog. Part. Nucl. Phys.* **102** (2018) 73 [`arXiv:1805.11112`] [INSPIRE].

[10] KM3NeT collaboration, *Letter of intent for KM3NeT 2.0*, *J. Phys. G* **43** (2016) 084001 [`arXiv:1601.07459`] [INSPIRE].

[11] Baikal-GVD collaboration, *Baikal-GVD: status and prospects*, *EPJ Web Conf.* **191** (2018) 01006 [`arXiv:1808.10353`] [INSPIRE].

[12] G.A. Askaryan, *Excess negative charge of an electron-photon shower and the coherent radio emission from it*, *Zh. Eksp. Teor. Fiz.* **41** (1961) 616 [INSPIRE].

[13] J.V. Jelley, J.H. Fruin, N.A. Porter and T.C. Weekes, *Radio pulses from extensive cosmic-ray air showers*, *Nature* **205** (1965) 327.

[14] Pierre Auger collaboration, *Observation of inclined EeV air showers with the radio detector of the Pierre Auger Observatory*, *JCAP* **10** (2018) 026 [`arXiv:1806.05386`] [INSPIRE].

[15] P. Schellart et al., *Detecting cosmic rays with the LOFAR radio telescope*, *Astron. Astrophys.* **560** (2013) A98 [`arXiv:1311.1399`] [INSPIRE].

[16] D. Ardouin et al., *Radio-Detection Signature of High Energy Cosmic Rays by the CODALEMA Experiment*, *Nucl. Instrum. Meth. A* **555** (2005) 148 [`astro-ph/0504297`] [INSPIRE].

[17] ARIANNA collaboration, *Design of the Second-Generation ARIANNA Ultra-High-Energy Neutrino Detector Systems*, in *2015 IEEE Nuclear Science Symposium and Medical Imaging Conference*, (2015) [DOI] [`arXiv:1511.07525`] [INSPIRE].

[18] ARA collaboration, *Performance of two Askaryan Radio Array stations and first results in the search for ultrahigh energy neutrinos*, *Phys. Rev. D* **93** (2016) 082003 [`arXiv:1507.08991`] [INSPIRE].

[19] RNO-G collaboration, *Design and Sensitivity of the Radio Neutrino Observatory in Greenland (RNO-G)*, 2021 *JINST* **16** P03025 [`arXiv:2010.12279`] [INSPIRE].

[20] IceCube-Gen2 collaboration, *IceCube-Gen2: The Window to the Extreme Universe*, `arXiv:2008.04323` [INSPIRE].

[21] T. Huege, *Radio detection of cosmic ray air showers in the digital era*, *Phys. Rept.* **620** (2016) 1 [`arXiv:1601.07426`] [INSPIRE].

[22] P. Schellart et al., *Polarized radio emission from extensive air showers measured with LOFAR*, *JCAP* **10** (2014) 014 [arXiv:1406.1355] [INSPIRE].

[23] P. Allison et al., *Measurement of the real dielectric permittivity ϵ_r of glacial ice*, *Astropart. Phys.* **108** (2019) 63 [arXiv:1712.03301] [INSPIRE].

[24] S.W. Barwick et al., *Observation of classically 'forbidden' electromagnetic wave propagation and implications for neutrino detection*, *JCAP* **07** (2018) 055 [arXiv:1804.10430] [INSPIRE].

[25] C. Deaconu et al., *Measurements and Modeling of Near-Surface Radio Propagation in Glacial Ice and Implications for Neutrino Experiments*, *Phys. Rev. D* **98** (2018) 043010 [arXiv:1805.12576] [INSPIRE].

[26] J.C. Hanson et al., *Radar absorption, basal reflection, thickness and polarization measurements from the Ross Ice Shelf, Antarctica*, *J. Glaciol.* **61** (2015) 438.

[27] J. Avva, J.M. Kovac, C. Miki, D. Saltzberg and A.G. Vieregg, *An in situ measurement of the radio-frequency attenuation in ice at Summit Station, Greenland*, *J. Glaciol.* **61** (2015) 1005 [arXiv:1409.5413] [INSPIRE].

[28] S. Barwick, D. Besson, P. Gorham and D. Saltzberg, *South polar in situ radio-frequency ice attenuation*, *J. Glaciol.* **51** (2005) 231.

[29] Pierre Auger collaboration, *Energy Estimation of Cosmic Rays with the Engineering Radio Array of the Pierre Auger Observatory*, *Phys. Rev. D* **93** (2016) 122005 [arXiv:1508.04267] [INSPIRE].

[30] C. Glaser et al., *NuRadioMC: Simulating the radio emission of neutrinos from interaction to detector*, *Eur. Phys. J. C* **80** (2020) 77 [arXiv:1906.01670] [INSPIRE].

[31] J. Alvarez-Muñiz, A. Romero-Wolf and E. Zas, *Cherenkov radio pulses from electromagnetic showers in the time-domain*, *Phys. Rev. D* **81** (2010) 123009 [arXiv:1002.3873] [INSPIRE].

[32] C. Welling, C. Glaser and A. Nelles, *Reconstructing the cosmic-ray energy from the radio signal measured in one single station*, *JCAP* **10** (2019) 075 [arXiv:1905.11185] [INSPIRE].

[33] C. Glaser et al., *NuRadioReco: A reconstruction framework for radio neutrino detectors*, *Eur. Phys. J. C* **79** (2019) 464 [arXiv:1903.07023] [INSPIRE].

[34] A.B. Migdal, *Bremsstrahlung and pair production in condensed media at high-energies*, *Phys. Rev.* **103** (1956) 1811 [INSPIRE].

[35] L. Landau and I. Pomeranchuk, *Limits of applicability of the theory of bremsstrahlung electrons and pair production at high-energies*, *Dokl. Akad. Nauk Ser. Fiz.* **92** (1953) 535 [INSPIRE].

[36] L. Gerhardt and S.R. Klein, *Electron and Photon Interactions in the Regime of Strong LPM Suppression*, *Phys. Rev. D* **82** (2010) 074017 [arXiv:1007.0039] [INSPIRE].

[37] Pierre Auger collaboration, *Advanced Functionality for Radio Analysis in the Offline Software Framework of the Pierre Auger Observatory*, *Nucl. Instrum. Meth. A* **635** (2011) 92 [arXiv:1101.4473] [INSPIRE].

[38] T.M. Jordan et al., *Modelling ice birefringence and oblique radio wave propagation for neutrino detection at the South Pole*, *Annals Glaciol.* **61** (2020) 84 [arXiv:1910.01471] [INSPIRE].

[39] Radar Echo Telescope collaboration, *Modeling in-ice radio propagation with parabolic equation methods*, arXiv:2011.05997 [INSPIRE].

[40] T. Ensslin, *Information field theory*, *AIP Conf. Proc.* **1553** (2013) 184 [arXiv:1301.2556] [INSPIRE].

[41] T.A. Enßlin, *Information theory for fields*, *Annalen Phys.* **531** (2019) 1800127.

[42] P. Arras, P. Frank, R. Leike, R. Westermann and T.A. Enßlin, *Unified radio interferometric calibration and imaging with joint uncertainty quantification*, Astron. Astrophys. **627** (2019) A134 [`arXiv:1903.11169`].

[43] P. Arras et al., *The variable shadow of M87**, `arXiv:2002.05218`.

[44] R.H. Leike, M. Glatzle and T.A. Enßlin, *Resolving nearby dust clouds*, Astron. Astrophys. **639** (2020) A138 [`arXiv:2004.06732`].

[45] R.H. Leike and T.A. Enßlin, *Charting nearby dust clouds using Gaia data only*, Astron. Astrophys. **631** (2019) A32 [`arXiv:1901.05971`].

[46] S. Hutschenreuter and T.A. Enßlin, *The Galactic Faraday depth sky revisited*, Astron. Astrophys. **633** (2020) A150 [`arXiv:1903.06735`].

[47] J. Knollmüller and T.A. Enßlin, *Metric Gaussian Variational Inference*, `arXiv:1901.11033`.

[48] S.W. Barwick et al., *Radio detection of air showers with the ARIANNA experiment on the Ross Ice Shelf*, Astropart. Phys. **90** (2017) 50 [`arXiv:1612.04473`] [INSPIRE].

[49] P. Arras et al., *Nifty5: Numerical information field theory v5*, *Astrophysics Source Code Library* (2019).

[50] IceCube collaboration, *A measurement of the diffuse astrophysical muon neutrino flux using eight years of IceCube data.*, PoS **ICRC2017** (2018) 1005 [INSPIRE].

[51] T. Huege, M. Ludwig and C.W. James, *Simulating radio emission from air showers with CoREAS*, AIP Conf. Proc. **1535** (2013) 128 [`arXiv:1301.2132`] [INSPIRE].

[52] S. Buitink et al., *Method for high precision reconstruction of air shower X_{max} using two-dimensional radio intensity profiles*, Phys. Rev. D **90** (2014) 082003 [`arXiv:1408.7001`] [INSPIRE].

[53] A. Anker et al., *Neutrino vertex reconstruction with in-ice radio detectors using surface reflections and implications for the neutrino energy resolution*, JCAP **11** (2019) 030 [`arXiv:1909.02677`] [INSPIRE].

[54] H. Schoorlemmer et al., *Energy and Flux Measurements of Ultra-High Energy Cosmic Rays Observed During the First ANITA Flight*, Astropart. Phys. **77** (2016) 32 [`arXiv:1506.05396`] [INSPIRE].

Chapter 6

Energy Reconstruction for RNO-G

6.1 Declaration of Authorship

The method to reconstruct the energy of neutrinos detected by the Radio Neutrino Observatory Greenland (RNO-G) presented in the publication "Reconstructing the neutrino energy for in-ice radio detectors", accepted for publication to the European Physical Journal C, was developed and implemented by me.

The simulations were performed by me using the *NuRadioMC* software framework, which was also used for the event reconstructions. Some of the software modules used in the reconstruction chain (such as bandpass filtering, resampling and noise simulation), were already part of the *NuRadioMC* framework. The code performing the major new techniques described in the publication (vertex reconstruction, electric field reconstruction and energy reconstruction) was both methodologically developed and implemented by me. All figures, except Fig. 2 (a schematic design by the collaboration) were also produced by me.

The text of the publication was written by me. It then underwent a collaboration internal review by Anna Nelles, Christian Glaser, and Simona Toscano, who suggested improvements to both text and figures. I implemented the changes. After that, it was distributed to the entire collaboration for review, where additional textual improvements were suggested.

The paper was submitted to the European Physical Journal on July 5, 2021 and accepted for publication on January 17, 2022.

6.2 Publication: Reconstructing the neutrino energy for in-ice radio detectors

Eur. Phys. J. C manuscript No.
(will be inserted by the editor)

Reconstructing the neutrino energy for in-ice radio detectors

A study for the Radio Neutrino Observatory Greenland (RNO-G)

J. A. Aguilar[1], **P. Allison**[2], **J. J. Beatty**[2], **H. Bernhoff**[3], **D. Besson**[4,5], **N. Bingefors**[6], **O. Botner**[6], **S. Bouma**[13], **S. Buitink**[7], **K. Carter**[8], **M. Cataldo**[13], **B. A. Clark**[9], **Z. Curtis-Ginsberg**[11], **A. Connolly**[2], **P. Dasgupta**[1], **S. de Kockere**[10], **K. D. de Vries**[10], **C. Deaconu**[11], **M. A. DuVernois**[12], **C. Glaser**[6], **A. Hallgren**[6], **S. Hallmann**[14], **J. C. Hanson**[15], **B. Hendricks**[17], **B. Hokanson-Fasig**[12], **C. Hornhuber**[4], **K. Hughes**[11], **A. Karle**[12], **J. L. Kelley**[12], **S. R. Klein**[16], **R. Krebs**[17], **R. Lahmann**[13], **U. Latif**[10], **T. Meures**[12], **Z. S. Meyers**[14,13], **K. Mulrey**[7], **A. Nelles**[14,13], **A. Novikov**[4], **E. Oberla**[11], **B. Oeyen**[18], **H. Pandya**[7], **I. Plaisier**[13,14], **L. Pyras**[14,13], **D. Ryckbosch**[18], **O. Scholten**[10,20], **D. Seckel**[19], **D. Smith**[11], **D. Southall**[11], **J. Torres**[2], **S. Toscano**[1], **D. Tosi**[12], **D. J. Van Den Broeck**[10,7], **N. van Eijndhoven**[10], **A. G. Vieregg**[11], **C. Welling**[a,13,14], **S. Wissel**[17,8], **R. Young**[4], **A. Zink**[13]

[1] Université Libre de Bruxelles, Science Faculty CP230, B-1050 Brussels, Belgium
[2] Dept. of Physics, Center for Cosmology and AstroParticle Physics, Ohio State University, Columbus, OH 43210, USA
[3] Uppsala University, Dept. of Engineering Sciences, Division of Electricity, Uppsala, SE-752 37, Sweden
[4] University of Kansas, Dept. of Physics and Astronomy, Lawrence, KS 66045, USA
[5] National Nuclear Research University MEPhI, Kashirskoe Shosse 31, 115409, Moscow, Russia
[6] Uppsala University, Dept. of Physics and Astronomy, Uppsala, SE-752 37, Sweden
[7] Vrije Universiteit Brussel, Astrophysical Institute, Pleinlaan 2, 1050 Brussels, Belgium
[8] Physics Dept. California Polytechnic State University, San Luis Obispo CA 93407, USA
[9] Dept. of Physics and Astronomy, Michigan State University, East Lansing MI 48824, USA
[10] Vrije Universiteit Brussel, Dienst ELEM, B-1050 Brussels, Belgium
[11] Dept. of Physics, Enrico Fermi Inst., Kavli Inst. for Cosmological Physics, University of Chicago, Chicago, IL 60637, USA
[12] Wisconsin IceCube Particle Astrophysics Center (WIPAC) and Dept. of Physics, University of Wisconsin-Madison, Madison, WI 53703, USA
[13] Erlangen Center for Astroparticle Physics (ECAP), Friedrich-Alexander-University Erlangen-Nuremberg, 91058 Erlangen, Germany
[14] DESY, Platanenallee 6, 15738 Zeuthen, Germany
[15] Whittier College, Whittier, CA 90602, USA
[16] Lawrence Berkeley National Laboratory, Berkeley, CA 94720, USA
[17] Dept. of Physics, Dept. of Astronomy & Astrophysics, Penn State University, University Park, PA 16801, USA
[18] Ghent University, Dept. of Physics and Astronomy, B-9000 Gent, Belgium
[19] Dept. of Physics and Astronomy, University of Delaware, Newark, DE 19716, USA
[20] KVI – Center for Advanced Radiation Technology, University of Groningen, Groningen, The Netherlands

Received: date / Accepted: date

Abstract Since summer 2021, the Radio Neutrino Observatory in Greenland (RNO-G) is searching for astrophysical neutrinos at energies >10 PeV by detecting the radio emission from particle showers in the ice around Summit Station, Greenland. We present an extensive simulation study that shows how RNO-G will be able to measure the energy of such particle cascades, which will in turn be used to estimate the energy of the incoming neutrino that caused them. The location of the neutrino interaction is determined using the differences in arrival times between channels and the electric field of the radio signal is reconstructed using a novel approach based on Information Field Theory. Based on these properties, the shower energy can be estimated. We show that this method can achieve an uncertainty of 13% on the logarithm of the shower energy after modest quality cuts and estimate how this can constrain the energy of the neutrino. The method presented in this paper is applicable to all similar radio neutrino detectors, such as the proposed radio array of IceCube-Gen2.

---

[a] e-mail: christoph.welling@desy.de, authors@rno-g.org

1 Neutrino detection with radio antennas

Neutrinos are unique messengers for high-energy astrophysical phenomena. Without an electric charge, they are not deflected by magnetic fields on their way to Earth and as they only interact via the weak force at very low cross-sections, they can travel vast distances undisturbed. Unfortunately, this also means they only have a small chance to interact within any detector one may build to observe them. For the high-energy neutrino observatories, the solution to this problem is to instrument large volumes of water [1,2] or ice [3,4] and detect Cherenkov light from charged particles created from neutrino interactions. This approach has led to the discovery of an astrophysical neutrino flux [5] and even the identification of some likely source candidates [6,7] for neutrinos beyond the 100 TeV energy scale. To explore the energy range beyond that, even larger detection volumes than the $\sim 1\,\mathrm{km}^3$ of the largest current optical detectors are required. Extending them to the necessary sizes would require large expenses in money and labor, because of the optical properties of water and ice. Deep sea water has an absorption length on the order of tens of meters [8]. While absorption lengths are larger in deep glacial ice, light gets scattered, with scattering lengths also on the order of tens of meters [9]. This limits the maximum possible spacing for optical detection modules, and thereby the affordable size of the detector.

Fortunately, high-energy particle showers in cold ice emit radio signals that are hardly scattered and show attenuation lengths around $\sim 1\,\mathrm{km}$[10,11,12]. This allows for the construction of a detector like the Radio Neutrino Observatory in Greenland [13], which will monitor a volume of around 100 cubic kilometers, making it a promising candidate for the first detection of EeV neutrinos.

Ultra-high energy neutrinos are expected to be produced by astrophysical sources (e.g. [14,15,16,17,18]) and by interaction of ultra-high energy cosmic rays interacting with cosmic photon backgrounds [19,20,21,22]. Cosmogenic neutrino fluxes are predicted to show different energy spectra than neutrinos from astrophysical sources, so distinguishing between them with any radio neutrino detector will require the ability to reconstruct the neutrino energy. The different models for astrophysical sources differ in their predicted high-energy neutrino spectra, so a spectrum measurement would provide valuable information to constrain these scenarios, especially when combined with information from other cosmic messengers. A good energy estimation is also important to efficiently suppress a background of high-energy muons that drops quickly with energy [23].

1.1 Radio emission from particle showers in ice

When a high-energy neutrino interacts, a fraction of its energy is transferred through deep-inelasting scattering with nucleons, which causes a hadronic shower to develop. In this hadronic shower, among other particles, pions are created. The neutral pions decay into two photons that cause electromagnetic sub-showers. Although the end product that produces the radio emission are many electromagnetic sub showers, these showers are referred to as hadronic showers. If an electron neutrino undergoes a charged current interaction, next to the hadronic shower, an electron is created which initiates an electromagnetic cascade. In that case, two particle showers are present, whose radio signals overlap. Charged current interaction of ν_μ and ν_τ can occur as well and create μ or τ particles, but these do not emit radio signals and are practically invisible for a radio detector by themselves. They may, however, cause secondary particle showers as they decay or propagate through stochastic energy losses which provides a detectable signature [23]. Therefore, in practical terms, the event reconstruction for a radio-based neutrino detector can be thought of as the reconstruction of a particle cascade.

As a particle shower develops in the ice, electrons in the ice are kicked out of their atomic shells and swept along in the shower. Additionally positrons in the shower front annihilate with electrons in the ice. Both effects cause an excess of negative charges to develop in the shower, which emits radio signals as they propagate [24,25]. This process has been confirmed experimentally in several dense media, including ice, at particle accelerators [26,27,28] and in air showers [29,30], where it is a subdominant emission process. If an observer is located on the Cherenkov cone ($\sim 56\,^\circ$ opening angle in ice), the radio emission of the entire shower development interferes constructively, i.e. reaches the observer at the same time, and causes a signal strong enough to be detected with radio antennas. Because of the longer wavelength, the radio signal can still be detectable a few degrees off the Cherenkov cone. As an observer moves away from the Cherenkov cone, the shorter wavelengths lose coherence first, leading to an overall weakening of the signal as well as a change in the shape of the frequency spectrum [31,32]. In the case of a charged-current interaction by an electron neutrino, two showers are created, whose radio signals interfere, leading to a more complex spectrum of the radio signal. At high energies, the electromagnetic shower is elongated by the LPM effect [33,34], which can increase its length to hundreds of meters, compared to the $\sim 10\,\mathrm{m}$ typical for a hadronic or lower-energy electromagnetic

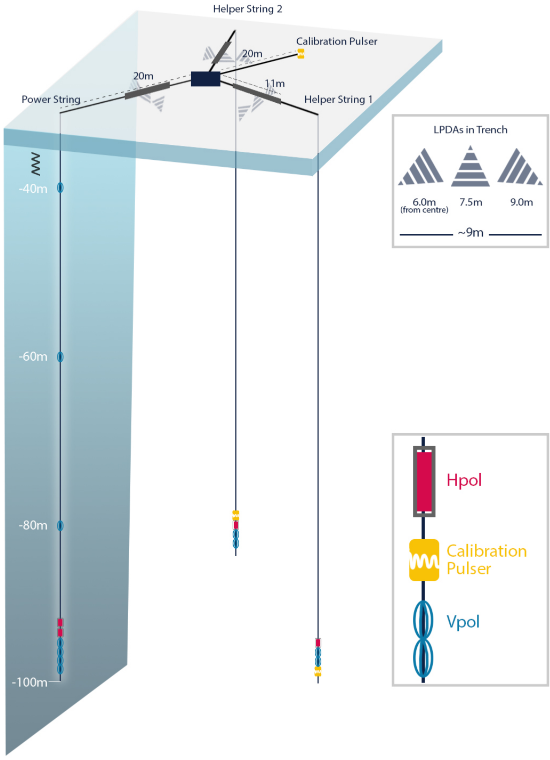

Fig. 1 Layout of one of the 35 detector stations that will make up the Radio Neutrino Observatory Greenland (RNO-G). From [13]

shower, and cause a more irregular shower development [35,36,37]. This change also affects the radio signal, as signals from different parts of the shower interfere with each other [38,39]. The result is a reduction of the radio emission and an irregular electric field spectrum with multiple maxima.

1.2 The Radio Neutrino Observatory Greenland

The Radio Neutrino Observatory Greenland (RNO-G) [13] is a detector for neutrinos with energies above 10 PeV, currently under construction near Summit Station on top of the ice sheet of Greenland. RNO-G is scheduled to be completed with 35 detector stations in 2023, making it the first discovery-scale detector for neutrinos at these energies.

The stations are positioned on a square grid with a spacing of 1.25 km between stations. With this spacing, many neutrino events will only be detected by a single station, which maximizes the effective volume of the detector, but presents a challenge for the reconstruction. In this paper, we will assume that only data from a single station is available, effectively turning each station into an independent detector.

An RNO-G station (see Fig. 1) can be seen as consisting of two sections: A *shallow component* with antennas buried about 2 m below the snow surface and a *deep component* with antennas placed in holes at a depth of up to 100 m. Both are centered around a DAQ box housing the station electronics and a small tower for communication antennas and solar panels.

The shallow component consists of three sets of three logarithmic-periodic dipole antennas (LPDAs) each, installed 2 m below the ice surface at a horizontal distance of 11 m from the station center. One LPDA in each set is pointed upwards, to detect air showers, while the others are pointed downwards at a 60 ° angle, making them sensitive to neutrino signals from below. The LPDAs have the advantage of being very sensitive, but they can only be deployed close to the surface because of their size (140 cm height, 146 cm width). At these shallow depths, the observable ice volume is smaller because of shielding effects from the changing index of refraction in the upper 100 m of the ice, so that only about 20% of triggered neutrino events are expected to be visible in the shallow component [13].

The deep component consists of three vertical cables, called *strings*, in boreholes going down to a depth of 100 m below the snow surface. One of the strings, called *power string*, holds a phased array consisting of four vertically polarized (Vpol) antennas. A phased array works by overlaying the signals from all four channels to reduce the noise, which was tested on the ARA detector [40] and will allow RNO-G to trigger on radio signals with a signal-to-noise ratio (SNR)[1] as low as 2. Directly above the phased array are two horizontally polarized (Hpol) antennas. Further up the string are three more Vpol antennas with a spacing of 20 m from each other.

The other two strings, called *helper strings*, are more sparsely instrumented, with two Vpol and one Hpol antenna on each string. Additionally, each string holds a radio pulser that can be used to calibrate the detector.

The Vpol antenna uses a *fat dipole* design with a height of 60 cm and a diameter of 12.7 cm, which is sensitive in the ~50 MHz to 600 MHz band and has an antenna response that is symmetric in azimuth. For the horizontal polarization, *quadslot antennas* with a height of 60 cm and a diameter of 20.32 cm are used, whose design is mostly limited by the diameter of the borehole [41]. Because of this constraint, the Hpol antennas have a smaller overall sensitivity and are only sensitive in the ~200 MHz to 400 MHz range. Combined with the tendency of the neutrino-induced radio signals to be more vertically polarized and stronger at lower frequencies,

---

[1] We define the SNR as half the peak-to-peak voltage amplitude divided by the root mean square of the noise.

this means only a small signal will be visible in the Hpol channels, if at all, for most events.

After a signal is received by one of the downhole antennas, it is fed into a Low Noise Amplifier (LNA) and sent to the surface via a Radio Frequency over Fiber (RFoF) transmitter. At the surface, the signal is amplified again by an LNA inside the DAQ box, digitized and stored on an SD card. This signal chain has a passband of 130 MHz to 700 MHz. From the DAQ the signals are transferred to a server at Summit Station via LTE communication. All components of the signal chain are located in separate RF-tight housings, which helps keep the noise level low, at an expected root mean square (RMS) of ~10 mV.

1.3 General reconstruction strategy

In general, the amplitude of the electric field $\vec{E}$ of the radio signal from a particle shower is proportional to the shower energy. In practice, it is more convenient to use the energy fluence of the radio signal

$$\Phi^E = c \cdot \epsilon \int \vec{E}^2(t)dt, \tag{1}$$

where c is the speed of light and ϵ the permittivity. Its square root is proportional to the shower energy as well, but has the advantage of being easier to determine from data and less affected by fluctuations from noise than the electric field amplitude.

The other parameters that affect the radio signal received at the detector can be expressed with the relation

$$\sqrt{\Phi^E} \propto E_\nu \cdot \kappa \cdot \exp\left(-\frac{l}{l_{\text{att}}}\right)/l \cdot f(\varphi) \tag{2}$$

where E_ν is the neutrino energy, κ is the fraction of the neutrino energy that is transferred into the shower, φ is the viewing angle, l is the distance the radio signal travels in the ice before reaching the antenna and l_{att} is the attenuation length of the ice. Based on this, we will first reconstruct geometric shower parameters and the energy of the particle shower, and then use this to estimate the neutrino energy.

This study focuses on the reconstruction based on the deep component of RNO-G. Due to the phased array trigger, this component is expected to detect most neutrino signals. An energy reconstruction study for the ARIANNA experiment has been performed previously [42,43]. Since the surface component of RNO-G has been modeled after the ARIANNA experiment, the reconstruction strategy should be similarly applicable for potential events detected with the LPDAs only.

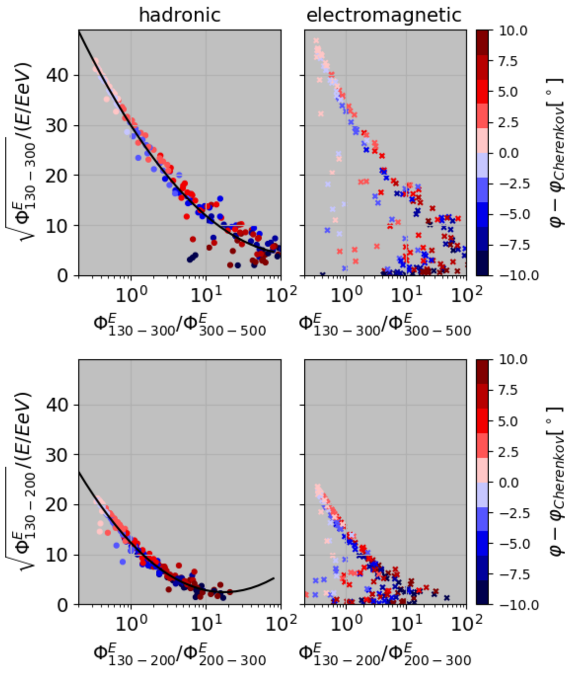

Fig. 2 Square root of the energy fluence of the radio signal emitted by a particle shower in ice divided by the shower energy as a function of the ratio between the energy fluence in different passbands for hadronic (left) and electromagnetic (right) showers. Radio signals were generated using the ARZ2019 model [44] for shower energies between 1×10^{15} eV and 1×10^{19} eV. The upper plot uses a lower passband of 130 MHz to 300 MHz and an upper passband of 300 MHz to 500 MHz, the lower plot uses 130 MHz to 200 MHz and 200 MHz to 300 MHz. Colors show the viewing angle relative to the Cherenkov angle. The viewing angle is calculated with respect to the position of the maximum of the charge-excess profile. The black line shows the parametrization for the hadronic showers.

2 Influence of the viewing angle

The last term in Eq. 2 parametrizes the contribution of the *viewing angle*, defined as the angle between the direction into which the signal is emitted and the shower axis. At the Cherenkov angle, the radio emission over the entire shower development interferes constructively, leading to a strong signal. As the viewing angle moves away from the Cherenkov angle, the radio signal gets weaker, but not equally over the whole frequency range. Shorter wavelengths lose coherence faster, which allows us to use the shape of the frequency spectrum of the radio pulse as a proxy for the viewing angle. This technique has already been demonstrated to work for air showers [45], so we adapt it here for neutrino detection.

To quantify the shape of the frequency spectrum, we define a *slope parameter*

$$s = \Phi^E_{130-300}/\Phi^E_{300-500} \tag{3}$$

as the ratio between the energy fluence of the radio signal in the 130 MHz to 300 MHz and the 300 MHz to 500 MHz passbands. More details of the procedure to reconstruct the electric field and the parameter s are discussed in Sec. 4.

The relation between the slope parameter and the energy fluence of the radio signal is shown in the upper plot of Fig. 2 for a fixed distance between shower and observer of 1 km and neglecting any attenuation by the ice. It is convenient to only use the energy fluence in the lower passband to estimate the shower energy, because it is less dependent on the viewing angle than higher frequencies, and also easier to reconstruct, because of the higher sensitivity of the Vpol antennas at lower frequencies.

For hadronic showers, the relation between $\lg(s)$ and $\sqrt{\Phi^E}/E$ can be parameterized by a parabola, for electromagnetic showers the relation is more complicated: The radio emission stems from the electrons and positrons in the shower, so the signal from electromagnetic showers tends to be a bit stronger than for hadronic showers of the same energy. However, outliers with a much weaker signal originate from showers affected by the LPM effect. These showers are elongated and/or show an irregular development, which can effectively lead to several shower maxima. This causes a loss of coherence of the radio signal emitted as the shower develops, thus, weakening it. It should also be noted that for such long showers, an observer will see different parts at different viewing angles, making this parameter rather ill-defined.

Since no method to distinguish between neutrino flavors has yet been developed for RNO-G, we assume that no information about the flavor or the interaction type (charged vs. neutral current) is available. We therefore only parameterize the relationship the between $\sqrt{\Phi^E}/E$ and s for hadronic showers with a parabola, and then use the result for both shower types.

If the difference between viewing and Cherenkov angle is large, the electric field spectrum can drop to close to 0 in the 300 MHz to 500 MHz band. The parametrization still holds for these cases, but even small uncertainties in the shape of the reconstructed spectrum can lead to large changes in the s parameter. We found empirically that we can mitigate this problem by using a slope parameter s' if s is larger than 10. This new slope parameter s' is defined similarly to s, but using the energy fluences in the 130 MHz to 200 MHz and the 200 MHz to 300 MHz bands, which can be parameterized the same way as s (see Fig. 2, bottom). The values of the parameters of the parabola fit are listed in Tab. 1.

	p_2	p_1	p_0
s	4.70	−22.20	29.99
s'	6.46	−16.00	12.49

Table 1 Parameters of the parabola parametrization to the hadronic showers shown in Fig. 2 that are used to reconstruct the shower energy from Eq. 4.

Using this parametrization, the shower energy can be calculated from the radio signal using

$$\begin{aligned} E_{\mathrm{sh}} &= \frac{\sqrt{\Phi^E_{130-300}/\mathrm{eV}}}{p_2 \cdot \lg(s)^2 + p_1 \cdot \lg(s) + p_0} \cdot \mathrm{EeV} \\ &= \sqrt{\Phi^E_{130-300}/\mathrm{eV}} \cdot f_{\varphi}(s) \cdot EeV \end{aligned} \tag{4}$$

where p_i are the parameters of the parabola from Tab. 1. If the s parameter is larger than 10, $\Phi^E_{130-200}$ and s' are used instead. The points in Fig. 2 are not exactly on the parametrization line. We can calculate the shower energy from Eq. 4 for these showers using the true values of Φ^E and s and compare them to the true shower energy. The difference is an estimate of the relative uncertainty on the shower energy we get from the chosen parametrization. Using the 68% quantile as a criterion, the relative uncertainty is 9%, which will turn out to be a subdominant uncertainty. However, these calculations were done at a fixed distance of 1 km and without the effects of attenuation. So before this equation can be used, the electric field needs to be reconstructed and the distance to the shower needs to be known to correct for attenuation during propagation.

3 Vertex reconstruction

After a neutrino event has been identified, the first step in the reconstruction process is to determine the location of the neutrino interaction. This is important for the energy reconstruction in order to be able to correct for the attenuation stemming from the signal propagation through the ice and the $\frac{1}{r}$ weakening of the signal amplitude with distance. Knowing the vertex location also allows us to determine the angle at which the radio signal arrives at the detector, which determines the antenna response.

3.1 Radio signal propagation through ice

The index of refraction n of glacial ice is not uniform but decreases with depth. Measurement from the South

Pole, Moore's Bay and Summit Station [46,47] all suggest that the index of refraction profile can be parameterized as a function of the depth z by

$$n(z) = n_0 - \Delta_z e^{z/z_0} \tag{5}$$

where n_0, Δ_z and z_0 are fit parameters that have to be determined from measurements. Because of this, the radio signals do not travel in a straight line but are bent downwards. Additionally, a radio signal may be reflected at the ice surface and reach the detector this way. This lets us divide the ray trajectories into three categories:

- *direct ray*: The ray path is bent, but the depth is monotonically in- or decreasing over the entire trajectory.
- *refracted ray*: The ray starts going upwards, but eventually bends downwards and reaches the detector from above.
- *reflected ray*: The ray is reflected at the ice surface and reaches the detector from above.

In many cases, two of these solutions exist and the antenna detects two radio pulses from the same particle shower. These kinds of events, dubbed *DnR* events, become more likely with increasing vertex distance, as the launch angles for both ray paths become more similar, making it more likely for both to be close enough to the Cherenkov angle for a strong enough signal.

Another consequence of the changing index of refraction is the existence of so-called *shadow zones* from where the refraction prevents the radio signal from reaching the antenna at all. These *shadow zones* become smaller the deeper in the ice the antenna is placed, so in many cases only the deeper antennas of the detector are able to receive signals.

Contrary to these naive assumptions, horizontal propagation of radio signals from the shadow zones has been observed at the South Pole, the Ross Ice Shelf as well as Summit Station in Greenland [46,47], likely due to local deviations from a smooth density profile. However, the measurements at Summit Station suggest that this propagation mode only has a coupling at the percent level, so it will be ignored in this paper. Additionally, birefringence may lead to a direction- and polarization-dependent index of refraction, which has been observed at the South Pole [48]. As of the time of writing, no such measurements are available for Summit Station, so this effect will be ignored here as well.

Assuming an index of refraction profile of the form as in Eq. 5, it is possible to find an analytic solution to the ray tracing problem [39]. For more complex profiles, other methods are available [49,50], but at the cost of larger computing times.

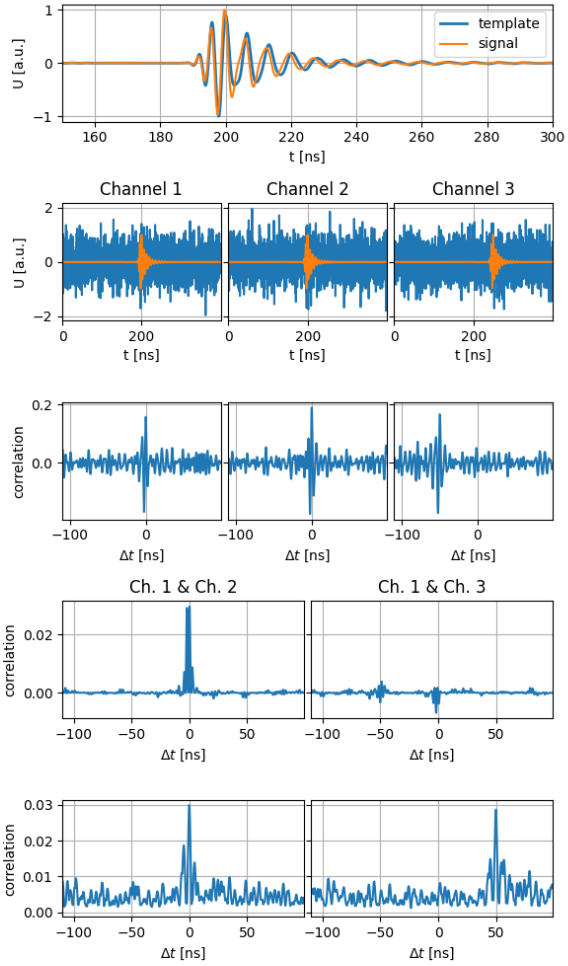

Fig. 3 Visualization of the template correlation method to determine the timing differences between channels. Top row: Zoom of waveforms of signal and template. Second row: Noisy waveforms (blue) and the original signals (orange) of three different channels. Third row: Correlation of those waveforms with the template. Fourth row: Product of the template correlation for channel 1 with those for the other two channels. Bottom row: Maximum of the product of the correlations for two channels as a function of the time shift applied to one of them.

3.2 Reconstruction method

To reconstruct the position of the interaction vertex, we first present a method to determine the relative timing between waveforms in two different channels, then we show how to use this knowledge for the vertex reconstruction.

Most neutrino events detected by RNO-G are expected to be just above the noise threshold, so a method that also works at low signal-to-noise ratios is needed. In the first step we apply a 10th order Butterworth filter with a passband of 130 MHz to 300 MHz to the waveforms to remove frequencies where noise is likely to be dominant over the actual radio signal from the shower.

A convenient way to determine the timing difference between two waveforms is to calculate the correlation function between them, given by the equation

$$\rho(\Delta n) = \frac{\sum_i (V_1)_i \cdot (V_2)_{i-\Delta n}}{\sqrt{\sum_i (V_1)_i^2} \cdot \sqrt{\sum_i (V_2)_i^2}} \qquad (6)$$

where Δn is the number of samples by which one waveform has been shifted and V_1 and V_2 are the voltages measured by both channels. The denominator is a normalization, so that $\rho(\Delta n) = 1$, if both waveforms are identical. However at low SNRs, performance of this method diminishes, as spurious correlations between noise become likely. To avoid this, we use a *template* that was derived by folding an electric field with the detector response, as discussed in the next paragraph. This process is visualized in Fig. 3: The top row shows three waveforms (orange) to which random noise was added, resulting in a noisy signal (blue). The three waveforms are identical, except that channel 3 was shifted by 50 ns. The second row shows the correlations of these waveforms with a template, which is identical to the original waveform as well in this example. In the next step (third row) we combine two of these correlations by multiplying them with each other. Note that for channels 1 and 2 there is a sharp peak, which is missing for channels 1 and 3. This is because the timing difference between channels 1 and 2 is 0, so their correlations have their maxima at the same position. Because of the 50 ns timing difference between them, the correlation maxima for channels 1 and 3 are at different positions and disappear when both are multiplied. So for there to be a peak in their product, one of the correlations would have to be shifted by 50 ns. Turning this reasoning around, we can determine the time difference between two waveforms by calculating their correlation functions with a template and shifting one of the correlations to find when their product has the largest maximum. This is shown in the bottom row of Fig. 3: For channels 1 and 2 the product of their correlation functions (from here on called *correlation product*) has its highest maximum at a time shift of 0 ns, for channels 1 and 3 it is at 50 ns, which is the correct result. By using the correlations to a template, the height of the maximum is also weighted by how *signal-like* the channel waveforms are, which will become useful later. While RNO-G records data with a sampling rate of 2.4 GHz, the Nyquist-Shannon sampling theorem [51] allows us to increase the timing precision by resampling the waveform. We use an upsampling to 5 GHz to achieve a time binning of 0.2 ns. The advantage this approach has compared to correlating the waveforms directly is that it avoids spurious correlations in the noise. Even at SNRs as low as 2.5, the time shift between waveforms can be determined with sub-nanosecond precision.

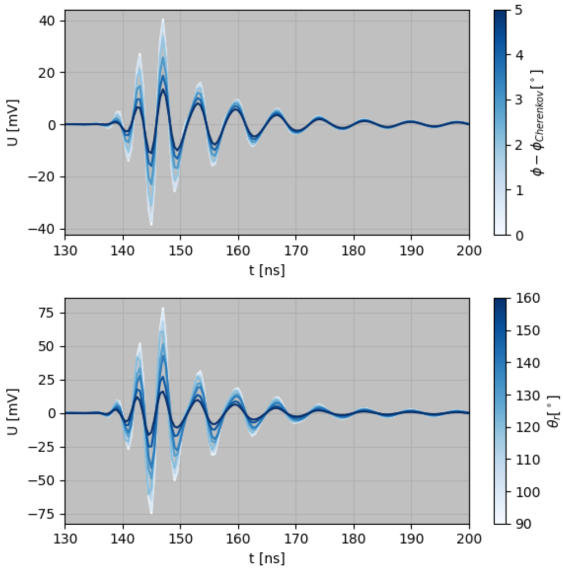

Fig. 4 Examples of waveforms measured by an RNO-G Vpol channel, filtered to the 130 MHz to 300 MHz passband, for different viewing angles (top) and zenith angles of the signal arrival direction (bottom).

This leads to the question what template to use. In the previous example, the template was identical to the signal, but in reality, the signal depends on the viewing angle and the direction from which the signal reaches the antenna. Fortunately, in the relatively small band of 130 MHz to 300 MHz, the shapes of the waveforms are mostly determined by the response of the antenna, amplifier and filters which are very well known. This is demonstrated in Fig. 4: While changes in the viewing angle and the signal arrival direction change the height of the individual peaks of the waveform, the position of each peak remains unchanged and their correlations with another waveform will have their maxima at the same positions as well. Therefore, the choice of which template to use has only a minor influence on the result of the timing reconstruction.

With a way to identify the relative timing of the radio signals, the next step is to use them to reconstruct the location of the neutrino vertex. Because of refraction, calculating the signal travel times from a given point to one of the antennas is not straightforward, and somewhat computationally expensive. Therefore, for each antenna depth used by RNO-G, a lookup table with travel times for a grid of possible vertex positions is created. By assuming radial symmetry of the propagation times, only the radial distance and the depth of the vertex position relative to the antenna need to be considered[2]. Because of the changing index of refraction, two ray tracing solutions exist, so the propagation times for both are stored. Using lookup tables has two advantages: It saves time, because the ray tracing only has to be done once, and it does not make any assumptions about the propagation. Moreover, we are able to calculate the propagation times for any given vertex position. So if changes to the ice model are necessary or more advanced ray tracing methods become available, all that is necessary is to update the lookup tables. For this paper, a grid spacing of 1 m in horizontal distance and 2 m in depth was used. This provides adequate precision, though we did not test how a larger spacing would impact the results.

With these lookup tables, the difference in signal arrival times between two channels can be determined for any potential vertex position. Then the product of template correlations for the corresponding time shift is calculated. By doing this for all channel pairs, the sum of all correlations can be used as an estimator for how well the signal timings match a given vertex position.

At this point, we do not know if the radio signal reached the detector via the direct, reflected or refracted path. While we know which channels measured a pulse above a certain SNR, a signal may still be present in the others, but hidden in the noise. Adding the result of the correlation product for channels without a signal or assuming the wrong ray type fortunately does not have serious negative effect on the reconstruction. The correlation of the template with pure noise is so small that it has little influence on the overall correlation sum for all channel pairs. If the wrong ray type is used, the correlation product may have a large enough maximum at a specific vertex position, but this point is usually far enough away from where other channel pairs have their maximum to not affect the reconstruction. Furthermore, for the correct ray types, all channel pairs with a signal will have their largest correlations corresponding to the same point, while wrong ray types or spurious correlations will result in large correlations at different points for each channel pair. Therefore, we use all possible pairs of Vpol channels together, and sum up the correlations for all possible combinations of ray types. The only condition is that the two channels are sufficiently far away from each other. If both channels are part of the phased array or on the same helper string, they are too close to be useful for vertex reconstruction, and therefore not used.

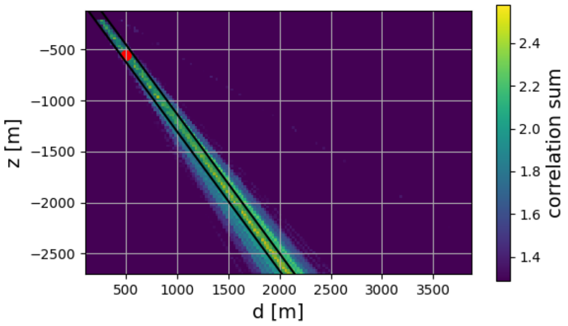

Fig. 5 Scan to restrict the vertex search volume. Results are projected in the horizontal distance v. depth plane, with the colors showing the maximum correlation sum over all azimuths. The black lines mark the volume in which the finer scan will be performed. The red dot marks the true vertex position.

In principle, we could now do a scan on a 3D grid over the entire detector volume, sum up the correlation products for all channel pairs at each point and find its maximum, but this would take too long and consume too much memory to be practical. Instead, we first perform a scan on a grid with a larger spacing. A convenient choice is to use cylindrical coordinates with a spacing in radius of 100 m, 2.5 ° in azimuth and 25 m in depth, and calculate the correlation sums for all points on this grid. We flatten this grid into 2 dimensions by taking the maximum correlation sum over all azimuths for each pair of radii and depths and fit a line to the radius vs. depth graph of the points with the largest correlation sums. To identify the azimuth of the neutrino vertex position, we sum up the correlations for all points belonging to the same azimuth and find the maximum. The result is a line in 3D space around which be lay a cuboid that marks the search volume (see Fig. 5).

Now the search volume is small enough to perform a scan over a smaller grid within a reasonable computational envelope. The result is shown in Fig. 6. The scan was done in 3D but we again only show the projection onto the horizontal distance r.

This already yields good results, but can be further improved if DnR pulses are present. In most cases with DnR pulses, only one of them will be clearly visible while the other is hidden in the noise. However, even these small signals can still yield valuable information. Using the time difference between DnR pulses works the same way as before, except this time the template correlation is done for a channel with itself. Like for the correlation between channels, we use the correlation products from all channels, as they are already weighted by the correlation with a template and spurious correlations usually disagree with the results from other channels, so they do not pose a problem. The

---

[2] To date, no measurements from Summit Station suggest any significant radial asymmetry for ray propagation. Should this change, the lookup tables would need to be adapted, which increases their size and computational cost, but is not a fundamental problem.

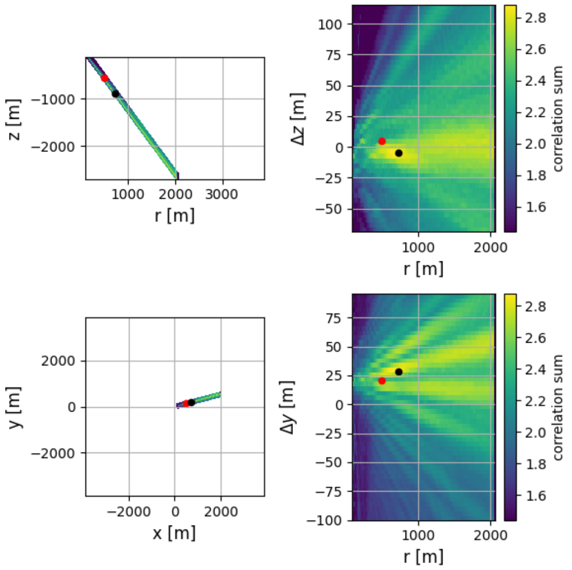

Fig. 6 Vertex reconstruction. Results are projected into the horizontal distance vs. depth (top) or east vs. west plane (bottom), with the colors showing the maximum correlation sums over all azimuths and depths, respectively. The left side shows results in coordinates relative to the station position. Zones that are outside the search volume are in white. The right shows coordinates relative to the vertex search region. The red dots mark the true vertex position, the black dots the position with the largest correlation sum.

effect of this can be seen in Fig. 7. Similarly to the correlations between channels, DnR correlations also have the shape of lines, but there are two advantages that make them very useful when combined with the results from correlating different channels: The time differences between DnR pulses change much more with vertex distance than the differences between channels, leading to much thinner lines. The lines are also at a different angle, so the point where they cross with the lines from the correlation sums between channels can be very well constrained. The contribution of the DnR pulses to the correlation sum is much smaller than from the channel pairs, for two reasons: The two pulses tend to differ in amplitude, so one of them is often just above, or even hidden under, the noise, so their correlation is small. Additionally the number of channel pairs is larger than the number of channels.

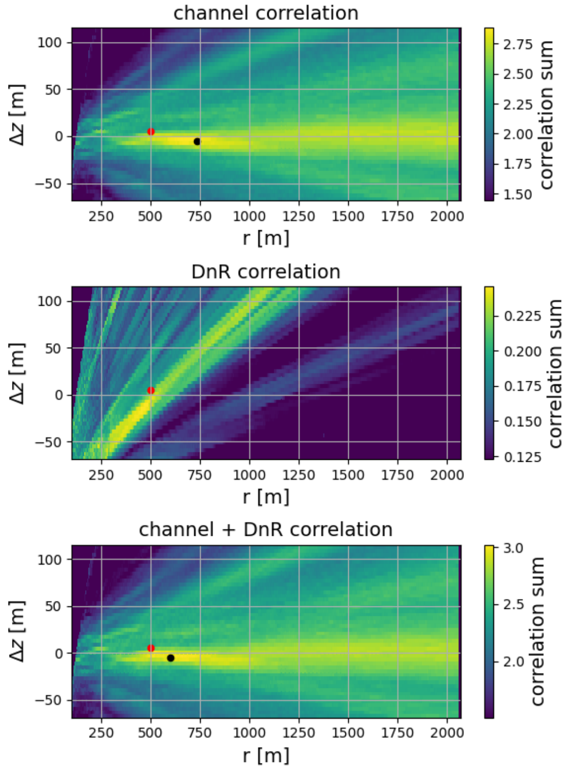

Fig. 7 Use of DnR pulses for vertex reconstruction. Top: Correlation sum using only the correlation products between channels. Middle: Correlation sum using DnR pulses. Bottom: Sum of both correlation between channels and DnR pulse correlation. Results are shown projected into the horizontal distance vs. depth plane, with colors showing the maximum correlation sum over all azimuths. The red dot marks the actual vertex position, the black dot the point with the largest correlation sum.

3.3 Performance of vertex reconstruction

To assess the performance of the neutrino vertex reconstruction (and of the energy reconstruction steps following after this), we produce a simulated data set using the NuRadioMC [39] and NuRadioReco [52] software packages. First, we generate a set of 10^7 neutrinos with isotropic directions, which interact at randomly selected points inside a cylinder with a radius of 3.9 km and a depth of 2.7 km below the ice surface (corresponding roughly to the ice thickness at Summit Station). Energies are randomly distributed between 5.0×10^{16} eV and 1.0×10^{19} eV with a spectrum following the extension of the spectral index measured by IceCube [53] combined with a model of the expected flux from the interaction of ultra-high energy cosmic rays with the cosmic microwave background and other photon fields [22]. Interactions are generated assuming a 1:1:1 flavor mixing due to oscillations and a probability of 0.71 to interact via charged current interaction. Absorption of the neutrino in the Earth is taken into account by applying a weighting to events when evaluating the results later.

For each generated shower, the radio emission is calculated using the ARZ2019 model [44] and propagated to each detector antenna using an analytic ray tracing method [39]. If the radio signal reaches an antenna, it is folded with the response of the antenna and of the

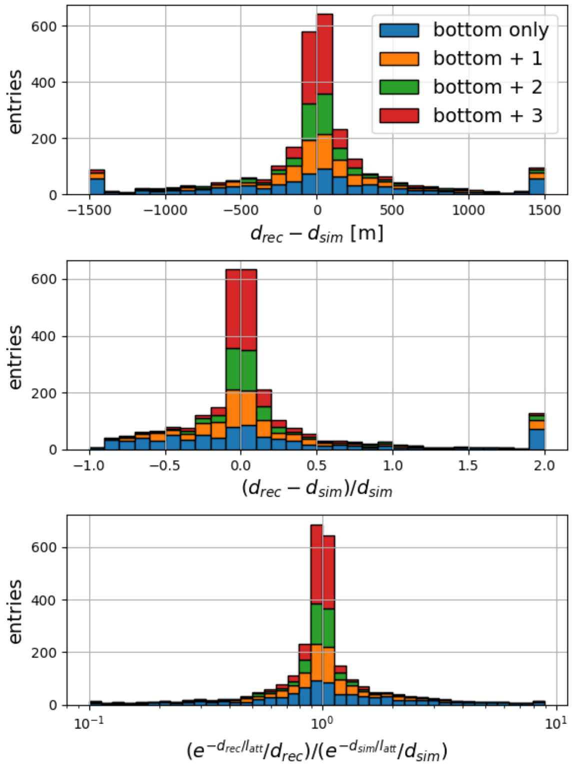

Fig. 8 Stacked histograms showing the performance of the vertex reconstruction method. Top: Difference between reconstructed and actual distance between shower and station. Middle: Relative uncertainties on the reconstructed distance. Bottom: Ratio between the expected attenuation of the radio signal using the reconstructed and the actual distance to the shower. Events are divided into four categories: Those where only channels of the phased array or on the helper strings detected a signal with SNR > 2.5, and those where 1, 2, or 3 of the additional channels on the power string detected a signal with SNR > 2.5. The outermost bins in all plots are overflow bins.

	btm & 1	btm & 2	btm & 3
$d_{\mathrm{rec}} - d_{\mathrm{sim}}$			
median [m] $\sigma_{68\%}$ [m]	38 [-118, 469]	28 [-91, 235]	0 [-80, 115]
$\Delta d/d_{\mathrm{sim}}$			
median $\sigma_{68\%}$	0.04 [-0.11, 0.59]	0.03 [-0.07, 0.29]	0.00 [-0.06, 0.11]
$\mathrm{att}_{\mathrm{rec}}/\mathrm{att}_{\mathrm{sim}}$			
median $\sigma_{68\%}$	0.96 [0.63, 1.12]	0.97 [0.77, 1.08]	1.00 [0.90, 1.07]

	bottom	btm & 1+	btm & 2+
$d_{\mathrm{rec}} - d_{\mathrm{sim}}$			
median [m] $\sigma_{68\%}$ [m]	7 [-302, 287]	8 [-156, 204]	8 [-85, 146]
$\Delta d/d_{\mathrm{sim}}$			
median $\sigma_{68\%}$	0.01 [-0.25, 0.35]	0.01 [-0.12, 0.21]	0.01 [-0.06, 0.14]
$\mathrm{att}_{\mathrm{rec}}/\mathrm{att}_{\mathrm{sim}}$			
median $\sigma_{68\%}$	0.99 [0.74, 1.33]	0.99 [0.83, 1.14]	0.99 [0.87, 1.07]

Table 2 Median and 68% quantiles of the absolute and relative uncertainties on the vertex distance, and the ratio between reconstructed and actual attenuation factor $\exp(-d/l_{\mathrm{att}})/d$. In the upper table, events are divided into categories where at least one of the channels at ∼100 m depth has detected a pulse with SNR ≥ 2.5, as well as exactly one, exactly two or exactly three of the upper channels on the power string. In the lower table, categories where at least one of the channels at ∼100 m depth has detected a signal and where *at least* one, two or three of the channels further up the power string detected a signal with SNR ≥ 2.5.

amplifier. As a proxy for the phased array trigger of RNO-G, the trigger is simulated as a simple high-low threshold trigger that triggers if the voltage exceeds a maximum of 20 mV and a minimum of −20 mV in both of the lower two channels of the phased array. If a trigger signal is given, Rayleigh-distributed noise with an RMS of 10 mV is added to the waveform of each channel. This means triggering at the 2σ level, which is the expected performance of the full phased array trigger. It should be noted that the trigger is performed before noise is added. With the real detector, most triggers will be from noise and have to be removed. But as event identification is not the focus of this paper, we assume a 100% pure event sample.

Finally, the waveforms are upsampled to a sampling rate of 5 GHz and the vertex reconstruction is performed.

The results are shown in Fig. 8 and Tab. 2. The signal arrival direction is much easier to reconstruct than the vertex distance, so we will only focus on the distance here. It turns out that for the performance of the vertex reconstruction, the SNR of the waveforms matters less than which channels detect a signal at all. Therefore it is useful to divide events into categories depending on which channels recorded a signal with SNR > 2.5, which is the SNR around which the signal becomes large enough to be reliably identified using the template correlation method.

Because the phased array trigger is at the bottom of the *power string* and the interaction vertex can lie in the *shadow zone* of the channels further up for some event geometries, the channels at ∼100 m depth are the most likely to detect a signal. Because they are all at roughly the same depth, their signal amplitudes, and therefore their SNRs, tend to be similar. As Fig. 8 shows, only the channels at the bottom of the detector are usually not enough to reconstruct distance to the vertex. If a signal with SNR > 2.5 is available from one more chan-

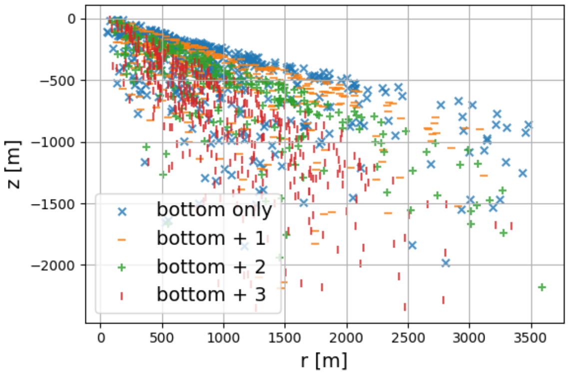

Fig. 9 Distribution of shower locations relative to the detector station for events that have signals with SNR > 2.5 only for the channels at $\sim$100 m depth and for 1, 2, or 3 of the other channels on the *power string* as well. For better readability, only every second event is drawn.

nel (typically the antenna at 80 m), the distance reconstruction is already good enough for the uncertainty on the signal attenuation to be better than a factor of 2. Additional channels improve the results even further.

Fig. 9 shows the distribution of vertex locations grouped per number of channels with a signal. The figure shows that rather than simply distance, the vertex location most prominently determines which of the upper channels detect a signal, as the vertex may simply be in the shadow zone for the channels further up. The shower energy plays a role as well, because channels at different depths will see the shower at slightly different viewing angles. So at least some of them have to be further off the Cherenkov angle and require a larger shower energy for the radio signal to still be strong enough to be detected. Additionally, showers with lower energies need to be closer to the station to be detectable, translating into larger differences between viewing angles. Fig. 10 shows the fraction of events falling into each of these categories as a function of energy relative to all triggered events. It also shows the probability for a DnR pulse to be detected by at least one channel, which greatly improves the vertex reconstruction (see Fig. 11 in comparison to Fig. 8). It shows an even greater dependence on shower energy, because the differences in viewing angles are larger between DnR signals than between channels. This makes the aforementioned effects even more significant, so that DnR pulses only become relevant at higher energies. One should keep in mind, however, that these efficiencies do not include the efficiency of identifying a neutrino event in the first place. Also, the phased array trigger is approximated with a simple threshold and some aspects of RNO-G, e.g. the noise level, are not yet confirmed by data at the time of writing.

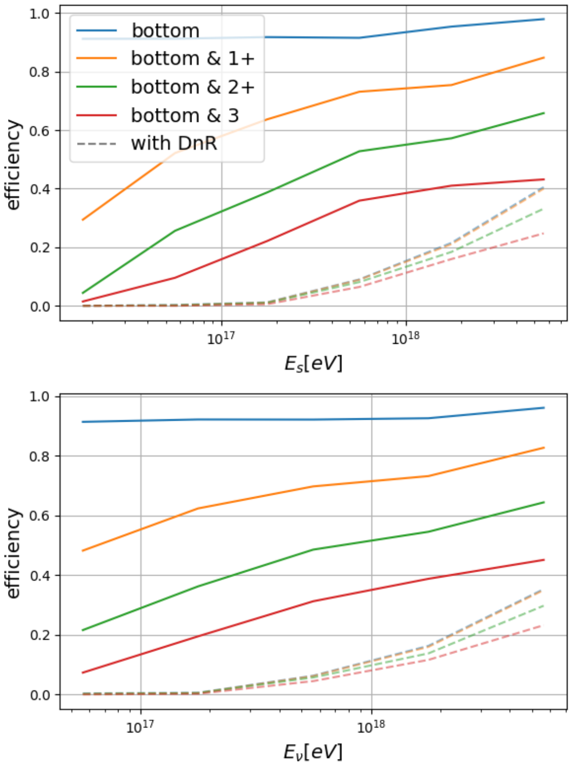

Fig. 10 Reconstruction efficiency based on a simplified trigger simulation. Probability for an event to have at least one channel with SNR > 2.5 in one of the channels at $\sim$100 m depth and to have SNR > 2.5 in the additional channels on the *power string* as well, as a function of shower energy (top) and neutrino energy (bottom). The dotted lines show the probability that at least one channel detected a second pulse that also has SNR > 2.5.

4 Electric field reconstruction

Next to the vertex distance, we need to reconstruct the electric field of the radio signal from the recorded voltage waveforms. The Vpol and Hpol antennas are almost exclusively sensitive to the $\vec{e}_\theta$ or $\vec{e}_\phi$ components of the electric field, so in principle one could simply divide the spectrum of the voltages by the response of antenna and amplifier in the frequency domain to obtain the spectrum of the electric field. Unfortunately, this method requires signals to have a large SNR. Especially if the antenna has a relatively low sensitivity, as is the case for the Hpol antennas, thermal noise can be amplified and distort the result.

Instead, we use a method based on *Information Field Theory* [54, 55], which allows us to reconstruct even low-SNR events by including prior knowledge about the properties of the radio signal. This method is described in detail in [56], where RNO-G is also given as an application example. Therefore we will only give a brief description of the method here.

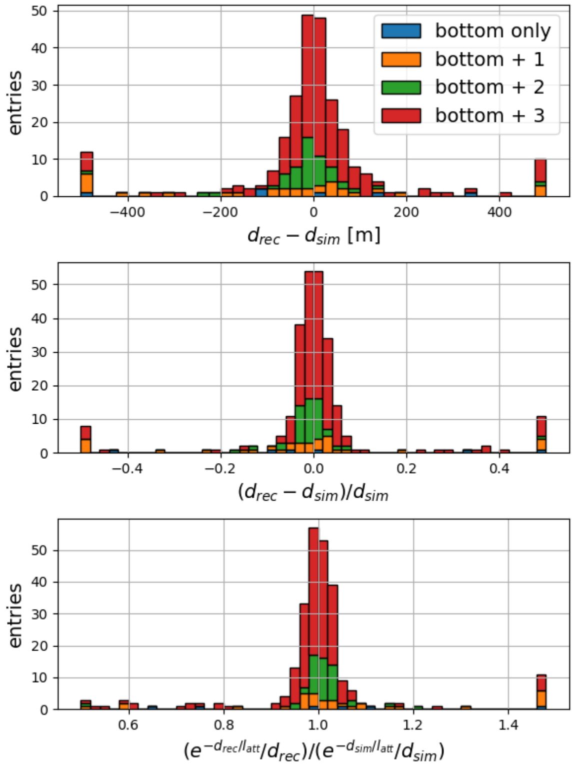

Fig. 11 Stacked histograms showing the performance of the vertex reconstruction for events where at least one channel detected two radio signals (DnR) with SNR > 2.5. Top: Difference between reconstructed and actual distance from station to shower. Middle: Relative uncertainty on the distance reconstruction. Bottom: Ratio of reconstructed and actual attenuation of the radio signal on its way from shower to detector. Events are divided into the same categories as in Fig. 8, but a much smaller subset of events (see Fig. 10) shows DnR signals.

4.1 Electric field reconstruction method

The problem of electric field reconstruction can be thought of as determining $P(\mathcal{E}|U)$, the probability of the radio signal having a given frequency spectrum $\mathcal{E}$, given the measured voltages U, defined in the time domain, and finding the most likely electric field. Using Bayes' theorem, this probability can be calculated using

$$P(\mathcal{E}|U) \propto P(\mathcal{E})P(U|\mathcal{E}), \tag{7}$$

if the prior probability $P(\mathcal{E})$ for the spectrum and the probability $P(U|\mathcal{E})$ for the measured voltages given a specific frequency spectrum are known.

We split the frequency spectrum into its absolute value and a phase

$$\mathcal{E}(f) = E(f) \cdot \exp(i \cdot \varphi(f)) \tag{8}$$

and model each component separately.

The absolute value of the frequency spectrum is modeled using a generative process

$$s(f) = \lg(E(f)) \tag{9}$$

$s(f)$ follows Gaussian statistics, with a correlation structure which is defined by its eigen-spectrum $\tau(k)$, which follows a power-law $\tau \propto k^{-\alpha}$, where k is the wave number[3], though small deviations from that are allowed. The slope $\alpha/2$ determines the smoothness of the electric field spectrum: A large value for α means only small k in the eigenspectrum of $s(f)$, leading so a very smooth $s(f)$, which becomes more and more jagged with decreasing α, as larger k become more likely. We choose a value for $\alpha/2$ that results in a rather smooth electric field spectrum, but leave the parameter some freedom to vary, should the data suggest a more jagged spectrum. With this, we can assign a prior probability to any $E(f)$, because the probability distribution of $s(f)$ is defined.

The phase is modeled by a linear function

$$\varphi(f) = \varphi_0 + mf \tag{10}$$

where φ_0 and m are Gaussian random variables. Such a phase leads to a single, short pulse, as is expected from an Askaryan signal. The slope m corresponds to a time shift in the time domain and is set based on the previously determined signal timing. It is, however, given some room to vary within a few nanoseconds, to correct for possible errors in determining the pulse time.

Finally, the polarization of the radio signal is described by a parameter ϕ_{pol} called *polarization angle*, so that

$$\vec{\mathcal{E}}(f) = \mathcal{E}(f) \cdot \cos(\phi_{\text{pol}}) \cdot \vec{e}_\theta + \mathcal{E}(f) \cdot \sin(\phi_{\text{pol}}) \cdot \vec{e}_\phi \tag{11}$$

The polarization angle is also modeled as a Gaussian random variable, but with a standard distribution chosen large enough to only have a negligible effect on the posterior distribution.

From equations 8-11, we can construct an operator that maps s, φ_0, m and ϕ_{pol} onto $\mathcal{E}(f)$. This operator is invertible, which allows us to assign a prior probability to any $\mathcal{E}(f)$. To do so, we calculate the values for $s(f)$, φ_0, m and ϕ_{pol} that lead to the given $\mathcal{E}$. Because the prior probabilities for these variables are known, and assumed to be independent of each other, we can calculate their joint probability

$$\begin{aligned} P(\mathcal{E}) &= P(s, \varphi_0, m, \phi_{pol}) \\ &= P(s) \cdot P(\varphi_0) \cdot P(m) \cdot P(\phi_{pol}) \end{aligned} \tag{12}$$

---

[3] Technically, since $E(f)$ is defined in the frequency domain, k is defined in the time domain. We will ignore this subtlety here and use the notation that is most commonly used to describe the correlation structure.

as the product of the individual probabilities.

The antenna and amplifier responses are applied to the electric field, which can be expressed in the frequency domain by a diagonal matrix $\mathcal{D}$. Then the result is translated into the time domain via a Fourier transformation $\mathcal{F}$ to obtain the expected voltage waveform $U(t) = \mathcal{F}\mathcal{D}\mathcal{E}(f)$. Neglecting uncertainties on the detector description and signal model, the difference between the expected and measured waveforms must be due to the noise N:

$$\begin{aligned} P(U|\mathcal{E}) &= P(N = U - \mathcal{F}\mathcal{D}\mathcal{E}) \\ &= \mathcal{N}(U - \mathcal{F}\mathcal{D}\mathcal{E}|0, \sigma_N) \end{aligned} \tag{13}$$

where the last term expresses the assumption that the noise is drawn from a Gaussian distribution centered around 0 V with a standard deviation of σ_N, which can be determined from forced trigger data. With this, the maximum of Eq. 7 can be determined using Metric Gaussian Variational Inference [57].

A strength of this method is that it only makes some general and well-founded assumptions about the properties of the radio signal. Considering that no experiment has yet detected a neutrino via its Askaryan emission, not relying on any physical model for the electric-field reconstruction is an advantage in itself, as it allows us to verify emission models by comparing the reconstructed electric field spectra to predictions.

The reconstruction method requires the radio signal received by all channels to be very similar, which is the case if the antennas are close enough together. How much the radio signal differs between channels depends very much on the event geometry, which is not known at this point, except for the vertex position. Thus, there are three groups of channels that can be used to reconstruct the electric field, assuming they detected a radio signal: The phased array channels along with the two Hpol antennas directly on top of them, and the three channels at the bottom of each helper string. In principle, the electric field could also be reconstructed for the other channels on the *power string*, but since they do not have any nearby Hpol antennas, it would have to be limited to the $\vec{e}_\theta$ component. It is also unlikely that a single channel will yield a better reconstruction than a group of three or six, so these channels are not used for the electric field reconstruction.

4.2 Performance of the electric field reconstruction

To asses the performance of the electric field reconstruction, we continue from the vertex reconstruction in Sec. 3.3.

In order to reconstruct the electric field of the radio signal, it is first necessary to identify which channels actually recorded a signal with a sufficiently high SNR. Only a tiny fraction of the radio signals that trigger RNO-G are actually from neutrinos, while the vast majority will come from thermal fluctuations or other radio sources in the environment. How to identify the few genuine neutrino events is its own topic, so here we assume that some method to do so is available. We can safely assume this is the case, as a proper event identification is necessary before an energy reconstruction could even start. We already used SNR = 2.5 as the analysis threshold, so we assume that if a pulse has SNR ≥ 2.5 in any channel, it can be identified and we just use the true pulse position as input. If a pulse is found, a region of ±50 ns around it is marked as a *signal region*. It should be noted that this only serves to mark the relevant section of the waveforms for the electric field reconstruction and no further information from this pulse finder is used. Any pulse with a lower SNR is classified as not found. As before, the maxima and minima are calculated from the noiseless waveforms for the purpose of calculating the SNR.

Next, we need to identify the directions from which the radio signals are received at each antenna. Using the reconstructed vertex position, we can calculate the expected signal propagation times for each ray path. With the template correlation method used for the vertex reconstruction, the signal arrival time is determined and compared to the expectation for each ray tracing solution to identify the most likely ray path. Once the correct ray tracing solution is found, the signal arrival direction and time shift relative to the other antennas can also be determined. This is done for every signal region. However, for most events, the Hpol channels will not detect a signal with a sufficiently high SNR to identify a signal region. In order to be able to use them for the electric field reconstruction, a linear function is fitted to the arrival times and zenith angles[4] as a function of depth of the Vpol antennas on the same string as the Hpol. This function is then used to extrapolate these values for the Hpol antennas. While this approach assumes a planar wave front, it is accurate enough for antennas that are spaced as closely as in this case.

As discussed above there are three groups of channels for which the electric field can be reconstructed: The phased array along with the two Hpol antennas directly above it, and the antennas on each of the helper strings. In principle, the phased array has twice the number of channels and is, thus, most promising to use for reconstructing the radio signal. However, depending on the event geometry, the SNR can vary greatly

---

[4] The azimuth is the same for all antennas on the same string.

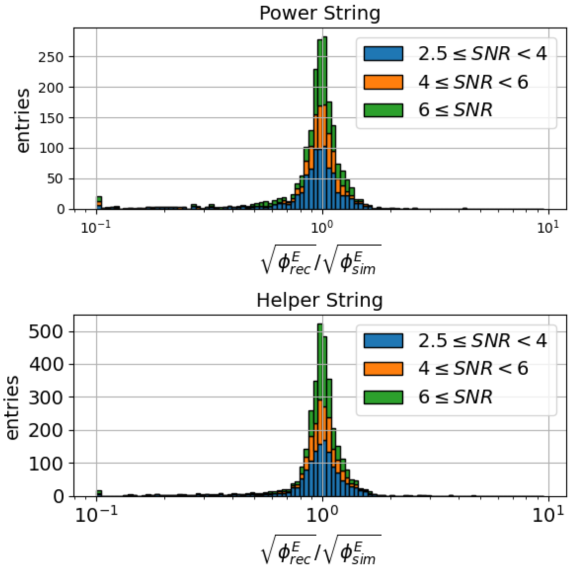

Fig. 12 Ratio between the square root of the energy fluence of the reconstructed and the actual radio signal detected at the power string (top) and the two helper strings (bottom). Results are divided into categories by the maximum signal-to-noise ratio of the channels used for the reconstruction. The outermost bins are overflow bins.

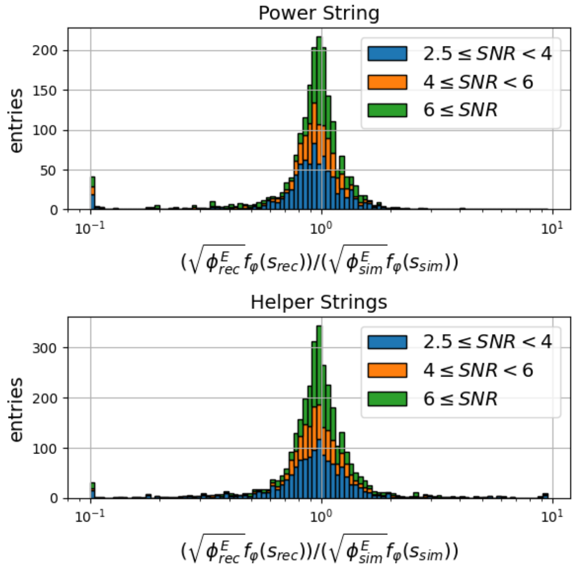

Fig. 13 Ratio of the square root of the energy fluence multiplied with the correction factor $f_\varphi(s)$ for the viewing angle defined in Eq. 4 calculated from the reconstructed and the actual radio signal at the power string (top) and each of the two helper strings (bottom). For events where $s > 10$, $f_\varphi(s')$ was used instead. Events are divided into categories by the maximum signal-to-noise ratio of the channels used in the reconstruction. The outermost bins are overflow bins.

	$2.5 \leq$ SNR < 4	$4 \leq$ SNR < 6	$6 \leq$ SNR
$\sqrt{\phi^E}$	Power String		
median σ_{68}	0.98 [0.79, 1.17]	0.96 [0.79, 1.08]	0.99 [0.85, 1.14]
$\sqrt{\phi^E} f_\varphi(s)$			
median σ_{68}	0.94 [0.71, 1.17]	0.93 [0.74, 1.08]	0.98 [0.76, 1.18]
$\sqrt{\phi^E}$	Helper Strings		
median σ_{68}	1.02 [0.85, 1.17]	1.00 [0.87, 1.10]	1.01 [0.88, 0.14]
$\sqrt{\phi^E} f_\varphi(s)$			
median σ_{68}	0.98 [0.73, 1.33]	0.97 [0.74, 1.28]	1.01 [0.85, 1.26]

Table 3 Median and 68% quantiles σ_{68} of the ratios between reconstructed and actual square root of the energy fluence shown in Fig. 12, as well as between the energy estimators $\sqrt{\phi^E} f_\varphi(s)$ calculated from the reconstructed and the actual electric field shown in Fig. 13. Shown are results for the channel groups at the bottom of the power string and of the helper strings, as well as for different maximum SNRs.

between strings. Therefore, we reconstruct the electric field for all channel groups (provided a *signal region* was found).

The performance of the electric field reconstruction with regards to the energy fluence ϕ^E of the radio signal is shown in Fig. 12. Except for a few outliers, which were shown to be easily identifiable in [56], the energy fluence is well-reconstructed, with the 68% quantiles at about 20% or better, even for low-SNR events, as shown in Tab. 3. Interestingly, the reconstructions using *helper strings* perform roughly as well as using the *power string*, even though only half as many channels are available.

In addition to the energy fluence, the shape of the electric field spectrum, expressed by the parameter s (see Eq. 3), is also needed to correct for the effect of the viewing angle (see Eq. 4). Fig. 13 shows the ratio of the energy estimator $\sqrt{\phi^E} f_\varphi(s)$ calculated from the reconstructed and from the true electric field spectrum. To reconstruct the shower energy, these still have to be corrected for propagation effects, which will be done in the next section. Because the attenuation length in ice is frequency dependent, correcting for attenuation will change the shape of the frequency spectrum as well, but this effect is small. Therefore, Fig. 13 gives an estimate of the uncertainty on the shower energy due to the electric field reconstruction. Looking at the 68% quantiles of the energy estimator compared to the energy fluence alone (see Tab. 3), the viewing angle correction $f_\varphi(s)$ increases the total uncertainty relatively little. This is because the expression in Eq. 4 is a function of the logarithm of s, so changes to s have a smaller impact.

5 Shower energy reconstruction

All information can now be combined to reconstruct the shower energy. First, a correction for the attenuation of the radio signal on its way from the shower to the station is needed. With the location of the shower known, the ray tracing can be redone to determine the path of the radio signal. Because the attenuation length changes with depth and frequency, the path loss $\mathcal{L}(f)$ is defined in the frequency domain using

$$\mathcal{L}(f) = \exp\left(-\int \frac{1}{l_{\text{att}}(\vec{x}, f)} ds\right) \tag{14}$$

by integrating over the ray path. $l_{\text{att}}(\vec{x}, f)$ is the depth- and frequency-dependent attenuation length. With this, we calculate the frequency spectrum of the electric field corrected for propagation effects as

$$\mathcal{E}_0(f) = \mathcal{E}(f)/\mathcal{L}(f)/\left(\frac{l}{l_{\text{ref}}}\right) \tag{15}$$

where l is the length of the ray path from the interaction vertex to the detector and l_{ref} the reference distance for which the parametrization Eq. 4 was calculated, in our case 1 km.

After these corrections the shower energy can be calculated from Eq. 4. Reconstructed electric fields are available from all three strings for 60% of events, while for 22% of the cases the reconstruction can use two of the strings. Just for 18% of the events the electric field can be reconstructed for one string only. If more than one field reconstruction is available, the shower energy is calculated per electric field and the final result is calculated as the mean of the energies.

5.1 Performance of the shower energy reconstruction

The results of the reconstruction of the shower energy are shown in Fig. 14. An energy resolution of better than a factor of 2 is achieved, if at least one of the channels of the *power string* above the phased array detected a pulse of SNR $\geq$ 2.5 and improves further if at least 2 additional channels are available. Unsurprisingly, the energy reconstruction works better for hadronic showers than for events from charged-current interactions of electron neutrinos, where potentially interfering hadronic and electromagnetic shower are present. The 68% quantiles on the $\lg(E_{\text{sh}}^{\text{rec}}/E_{\text{sh}}^{\text{sim}})$ is $[-0.15, 0.18]$ with the 1 channel cut and $[-0.13, 0.12]$ with the 2 channel cut. On a linear scale the 68% quantiles of $E_{\text{sh}}^{\text{rec}}/E_{\text{sh}}^{\text{sim}}$ are $[0.58, 1.66]$ and $[0.65, 1.49]$, respectively. The uncertainty is smaller for events that only produce a hadronic shower, with a 68% quantiles of $[0.70, 1.54]$ and $[0.74, 1.34]$, while for events that produce both a hadronic and an electromagnetic shower it is $[0.47, 1.86]$ and $[0.57, 1.63]$ for the 1 channel and the 2 channels cuts, respectively.

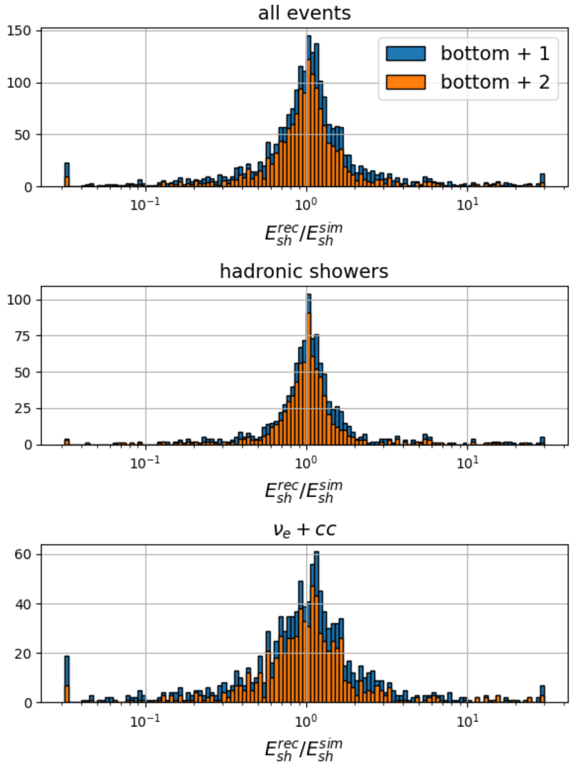

Fig. 14 Ratio between reconstructed and actual shower energy for all events (top), hadronic showers (middle) and charged-current interactions of electron neutrinos (bottom). Shown are results of events where at least one of the channels at ∼100 m as well as at least one (blue) or at least two (orange) of the other channels on the *power string* detected a signal with SNR$\geq$ 2.5. The outermost bins are overflow bins.

The energy resolution as a function of neutrino energy is shown in Fig. 15, along with Fig. 16 showing the statistical power of each energy bin. For hadronic showers, the relative uncertainty decreases with increasing energy, which is not the case for the events with electromagnetic showers. Especially if at least 2 of the channels above the phased array have a signal with SNR $\geq$ 2.5, the reconstruction tends to underestimate for shower energies above $\sim 1 \times 10^{18}$ eV. This is roughly the energy where the LPM effect starts to have a strong impact on the radio signal from the electromagnetic shower. This effect is already visible in Fig. 2, but another effect is relevant here as well: Because the electromagnetic shower is elongated, but the hadronic one is not, their maxima may be seen at different viewing angles, so that only one of the radio signals is detected, while the other falls below the noise level. In that case, we are practically only reconstructing the energy of one of the

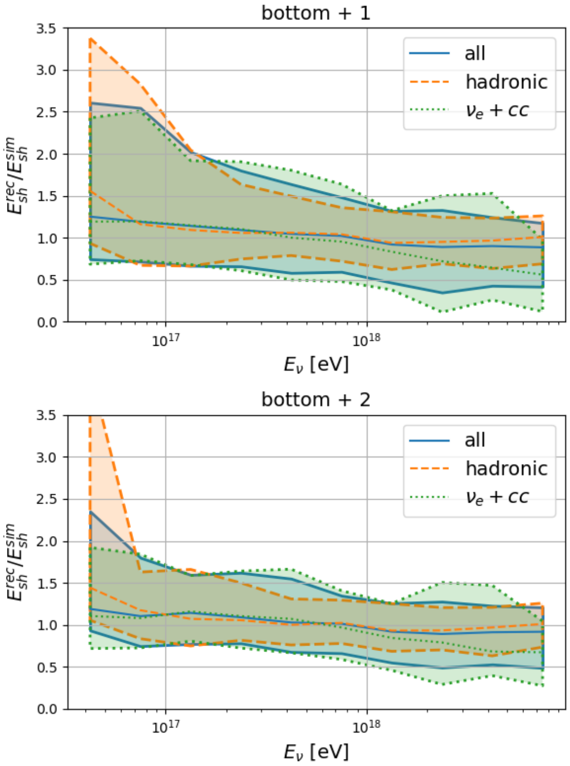

Fig. 15 Median and 68% quantiles of the ratios between reconstructed and actual shower energies as function of neutrino energy. The results are shown for events that only produced a hadronic showers, as well as for charged-current interactions of electron neutrinos. The top panel shows events where at least one of the channels at ∼100 m detected a pulse with SNR ≥ 2.5 as well as at least one of the other channels on the *power string*, the bottom panel shows results with at least two additional channels on the *power string*.

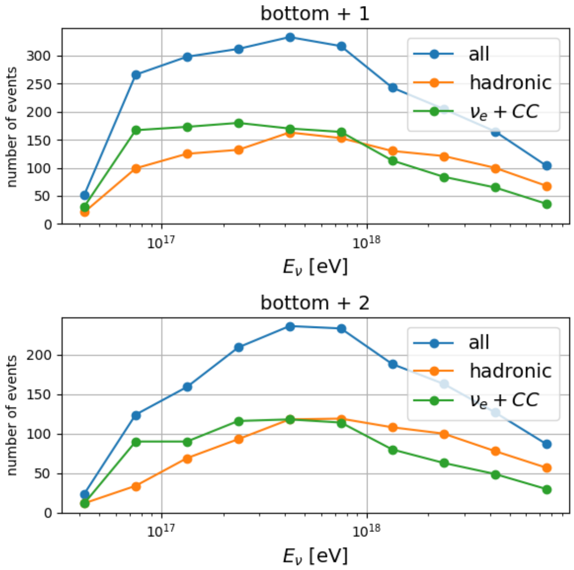

Fig. 16 Number of events contained in each of the energy bins in Fig. 15. Events are divided into the same categories as explained in Fig. 15

subshowers. If the energy further increases, the electromagnetic shower will consist of multiple spatially displaced sub showers [39]. Then, only the energy of one of the sub showers might be reconstructed which further complicates the reconstruction. As we are still defining the true shower energy as being equal to the neutrino energy for these events, this causes the $E_{\mathrm{sh}}^{\mathrm{rec}}/E_{\mathrm{sh}}^{\mathrm{sim}}$ to decrease for these events.

5.2 Influence of systematic uncertainties

So far, we have assumed a perfectly calibrated detector without any experimental uncertainties except for interference with thermal noise. This is not achievable in reality. At the time of writing, RNO-G is in its first deployment season, which of course means that no in-situ calibration data is available. A thorough estimation of systematic uncertainties will only be possible later when the performance of RNO-G is tested in the field. Instead, we will explore common sources of systematic uncertainties to estimate what uncertainties on the detector performance would be acceptable for the energy resolution to remain useful. In particular, the three most important uncertainties are the antenna response, timing uncertainties between different channels, and the index of refraction of the ice.

The antenna responses for RNO-G have been carefully simulated, but in-situ calibration of the antennas after deployment is challenging. Calibration campaigns to verify the simulated antenna responses are planned for future deployment seasons, but some uncertainty is unavoidable. The same is true for the response of the amplifiers or any other element of the signal chain. However, as these have been calibrated in the lab before deployment, mimicking the situation in the field, the antenna uncertainties are expected to be larger than the uncertainties on the amplifier response. By assuming uncertainties on the antenna response and investigating the effect it has on the energy reconstruction, we can estimate the required accuracy with which the antennas will have to be calibrated. We will consider two primary ways for the antenna response to affect the result: A wrong overall amplitude, or a wrong shape of the antenna response.

If the overall amplitude of the antenna response is wrong, the consequences are straightforward: $\sqrt{\phi_{\mathrm{rec}}^{E}}$ is proportional to the amplitude of the antenna response, and also proportional to the energy estimator. This means the relative uncertainty on the amplitude of the antenna response simply propagates linearly onto the reconstructed energy. More problematic are differences in overall scale between antennas. However, since

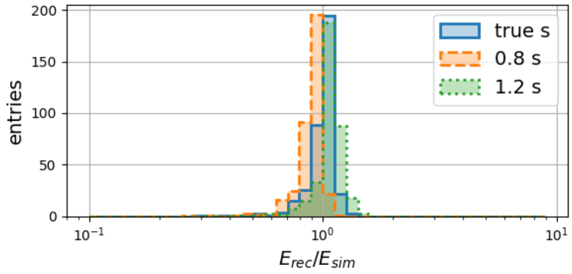

Fig. 17 The estimated shower energy according to Eq. 4, calculated for the radio signals from simulated hadronic showers using the true s parameter (blue, solid) and an s parameter that is under- (orange) or overestimated (green) by 20%.

great care has been taken to produce uniform antennas, we will not discuss this uncertainty at this point without in-field data to suggest large differences. Other radio-based detectors have demonstrated antenna calibrations at the 10% level [58], so we do expect to be able to obtain a similar performance. It should also be noted that systematic differences between Hpol and Vpol antennas can introduce uncertainties in the reconstruction of the electric field, similarly to an overall amplitude mismatch.

An incorrect shape of the antenna response is hard to quantify, but can be assessed qualitatively. In [56] it is shown that Information Field Theory can still reconstruct the electric field if there are uncertainties on the shape of the antenna response, as well as uncertainties on the phase of the antenna and signal chain, but the same difference will show up in the shape of the reconstructed electric field spectrum. This means that as a consequence the reconstructed slope parameter s (see Eq. 3) would be affected. To see what an uncertainty on s would mean for the reconstructed energy, we generate radio signals from simulated hadronic showers, in the same way as was done to create Fig. 2. Then we determine Φ_E and s and use it to estimate the energy using Eq. 4, but after applying an error to s. Even assuming a 20% uncertainty on s from the antenna response, Fig. 17 shows that it has only a very small influence on the reconstructed shower energies, only shifting the mean of the $E_{\text{rec}}/E_{\text{sim}}$ distributions by -0.05 and 0.04 compared to using the true s. While the uncertainties on the antenna responses that RNO-G will have is unknown at this point, these results provide guidance to what precision the detector needs to be calibrated.

Uncertainties on the timing can be caused by delays in the signal chain that are unaccounted for. These can be reduced by careful calibration before deployment and are expected to be very stable in time. A more severe cause of uncertainties is due to the position of the antennas, either because of the leeway on their exact position within their hole or because of some tilt of the hole itself. This would have the same effect as an uncertainty on the timing, because the radio signal arrives at a different time from what is expected for the assumed antenna positions. To simulate this we shift the waveforms of each channel by a random offset drawn from a normal distribution with a standard deviation of $\sigma_t = 0.3$ ns and redo the energy reconstruction. The ARA collaboration has shown a timing calibration to around 0.1 ns or better [59], so this is a rather pessimistic assumption. Comparing the resulting energy reconstruction (Fig. 18) to Fig. 14 we see that the number of outliers is increased, especially if only one of the channels above the phased array detected a radio signal. Most events still remain little affected and the 68% quantiles on $\lg(E_{\text{sh}}^{\text{rec}}/E_{\text{sh}}^{sim})$ only grow from $[-0.16, 0.18]$ to $[-0.19, 0.20]$ or from $[-0.13, 0.12]$ to $[-0.17, 0.14]$ with the 1 or 2 channel cut, respectively.

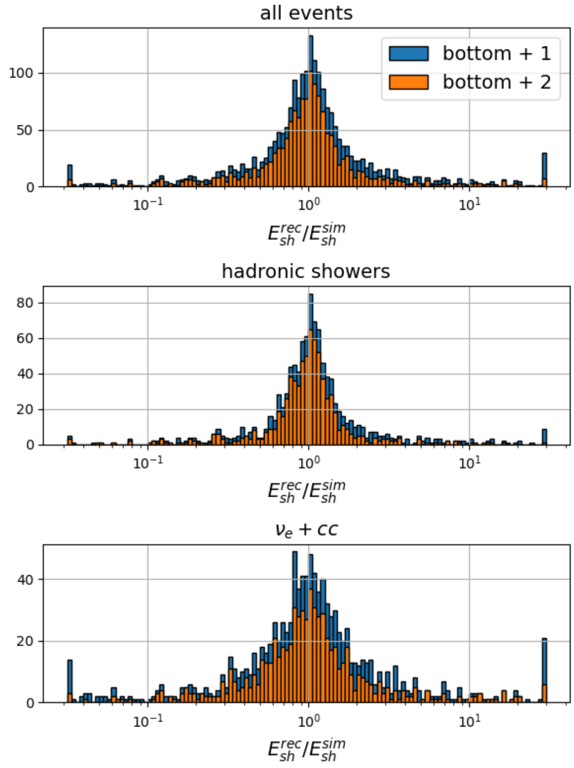

Fig. 18 Ratio between reconstructed and actual shower energy if a random time offset drawn from a normal distribution with $\sigma_t = 0.3ns$ is applied to each channel. Shown are results of events where at least one of the channels at ∼100 m as well as at least one (blue) or at least two (orange) of the other channels on the *power string* detected a signal with SNR$\geq$ 2.5. The outermost bins are overflow bins.

Finally, we consider uncertainties on the index of refraction of the ice. A profile of the index of refraction as a function of depth of the ice near Summit Station has been developed [47], but only to a depth of 120 m.

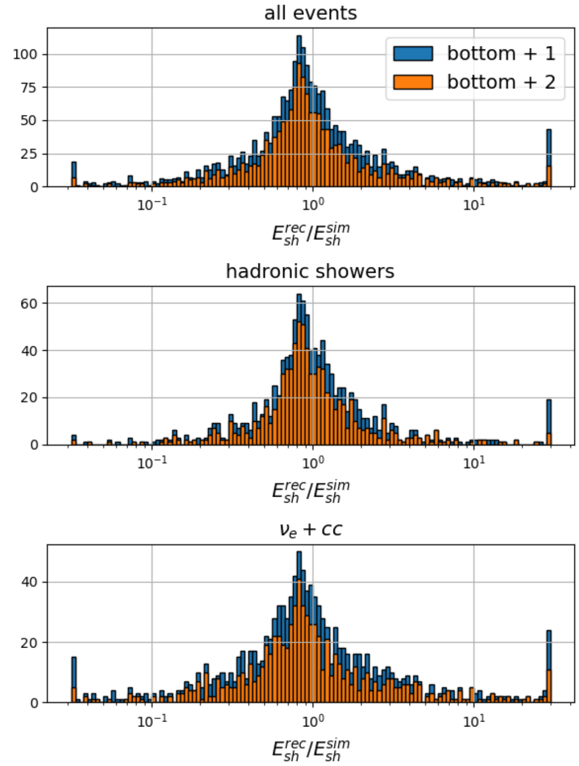

Fig. 19 Ratio between reconstructed and actual shower energy if the index of refraction models used for simulation and reconstruction differ. Shown are results of events where at least one of the channels at ∼100 m as well as at least one (blue) or at least two (orange) of the other channels on the *power string* detected a signal with SNR ≥ 2.5. The outermost bins are overflow bins.

In the future, dedicated measuring campaigns will develop a profile for the entire detection volume, as it has been done in other places. A compilation of index of refraction measurements at various places in Antarctica can be found at [46] along with the parameters for the parametrization in Eq. 5. To assess the effect that uncertainties of these measurements have on the energy reconstruction, we rerun the Monte Carlo simulations, but change the Δ_z parameter of the index of refraction profile from the original value of $\Delta_z = 0.51$ to $\Delta_z = 0.50$ and the z_0 parameter from 37.25 m to 36.25 m. We then rerun the entire energy reconstruction assuming the original values of Δ_z and z_0. Both of these assumed uncertainties are similar to those shown in [46].

Fig. 19 shows the impact that ice model uncertainties have on the reconstructed energy, resulting in 68% quantiles of $[-0.29, 0.28]$ and $[-0.27, 0.23]$ on $\lg(E_r/E_s)$ for the 1 channel and 2 channel cuts, respectively. This means uncertainties on the index of refraction profile of the ice can have a significant impact on the energy reconstruction and careful calibration measurements will be required. For completeness, it should be mentioned that this study does not yet account for other potential ice effects such as birefringence or layers in the ice, as discussed in [60]. However, information about these effects on radio emission in the ice at Greenland are currently not quantifiable beyond speculation, which is why we chose to exclude them at this point.

6 Neutrino energy

If a neutrino interacts in the ice, only a certain fraction of its energy will be transferred to the nucleon it interacted with, while the rest remains with the neutrino (in the case of neutral current interactions) or the charged lepton created (in the case of charged current interactions). This fraction is randomly distributed and can typically not be measured for a given event, so it represents an irreducible uncertainty on the achievable energy resolution of any neutrino detector. In the case of an electron neutrino interacting via charged current interaction (referred to as a ν_e+CC event), the electron initiates a shower as well, so that the entire neutrino energy ends up in the two showers. Measuring both showers results in a reduction of the uncertainty on the neutrino energy, which could exploited if such events could be uniquely identified. So far, no method to do so has been developed, so we will not discuss this option here. Instead, we treat all cases together where a shower energy has been reconstructed as described above.

We can use Bayes' theorem to estimate the probability $p(E_\nu|E_r)$ for the neutrino to have an energy E_ν given that the energy of the shower was reconstructed to be E_r. Since the energies in question are distributed over several orders of magnitude, it is convenient to think about the problem in terms of the base 10 logarithm $\lg(E)$ and we thus get:

$$p(\lg(E_\nu)|\lg(E_r)) = \frac{p(\lg(E_r)|\lg(E_\nu)) \cdot p(\lg(E_\nu))}{p(\lg(E_r))} \tag{16}$$

If we know that neutrinos follow a given spectrum S, the energy distribution of neutrinos interacting in the detector volume is given by

$$p(\lg(E_\nu)|S) = \frac{\varPhi_\nu(E_\nu)/\lambda_\nu(E_\nu) \cdot E_\nu}{\int_{E_-}^{E_+} \varPhi_\nu(E'_\nu)/\lambda_\nu(E'_\nu) \cdot E'_\nu \cdot dE'_\nu} \tag{17}$$

where $\varPhi_\nu$ is the neutrino flux and λ_ν is the interaction length. The E_ν term comes from the Jacobian when transforming from E_ν to $\lg(E_\nu)$. The problem now is that no neutrino has been detected at these energies yet, so we cannot know the spectrum. Instead, we have to consider a range of spectra S, to each of which we

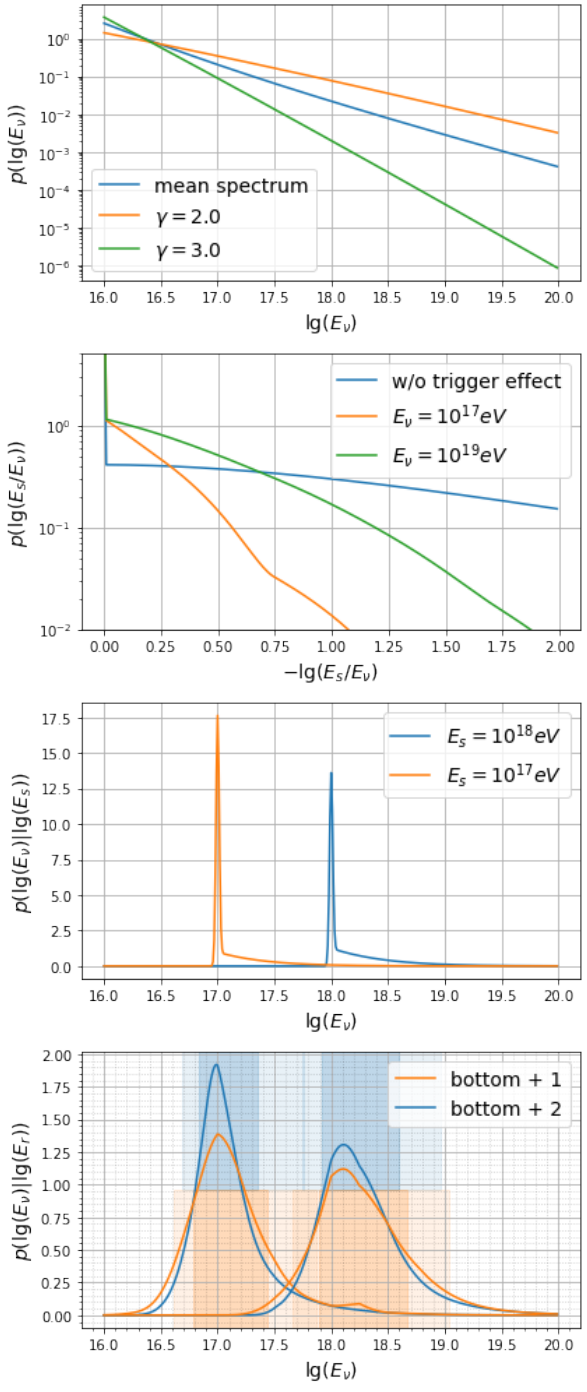

Fig. 20 Top: Energy distribution of neutrinos interacting in the detector volume assuming a power law spectrum with specific indices (green, orange) and over a distribution of spectra (blue). Second row: Distribution of the fraction of the neutrino energy that goes into the shower for neutrino-nucleon interactions (blue) and the distribution when trigger efficiencies are included (orange, green). Third row: Probability for a shower with a given energy to have been generated by a neutrino with energy E_ν. Bottom: The same distribution as above, but assuming an uncertainty on the reconstructed shower energy. The shaded regions mark the 68% and 90% quantiles of the distributions.

assign a prior probability $p(S)$. Then we can calculate the expected neutrino energy spectrum using:

$$p(\lg(E_\nu)) = \int_{S_-}^{S_+} p(\lg(E_\nu)|S) \cdot p(S) dS \qquad (18)$$

What spectra are considered possible or even probable has to be based on our prior knowledge and is of course very subjective. For our calculations, here, we assume a power law spectrum

$$\Phi_\nu(E_\nu) \propto E_\nu^{-\gamma} \qquad (19)$$

where the spectral index is equally likely for all values $2 < \gamma < 3$. The resulting neutrino energy distribution is shown in Fig. 20, (top).

It is of course possible that a single power-law cannot describe the neutrino flux, especially across the entire energy range. It seems probable, for example, that a power-law from an astrophysical flux at PeV energies will be dominated by a cosmogenic flux [22], not following a power-law, at EeV energies.

For the sake of clarity, we will only discuss generic power law spectra here, as extrapolation of the neutrino flux detected by IceCube. Still, we have tested a cosmogenic neutrino flux and even different spectral indices (see [61] for details) and have found the results to be very similar. The code used for these calculations is available online [62] and allows one to test other spectral models. We also note that ultimately, the goal is to obtain a neutrino energy spectrum rather than a single event energy. For this an adapted, iterative approach will certainly be useful.

For events that only produce a hadronic shower, the fraction of the neutrino energy that goes into the shower is given by the inelasticity y. It should be mentioned that the inelasticity distribution carries uncertainties. The inelasticity has only been measured experimentally to TeV energies [63] and at even higher energies, aspects such as nuclear modifications to neutrino cross-sections [64] or electromagnetic contributions, subdominant to deep-inelastic scattering [65,66] may become relevant. We ignore the uncertainties for the purpose of this paper and use the inelasticity distribution as implemented in NuRadioMC [39] based on [67,68,69].

If an electron neutrino undergoes charged current interaction, all the energy ends up in the two showers produced, so that effectively $E_s = E_\nu$. For a neutrino event whose flavor and interaction type we do not know, we can combine these two scenarios with

$$p(\lg(\frac{E_s}{E_\nu})) = p(\lg(\frac{E_s}{E_\nu})|h) \cdot P(h) + p(\lg(\frac{E_s}{E_\nu})|e) \cdot P(e) \quad (20)$$

where $p(\lg(\frac{E_s}{E_\nu})|h) = p(\lg(y))$ is the $\frac{E_s}{E_\nu}$ distribution assuming only a hadronic shower was produced, which is equal to the inelasticity distribution, and $p(\lg(\frac{E_s}{E_\nu})|e) = \delta(\lg(\frac{E_s}{E_\nu}))$ assuming an electromagnetic shower was produced as well. The probability $P(e) = 1 - P(h) = \frac{1}{3} \cdot 0.71$ for this is the probability for the neutrino flavor being ν_e, assuming equal mixing, times the probability for it to undergo a charged current interaction. One can simply update this probability in case additional information about the interaction type is reconstructed.

While this is the distribution for showers produced in the ice, it is not necessarily the distribution for the showers that are detected, because events with large $\frac{E_s}{E_\nu}$ have a higher chance of triggering the detector. Therefore the probability $p_T(E_s)$ for a shower with a given energy to trigger the detector needs to be included[5]. This trigger probability is different for the two event types, especially at higher energies when the radio signal is affected by the elongation of the electromagnetic shower from the LPM effect. Considering these effects, we get

$$p(\lg(E_s)|\lg(E_\nu)) = \delta(\lg(\frac{E_s}{E_\nu})) \cdot p_T(E_s|e) \cdot P(e) + p\left(\lg(y) = \lg(\frac{E_s}{E_\nu})\right) \cdot p_T(E_s|h) \cdot P(h) \tag{21}$$

Including the trigger efficiency shifts the $\frac{E_s}{E_\nu}$ distribution towards larger $\frac{E_s}{E_\nu}$ (see Fig. 20, second row). This effect is much stronger at low energies, where the trigger efficiency falls off faster towards lower shower energies.

At this point, we could calculate $p(\lg(E_\nu)|\lg(E_s))$ using the mean spectrum from Fig. 20, top and the $\frac{E_s}{E_\nu}$ distributions, to get the best possible neutrino energy resolution if we were able to reconstruct the shower energy perfectly (Fig. 20, third row). Properly quantifying this best-case energy resolution is made difficult by the delta distribution from the ν_e+CC events, so we apply a small uncertainty on the shower energy of 2% here. The uncertainty is small enough to conserve the shape of the $p(\lg(E_\nu)|\lg(E_s))$ distribution, but it removes the jump when integrating over the probability density. Thus, we can calculate the 68% quantiles for the two example distributions, which are $[16.99, 17.08]$ and $[17.99, 18.21]$. Although the distribution is sharply peaked at the shower energy and falls off quickly, it has long tails. The reason for the higher peak and the smaller uncertainty quantiles at 1×10^{17} eV compared to 1×10^{18} eV is the reduced trigger efficiency of ν_e+CC events at high energies. From this plot we see that even with a perfect shower energy reconstruction, the neutrino energy resolution would be limited.

The obtainable shower energy resolution is energy-dependent and also different for ν_e undergoing charged current interactions as shown in Fig. 15. Similarly to that plot, we determine the median and the 68% quantiles for $\lg(E_r/E_s)$ as a function of the shower energy. We approximate $p(\lg(E_r)|\lg(E_s))$ as a normal distribution $\mathcal{N}(\lg(E_r/E_s)|\mu_E, \sigma_E)$ and use the median as the offset μ_E and half the width of the 68% quantiles as the standard deviation σ_E. We only determined the shower energy resolution for the energy range 5×10^{16} eV to 1×10^{19} eV, so for energies outside of this range, we use the resolutions from the 5×10^{16} eV and 1×10^{19} eV energy bins. This allows us to calculate the posterior probability of the reconstructed shower energy for a given neutrino energy as

$$p(\lg(E_r)|\lg(E_\nu)) = \int \mathcal{N}(\lg(E_r/E_s)|\mu_E, \sigma_E) \cdot p(\lg(E_s)|\lg(E_\nu))\, d\lg(E_s) \tag{22}$$

which again has to be calculated separately for the two event types and then combined using $P(h)$ and $P(e)$.

Finally, the denominator of Eq. 16 just serves to make sure it is properly normalized and can be determined by integrating the numerator over $\lg(E_\nu)$. As integration limits we use $16 < \lg(E_\nu) < 20$. The resulting neutrino energy resolution for the shower energy resolutions shown in Sec. 5 is shown in Fig. 20 (bottom) for neutrino energies of 1×10^{17} eV and 1×10^{18} eV. Including the uncertainty on the shower energy changes the 68% quantiles to $[16.83, 17.35]$ and $[17.92, 18.59]$ with the stricter quality cut of requiring at least 2 additional channels on the *power string* or to $[16.79, 17.44]$ and $[17.89, 18.67]$ when requiring only one additional channel.

The larger uncertainty at 1×10^{18} eV has two reasons, both caused by the LPM effect: The trigger probability for events that only produce a hadronic shower, and are therefore affected by the uncertainty on $\frac{E_s}{E_\nu}$, is larger and the uncertainty on the shower energy is larger for ν_e+CC events at higher energies. To improve this, the most promising strategy is to improve the shower energy resolution for events from electron neutrinos undergoing charged current interactions and to develop a method to identify these events, as discussed in more detail in [61].

It should be noted that in this analysis we have not considered any background, which can come from several sources for a radio experiment. Air showers from cosmic rays can produce radio signals, as they propagate through the air and when a not yet fully developed air shower reaches the ice surface [70]. Additionally,

---

[5] To be precise, it would need to be the probability for the shower to trigger the detector, to be identified as a neutrino and to meet any quality criteria required for an energy reconstruction. The efficiency to identify neutrino events is not yet known, so we only use the trigger efficiency here.

high-energy muons produced in an air shower can penetrate deep into the ice and produce showers there [23]. At this point, it has to be assumed that these would be difficult to distinguish from neutrino-induced showers. If detectable, all of these backgrounds would show a different spectrum as function of energy. The backgrounds can be mitigated by detecting the air shower using the upward-pointing antennas at the surface.

Other backgrounds are radio emissions from the environment around the detector. Windy weather conditions have been found to produce radio pulses, potentially because of triboelectric effects of the snow, which may mimic neutrino signals [71,72]. However, a single, large pulse would be required for it to be mistaken for a neutrino signal, and the direction of the signal would likely reconstructed to the surface. This background can also be reduced by vetoing high-winds periods. Finally, human activity around the detection site inevitably produces radio emission. The nature and characteristics of this background are very difficult to predict and unique to each site. This will have to be investigated and subsequently modeled once RNO-G stations have gathered a sufficient amount of data in the field.

Including these background in our model at this point is very difficult. The background from air showers is not well-constrained yet, as for example models for the PeV muon flux have not been experimentally confirmed and rates of air shower emission depend on partly not well-known details of the ice. The veto efficiency of the surface antennas of RNO-G depends on the in-situ trigger performance, which is in-turn a function of the anthropogenic background. The background from the environment will have to be measured in situ and modeled throughout the year. Together with the large uncertainties on the expected neutrino flux, we can not yet give a good estimate of the purity of the data set that we expect to achieve. We therefore decided to ignore the background for now in the modeling of the energy resolution. This will have to be revisited once more information is available.

7 Summary and conclusion

We have presented a method to reconstruct the energy of neutrinos above above 50 PeV using their radio signature in ice. The method has been developed for the Radio Neutrino Observatory in Greenland (RNO-G), but is applicable more general to radio detectors of similar design such as the one proposed for IceCube-Gen2 [73].

Starting in Summer 2021, RNO-G will be the first discovery-scale radio detector array for astrophysical neutrinos. By detecting radio signals from particle showers in the ice sheet of Greenland at distances up to several kilometers, RNO-G will have an effective volume of roughly $\sim$100 km^3 at the highest energies. To measure the neutrino spectrum or to track energy dependent new physics phenomena, it is essential to be able to reconstruct the energy of the particle showers producing the radio signal, which are used to estimate the neutrino energy.

We have presented a method to reconstruct the shower energy using the data available if a radio signal was detected in only one RNO-G station, incorporating all data from channels deployed deep in the ice. Using this method and MC simulations, a resolution on the shower energy of $\sim$30 % is estimated for hadronic showers after moderate quality cuts. We have furthermore estimated the resolution on the neutrino energy this would provide, and found this to be about a factor of two on the neutrino energy for a reconstructed shower energy of 1×10^{17} eV. The LPM effect causes the uncertainty to increase at higher energies.

For RNO-G an energy-dependent fraction of the detected neutrinos (50% at 1 EeV) are expected to have a signal in more than one station. These events will provide an excellent verification of the method and its systematic uncertainties and can improve the estimation of the shower energy even further.

The presented method is in general applicable to any type of radio neutrino station in ice that features deep antennas sensitive to two polarizations, distributed at different depths along a string.

Acknowledgements We are thankful to the staff at Summit Station for supporting our deployment work in every way possible. Also to our colleagues from the British Antarctic Survey for getting excited about building and operating the BigRAID drill for our project.

We would like to acknowledge our home institutions and funding agencies for supporting the RNO-G work; in particular the Belgian Funds for Scientific Research (FRS-FNRS and FWO) and the FWO programme for International Research Infrastructure (IRI), the National Science Foundation through the NSF Award ID 2118315 and the IceCube EPSCoR Initiative (Award ID 2019597), the German research foundation (DFG, Grant NE 2031/2-1), the Helmholtz Association (Initiative and Networking Fund, W2/W3 Program), the University of Chicago Research Computing Center, and the European Research Council under the European Unions Horizon 2020 research and innovation programme (grant agreement No 805486).

References

1. KM3NET collaboration, *Letter of intent for KM3net 2.0*, *Journal of Physics G: Nuclear and Particle Physics* **43** (2016) 084001.

2. Baikal-GVD collaboration, *Baikal-GVD: status and prospects*, *EPJ Web Conf.* **191** (2018) 01006 [`1808.10353`].
3. AMANDA collaboration, *Search for neutrino-induced cascades with AMANDA*, *Astropart. Phys.* **22** (2004) 127 [`astro-ph/0405218`].
4. IceCube collaboration, *The first search for extremely-high energy cosmogenic neutrinos with the IceCube Neutrino Observatory*, *Phys. Rev. D* **82** (2010) 072003 [`1009.1442`].
5. IceCube collaboration, *Evidence for High-Energy Extraterrestrial Neutrinos at the IceCube Detector*, *Science* **342** (2013) 1242856 [`1311.5238`].
6. IceCube, Fermi-LAT, MAGIC, AGILE, ASAS-SN, HAWC, H.E.S.S., INTEGRAL, Kanata, Kiso, Kapteyn, Liverpool Telescope, Subaru, Swift NuSTAR, VERITAS, VLA/17B-403 collaboration, *Multimessenger observations of a flaring blazar coincident with high-energy neutrino IceCube-170922A*, *Science* **361** (2018) eaat1378 [`1807.08816`].
7. R. Stein et al., *A tidal disruption event coincident with a high-energy neutrino*, *Nature Astronomy* **5** (2021) 510–518.
8. ANTARES collaboration, *Transmission of light in deep sea water at the site of the ANTARES Neutrino Telescope*, *Astropart. Phys.* **23** (2005) 131 [`astro-ph/0412126`].
9. M. Ackermann et al., *Optical properties of deep glacial ice at the South Pole*, *J. Geophys. Res.* **111** (2006) D13203.
10. J. Avva, J. M. Kovac, C. Miki, D. Saltzberg and A. G. Vieregg, *An in situ measurement of the radio-frequency attenuation in ice at Summit Station, Greenland*, *J. Glaciol.* **61** (2015) 1005 [`1409.5413`].
11. J. C. Hanson, S. W. Barwick, E. C. Berg, D. Z. Besson, T. J. Duffin, S. R. Klein et al., *Radar absorption, basal reflection, thickness and polarization measurements from the ross ice shelf, antarctica*, *Journal of Glaciology* **61** (2015) 438–446.
12. S. Barwick, D. Besson, P. Gorham and D. Saltzberg, *South polar in situ radio-frequency ice attenuation*, *Journal of Glaciology* **51** (2005) 231–238.
13. RNO-G collaboration, *Design and Sensitivity of the Radio Neutrino Observatory in Greenland (RNO-G)*, *JINST* **16** (2021) P03025 [`2010.12279`].
14. K. Fang, K. Kotera, K. Murase and A. V. Olinto, *Testing the Newborn Pulsar Origin of Ultrahigh Energy Cosmic Rays with EeV Neutrinos*, *Phys. Rev. D* **90** (2014) 103005 [`1311.2044`].
15. D. Boncioli, D. Biehl and W. Winter, *On the common origin of cosmic rays across the ankle and diffuse neutrinos at the highest energies from low-luminosity gamma-ray bursts*, *The Astrophysical Journal* **872** (2019) 110.
16. K. Murase, Y. Inoue and C. D. Dermer, *Diffuse Neutrino Intensity from the Inner Jets of Active Galactic Nuclei: Impacts of External Photon Fields and the Blazar Sequence*, *Phys. Rev. D* **90** (2014) 023007 [`1403.4089`].
17. X. Rodrigues, J. Heinze, A. Palladino, A. van Vliet and W. Winter, *AGN jets as the origin of UHECRs and perspectives for the detection of EeV astrophysical neutrinos*, `2003.08392`.
18. K. Murase, *High energy neutrino early afterglows gamma-ray bursts revisited*, *Phys. Rev. D* **76** (2007) 123001 [`0707.1140`].
19. K. Greisen, *End to the cosmic ray spectrum?*, *Phys. Rev. Lett.* **16** (1966) 748.
20. V. S. Berezinsky and G. T. Zatsepin, *Cosmic rays at ultrahigh-energies (neutrino?)*, *Phys. Lett. B* **28** (1969) 423.
21. G. T. Zatsepin and V. A. Kuzmin, *Upper limit of the spectrum of cosmic rays*, *JETP Lett.* **4** (1966) 78.
22. A. van Vliet, R. Alves Batista and J. R. Hörandel, *Determining the fraction of cosmic-ray protons at ultrahigh energies with cosmogenic neutrinos*, *Phys. Rev. D* **100** (2019) 021302 [`1901.01899`].
23. D. García-Fernández, A. Nelles and C. Glaser, *Signatures of secondary leptons in radio-neutrino detectors in ice*, *Phys. Rev. D* **102** (2020) 083011 [`2003.13442`].
24. G. A. Askaryan, *Excess negative charge of an electron-photon shower and the coherent radio emission from it*, *Zhur. Eksptl'. i Teoret. Fiz.* **41** (1961) .
25. J. V. Jelley, J. H. Fruin, N. A. Porter and T. C. Weekes, *Radio pulses from extensive cosmic-ray air showers*, *Nature* **205** (1965) 327.
26. D. Saltzberg et al., *Observation of the Askaryan Effect: Coherent Microwave Cherenkov Emission from Charge Asymmetry in High-Energy Particle Cascades*, *Physical Review Letters* **86** (2001) 2802–2805.
27. P. W. Gorham et al., *Accelerator measurements of the Askaryan effect in rock salt: A Roadmap toward teraton underground neutrino detectors*, *Phys. Rev. D* **72** (2005) 023002 [`astro-ph/0412128`].
28. ANITA collaboration, *Observations of the Askaryan effect in ice*, *Phys. Rev. Lett.* **99** (2007) 171101 [`hep-ex/0611008`].
29. P. Schellart et al., *Polarized radio emission from extensive air showers measured with LOFAR*, *JCAP* **10** (2014) 014 [`1406.1355`].
30. Pierre Auger collaboration, *Probing the radio emission from air showers with polarization measurements*, *Phys. Rev. D* **89** (2014) 052002 [`1402.3677`].
31. J. Alvarez-Muniz, R. A. Vazquez and E. Zas, *Calculation methods for radio pulses from high-energy showers*, *Phys. Rev. D* **62** (2000) 063001 [`astro-ph/0003315`].
32. J. Alvarez-Muniz, A. Romero-Wolf and E. Zas, *Cherenkov radio pulses from electromagnetic showers in the time-domain*, *Phys. Rev. D* **81** (2010) 123009 [`1002.3873`].
33. L. D. Landau and I. Pomeranchuk, *Limits of applicability of the theory of bremsstrahlung electrons and pair production at high-energies*, *Dokl. Akad. Nauk Ser. Fiz.* **92** (1953) 535.
34. A. B. Migdal, *Bremsstrahlung and pair production in condensed media at high-energies*, *Phys. Rev.* **103** (1956) 1811.
35. T. Stanev, C. Vankov, R. E. Streitmatter, R. W. Ellsworth and T. Bowen, *Development of ultrahigh-energy electromagnetic cascades in water and lead including the Landau-Pomeranchuk-Migdal effect*, *Phys. Rev. D* **25** (1982) 1291.
36. L. Gerhardt and S. R. Klein, *Electron and Photon Interactions in the Regime of Strong LPM Suppression*, *Phys. Rev. D* **82** (2010) 074017 [`1007.0039`].
37. E. Konishi, A. Adachi, N. Takahashi and A. Misaki, *On the characteristics of individual cascade showers with the LPM effect in extremely high-energies*, *J. Phys. G* **17** (1991) 719.

38. J. Alvarez-Muniz, R. A. Vazquez and E. Zas, *Characterization of neutrino signals with radiopulses in dense media through the LPM effect*, *Phys. Rev. D* **61** (2000) 023001 [`astro-ph/9901278`].
39. C. Glaser et al., *NuRadioMC: Simulating the radio emission of neutrinos from interaction to detector*, *Eur. Phys. J. C* **80** (2020) 77 [`1906.01670`].
40. ARA collaboration, *Design and performance of an interferometric trigger array for radio detection of high-energy neutrinos*, *Nucl. Instrum. Meth. A* **930** (2019) 112 [`1809.04573`].
41. D. Smith for the RNO-G Collaboration, *Hardware Development for the Radio Neutrino Observatory in Greenland (RNO-G)*, *PoS* **ICRC2021** (2021) 1058.
42. ARIANNNA collaboration, *Neutrino vertex reconstruction with in-ice radio detectors using surface reflections and implications for the neutrino energy resolution*, *JCAP* **2019** (2019) 030.
43. ARIANNA collaboration, *Neutrino direction and energy resolution of Askaryan detectors*, *PoS* **ICRC2019** (2020) 899 [`1911.02093`].
44. J. Alvarez-Muñiz, A. Romero-Wolf and E. Zas, *Practical and accurate calculations of Askaryan radiation*, *Phys. Rev. D* **84** (2011) 103003.
45. C. Welling, C. Glaser and A. Nelles, *Reconstructing the cosmic-ray energy from the radio signal measured in one single station*, *JCAP* **10** (2019) 075 [`1905.11185`].
46. S. Barwick et al., *Observation of classically `forbidden' electromagnetic wave propagation and implications for neutrino detection.*, *JCAP* **2018** (2018) 055.
47. C. Deaconu et al., *Measurements and Modeling of Near-Surface Radio Propagation in Glacial Ice and Implications for Neutrino Experiments*, *Phys. Rev. D* **98** (2018) 043010 [`1805.12576`].
48. I. Kravchenko, D. Besson, A. Ramos and J. Remmers, *Radio frequency birefringence in south polar ice and implications for neutrino reconstruction*, *Astroparticle Physics* **34** (2011) 755.
49. T. Winchen, *RadioPropa — A Modular Raytracer for In-Matter Radio Propagation*, *EPJ Web Conf.* **216** (2019) 03002 [`1810.01780`].
50. Radar Echo Telescope collaboration, *Modeling in-ice radio propagation with parabolic equation methods*, `2011.05997`.
51. C. Shannon, *Communication in the presence of noise*, *Proceedings of the IRE* **37** (1949) 10.
52. C. Glaser, A. Nelles, I. Plaisier, C. Welling et al., *NuRadioReco: A reconstruction framework for radio neutrino detectors*, *Eur. Phys. J. C* **79** (2019) 464 [`1903.07023`].
53. IceCube collaboration, *A measurement of the diffuse astrophysical muon neutrino flux using eight years of IceCube data.*, *PoS* **ICRC2017** (2017) 1005.
54. T. A. Enßlin, *Information field theory*, *AIP Conference Proceedings* **1553** (2013) 184.
55. T. A. Enßlin, *Information theory for fields*, *Annalen der Physik* **531** (2019) 1800127.
56. C. Welling, P. Frank, T. A. Enßlin and A. Nelles, *Reconstructing non-repeating radio pulses with Information Field Theory*, *JCAP* **04** (2021) 071 [`2102.00258`].
57. J. Knollmüller and T. A. Enßlin, *Metric Gaussian Variational Inference*, `1901.11033`.
58. Pierre Auger collaboration, *Calibration of the logarithmic-periodic dipole antenna (LPDA) radio stations at the Pierre Auger Observatory using an octocopter*, *JINST* **12** (2017) T10005 [`1702.01392`].
59. P. Dasgupta and K. Hughes for the ARA Collaboration, *The calibration of the geometry and antenna delay of the Askaryan Radio Array Station 4 and 5*, *PoS* **ICRC2021** (2021) 1086.
60. B. Oeyen, I. Plaisier, A. Nelles, C. Glaser and T. Winchen, *Effects of firn ice models on radio neutrino simulations using a RadioPropa ray tracer*, *PoS* **ICRC2021** (2021) 1027.
61. C. Welling for the RNO-G Collaboration, *Energy reconstruction with the Radio Neutrino Observatory Greenland*, *PoS* **ICRC2021** (2021) 1033.
62. `https://gitlab.desy.de/christoph.welling/radio-neutrino-energy`.
63. IceCube collaboration, *Measurements using the inelasticity distribution of multi-TeV neutrino interactions in IceCube*, *Phys. Rev. D* **99** (2019) 032004.
64. S. R. Klein, S. A. Robertson and R. Vogt, *Nuclear effects in high-energy neutrino interactions*, *Phys. Rev. C* **102** (2020) 015808.
65. D. Seckel, *Neutrino-Photon Reactions in Astrophysics and Cosmology*, *Phys. Rev. Lett.* **80** (1998) 900.
66. B. Zhou and J. F. Beacom, *W-boson and trident production in TeV–PeV neutrino observatories*, *Phys. Rev. D* **101** (2020) 036010.
67. A. Cooper-Sarkar, P. Mertsch and S. Sarkar, *The high energy neutrino cross-section in the Standard Model and its uncertainty*, *JHEP* **08** (2011) 042 [`1106.3723`].
68. A. Connolly, R. S. Thorne and D. Waters, *Calculation of High Energy Neutrino-Nucleon Cross Sections and Uncertainties Using the MSTW Parton Distribution Functions and Implications for Future Experiments*, *Phys. Rev. D* **83** (2011) 113009 [`1102.0691`].
69. R. Gandhi, C. Quigg, M. H. Reno and I. Sarcevic, *Ultrahigh-energy neutrino interactions*, *Astropart. Phys.* **5** (1996) 81 [`hep-ph/9512364`].
70. K. D. de Vries, S. Buitink, N. van Eijndhoven, T. Meures, A. Ó Murchadha and O. Scholten, *The cosmic-ray air-shower signal in Askaryan radio detectors*, *Astropart. Phys.* **74** (2016) 96 [`1503.02808`].
71. ARIANNA collaboration, *Radio detection of air showers with the ARIANNA experiment on the Ross Ice Shelf*, *Astropart. Phys.* **90** (2017) 50 [`1612.04473`].
72. M. Mikhailova, E. Bondarev, A. Nozdrina, H. Landsman and D. Z. Besson, *Triboelectric Backgrounds to radio-based UHE Neutrino Exeperiments*, `2103.06079`.
73. IceCube-Gen2 collaboration, *IceCube-Gen2: the window to the extreme Universe*, *J. Phys. G* **48** (2021) 060501 [`2008.04323`].

Bibliography

[1] V. F. Hess, *Über Beobachtungen der durchdringenden Strahlung bei sieben Freiballonfahrten*, *Phys. Z.* **13** (1912) 1084.

[2] FERMI-LAT collaboration, *The spectrum of isotropic diffuse gamma-ray emission between 100 MeV and 820 GeV*, *Astrophys. J.* **799** (2015) 86 [`1410.3696`].

[3] ICECUBE collaboration, *The IceCube high-energy starting event sample: Description and flux characterization with 7.5 years of data*, `2011.03545`.

[4] ICECUBE collaboration, *The IceCube Neutrino Observatory - Contributions to ICRC 2017 Part II: Properties of the Atmospheric and Astrophysical Neutrino Flux*, `1710.01191`.

[5] ICECUBE collaboration, *Measurement of the Atmospheric ν_e Spectrum with IceCube*, *Phys. Rev. D* **91** (2015) 122004 [`1504.03753`].

[6] PIERRE AUGER, TELESCOPE ARRAY collaboration, *The energy spectrum of ultra-high energy cosmic rays measured at the Pierre Auger Observatory and at the Telescope Array*, *PoS* **ICRC2019** (2020) 234 [`2001.08811`].

[7] W. Apel, J. Arteaga-Velázquez et al., *The spectrum of high-energy cosmic rays measured with kascade-grande*, *Astroparticle Physics* **36** (2012) 183.

[8] TELESCOPE ARRAY collaboration, *Energy Spectrum of Ultra-High-Energy Cosmic Rays Measured by The Telescope Array*, *PoS* **ICRC2017** (2018) 535.

[9] PIERRE AUGER collaboration, *Combined fit of spectrum and composition data as measured by the Pierre Auger Observatory*, *JCAP* **04** (2017) 038 [`1612.07155`].

[10] PIERRE AUGER collaboration, *Large-scale cosmic-ray anisotropies above 4 EeV measured by the Pierre Auger Observatory*, *Astrophys. J.* **868** (2018) 4 [`1808.03579`].

[11] PIERRE AUGER collaboration, *Cosmic-ray anisotropies in right ascension measured by the Pierre Auger Observatory*, *Astrophys. J.* **891** (2020) 142 [`2002.06172`].

[12] TELESCOPE ARRAY collaboration, *Indications of Intermediate-Scale Anisotropy of Cosmic Rays with Energy Greater Than 57 EeV in the Northern Sky Measured with the Surface Detector of the Telescope Array Experiment*, *Astrophys. J. Lett.* **790** (2014) L21 [`1404.5890`].

[13] TELESCOPE ARRAY collaboration, *Evidence for a Supergalactic Structure of Magnetic Deflection Multiplets of Ultra-High Energy Cosmic Rays*, *Astrophys. J.* **899** (2020) 86 [`2005.07312`].

[14] Pierre Auger collaboration, *An Indication of anisotropy in arrival directions of ultra-high-energy cosmic rays through comparison to the flux pattern of extragalactic gamma-ray sources*, *Astrophys. J. Lett.* **853** (2018) L29 [`1801.06160`].

[15] Pierre Auger collaboration, *Searches for Anisotropies in the Arrival Directions of the Highest Energy Cosmic Rays Detected by the Pierre Auger Observatory*, *Astrophys. J.* **804** (2015) 15 [`1411.6111`].

[16] Pierre Auger collaboration, *Search for magnetically-induced signatures in the arrival directions of ultra-high-energy cosmic rays measured at the Pierre Auger Observatory*, *JCAP* **06** (2020) 017 [`2004.10591`].

[17] IceCube, Pierre Auger, Telescope Array collaboration, *Search for correlations between the arrival directions of IceCube neutrino events and ultrahigh-energy cosmic rays detected by the Pierre Auger Observatory and the Telescope Array*, *JCAP* **01** (2016) 037 [`1511.09408`].

[18] Telescope Array, Pierre Auger collaboration, *UHECR arrival directions in the latest data from the original Auger and TA surface detectors and nearby galaxies*, *PoS* **ICRC2021** (2021) 308.

[19] KASCADE-Grande collaboration, *KASCADE-Grande measurements of energy spectra for elemental groups of cosmic rays*, *Astropart. Phys.* **47** (2013) 54 [`1306.6283`].

[20] Telescope Array collaboration, *The Cosmic-Ray Composition between 2 PeV and 2 EeV Observed with the TALE Detector in Monocular Mode*, *Astrophys. J.* **909** (2021) 178 [`2012.10372`].

[21] Auger collaboration, *Mass Composition of Cosmic Rays with Energies above $10^{17.2}$ eV from the Hybrid Data of the Pierre Auger Observatory*, *PoS* **ICRC2019** (2020) 482.

[22] Pierre Auger collaboration, *Measurement of the Fluctuations in the Number of Muons in Extensive Air Showers with the Pierre Auger Observatory*, *Phys. Rev. Lett.* **126** (2021) 152002 [`2102.07797`].

[23] D. Bergman and T. Stroman, *Telescope Array measurement of UHECR composition from stereoscopic fluorescence detection*, *PoS* **ICRC2017** (2018) 538.

[24] A. D. Angelis and M. Pimenta, *Introduction to Particle and Astroparticle Physics*, vol. 1. Springer, 2 ed., 2018.

[25] A. M. Hillas, *The origin of ultra-high-energy cosmic rays*, *Annual Review of Astronomy and Astrophysics* **22** (1984) 425 [`https://doi.org/10.1146/annurev.aa.22.090184.002233`].

[26] R. de Menezes, R. Nemmen et al., *Gamma-ray observations of low-luminosity active galactic nuclei*, *Mon. Not. Roy. Astron. Soc.* **492** (2020) 4120 [`2001.03184`].

[27] MAGIC collaboration, *Measurement of the Crab Nebula spectrum over three decades in energy with the MAGIC telescopes*, *JHEA* **5-6** (2015) 30 [`1406.6892`].

[28] MAGIC collaboration, *MAGIC eyes to the extreme: testing the blazar emission models on EHBLs*, *PoS* **ICRC2019** (2021) 768 [`1908.10800`].

[29] A. Domínguez, J. D. Finke et al., *Detection of the cosmic gamma-ray horizon from multiwavelength observations of blazars*, *Astrophys. J.* **770** (2013) 77 [`1305.2162`].

[30] HESS collaboration, *Measurement of the EBL spectral energy distribution using the VHE γ-ray spectra of H.E.S.S. blazars*, *Astron. Astrophys.* **606** (2017) A59 [`1707.06090`].

[31] M. Ahlers, *Multi-Messenger Aspects of Cosmic Neutrinos*, *PoS* **ICRC2015** (2016) 022.

[32] ICECUBE collaboration, *Evidence for High-Energy Extraterrestrial Neutrinos at the IceCube Detector*, *Science* **342** (2013) 1242856 [`1311.5238`].

[33] ICECUBE collaboration, *Observation of High-Energy Astrophysical Neutrinos in Three Years of IceCube Data*, *Phys. Rev. Lett.* **113** (2014) 101101 [`1405.5303`].

[34] K. Murase and E. Waxman, *Constraining High-Energy Cosmic Neutrino Sources: Implications and Prospects*, *Phys. Rev. D* **94** (2016) 103006 [`1607.01601`].

[35] F. Capel, D. J. Mortlock et al., *Bayesian constraints on the astrophysical neutrino source population from IceCube data*, *Phys. Rev. D* **101** (2020) 123017 [`2005.02395`].

[36] ICECUBE collaboration, *Flavor Ratio of Astrophysical Neutrinos above 35 TeV in IceCube*, *Phys. Rev. Lett.* **114** (2015) 171102 [`1502.03376`].

[37] ICECUBE collaboration, *Measurement of Astrophysical Tau Neutrinos in IceCube's High-Energy Starting Events*, `2011.03561`.

[38] K. Mannheim, *The Proton blazar*, *Astron. Astrophys.* **269** (1993) 67 [`astro-ph/9302006`].

[39] R. J. Protheroe, *High-energy neutrinos from blazars*, *ASP Conf. Ser.* **121** (1997) 585 [`astro-ph/9607165`].

[40] ICECUBE, FERMI-LAT, MAGIC, AGILE, ASAS-SN, HAWC, H.E.S.S., INTEGRAL, KANATA, KISO, KAPTEYN, LIVERPOOL TELESCOPE, SUBARU, SWIFT NUSTAR, VERITAS, VLA/17B-403 collaboration, *Multimessenger observations of a flaring blazar coincident with high-energy neutrino IceCube-170922A*, *Science* **361** (2018) eaat1378 [`1807.08816`].

[41] ICECUBE collaboration, *Neutrino emission from the direction of the blazar TXS 0506+056 prior to the IceCube-170922A alert*, *Science* **361** (2018) 147 [`1807.08794`].

[42] R. Stein et al., *A tidal disruption event coincident with a high-energy neutrino*, *Nature Astron.* **5** (2021) 510 [`2005.05340`].

[43] ICECUBE collaboration, *The contribution of Fermi-2LAC blazars to the diffuse TeV-PeV neutrino flux*, *Astrophys. J.* **835** (2017) 45 [`1611.03874`].

[44] ICECUBE collaboration, *Search for Neutrinos from Populations of Optical Transients*, *PoS* **ICRC2019** (2020) 1016 [`1908.08547`].

[45] X. Rodrigues, J. Heinze et al., *Active Galactic Nuclei Jets as the Origin of Ultrahigh-Energy Cosmic Rays and Perspectives for the Detection of Astrophysical Source Neutrinos at EeV Energies*, *Phys. Rev. Lett.* **126** (2021) 191101 [`2003.08392`].

[46] D. Boncioli, D. Biehl et al., *On the common origin of cosmic rays across the ankle and diffuse neutrinos at the highest energies from low-luminosity Gamma-Ray Bursts*, *Astrophys. J.* **872** (2019) 110 [`1808.07481`].

[47] K. Murase, *High energy neutrino early afterglows gamma-ray bursts revisited*, *Phys. Rev. D* **76** (2007) 123001 [`0707.1140`].

[48] C. Guépin, K. Kotera et al., *Ultra-High Energy Cosmic Rays and Neutrinos from Tidal Disruptions by Massive Black Holes*, *Astron. Astrophys.* **616** (2018) A179 [`1711.11274`].

[49] V. S. Berezinsky and G. T. Zatsepin, *Cosmic rays at ultrahigh-energies (neutrino?)*, *Phys. Lett. B* **28** (1969) 423.

[50] K. Kotera, D. Allard et al., *Cosmogenic neutrinos: parameter space and detectabilty from PeV to ZeV*, *Journal of Cosmology and Astroparticle Physics* **2010** (2010) 013.

[51] TELESCOPE ARRAY collaboration, *Telescope Array Combined Fit to Cosmic Ray Spectrum and Composition*, *PoS* **ICRC2021** (2021) 338.

[52] M. S. Muzio, M. Unger et al., *Progress towards characterizing ultrahigh energy cosmic ray sources*, *Phys. Rev. D* **100** (2019) 103008 [`1906.06233`].

[53] J. Heinze, A. Fedynitch et al., *A new view on Auger data and cosmogenic neutrinos in light of different nuclear disintegration and air-shower models*, *Astrophys. J.* **873** (2019) 88 [`1901.03338`].

[54] R. Alves Batista, D. Boncioli et al., *Secondary neutrino and gamma-ray fluxes from SimProp and CRPropa*, *JCAP* **05** (2019) 006 [`1901.01244`].

[55] A. van Vliet, R. Alves Batista et al., *Determining the fraction of cosmic-ray protons at ultrahigh energies with cosmogenic neutrinos*, *Phys. Rev. D* **100** (2019) 021302 [`1901.01899`].

[56] B. Eichmann, J. P. Rachen et al., *Ultra-High-Energy Cosmic Rays from Radio Galaxies*, *JCAP* **02** (2018) 036 [`1701.06792`].

[57] D. Wanderman and T. Piran, *The luminosity function and the rate of Swift's Gamma Ray Bursts*, *Mon. Not. Roy. Astron. Soc.* **406** (2010) 1944 [`0912.0709`].

[58] G. Hasinger, T. Miyaji et al., *Luminosity-dependent evolution of soft x-ray selected AGN: New Chandra and XMM-Newton surveys*, *Astron. Astrophys.* **441** (2005) 417 [`astro-ph/0506118`].

[59] J. Law-Smith, E. Ramirez-Ruiz et al., *Tidal Disruption Event Host Galaxies in the Context of the Local Galaxy Population*, *Astrophys. J.* **850** (2017) 22 [`1707.01559`].

[60] J. Matthews, *A Heitler model of extensive air showers*, *Astropart. Phys.* **22** (2005) 387.

[61] T. K. Gaisser and A. M. Hillas, *Reliability of the Method of Constant Intensity Cuts for Reconstructing the Average Development of Vertical Showers*, in *International Cosmic Ray Conference*, vol. 8 of *International Cosmic Ray Conference*, p. 353, Jan., 1977.

[62] C. Song, Z. Cao et al., *Energy estimation of UHE cosmic rays using the atmospheric fluorescence technique*, *Astropart. Phys.* **14** (2000) 7 [`astro-ph/9910195`].

[63] H. M. J. Barbosa, F. Catalani et al., *Determination of the calorimetric energy in extensive air showers*, *Astropart. Phys.* **22** (2004) 159 [`astro-ph/0310234`].

[64] Pierre Auger collaboration, *Data-driven estimation of the invisible energy of cosmic ray showers with the Pierre Auger Observatory*, *Phys. Rev. D* **100** (2019) 082003 [`1901.08040`].

[65] J. W. Elbert, *COSMIC RAY MULTIPLE MUON EVENTS IN DEEP DETECTORS.*, in *16th International Cosmic Ray Conference*, pp. 405–409, 1979.

[66] T. K. Gaisser and S. Verpoest, *Profiles of energetic muons in the atmosphere*, *Astropart. Phys.* **133** (2021) 102630 [`2106.12247`].

[67] R. Enberg, M. H. Reno et al., *Prompt neutrino fluxes from atmospheric charm*, *Phys. Rev. D* **78** (2008) 043005 [`0806.0418`].

[68] IceCube collaboration, *Observation and Characterization of a Cosmic Muon Neutrino Flux from the Northern Hemisphere using six years of IceCube data*, *Astrophys. J.* **833** (2016) 3 [`1607.08006`].

[69] KASCADE collaboration, *KASCADE measurements of energy spectra for elemental groups of cosmic rays: Results and open problems*, *Astropart. Phys.* **24** (2005) 1 [`astro-ph/0505413`].

[70] Pierre Auger collaboration, *The Pierre Auger Cosmic Ray Observatory*, *Nucl. Instrum. Meth. A* **798** (2015) 172 [`1502.01323`].

[71] Telescope Array collaboration, *Telescope array experiment*, *Nucl. Phys. B Proc. Suppl.* **175-176** (2008) 221.

[72] TAIGA collaboration, *TAIGA - an advanced hybrid detector complex for astroparticle physics, cosmic ray physics and gamma-ray astronomy*, *PoS* **ICRC2021** (2021) 731.

[73] MAGIC collaboration, *Protons Spectrum from MAGIC Telescopes data*, *PoS* **ICRC2021** (2021) 231.

[74] CTA Consortium collaboration, *The Cherenkov Telescope Array*, *PoS* **ICRC2019** (2020) 741 [`1907.08530`].

[75] H.E.S.S. collaboration, *The H.E.S.S. experiment : current status and future prospects*, *PoS* **ICRC2019** (2020) 656.

[76] MAGIC collaboration, *Performance of the MAGIC stereo system obtained with Crab Nebula data*, *Astropart. Phys.* **35** (2012) 435 [`1108.1477`].

[77] VERITAS collaboration, *VERITAS: Status and Recent Results*, *EPJ Web Conf.* **209** (2019) 01028.

[78] HiRes collaboration, *First observation of the Greisen-Zatsepin-Kuzmin suppression*, *Phys. Rev. Lett.* **100** (2008) 101101 [`astro-ph/0703099`].

[79] Pierre Auger collaboration, *The Fluorescence Detector of the Pierre Auger Observatory*, *Nucl. Instrum. Meth. A* **620** (2010) 227 [`0907.4282`].

[80] Pierre Auger collaboration, *Reconstruction of events recorded with the surface detector of the Pierre Auger Observatory*, *JINST* **15** (2020) P10021 [`2007.09035`].

[81] Pierre Auger collaboration, *Depth of Maximum of Air-Shower Profiles at the Pierre Auger Observatory: Measurements at Energies above* $10^{17.8}$ *eV*, *Phys. Rev. D* **90** (2014) 122005 [`1409.4809`].

[82] Telescope Array collaboration, *Depth of Ultra High Energy Cosmic Ray Induced Air Shower Maxima Measured by the Telescope Array Black Rock and Long Ridge FADC Fluorescence Detectors and Surface Array in Hybrid Mode*, *Astrophys. J.* **858** (2018) 76 [`1801.09784`].

[83] Pierre Auger collaboration, *Muons in Air Showers at the Pierre Auger Observatory: Measurement of Atmospheric Production Depth*, *Phys. Rev. D* **90** (2014) 012012 [`1407.5919`].

[84] Pierre Auger collaboration, *Testing Hadronic Interactions at Ultrahigh Energies with Air Showers Measured by the Pierre Auger Observatory*, *Phys. Rev. Lett.* **117** (2016) 192001 [`1610.08509`].

[85] O. Scholten, K. Werner et al., *A Macroscopic Description of Coherent Geo-Magnetic Radiation from Cosmic Ray Air Showers*, *Astropart. Phys.* **29** (2008) 94 [`0709.2872`].

[86] G. A. Askar'yan, *Excess negative charge of an electron-photon shower and its coherent radio emission*, *Zh. Eksp. Teor. Fiz.* **41** (1961) 616.

[87] CORSIKA 8 collaboration, *Simulations of radio emission from air showers with CORSIKA 8*, *PoS* **ICRC2021** (2021) 427.

[88] K. D. de Vries, A. M. van den Berg et al., *Coherent cherenkov radiation from cosmic-ray-induced air showers*, *Phys. Rev. Lett.* **107** (2011) 061101.

[89] LOFAR collaboration, *Measuring a Cherenkov ring in the radio emission from air showers at 110–190 MHz with LOFAR*, *Astropart. Phys.* **65** (2015) 11 [`1411.6865`].

[90] LOFAR collaboration, *The radio emission pattern of air showers as measured with LOFAR—a tool for the reconstruction of the energy and the shower maximum*, *JCAP* **05** (2015) 018 [`1411.7868`].

[91] C. Glaser, S. de Jong et al., *An analytic description of the radio emission of air showers based on its emission mechanisms*, *Astropart. Phys.* **104** (2019) 64 [`1806.03620`].

[92] Pierre Auger collaboration, *Probing the radio emission from air showers with polarization measurements*, *Phys. Rev. D* **89** (2014) 052002 [`1402.3677`].

[93] LOFAR collaboration, *Polarized radio emission from extensive air showers measured with LOFAR*, *JCAP* **10** (2014) 014 [`1406.1355`].

[94] Pierre Auger collaboration, *Observation of inclined EeV air showers with the radio detector of the Pierre Auger Observatory*, *JCAP* **10** (2018) 026 [`1806.05386`].

[95] J. V. Jelley, J. H. Fruin et al., *Radio pulses from extensive cosmic-ray air showers*, *Nature* **205** (1965) 327.

[96] LOPES collaboration, *Detection and imaging of atmospheric radio flashes from cosmic ray air showers*, *Nature* **435** (2005) 313 [`astro-ph/0505383`].

[97] TUNKA-REX collaboration, *Measurement of cosmic-ray air showers with the Tunka Radio Extension (Tunka-Rex)*, *Nucl. Instrum. Meth. A* **802** (2015) 89 [`1509.08624`].

[98] PIERRE AUGER collaboration, *Recent Results of the Auger Engineering Radio Array (AERA)*, *PoS* **ICRC2017** (2018) 492.

[99] PIERRE AUGER collaboration, *A Large Radio Detector at the Pierre Auger Observatory - Measuring the Properties of Cosmic Rays up to the Highest Energies*, *PoS* **ICRC2019** (2021) 395.

[100] PIERRE AUGER collaboration, *First results from the AugerPrime Radio Detector*, *PoS* **ICRC2021** (2021) 270.

[101] D. Charrier et al., *Autonomous radio detection of air showers with the TREND50 antenna array*, *Astropart. Phys.* **110** (2019) 15 [`1810.03070`].

[102] LOFAR collaboration, *LOFAR: Detecting Cosmic Rays with a Radio Telescope*, in *32nd International Cosmic Ray Conference*, vol. 3, pp. 192–195, 9, 2011, `1109.5805`, DOI.

[103] LOFAR collaboration, *Cosmic Ray Physics with the LOFAR Radio Telescope*, *J. Phys. Conf. Ser.* **1181** (2019) 012020 [`1903.08474`].

[104] T. Huege et al., *Ultimate precision in cosmic-ray radio detection — the SKA*, *EPJ Web Conf.* **135** (2017) 02003 [`1608.08869`].

[105] LOPES collaboration, *LOPES-3D, an antenna array for full signal detection of air-shower radio emission*, *Nucl. Instrum. Meth. A* **696** (2012) 100 [`1303.6808`].

[106] ANITA collaboration, *The Antarctic Impulsive Transient Antenna Ultra-high Energy Neutrino Detector Design, Performance, and Sensitivity for 2006-2007 Balloon Flight*, *Astropart. Phys.* **32** (2009) 10 [`0812.1920`].

[107] S. Wissel et al., *Concept Study for the Beamforming Elevated Array for Cosmic Neutrinos (BEACON)*, *PoS* **ICRC2019** (2020) 1033.

[108] S. Wissel et al., *Prospects for high-elevation radio detection of >100 PeV tau neutrinos*, *JCAP* **11** (2020) 065 [`2004.12718`].

[109] PIERRE AUGER collaboration, *Reconstruction of air-shower measurements with AERA in the presence of pulsed radio-frequency interference*, *EPJ Web Conf.* **216** (2019) 03007 [`1906.05148`].

[110] PIERRE AUGER collaboration, *Energy Estimation of Cosmic Rays with the Engineering Radio Array of the Pierre Auger Observatory*, *Phys. Rev. D* **93** (2016) 122005 [`1508.04267`].

[111] TUNKA-REX collaboration, *Radio measurements of the energy and the depth of the shower maximum of cosmic-ray air showers by Tunka-Rex*, *JCAP* **01** (2016) 052 [`1509.05652`].

[112] LOFAR collaboration, *Depth of shower maximum and mass composition of cosmic rays from 50 PeV to 2 EeV measured with the LOFAR radio telescope*, *Phys. Rev. D* **103** (2021) 102006 [`2103.12549`].

[113] PIERRE AUGER collaboration, *Measurement of the Radiation Energy in the Radio Signal of Extensive Air Showers as a Universal Estimator of Cosmic-Ray Energy*, *Phys. Rev. Lett.* **116** (2016) 241101 [`1605.02564`].

[114] K. Mulrey et al., *On the cosmic-ray energy scale of the LOFAR radio telescope*, *JCAP* **11** (2020) 017 [`2005.13441`].

[115] TUNKA-REX, LOPES collaboration, *A comparison of the cosmic-ray energy scales of Tunka-133 and KASCADE-Grande via their radio extensions Tunka-Rex and LOPES*, *Phys. Lett. B* **763** (2016) 179 [`1610.08343`].

[116] E. M. Holt, *Combined Detection of Muons and Radio Emission of Cosmic-Ray Air Showers*, Ph.D. thesis, Karlsruher Institut für Technologie (KIT), 2018. 10.5445/IR/1000083318.

[117] PIERRE AUGER collaboration, *Estimating the mass of cosmic rays by combining radio and muon measurements*, *EPJ Web Conf.* **216** (2019) 02002.

[118] E. M. Holt, F. G. Schröder et al., *Enhancing the cosmic-ray mass sensitivity of air-shower arrays by combining radio and muon detectors*, *Eur. Phys. J. C* **79** (2019) 371 [`1905.01409`].

[119] LOPES collaboration, *Reconstruction of the energy and depth of maximum of cosmic-ray air-showers from LOPES radio measurements*, *Phys. Rev. D* **90** (2014) 062001 [`1408.2346`].

[120] S. Buitink, A. Corstanje et al., *Method for high precision reconstruction of air shower $X_{\max}$ using two-dimensional radio intensity profiles*, *Phys. Rev. D* **90** (2014) 082003.

[121] C. Welling, C. Glaser et al., *Reconstructing the cosmic-ray energy from the radio signal measured in one single station*, *JCAP* **10** (2019) 075 [`1905.11185`].

[122] TUNKA-REX collaboration, *Tunka-Rex: energy reconstruction with a single antenna station*, *EPJ Web Conf.* **135** (2017) 01004 [`1611.09614`].

[123] K. Mulrey, *Cross-calibrating the energy scales of cosmic-ray experiments using a portable radio array*, *PoS* **ICRC2021** (2021) 414.

[124] LOFAR collaboration, *Radio detection of air showers with the ARIANNA experiment on the Ross Ice Shelf*, *Astropart. Phys.* **90** (2017) 50 [`1612.04473`].

[125] ARIANNA collaboration, *Cosmic-ray detection with and novel reconstruction algorithms for the ARIANNA experiment*, *PoS* **ICRC2019** (2020) 366.

[126] ANITA collaboration, *Observation of Ultra-high-energy Cosmic Rays with the ANITA Balloon-borne Radio Interferometer*, *Phys. Rev. Lett.* **105** (2010) 151101 [`1005.0035`].

[127] H. Schoorlemmer et al., *Energy and Flux Measurements of Ultra-High Energy Cosmic Rays Observed During the First ANITA Flight*, *Astropart. Phys.* **77** (2016) 32 [`1506.05396`].

[128] PUEO collaboration, *The Payload for Ultrahigh Energy Observations (PUEO): a white paper*, *JINST* **16** (2021) P08035 [`2010.02892`].

[129] E. Vitagliano, I. Tamborra et al., *Grand Unified Neutrino Spectrum at Earth: Sources and Spectral Components*, *Rev. Mod. Phys.* **92** (2020) 45006 [`1910.11878`].

[130] J. A. Formaggio and G. P. Zeller, *From eV to EeV: Neutrino Cross Sections Across Energy Scales*, *Rev. Mod. Phys.* **84** (2012) 1307 [`1305.7513`].

[131] ICECUBE collaboration, *Measurement of the multi-TeV neutrino cross section with IceCube using Earth absorption*, *Nature* **551** (2017) 596 [`1711.08119`].

[132] A. Connolly, R. S. Thorne et al., *Calculation of High Energy Neutrino-Nucleon Cross Sections and Uncertainties Using the MSTW Parton Distribution Functions and Implications for Future Experiments*, *Phys. Rev. D* **83** (2011) 113009 [`1102.0691`].

[133] S. L. Glashow, *Resonant Scattering of Antineutrinos*, *Phys. Rev.* **118** (1960) 316.

[134] ICECUBE collaboration, *Detection of a particle shower at the Glashow resonance with IceCube*, *Nature* **591** (2021) 220.

[135] S. I. Klimushin, E. V. Bugaev et al., *Precise parametrizations of muon energy losses in water*, in *27th International Cosmic Ray Conference*, 6, 2001, `hep-ph/0106010`.

[136] Y. S. Jeong, M. V. Luu et al., *Tau energy loss and ultrahigh energy skimming tau neutrinos*, *Phys. Rev. D* **96** (2017) 043003 [`1704.00050`].

[137] D. García-Fernández, A. Nelles et al., *Signatures of secondary leptons in radio-neutrino detectors in ice*, *Phys. Rev. D* **102** (2020) 083011 [`2003.13442`].

[138] C. Glaser et al., *NuRadioMC: Simulating the radio emission of neutrinos from interaction to detector*, *Eur. Phys. J. C* **80** (2020) 77 [`1906.01670`].

[139] L. D. Landau and I. Pomeranchuk, *Limits of applicability of the theory of bremsstrahlung electrons and pair production at high-energies*, *Dokl. Akad. Nauk Ser. Fiz.* **92** (1953) 535.

[140] A. B. Migdal, *Bremsstrahlung and pair production in condensed media at high-energies*, *Phys. Rev.* **103** (1956) 1811.

[141] S. Klein, *Suppression of Bremsstrahlung and pair production due to environmental factors*, *Rev. Mod. Phys.* **71** (1999) 1501 [`hep-ph/9802442`].

[142] J. Alvarez-Muniz and E. Zas, *The LPM effect for EeV hadronic showers in ice: Implications for radio detection of neutrinos*, *Phys. Lett. B* **434** (1998) 396 [`astro-ph/9806098`].

[143] ICECUBE collaboration, *An improved muon track reconstruction for IceCube*, *PoS* **ICRC2019** (2021) 846 [`1908.07961`].

[144] KM3NET collaboration, *KM3NeT/ARCA Event Reconstruction Algorithms*, *PoS* **ICRC2017** (2018) 950.

[145] ICECUBE collaboration, *Characterization of the Atmospheric Muon Flux in IceCube*, *Astropart. Phys.* **78** (2016) 1 [`1506.07981`].

[146] KM3NET collaboration, *Comparison of the measured atmospheric muon rate with Monte Carlo simulations and sensitivity study for detection of prompt atmospheric muons with KM3NeT*, *JINST* **16** (2021) C09035 [`2110.10016`].

[147] ICECUBE collaboration, *IceTop as veto for IceCube: results*, *PoS* **ICRC2019** (2020) 445 [`1908.07008`].

[148] ICECUBE collaboration, *Energy Reconstruction Methods in the IceCube Neutrino Telescope*, *JINST* **9** (2014) P03009 [`1311.4767`].

[149] ANTARES collaboration, *ANTARES: the first undersea neutrino telescope*, *Nucl. Instrum. Meth. A* **656** (2011) 11 [`1104.1607`].

[150] ANTARES collaboration, *All-flavor Search for a Diffuse Flux of Cosmic Neutrinos with Nine Years of ANTARES Data*, *Astrophys. J. Lett.* **853** (2018) L7 [`1711.07212`].

[151] ANTARES collaboration, *Measurement of Atmospheric Neutrino Oscillations with the ANTARES Neutrino Telescope*, *Phys. Lett. B* **714** (2012) 224 [`1206.0645`].

[152] KM3NET collaboration, *Letter of intent for KM3NeT 2.0*, *J. Phys. G* **43** (2016) 084001 [`1601.07459`].

[153] KM3NET collaboration, *Atmospheric neutrinos with the first detection units of KM3NeT-ARCA*, *PoS* **ICRC2021** (2021) 1134 [`2107.12721`].

[154] KM3NET collaboration, *Comparison of the measured atmospheric muon rate with Monte Carlo simulations and sensitivity study for detection of prompt atmospheric muons with KM3NeT*, *PoS* **ICRC2021** (2021) 1112 [`2107.09347`].

[155] KM3NET collaboration, *First neutrino oscillation measurement in KM3NeT/ORCA*, *PoS* **ICRC2021** (2021) 1123.

[156] BAIKAL-GVD collaboration, *Neutrino Telescope in Lake Baikal: Present and Nearest Future*, *PoS* **ICRC2021** (2021) 002 [`2109.14344`].

[157] BAIKAL-GVD collaboration, *Observations of track-like neutrino events with Baikal-GVD*, *PoS* **ICRC2021** (2021) 1177 [`2108.04704`].

[158] BAIKAL-GVD collaboration, *The Baikal-GVD neutrino telescope: search for high-energy cascades*, *PoS* **ICRC2021** (2021) 1144 [`2108.01894`].

[159] ICECUBE collaboration, *The IceCube Neutrino Observatory: Instrumentation and Online Systems*, *JINST* **12** (2017) P03012 [`1612.05093`].

[160] ICECUBE collaboration, *The Design and Performance of IceCube DeepCore*, *Astropart. Phys.* **35** (2012) 615 [`1109.6096`].

[161] ICECUBE collaboration, *Characteristics of the diffuse astrophysical electron and tau neutrino flux with six years of IceCube high energy cascade data*, *Phys. Rev. Lett.* **125** (2020) 121104 [`2001.09520`].

[162] ICECUBE-GEN2 collaboration, *IceCube-Gen2: the window to the extreme Universe*, *J. Phys. G* **48** (2021) 060501 [`2008.04323`].

[163] ANTARES collaboration, *Transmission of light in deep sea water at the site of the ANTARES Neutrino Telescope*, *Astropart. Phys.* **23** (2005) 131 [`astro-ph/0412126`].

[164] A. Avrorin, V. Aynutdinov et al., *Asp-15—a stationary device for the measurement of the optical water properties at the nt200 neutrino telescope site, Nuclear Instruments and Methods in Physics Research Section A: Accelerators, Spectrometers, Detectors and Associated Equipment* **693** (2012) 186.

[165] M. Ackermann et al., *Optical properties of deep glacial ice at the South Pole*, *J. Geophys. Res.* **111** (2006) D13203.

[166] T. Huege and D. Besson, *Radio-wave detection of ultra-high-energy neutrinos and cosmic rays*, *Progress of Theoretical and Experimental Physics* **2017** (2017) .

[167] D. Saltzberg et al., *Observation of the Askaryan Effect: Coherent Microwave Cherenkov Emission from Charge Asymmetry in High-Energy Particle Cascades*, *Physical Review Letters* **86** (2001) 2802–2805.

[168] P. W. Gorham et al., *Accelerator measurements of the Askaryan effect in rock salt: A Roadmap toward teraton underground neutrino detectors*, *Phys. Rev. D* **72** (2005) 023002 [`astro-ph/0412128`].

[169] ANITA collaboration, *Observations of the Askaryan effect in ice*, *Phys. Rev. Lett.* **99** (2007) 171101 [`hep-ex/0611008`].

[170] ARA collaboration, *Simulation of Ultrahigh Energy Neutrino Radio Signals in the ARA Experiment*, in *33rd International Cosmic Ray Conference*, p. 1161, 2013.

[171] J. Alvarez-Muniz and E. Zas, *Cherenkov radio pulses from Eev neutrino interactions: The LPM effect*, *Phys. Lett. B* **411** (1997) 218 [`astro-ph/9706064`].

[172] J. Alvarez-Muniz, R. A. Vazquez et al., *Calculation methods for radio pulses from high-energy showers*, *Phys. Rev. D* **62** (2000) 063001 [`astro-ph/0003315`].

[173] J. Alvarez-Muniz, A. Romero-Wolf et al., *Cherenkov radio pulses from electromagnetic showers in the time-domain*, *Phys. Rev. D* **81** (2010) 123009 [`1002.3873`].

[174] M. Reininghaus and R. Ulrich, *CORSIKA 8 – Towards a modern framework for the simulation of extensive air showers*, *EPJ Web Conf.* **210** (2019) 02011 [`1902.02822`].

[175] T. Huege and C. W. James, *Full Monte Carlo simulations of radio emission from extensive air showers with CoREAS*, in *33rd International Cosmic Ray Conference*, p. 0548, 7, 2013, `1307.7566`.

[176] RNO-G collaboration, *The Radio Neutrino Observatory Greenland (RNO-G)*, *PoS* **ICRC2021** (2021) 001.

[177] S. W. Barwick et al., *Observation of classically 'forbidden' electromagnetic wave propagation and implications for neutrino detection*, *JCAP* **07** (2018) 055 [`1804.10430`].

[178] C. Deaconu, A. G. Vieregg et al., *Measurements and Modeling of Near-Surface Radio Propagation in Glacial Ice and Implications for Neutrino Experiments*, *Phys. Rev. D* **98** (2018) 043010 [`1805.12576`].

[179] J. Avva, J. M. Kovac et al., *An in situ measurement of the radio-frequency attenuation in ice at Summit Station, Greenland*, *J. Glaciol.* **61** (2015) 1005 [`1409.5413`].

[180] T. Barrella, S. Barwick et al., *Ross Ice Shelf in situ radio-frequency ice attenuation*, *J. Glaciol.* **57** (2011) 61 [`1011.0477`].

[181] D. Z. Besson et al., *In situ radioglaciological measurements near Taylor Dome, Antarctica and implications for UHE neutrino astronomy*, *Astropart. Phys.* **29** (2008) 130 [`astro-ph/0703413`].

[182] S. Barwick, D. Besson et al., *South polar in situ radio-frequency ice attenuation*, *Journal of Glaciology* **51** (2005) 231–238.

[183] D. Besson, I. Kravchenko et al., *Radio Frequency Birefringence in South Polar Ice and Implications for Neutrino Reconstruction*, *Astropart. Phys.* **34** (2011) 755 [`1005.4589`].

[184] R. L. Hawley, T. A. Neumann et al., *Greenland ice sheet elevation change: Direct observation of process and attribution at summit*, *Geophysical Research Letters* **47** (2020) e2020GL088864 [`https://agupubs.onlinelibrary.wiley.com/doi/pdf/10.1029/2020GL088864`].

[185] L. Pyras, I. Plaisier et al., *Radio Detection of EeV Neutrinos in Dielectric Media using the Askaryan Effect*. DESY, 2022, 10.3204/PUBDB-2021-03021.

[186] PIERRE AUGER collaboration, *Probing the origin of ultra-high-energy cosmic rays with neutrinos in the EeV energy range using the Pierre Auger Observatory*, *JCAP* **10** (2019) 022 [`1906.07422`].

[187] GRAND collaboration, *The Giant Radio Array for Neutrino Detection (GRAND): Science and Design*, *Sci. China Phys. Mech. Astron.* **63** (2020) 219501 [`1810.09994`].

[188] J. W. Nam et al., *Design and implementation of the TAROGE experiment*, *Int. J. Mod. Phys. D* **25** (2016) 1645013.

[189] ANITA collaboration, *Observational Constraints on the Ultra-high Energy Cosmic Neutrino Flux from the Second Flight of the ANITA Experiment*, *Phys. Rev. D* **82** (2010) 022004 [`1003.2961`].

[190] ANITA collaboration, *Constraints on the diffuse high-energy neutrino flux from the third flight of ANITA*, *Phys. Rev. D* **98** (2018) 022001 [`1803.02719`].

[191] ANITA collaboration, *Constraints on the ultrahigh-energy cosmic neutrino flux from the fourth flight of ANITA*, *Phys. Rev. D* **99** (2019) 122001 [`1902.04005`].

[192] ANITA collaboration, *Characteristics of Four Upward-pointing Cosmic-ray-like Events Observed with ANITA*, *Phys. Rev. Lett.* **117** (2016) 071101 [`1603.05218`].

[193] ANITA collaboration, *Observation of an Unusual Upward-going Cosmic-ray-like Event in the Third Flight of ANITA*, *Phys. Rev. Lett.* **121** (2018) 161102 [`1803.05088`].

[194] ANITA collaboration, *Unusual Near-Horizon Cosmic-Ray-like Events Observed by ANITA-IV*, *Phys. Rev. Lett.* **126** (2021) 071103 [`2008.05690`].

[195] J. H. Collins, P. S. Bhupal Dev et al., *R-parity Violating Supersymmetric Explanation of the Anomalous Events at ANITA*, *Phys. Rev. D* **99** (2019) 043009 [`1810.08479`].

[196] L. Heurtier, Y. Mambrini et al., *Dark matter interpretation of the ANITA anomalous events*, *Phys. Rev. D* **99** (2019) 095014 [`1902.04584`].

[197] P. Motloch, J. Alvarez-Muñiz et al., *Can transition radiation explain the ANITA event 3985267?*, *Phys. Rev. D* **95** (2017) 043004 [`1606.07059`].

[198] I. M. Shoemaker, A. Kusenko et al., *Reflections On the Anomalous ANITA Events: The Antarctic Subsurface as a Possible Explanation*, *Annals Glaciol.* **61** (2020) 92 [`1905.02846`].

[199] D. Smith et al., *Experimental tests of sub-surface reflectors as an explanation for the ANITA anomalous events*, *JCAP* **04** (2021) 016 [`2009.13010`].

[200] RICE, ARA collaboration, *Status of RICE and preparations for the next generation radio neutrino experiment in Antarctica*, *Nucl. Instrum. Meth. A* **692** (2012) 233.

[201] I. Kravchenko, S. Hussain et al., *Updated Results from the RICE Experiment and Future Prospects for Ultra-High Energy Neutrino Detection at the South Pole*, *Phys. Rev. D* **85** (2012) 062004 [`1106.1164`].

[202] ARA collaboration, *Constraints on the diffuse flux of ultrahigh energy neutrinos from four years of Askaryan Radio Array data in two stations*, *Phys. Rev. D* **102** (2020) 043021 [`1912.00987`].

[203] P. Allison et al., *Design and performance of an interferometric trigger array for radio detection of high-energy neutrinos*, *Nucl. Instrum. Meth. A* **930** (2019) 112 [`1809.04573`].

[204] ARIANNA collaboration, *Targeting ultra-high energy neutrinos with the ARIANNA experiment*, *Adv. Space Res.* **64** (2019) 2595 [`1903.01609`].

[205] ARIANNA collaboration, *Probing the angular and polarization reconstruction of the ARIANNA detector at the South Pole*, *JINST* **15** (2020) P09039 [`2006.03027`].

[206] RNO-G collaboration, *Design and Sensitivity of the Radio Neutrino Observatory in Greenland (RNO-G)*, *JINST* **16** (2021) P03025 [`2010.12279`].

[207] C. Glaser, A. Nelles et al., *NuRadioReco: A reconstruction framework for radio neutrino detectors*, *Eur. Phys. J. C* **79** (2019) 464 [`1903.07023`].

[208] G. Gaswint, *Quantifying the Neutrino Energy and Pointing Resolution of the ARIANNA Detector*, Ph.D. thesis, University Of California Irvine, 2021.

[209] RNO-G collaboration, *Direction Reconstruction for the Radio Neutrino Observatory Greenland (RNO-G)*, *PoS* **ICRC2021** (2021) 1026.

[210] ARIANNA collaboration, *Capabilities of ARIANNA: Neutrino Pointing Resolution and Implications for Future Ultra-high Energy Neutrino Astronomy*, *PoS* **ICRC2021** (2021) 1151.

[211] T. A. Enßlin, *Information field theory*, *AIP Conference Proceedings* **1553** (2013) 184 [`https://aip.scitation.org/doi/pdf/10.1063/1.4819999`].

[212] T. A. Enßlin, *Information theory for fields*, *Annalen der Physik* **531** (2019) 1800127 [`https://onlinelibrary.wiley.com/doi/pdf/10.1002/andp.201800127`].

[213] C. Glaser, S. McAleer et al., *Deep learning reconstruction of the neutrino energy with a shallow Askaryan detector*, *PoS* **ICRC2021** (2021) 1051.